



**LUT**  
Lappeenranta  
University of Technology

Giteshkumar Patel

## **COMPUTATIONAL FLUID DYNAMICS ANALYSIS OF STEAM CONDENSATION IN NUCLEAR POWER PLANT APPLICATIONS**

Thesis for the degree of Doctor of Science (Technology) to be presented with due permission for public examination and criticism in the room 2305 at Lappeenranta University of Technology, Lappeenranta, Finland on the 4<sup>th</sup> of April, 2017, at noon.

Acta Universitatis  
Lappeenrantaensis 738

- Supervisor Professor Juhani Hyvärinen  
LUT School of Energy Systems  
Lappeenranta University of Technology  
Finland
- Associate Professor Teemu Turunen-Saaresti  
LUT School of Energy Systems  
Lappeenranta University of Technology  
Finland
- Reviewers Professor Satoru Yamamoto  
Mathematical Modeling and Computation Lab  
Tohoku University  
Japan
- Doctor Marco Pellegrini  
Institute of Applied Energy  
Nuclear Power Engineering Center  
Japan
- Opponent Associate Professor Pavel Kudinov  
School of Engineering Science  
KTH Royal Institute of Technology  
Sweden

ISBN 978-952-335-061-8  
ISBN 978-952-335-062-5 (PDF)  
ISSN-L 1456-4491  
ISSN 1456-4491  
Lappeenrannan teknillinen yliopisto  
Yliopistopaino 2017

# Abstract

**Giteshkumar Patel**

**Computational fluid dynamics analysis of steam condensation in nuclear power plant applications**

Lappeenranta 2017

176 pages

Acta Universitatis Lappeenrantaensis 738

Diss. Lappeenranta University of Technology

ISBN 978-952-335-061-8, ISBN 978-952-335-062-5 (PDF)

ISSN-L 1456-4491, ISSN 1456-4491

Detailed experimental and numerical investigations of safety systems and various key components of nuclear power plant are important from both view points of safety and economical aspects. This thesis presents the computational fluid dynamics (CFD) analysis of steam condensation phenomena appearing in a pressure suppression pool (PSP) of a boiling water reactor (BWR) and in a low-pressure (LP) steam turbine.

The PSP is one of the key systems which provide a large pressure and heat sink by condensing steam into a denser volume of water. In this thesis, two direct contact condensation (DCC) modes appearing during steam blowdown in BWR PSP are investigated. 2D and 3D simulations of a PSP test facility were conducted by using the Eulerian-Eulerian two-fluid approach. For this purpose, two CFD codes, OpenFOAM and NEPTUNE\_CFD were used. The interfacial heat transfer between steam and water was modelled by using different DCC models. The open pool test facility (POOLEX) and the pressurizing drywell-wetwell suppression pool facility (PPOOLEX) tests of Lappeenranta University of Technology (LUT) were used as references. Various issues namely performance of DCC models, significance of reference bubble diameter, and sensitivity of subcooling rate on DCC phenomena were studied. The results confirmed that the surface divergence model by Lakehal et al. (2008) predicts the mildly sheared interfacial DCC case well. The incompressible solver was not able to predict rapid pressure variation in chugging simulations. The compressible two-phase solver of OpenFOAM was stable enough and able to invoke the chugging phenomenon of POOLEX steam blowdown tests. The surface renewal model of by Hughes and Duffey (1991) and the DCC model of Coste (2004) achieved good predictions of the chugging simulations of the POOLEX test. The influence of grid refinement on the DCC phenomena was assessed employing a grid convergence index for POOLEX simulations. Results indicate that an adequate grid density is essential to resolve the flow details and to acquire the correct rates of DCC. In the PPOOLEX chugging simulations, different issues namely the performance of different DCC models, the influence of turbulence modeling, interfacial momentum transfer, geometry and interface initialization were briefly analyzed. The significance of interfacial area modelling on the chugging DCC was examined by employing the Rayleigh-Taylor Interfacial area model by Pellegrini et al. (2015). The results showed that interfacial area

modeling and turbulence modelling were the dominant factors for the chugging DCC modelling in the PPOOLEX simulations.

Steam turbines are vital for power generation, and therefore, the studies aiming to the efficiency improvement of steam turbines are crucial for efficient power plants. As the exhaust pressure of steam turbines is designed to be low to achieve the maximum energy output, the steam temperature drops due to rapid expansion in the last stages of the LP steam turbine. Steam condenses and, as a result, additional losses appear. The presence of moisture in the LP turbine decreases the overall efficiency. This thesis was partially aimed to study the non-equilibrium condensing steam flow in LP turbine by using the ANSYS CFD codes. In all simulations, the mixture of vapour and liquid phases was solved by employing Reynolds-averaged Navier-Stokes equations based on the Eulerian-Eulerian approach. The classical nucleation theory was adopted to model nucleation process. Droplet growth models were used to calculate the droplet growth rate. Throughout this work, condensing steam flows were modelled with various computational domains including convergent-divergent nozzles, a stationary cascade of turbine and 3D stator-rotor stage. The influence of local geometrical details of steam turbine blades including blade trailing edge shapes, dimple inclusion and blade surface tapering on the flow expansion, condensation phenomena and corresponding loss generation was studied. The study demonstrated that the shape and size of the blades have a significant impact on the entire condensing flow field and the loss generation in the LP turbine. The results revealed that the elliptic trailing edge shape resulted in minimum losses. After including dimple profiles, the Wilson point was altered and the location of condensation disturbance was changed. Overall 8% reduction was noted in total loss with 100  $\mu\text{m}$  dimple profile compared to the base profile without dimple. The influence of turbulence modelling studies revealed that the accurate turbulence modelling is required for precise condensing steam flow prediction. The modified two-equation turbulence models are able to predict accurate wet-steam flows.

**Keywords:** CFD, Steam, Two-phase flow, Condensation, Pressure suppression pool, Low-pressure steam turbine, Interfacial area, Chugging, Surface tapering, Trailing edge, Dimple, Turbulence modelling, Loss coefficients

## Acknowledgements

This work was carried out in the LUT School of Energy Systems at Lappeenranta University of Technology (LUT), Finland, between 2011 and 2017. The research conducted in this study has received funding from the Finnish Nuclear Waste Management Fund (VYR) via The Finnish Research Programmes on Nuclear Power Plant Safety SAFIR2014 and SAFIR2018, from the Academy of Finland via the Doctoral Programme for Nuclear Engineering and Radiochemistry (YTERA) and from the Finnish Cultural Foundation.

First and foremost, I express my sincere gratitude to my supervisors Professor Juhani Hyvärinen and Associate Professor Teemu Turunen-Saaresti for their advice, support, and willingness to allow me to pursue this research. It has been a great pleasure working with and learning from them. I would also like to thank my supervisors for their encouragement to participate in several national/international courses and conferences.

I am grateful to Professor Saturo Yamamoto and Dr. Marco Pellegrini for reviewing and evaluating the thesis. Their insightful comments and suggestions helped a great deal to improve the thesis.

Two persons, Dr. Vesa Tanskanen and Dr. Yogini Patel, deserve my warmest thanks for their help, offering valuable advice, constructive ideas during this work, and especially for their patience and feedback during the writing process. It has been a wonderful experience working with them.

I express my profound gratitude to Riitta Kyrki-Rajamäki, Professor Emerita, LUT, for her supervision, thoughtful advice, and all the support she provided during this work. Without her help this project would not have been possible.

I also express my sincere thanks to Dr. Timo Pättikangas and Mr. Juho Peltola from VTT for their assistance and help during the work.

I wish to thank Dr. Heikki Purhonen, Dr. Vesa Tanskanen, Ms. Anne Jordan, Ms. Elina Hujala and Mr. Ville Rintala for their friendly talks and interesting discussions especially during coffee breaks. I would also like to thank Dr. Juhani Vihavainen, Mr. Markku Puustinen, Dr. Heikki Suikkanen and Mr. Lauri Pyy. I gratefully acknowledge Professor Jari Backman and Associate Professor Aki Grönman. It is a pleasure to thank all of my colleagues and friends at the Nuclear Engineering Laboratory, the Nuclear Safety Research Unit and the Laboratory of Fluid Dynamics at LUT. I also wish to thank the CSC-IT Center for Science Ltd., Finland, for allowing me to use their cluster.

It is my fortune to gratefully acknowledge the support of some special individuals, Ms. Heta Jurvanen and Mr. Tomppa Jurvanen. They were always beside me during the happy and hard moments to push me and motivate me. I cannot express my deepest feelings and high appreciation through this acknowledgement sufficiently since they deserve much more.

Most importantly, I wish to express my deep gratitude to my parents, Narayanbhai and

Sitaben, for their unconditional love, constant inspiration, and giving me the life I dreamed of. Without their encouragement, I would have never imagined achieving this height in my career. Both have always expressed how proud they are of me and how much they love me. I, too, am proud of them and love them very much. Words cannot express the feelings I have for my family and for other loved ones for their kind support, patience, and motivation during this journey. I am especially grateful to my dear brother, Rakesh, and sister, Surekha, and their families for their unfailing support and love. I also convey my appreciation to Yogini's family for their kind support. Finally, I would like to thank Yogini for her endless love, patience, support and unwavering belief in me throughout this entire journey. For all these reasons and many, many more, I am eternally grateful. Thank you, Yogini, for being persistent, for encouraging me, and for the many precious memories along the way.

Gitesh Patel  
March 2017  
Lappeenranta, Finland

*To my family*



# Contents

**Abstract**

**Acknowledgments**

**Contents**

<b>List of publications</b>	<b>11</b>
<b>Nomenclature</b>	<b>15</b>
<b>1 Introduction</b>	<b>19</b>
1.1 Background . . . . .	19
1.2 Objective of the study . . . . .	25
1.3 Outline of the thesis . . . . .	28
<b>2 Literature review</b>	<b>29</b>
2.1 A brief review of pressure suppression pool studies . . . . .	29
2.1.1 Experimental studies of pressure suppression pool . . . . .	29
2.1.2 Theoretical developments . . . . .	31
2.1.3 Numerical studies . . . . .	32
2.2 A brief review of condensing steam flow studies in LP turbines . . . . .	33
2.2.1 Experimental studies on wet-steam flows . . . . .	33
2.2.2 Theoretical and numerical developments on wet-steam flows . . . . .	35
<b>3 Pressure suppression pool experiments</b>	<b>37</b>
3.1 POOLEX experiments . . . . .	37
3.1.1 POOLEX STB-31 experiment . . . . .	37
3.1.2 POOLEX STB-28 experiment . . . . .	41
3.2 PPOOLEX experiments . . . . .	43
3.2.1 PPOOLEX DCC-05 experiment . . . . .	45
<b>4 Numerical modelling</b>	<b>47</b>
4.1 Physical models for DCC in suppression pool . . . . .	47
4.1.1 Governing equations . . . . .	47
4.1.2 Phase change and heat transfer models . . . . .	48
4.1.3 Turbulence models . . . . .	51
4.1.4 Rayleigh-Taylor instability (RTI) model . . . . .	52
4.1.5 Thermodynamics properties for DCC simulations . . . . .	54
4.2 Physical models for condensing steam flows in LP turbine . . . . .	54
4.2.1 Governing equations . . . . .	54
4.2.2 Models for nucleation and droplet growth . . . . .	55
4.2.3 Equation of state and thermodynamic properties . . . . .	57
4.2.4 Turbulence models . . . . .	58

4.3	Grid convergence error . . . . .	60
<b>5</b>	<b>Computational models and simulation strategies</b>	<b>63</b>
5.1	CFD models of pressure suppression pool . . . . .	63
5.1.1	Geometrical details and grid generation . . . . .	63
5.1.2	Simulation set-up . . . . .	68
5.2	CFD models of wet-steam flows . . . . .	71
5.2.1	Geometrical details and grid generation . . . . .	71
5.2.2	Simulation set-up . . . . .	77
<b>6</b>	<b>Analysis of CFD results of pressure suppression pool</b>	<b>79</b>
6.1	Results of POOLEX STB-31 experiment . . . . .	79
6.1.1	Grid independence study . . . . .	79
6.1.2	Comparison of CFD results . . . . .	82
6.2	Results of POOLEX STB-28 experiment . . . . .	88
6.2.1	Influence of grid on chugging . . . . .	91
6.2.2	Influence of DCC model on chugging . . . . .	96
6.2.3	Influence of subcooling rate on chugging . . . . .	101
6.3	Results of PPOOLEX DCC-05 experiment . . . . .	110
<b>7</b>	<b>CFD simulation results of wet-steam flows</b>	<b>121</b>
7.1	Analysis of turbine blade shape influence on condensing steam flows . . .	121
7.1.1	Effect of blade trailing edge shape . . . . .	122
7.1.2	Effect of dimple pattern on blade surface . . . . .	129
7.1.3	Effect of blade surface tapering . . . . .	134
	7.1.3.1 Pressure surface tapering . . . . .	134
	7.1.3.2 Suction surface tapering . . . . .	138
7.2	Analysis of turbulence modelling influence on condensing steam flows . .	141
<b>8</b>	<b>Conclusions and Suggestions for Future Research</b>	<b>153</b>
8.1	Conclusions . . . . .	153
8.1.1	Direct contact condensation modelling of pressure suppression pool tests . . . . .	153
8.1.2	Condensation modelling of LP turbine flows . . . . .	155
8.2	Future suggestions . . . . .	158
	<b>References</b>	<b>159</b>

---

## List of publications

This thesis is based on the following publications which are referred to in the text as I-VI. The publications are reproduced with kind permission from the publishers.

- I** Patel, G., Tanskanen, V., Kyrki-Rajamäki, R. (2014). Numerical modelling of low-Reynolds number direct contact condensation in a suppression pool test facility. *Annals of Nuclear Energy*. Vol. 71, pp. 376-387.
- II** Patel, G., Tanskanen, V., Rintala, V., Hyvärinen, J. (2015). Numerical study of direct contact condensation of steam on stable interface in a BWR suppression pool test facility. *In: The 16th International Topical Meeting on Nuclear Reactor Thermal Hydraulics (NURETH-16)*. Chicago, IL, USA. pp. 1-14.
- III** Patel, G., Tanskanen, V., Hujala, E., Hyvärinen, J. (2016). Direct contact condensation modeling in pressure suppression pool system (SI:NURESAFE 2016). *Nuclear Engineering and Design*. Vol. xx, pp. xx-xx. In Press.
- IV** Patel, Y., Patel, G., and Turunen-Saaresti, T. (2015). Influence of turbulence modelling on non-equilibrium condensing flows in nozzle and turbine cascade. *International Journal of Heat and Mass Transfer*. Vol. 88, pp. 165-180.
- V** Patel, G., Patel, Y., and Turunen-Saaresti, T. (2015). Influence of trailing edge geometry on the condensing steam flow in low-pressure steam turbine. *In: Proceedings of ASME Turbo Expo 2015: Turbine Technical Conference and Exposition*. Montreal, Canada. Vol. 8, pp. 1-11.
- VI** Patel, Y., Patel, G., and Turunen-Saaresti, T. (2016). Influence of turbulence modelling to condensing steam flow in the 3D low-pressure steam turbine stage. *In: Proceedings of ASME Turbo Expo 2016: Turbomachinery Technical Conference and Exposition*. Seoul, South Korea. pp. 1-11.

## **Author's contribution**

The author's contribution to the publications I-VI is discussed below.

### **Publication I**

The author was responsible for the planning of the paper. The author implemented the models into the two-phase flow solver of OpenFOAM used in this paper. All the simulations with OpenFOAM CFD code were conducted by the author. The paper was written and revised together with the co-author, Vesa Tanskanen, D.Sc.

### **Publication II**

The author was in charge of the preparation of the paper and performed all the numerical simulations. The paper was post-processed and written by the author. The paper was revised by the author together with the help of co-authors.

### **Publication III**

The author participated in the planning of the paper. All the simulated results of OpenFOAM CFD code were carried out by the author. The author designed the CFD model and the corresponding grid generation in it. The author participated in the writing of the paper and its revision together with the co-author, Vesa Tanskanen, D.Sc.

### **Publication IV**

The author participated in the planning of the paper and the corresponding CFD simulations. The author contributed to the post-processing of the CFD results, as well as the writing and revising of the paper.

### **Publication V**

The author planned the paper. The grid generation and CFD simulations were done by the author with the help of the co-author, Yogini Patel, D.Sc. The author revised the paper together with co-authors.

### **Publication VI**

The author participated in the design of the CFD model and the corresponding grid generation utilized to the paper. The author contributed in the post-processing and the writing of the paper.

## Other publications

In addition to Publications I-VI, the author has written technical reports on the simulations of direct contact condensation in the pressure suppression pool (PSP) systems. During the course of study, the author has written and also contributed to other papers on condensation modelling in nuclear power plant applications. These publications are listed below.

1. Patel, G., Tanskanen, V., (2012). CFD simulation of air Discharge into the suppression pool with OpenFOAM. *SAFIR2014 Research Report*. NuFoam-1/2011. Lappeenranta University of Technology. pp. 1-27.
2. Patel, G., Tanskanen, V., (2013). Implementation of DCC models to OpenFOAM and initial CFD calculations of STB-31 POOLEX experiment. *SAFIR2014 Research Report*. NuFoam-1/2012. Lappeenranta University of Technology. pp. 1-31.
3. Patel, G., Tanskanen, V., (2014). CFD modeling of the STB-31 POOLEX experiment. *SAFIR2014 Research Report*. NuFoam-1/2013. Lappeenranta University of Technology. pp. 1-26.
4. Patel, G., Tanskanen, V., (2015). CFD modelling of the STB-28 POOLEX experiment with OpenFOAM. *SAFIR2014 Research Report*. NuFoam-1/2014. Lappeenranta University of Technology. pp. 1-20.
5. Patel, G., Tanskanen, V., (2016). Comparison of Eulerian OpenFOAM and NEPTUNE\_CFD results for chugging condensation mode. *SAFIR2018 Research Report*. NURESA-D3.3.1/2015. Lappeenranta University of Technology. pp. 1-29.
6. Patel, G., Tanskanen, V., Kyrki-Rajamäki, R., (2013). CFD modeling of low rate direct contact condensation phenomena in a pressure suppression pool by Eulerian two-phase flow approach, *In: Open Source CFD International Conference*, Hamburg, Germany, pp. 1-16.
7. Tanskanen, V., Patel, G., Puustinen, M., Hujala, E., Kyrki-Rajamäki, R., Hyvärinen, J., (2015). CFD modelling of chugging condensation regime of BWR suppression pool experiments. *In: The 16th International Topical Meeting on Nuclear Reactor Thermal Hydraulics (NURETH-16)*. Chicago, IL, USA. pp. 1-14.
8. Patel, G., Tanskanen, V., Hujala, E., Hyvärinen, J. (2016). Numerical modelling of direct contact condensation of steam in BWR pressure suppression pool system, Nuclear Science and Technology Symposium-NST2016, Helsinki, Finland, pp. 1-4.
9. Patel, Y., Patel, G., and Turunen-Saaresti, T., (2013). The effect of turbulence and real gas models on the two phase spontaneously condensing flows in nozzle. *In: Proceedings of ASME Turbo Expo 2013: Turbine Technical Conference and Exposition*. San Antonio, Texas, USA, Vol. 5B, pp.1-8.

10. Patel, Y., Turunen-Saaresti, T., Patel, G., and Grönman, A., (2014). Numerical investigation of turbulence modelling on condensing steam flows in turbine cascade. *In: Proceedings of ASME Turbo Expo 2014: Turbine Technical Conference and Exposition*. Düsseldorf, Germany, Vol. 1B, pp. 1-14.
11. Patel, G., Patel, Y., Turunen-Saaresti, T., and Grönman, A., (2017). Numerical investigation of turbulence modelling on condensing steam flows in turbine cascade. *In: Proceedings of ASME Turbo Expo 2017: Turbomachinery Technical Conference and Exposition*. Charlotte, NC, USA, pp. 1-11.

## Nomenclature

### Latin alphabet

$a_i$	interfacial area	$m^{-1}$
$A$	Atwood number	—
$B, C$	virial coefficients	—
$C_p$	specific heat at constant pressure	$J\ kg^{-1}\ K^{-1}$
$C_v$	specific heat at constant volume	$J\ kg^{-1}\ K^{-1}$
$C_D$	drag coefficient	—
$d$	bubble diameter	$m$
$D_{T,eff}$	phase effective thermal diffusivity	$m^2\ s^{-1}$
$e_a$	relative error	—
$f_u$	droplet response coefficient	—
$g$	gravitational acceleration	$m\ s^{-2}$
$G$	production	$kg\ m^{-1}\ s^{-3}$
$h$	specific enthalpy	$J\ kg^{-1}$
$K_t$	thermal conductivity	$W\ m^{-1}\ K^{-1}$
$h_i$	heat transfer coefficients	$W\ m^{-2}\ K^{-1}$
$h_{lv}$	specific enthalpy of evaporation	$J\ kg^{-1}$
$H$	total enthalpy	$J\ kg^{-1}$
$H_i$	interfacial enthalpy	$J\ kg^{-1}$
$I$	nucleation rate	$m^{-3}\ s^{-1}$
$k$	turbulence kinetic energy	$m^2\ s^{-2}$
$K_b$	Boltzmann's constant	—
$Kn$	Knudsen number	—
$L$	length scale	$m$
$M$	liquid mass	$kg$
$M_m$	molecular mass	$kg\ mol^{-1}$
$N_d$	number of liquid droplets per unit volume	$m^{-3}$
$N$	total number of cells	—
$Nu$	Nusselt number	—
$P$	pressure	$Pa$
$Pr$	Prandtl number	—
$q$	heat flux	$W\ m^{-2}$
$q_c$	condensation coefficient	—
$q_m$	mass flow rate	$kg\ s^{-1}$
$Q$	volumetric interfacial heat transfer rate	$W\ m^{-3}$
$r$	radius	$m$
$r_*$	critical radius	$m$
$\bar{r}$	average radius	$m$

$\mathbf{R}_T$	turbulent stress tensor	Pa
$R$	gas constant	$\text{J kg}^{-1} \text{K}^{-1}$
$Re$	Reynolds number	—
$s$	entropy	$\text{J kg}^{-1} \text{K}^{-1}$
$S$	supersaturation	—
$S_k$	turbulence kinetic energy source term	$\text{kg m}^{-1} \text{s}^{-3}$
$S_C$	mass source term	$\text{kg m}^{-2} \text{s}^{-1}$
$S_E$	energy source term	$\text{W m}^{-3}$
$S_M$	momentum source term	$\text{kg m}^{-2} \text{s}^{-2}$
$S_\omega$	specific dissipation rate source term	$\text{kg m}^{-3} \text{s}^{-2}$
$t$	time	s
$T$	temperature	K
$T_L$	lagrangian integral timescale	s
$u$	velocity component	$\text{m s}^{-1}$
$u'$	fluctuating velocity component	$\text{m s}^{-1}$
$\mathbf{U}$	velocity	$\text{m s}^{-1}$
$V$	velocity scale	$\text{m s}^{-1}$
$y$	normal distance from the wall	m
$y^+$	non-dimensional wall distance	—

### Greek alphabet

$\alpha$	phase volume fraction	—
$\beta$	liquid phase mass fraction	—
$\gamma$	specific heat ratio	—
$\Gamma$	mass generation rate	$\text{kg m}^{-3} \text{s}^{-1}$
$\Gamma_E$	effective thermal conductivity	$\text{W m}^{-1} \text{K}^{-1}$
$\varepsilon$	turbulence dissipation rate	$\text{m}^2 \text{s}^{-3}$
$\zeta$	Markov energy loss coefficient	—
$\eta$	wave amplitude	$\text{kg m s}^{-2}$
$\theta$	non-isothermal correction factor	—
$\kappa$	wave number	$\text{m}^{-1}$
$\lambda$	thermal conductivity	$\text{W m}^{-1} \text{K}^{-1}$
$\mu$	dynamic viscosity	$\text{Pa s}$
$\mu_T$	turbulent viscosity	$\text{kg m}^{-1} \text{s}^{-1}$
$\nu$	kinematic viscosity	$\text{m}^2 \text{s}^{-1}$
$\rho$	density	$\text{kg m}^{-3}$
$\sigma$	liquid surface tension	$\text{N m}^{-1}$
$\sigma_k, \sigma_\varepsilon$	turbulent Prandtl numbers	—
$\tau$	viscous stress tensor	Pa
$\tau_{ij}$	stress tensor component	Pa
$\tau_p$	droplet response time	s
$\tau_T$	Taylor time microscale	s

---

$\chi$	turbulence intensity	—
$\omega$	specific dissipation rate	$\text{s}^{-1}$

### Subscript

0, 1, 2	total, inlet, outlet condition of domain
$a$	steam
$b$	water
B	bubble
$d$	droplet
ext	extrapolated value
$i, j$	cartesian tensor notation, grid index
int	interfacial
K	Kolmogorov scale
$l$	liquid phase
$m$	mixture
$m, n$	grid index
$\phi$	phase ' $\phi$ '
sat	saturation
T	turbulence
$v$	vapour phase
$x$	cartesian coordinate

### Abbreviations

2D	two-dimensional
3D	three-dimensional
BWR	boiling water reactor
CD	convergent-divergent
CFD	computational fluid dynamics
CFL	Courant-Friedrichs-Lewy
CNT	classical nucleation theory
CTE	conic trailing edge
D100, D200	dimple structures of 100 $\mu\text{m}$ and 200 $\mu\text{m}$ at pressure surface
DCC	direct contact condensation
ECCS	emergency core cooling system
EHS	Effective Heat Source
EMS	Effective Momentum Source
ETE	elliptic trailing edge
EOS	equation of state
FAS	full-approximation storage
FFT	Fast Fourier Transform
GCI	grid convergence index

KTH	Kungliga Tekniska högskolan
LES	large eddy simulation
Lk- $\varepsilon$	Lahey k- $\varepsilon$
LOCA	loss of coolant accident
LP	low pressure
LUT	Lappeenranta University of Technology
MSk- $\varepsilon$	modified standard k- $\varepsilon$
MSST k- $\omega$	modified SST k- $\omega$
NPPs	nuclear power plants
NuFoam	OpenFOAM CFD-solver for nuclear safety related flow simulations
NURESA	Development and Validation of CFD Methods for Nuclear Reactor Safety Assessment
PACTEL	Parallel Channel Test Loop
PIV	Particle Image Velocimetry
POOLEX	open pool test facility
PPOOLEX	pressurizing drywell-wetwell suppression pool facility
PS11, PS13	pressure surface tapering of 11° and 13°
PSP	pressure suppression pool
PWRs	pressurized water reactors
RANS	Reynolds-averaged Navier-Stokes
RMS	root-mean-square
RTE	semicircular trailing edge
RTI	Rayleigh-Taylor instability
SAFIR	The Finnish Research Programme on Nuclear Power Plant Safety
SS5, SS11	suction surface tapering of 5° and 11°
SST	shear-stress transport
STE	square trailing edge
VOF	volume of fluid

# 1 Introduction

## 1.1 Background

Nuclear energy is the world's largest source of CO<sub>2</sub> emission-free energy (NEA, 2015). Regardless of the numerous advantages in using nuclear generated power, the nuclear power safety has been considered the most important issue during the past decades. Therefore, the constructors and the operators of nuclear power plants (NPPs), and the regulating authorities of nuclear technologies always acknowledge the nuclear power safety as a top priority. Along with NPP safety system studies, the analysis of various key components of NPPs is also profitable, e.g. steam turbine which plays a key role in power production. Worldwide, more than 60% share of the total electricity generation is held by steam turbines. Therefore, the studies aiming to the efficiency improvement of steam turbines are crucial for efficient power plants because they are responsible for transforming thermal energy into mechanical energy. NPPs are always built with multiple layers of safety systems and structures designed to protect the plant, the workers at site and the community. The containment structure of light water reactor NPPs provides a confinement and a shielding against the direct release of radioactive material to the environment in transients and postulated accidents. The schematic of the ASEA-Atom type boiling water reactor (BWR) containment of the Olkiluoto 1&2 NPP units is shown in Figure 1.1.

These structures are designed to handle loads and released energy during a design basis accident. Due to the absence of secondary side steam generators in BWRs, the reactor coolant system is more compact than in pressurized water reactors (PWRs). The construction of the pressure suppression pool (PSP) is essential in BWRs containment because the pressure build-up and the released energy in the containment during a loss of coolant accident (LOCA) or safety valve actuation are mitigated by the PSP. Further, PSP is the emergency core cooling system's (ECCS) coolant source. It provides a barrier for direct fission product release by filtering or storing radioactive material conveyed with the coolant to the pool water and it works as a passive heat sink when the reactor is isolated from the main heat sink and also during and after a LOCA.

The most studied vapour condensation issues in the fundamental engineering literature include either dropwise condensation or filmwise condensation along a wall which separates the vapour and the coolant physically. However, the condensation heat transfer appearing either in BWRs containment systems or in rapid depressurization system of current PWRs during transient and accidents conditions can be categorized as direct contact condensation (DCC) in which the continuous vapour and liquid phases share a large interface where the phase change takes place. Figure 1.2 shows the DCC experienced throughout transients and postulated accident scenarios in BWRs and in PWRs.

Steam released from the reactor vessel is vented through the blowdown pipes via the upper drywell of the PSP system in case of LOCA or through quenchers in case of safety relief valve (SRV) operation. Pure steam condenses in the pressure suppression water pool, if the pool water remains under saturation. Condensation is incomplete if steam contains

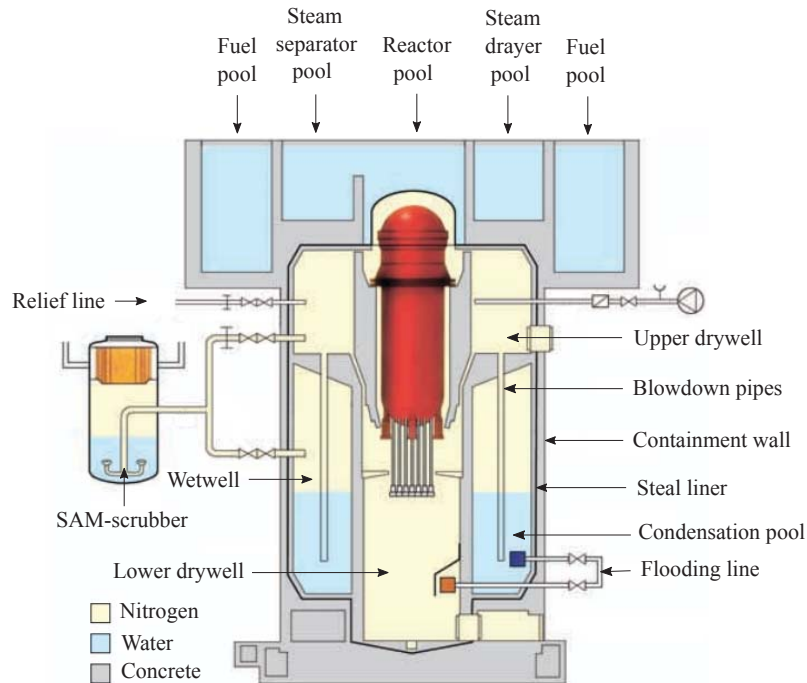


**Figure 1.1.** Schematic of the BWR containment of the Olkiluoto 1&2 NPP units (TVO, 2008).

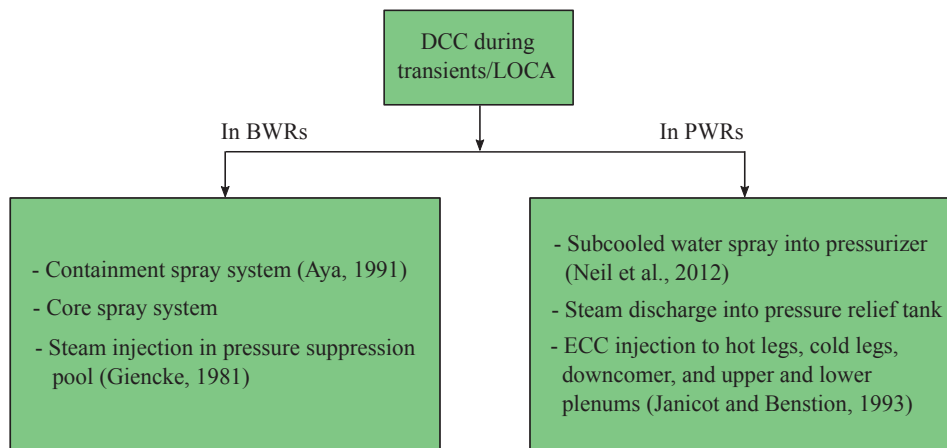


**Figure 1.2.** Typical DCC result in BWRs and in PWRs during transients and postulated accident conditions.

non-condensables e.g. nitrogen from the drywell. Several different DCC modes may appear during a blowdown event in PSP. Figure 1.3 shows the details of typical DCC modes

of steam blowdown. By varying mass flux and increasing pool temperature, different condensation modes can be observed, varying from the DCC onto stable interfaces, through oscillatory interfaces and chugging bubbles, to condensation within quasi-steady jet interfaces (Lahey and Moody, 1993). In this dissertation, two DCC modes appearing during steam blowdown in BWR PSP are studied. The condensation mode map of Lahey and Moody (1993) demonstrates quite well the conditions seen in the POOLEX/PPOOLEX tests of LUT, although a pipe diameter based map would be more accurate.

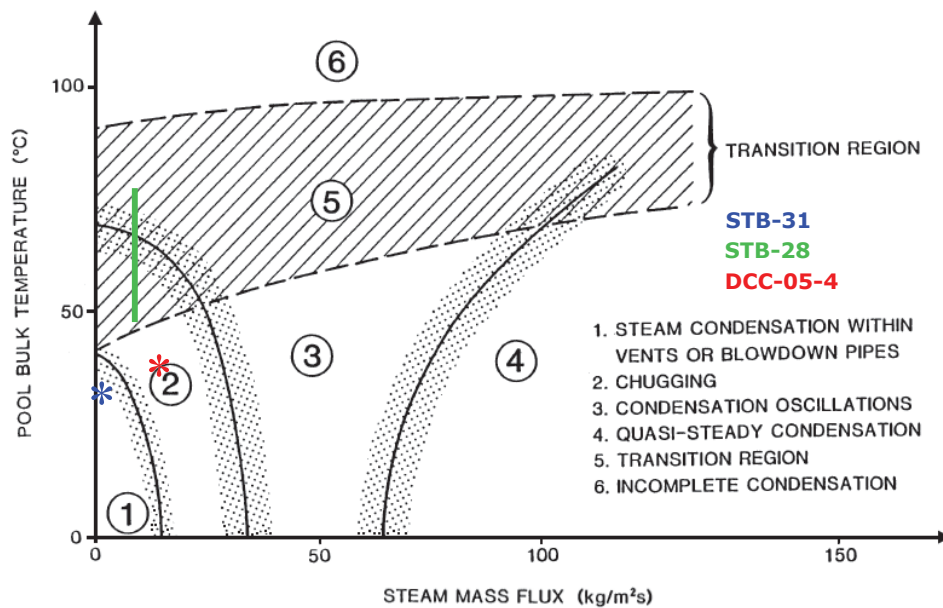


**Figure 1.3.** Condensation mode map of typical DCC modes appearing during steam blowdown events in condensation pool during safety valve actuation or LOCA (Lahey and Moody, 1993). The steam blows of the open pool test facility (POOLEX) and the pressurizing drywell-wetwell suppression pool facility (PPOOLEX) tests of Lappeenranta University of Technology (LUT) are marked.

In chugging DCC mode, the steam/water interface moves in and out of the blowdown pipe in a periodic manner (Figure 1.4) and the injected steam interacts with the pool water by heat transfer, rapid condensation and momentum exchange. As a whole, the discharge of steam into the condensation pool is a quite intricate event which is associated with hydrodynamics and thermodynamics including bubble dynamics, thermal stratification, turbulent mixing, natural circulation, and steam condensation within the water pool, ducts, and at wall surfaces (Tanskanen and Jordan, 2011). Furthermore, the pool water acceleration during steam blowdown and bubble collapsing events instigates a pressure pulse in the water pool which induces hydrodynamic loads to the pool structures and submerged venting systems.

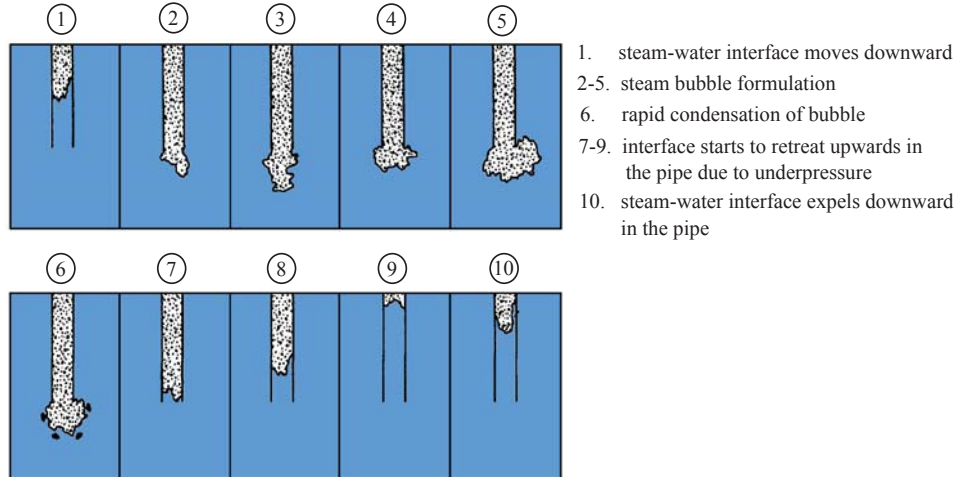


**Figure 1.4.** Schematic of chugging phenomena occurs during steam blowdown in PSP (Sargis et al., 1978).

As the DCC of steam in water pool contains the long and very short time scale phenomena, the analysis of condensation is challenging. The rapid pressure oscillations resulting from steam condensation are generally unfavorable for the delicate measurement instrumentation and for the time-stepping of transient simulations. Nevertheless, steam blowdown experiments are essential to improve the understanding of the physics involved. Therefore, a detailed analysis of steam blowdown phenomena either by experiments or with numerical simulations has a great importance from the nuclear reactor safety point of view.

Further, the investigation of other vital components of NPPs such as steam turbine is essential. The current projected trends of the world's energy demand forecast that the overall energy consumption in the world will rise by 48% by 2040 owing to the growth in world economy, industrialization and globalisation, etc. (IEA, 2016). In large power plants, steam turbines are usually divided into three stages, namely high-pressure (HP), intermediate-pressure and low-pressure (LP). Especially, the research on LP steam turbine stages is essential due to their relatively lower efficiency and recurrent maintenance compared to HP steam turbine. Moreover, the last few LP turbine stages generates much more than 10% of the total output which provides a special motivation for their research.

The exhaust pressure of steam turbines is designed to be low i.e. sub-atmospheric pressures, to gain the maximum energy output. The steam temperature decreases due to rapid expansion in the last stages of the turbine. As a consequence of the rapid expansion, the steam first subcools and fine droplet nuclei form. This mixture of steam and fine water droplets is referred to as 'wet-steam'. The typical condensation process in nozzles and steam turbines can be categorized into two types: homogeneous and heterogeneous. The homogeneous condensation happens more spontaneously and in the absence of preferen-

tial nucleation sites e.g. chemical impurities or surfaces. The heterogeneous condensation mostly occurs due to insoluble or/and soluble chemical impurities in the steam. In steam turbine flows, the homogeneous condensation is more significant than the heterogeneous condensation (Gerber, 2002). Figure 1.5 shows the schematic of homogeneous condensation appearing in a supersonic convergent-divergent (CD) nozzle.

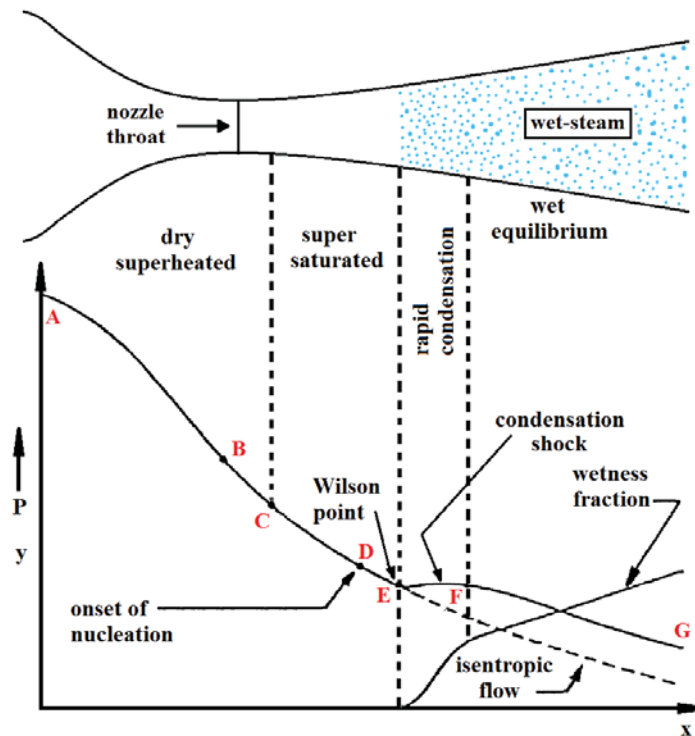


**Figure 1.5.** The schematic of homogeneous condensation occurring in a supersonic CD nozzles (Guha, 1995).

At the nozzle inlet, steam is dry and in superheated state (point A), and it continues to expand up to nozzle throat (point B) where it acquires a sonic condition. At point C, the steam expansion line crosses the saturation line and steam becomes subcooled or super-saturated. However, steam remains dry in a meta-stable state (region between point C and D) until the supersaturation becomes sufficiently high to provoke as appreciable nucleation rate. At point D, the process of tiny droplet nuclei formation i.e. nucleation begins. The nucleation phenomena generate an enormous number ( $10^{14}$  -  $10^{17}$  nuclei per kg of steam) of tiny droplets being subnanometer of size (Guha, 1995). At the utmost subcooling level (i.e. point E), the process of nucleation terminates. The point E is called Wilson Point. The zone between point D to point E is known as the nucleation region. The generated liquid droplets rapidly grow in size by releasing latent heat to surrounding vapour phase. The heat release rate in rapid condensation is quite high and as a consequence a

sharp increment results in the temperature and pressure of the vapour (point E to point F). This increment in the pressure (i.e. point F) is commonly known as 'condensation disturbance'. Following point F, the vapour returns to the thermodynamic equilibrium state in which the vapour and droplets temperatures remain close to the saturation level till point G.

In the LP turbine stages, after the droplet formulation, the droplets grow in size further downstream (Figure 1.6).

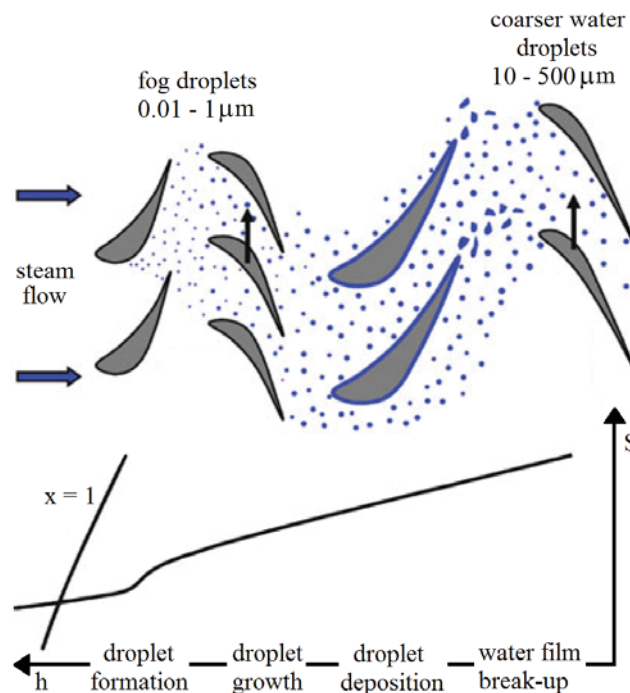


**Figure 1.6.** Schematic of wetness generation in LP turbine stages (Starzmann et al., 2013a). Here, the blue colour around the blade surfaces signifies the droplet deposition and liquid films.

The fog droplets and the coarser water droplets from the previous stage start to deposit onto the blade surfaces resulting in water films. Because of the drag effect, these water films are conveyed to the trailing edges of blades. Due to aerodynamic forces, these films are disrupted and broken up and secondary coarse water droplets are formed. These secondary water droplets are smaller in number than the primary fog droplets, but their size, and therefore mass, is considerably larger. These large water droplets impinge on the succeeding blades leading edges with a high relative velocity and negative incident angle. As a consequence, severe erosion is prompted on the blade surfaces.

Steam condensation in the LP turbine introduces additional losses e.g. irreversible thermodynamic losses, mechanical losses or erosion. According to Baumann's rule (the pres-

ence of 1% average wetness results in a reduction of turbine efficiency by approximately 1% (Baumann, 1912)), the presence of moisture in the LP stages of steam turbines has a negative impact on efficiency and reliability as well. Therefore, as the power plant efficiency is mainly dependent on the efficiency of the energy conversion in the steam turbine, the experimental and numerical analyses of the condensing flow in a steam turbine are essential for the turbine designers and manufacturers to account for wetness effects during blade profile selection and whole stage design. Even a marginal advancement in the LP turbine performance could prove significantly profitable.

## 1.2 Objective of the study

The flow phenomena in PSP are inherently three dimensional and include a two-phase and/or multiphase flow with rapid heat and mass transfer, irregular violent pressure oscillations, thermal stratification, mixing, etc. The nature and efficiency of steam DCC phenomena in a condensation pool depend on the subcooling of the pool liquid, the mass flux of injected vapour, drywell and wetwell volumes, the geometry of the vents and their corresponding exit shapes, and the fraction of non-condensables within the vapour. Although, the blowdown of steam enables the rapid containment depressurization and efficient heat removal, the DCC phenomena impose hydrodynamic loads on pool structures e.g. the containment wetwell experiences pressure loads on the pool walls and drag loads on the submerged pool structures. Therefore, a proper investigation of the steam blowdown event in PSP and the corresponding analysis of loads induced due to rapid condensation are important in order to ensure that the containment structural design resists these loads. The analysis of transport processes, the general performance and thus mixing/thermal stratification of the suppression pool during steam blowdown is important as well. Further, the flow time-scales and violent conditions of steam blowdown make the investigation of DCC phenomena of BWR PSP challenging both with experiments and with computational fluid dynamics (CFD) simulations.

The application of CFD for nuclear safety related analysis has gained popularity among the nuclear industry worldwide. In this thesis, the CFD simulations of DCC modes occurring during steam blowdown have been conducted by employing the Eulerian-Eulerian two-fluid approach of the OpenFOAM and NEPTUNE\_CFD CFD codes. The interfacial heat transfer between steam and water has been modelled by applying different DCC models. The steam blowdown tests of the POOLEX and the PPOOLEX of LUT, and earlier and recent NEPTUNE\_CFD simulation results by Tanskanen (2012), Tanskanen et al. (2014) and Patel et al. (2016) have been used as references.

The research on condensing steam flow of LP turbines has a prime interest owing to relatively moderate efficiency. Experimental LP turbine facilities are rare worldwide. Precise measurement of the non-equilibrium wet-steam flow in a LP turbine, including key parameters e.g. droplet size and their corresponding distribution, moisture level, etc., is very challenging (Bosdas, 2016). However, comprehensive experiments of LP turbine flow fields are important for a better understanding of condensing flows and also for model

validation purposes.

CFD has been applied frequently in turbomachinery flow research in the past few decades. Due to the significance of computer technology and its rapid developments, CFD simulations of wet-steam flows are feasible and affordable. Therefore, this dissertation is partially aimed to investigate the condensing steam flow of LP turbine by using the CFD approach. However, the accurate modelling of complex aerodynamics and thermodynamics phenomena, and corresponding loss generation appearing in LP turbine flows still presents a considerable challenge to recent CFD methods and solvers because the flow and corresponding expansion phenomena occur in a non-equilibrium way. Further, the preciseness of the numerical results of wet-steam flow depends on several key issues e.g. computational grid quality, boundary conditions, thermodynamic properties of vapour, nucleation and droplet growth modelling, and turbulence models. In LP turbine flows, the expansion of steam flow and the condensation phenomena depend on both the flow passage and the operating conditions. The condensation process is rather sensitive to the blade shape and thickness. As the shapes and the size of the blades influences on the pressure fields, it could be anticipated that the trailing edge shapes should have significant impact on the entire condensation process and the corresponding loss generation. Therefore, the quantification of LP turbine blade shape modification influence on the flow expansion, condensation phenomena and corresponding loss generation is conducted in this work. Various modifications including blade trailing edge shapes, addition of dimple feature to the blade pressure surface and blade shape modification via blade pressure and suction surfaces' tapering are studied.

In general, precise modelling of wall-bounded shear layers and free shear layers are crucial for turbomachinery flows. Especially, the LP turbine flow incorporates numerous intricate flow phenomena e.g. flow transition, flow separation, secondary flow mixing, tip clearance flows, and stator-rotor interaction. The common thread among all of these phenomena is turbulence. As turbulence plays a vital role in the transport processes of mass, momentum and energy in main flow regions and in near wall regions, the correct turbulence modelling is very essential for LP turbine flow analysis and design. Thus, in this dissertation, the effect of turbulence modelling on wet-steam flow is studied by modifying the two-equation turbulence models.

In this work, the condensing steam flow has been modelled by employing the Eulerian-Eulerian approach of ANSYS FLUENT and ANSYS CFX in which the mixture of vapour and condensed liquid phase has been solved by compressible Reynolds-averaged Navier-Stokes (RANS) equations. The classical nucleation theory (CNT) was used for nucleation modelling.

The objectives of this dissertation are the following:

- To enhance the ability of the CFD solvers to model heat and mass transfer processes of PSP during a steam blowdown event. This can be reached by comparing the results of different solvers in different conditions.
- To test whether incompressible OpenFOAM and compressible NEPTUNE\_CFD

solvers yield coherent DCC results in a mildly sheared stable interface case and to demonstrate that incompressible flow solution fails if the DCC rate is higher.

- To test how significant are the differences of results between 2D and 3D models and whether the effect of different subcooling rates is reasonably visible in the simulation results of the chugging mode.
- To test if the chugging frequency changes significantly if the interfacial turbulence modelling changes.
- To show the effect of drywell on the simulation results of chugging mode.
- To quantify the differences between the OpenFOAM and NEPTUNE\_CFD results.
- To study the effect of grid resolution on the results by using grid convergence index (GCI) algorithm, and to prove the coherence between the Rayleigh-Taylor instability modelling results and the dense grid simulation results.
- To model non-equilibrium condensing steam flow in nozzles, turbine stator cascade and stator-rotor stage by employing the Eulerian-Eulerian approach of the ANSYS CFD codes.
- To analyze the influence of blade shape modification including trailing edge shapes, dimple inclusion and surface tapering on condensing steam flows.
- To quantify the influence of turbulence and its modelling on condensation steam flow modelling by adopting two-equation turbulence models.
- To acquire the information of losses generated during condensation process and to employ that information for validation purposes.
- To compare the obtained CFD results of wet-steam flow with the experimental data available in the literature.
- To provide recommendations and potential suggestions for DCC and wet-steam flow modelling.

### 1.3 Outline of the thesis

The content of this thesis is divided into eight chapters. A brief description of each chapter content is listed below.

Chapter 1 presents the details on the significance of PSP analysis for nuclear reactor safety and the DCC phenomena which occur during steam blowdown. Following this, the relevance of the LP turbine condensing steam flow and the corresponding loss mechanism investigation is discussed. Then, a subsection describes the objectives of this work. In the end, the thesis structure is described.

Chapter 2 includes a literature review. This chapter contains a brief discussion of the earlier experimental work conducted for PSP studies. Also, the previous theoretical and numerical efforts on DCC modelling are discussed. Following this, a brief description of experimental, analytical and numerical works of steam condensing flow in LP turbine is presented.

Chapter 3 briefly describes the installed experimental facilities of suppression pool at LUT. This chapter discusses the selected PSP test configurations and the corresponding test conditions.

Chapter 4 presents the numerical models employed for DCC and condensing steam flow simulations. The subsections of this chapter summarise the heat and mass transfer models, turbulence models, nucleation and droplet growth models and thermodynamic properties. This chapter also includes the details of Rayleigh-Taylor instability modelling and grid conversion index algorithm used for grid convergence error estimation.

Chapter 5 includes descriptions of the computational domains and their grid generation used for DCC and condensing steam flow simulations. Then, a summary of CFD simulations settings is presented.

Chapter 6 summaries the achieved simulation results of DCC of steam. This chapter shows the qualitative and quantitative analysis of the simulated cases of both the POOLEX and the PPOOLEX facilities. Also, the influence of grid density on DCC phenomena is discussed.

Chapter 7 presents the numerical results of condensing steam flow in LP turbine. This chapter describes the influence of blade trailing edge shapes, dimple inclusion and blade surface tapering on the condensation and loss mechanism in LP turbine flow. Also, the results of turbulence modelling influence on condensation phenomena are discussed.

The findings of this dissertation are described in chapter 8. In the end, recommendations for future work and potential suggestions for DCC and wet-steam flow modelling are listed.

## 2 Literature review

This chapter describes the previous studies concerning PSP and condensing steam flow in LP turbines.

### 2.1 A brief review of pressure suppression pool studies

Numerous researchers have conducted analyses of steam injection in a suppression pool experimentally, theoretically and numerically. However, an accurate analysis of the blowdown event in PSP safety system is demanding due to the complex and rapid transport processes involved. Following subsections of this chapter briefly describe the previous efforts made by other researchers on PSP studies.

#### 2.1.1 Experimental studies of pressure suppression pool

Extensive experimental investigations of air/steam blowdown into sub-cooled water have been conducted by several researchers using various injection systems with both horizontal and vertical blowdown pipes. However, the DCC modes in horizontal, vertical, and nozzle type steam injections, the geometry itself and the various injectors like spargers cause the steam/water interface structures in horizontal and nozzled systems to be quite different from the typical large diameter vertical pipe systems of General Electric's MARK I and MARK II, and Nordic ASEA-Atom type BWR's (Kang and Song, 2008; Gulawani et al., 2009).

A number of experimental studies with a horizontal injection system were conducted during the '70s e.g. Kerney et al. (1972), McIntyre et al. (1975), Chuang (1977), Varzaly et al. (1977). These experimental studies were encouraged due to MARK III containment design. Later, many researchers performed experimental analyses of steam condensation with horizontal blowdown mostly with nozzle injectors or vents e.g. Seong et al. (2000), Youn et al. (2003), Kim et al. (2004), Wu et al. (2007), Norman and Revankar (2010). A more detailed review of the horizontal experiments was conducted by Tanskanen (2012).

Some major experimental studies have been performed on various aspects using vertical steam injection. For example, significant experiments were conducted in the Marviken facility to analyze the pressure suppression principle for a MARK II type containment during 1972-1981 (Wikdahl, 2007). These experiments were also aimed at the dynamic processes of the condensation. McIntyre et al. (1976) and Grafton et al. (1977) performed experiments of a suppression pool with a single vertical pipe to investigate the responses of pool during LOCA situations. Following, Kennedy et al. (1978) performed experiments on MARK I suppression pool with a scale down test facility to analyze the impact of the rigidity of the blowdown pipe header on the pressure impact loads. Marks and Andeen (1979) conducted experiments of chugging and condensation oscillation modes and described the characteristics of the pressure response. They described both the regimes and

the internal chug. The works of Aya et al. (1980, 1983) and Aya and Nariai (1985), include chugging oscillations experiments with small test facility (blowdown pipe: 1 m height and 18 mm in diameter). They measured the frequency and amplitude of the chugging oscillations. The experimental study by Aust and Seeliger (1982) emphasized the mitigation of dynamic loads by pipe design in suppression pool. Later, Chan and Lee (1982a) performed experiments of steam injection in the subcooled water pool and recorded the motion of steam/water interface using a high-speed video camera. They systematically classified the steam blowdown event in terms of a condensation regime map based on the steam injection rate and the pool water temperature. Chen and Dhir (1982) performed experiments on air discharge in water pool to develop a model for bubble growth at a vertical pipe exit. They recorded the bubble growth with high speed camera and the vent line pressure via fully active strain-gauge type transducers. Experimental investigations of suppression pool with multiple blowdown pipes have been presented in the works of Kukita et al. (1984, 1987). Their analysis included a 20 degree sector of annular wetwell. Further, Nariai and Aya (1986) analyzed the flow oscillation during DCC, pressure oscillations at pressure suppression containment and cold leg flow oscillations at ECC water injection experimentally. Later on, smaller scale blowdown experiments were performed by Meier et al. (1998) and Meier (1999) with a transparent tank using steam and non-condensables to analyse the effect of pipe length and compressibility of the gas in piping on the bubble size, shape, and frequency. Subsequently, the major experimental works concerning suppression pool have been conducted with the PANDA and LINX experimental facilities. The PANDA facility was employed to analyze passive containment cooling systems and the interaction between the various system components during long-term cooling (Smith, 2007) while the LINX facility was utilized to investigate different issues of suppression pools, e.g. condensation, mixing, the effect of non-condensable gases and stratification (Hart et al., 2001). Further, extensive experimental studies have been performed by Laine and Puustinen (2005) and Puustinen et al. (2013a) both with POOLEX with a long and straight blowdown pipe, and with PPOOLEX test facilities aiming at different issues of BWR containment such as dynamics loading of pool structures, thermal stratifications and mixing, wall condensation, and the behaviour of parallel blowdown pipes. Rassame et al. (2015) performed an experimental analysis to analyze the behavior of void in the PSP during the blowdown period of a LOCA. In their experiments, they injected air, steam-air mixture and pure steam at a range of various flow rates from the drywell in the suppression pool (SP) via a downcomer pipe. They observed three different phases of blowdown: initial phase, a quasi-steady, and a chugging phase. Laine et al. (2015) carried out sparger experiments with the PPOOLEX test facility of LUT. Their experiments consisted of two small steam flow rate stratification periods and two higher flow rate mixing periods. These experiments were aimed for the validation purposes in the development of the Effective Momentum Source (EMS) and Effective Heat Source (EHS) models implemented in GOTHIC code by Kungliga Tekniska högskolan (KTH). Recently, Pellegrini et al. (2016) performed steam blowdown experiments with the transparent test facility. They utilized two quenchers: one with a bottom end open pipe without holes and the second with a the multi-hole quencher. They recorded the blowdown event via high-speed video camera. Their tests were aimed to measure water

temperature to support the interpretation of the pool mixing during an accident.

Numerous experimental works have also been performed regarding steam injection with spargers. For example, Arinobu (1980) experimentally investigated the dynamic phenomena of steam injection. He studied the influence of parameters on the wall pressure amplitude and proposed an empirical expression of dominant frequency. Cho et al. (2001) performed an experimental study of pressure oscillation and thermal mixing induced due to DCC of steam blowdown in water pool with various steam mass fluxes and pool water temperatures. They used eight different spargers for steam injection. Following, Park et al. (2007) organized a series of steam condensation tests with multi-hole sparger to determine the transition region from the condensation oscillation regime to the stable condensation regime. They studied dynamic load on the quench tank and the frequencies of the pressure waves induced due to condensation and proposed a condensation regime map for a multi-hole sparger. Hong et al. (2012) investigated the dynamic characteristics of steam jet condensation frequency. They performed experiments over a range of steam mass flux ( $200\text{-}900\text{ kgm}^{-2}\text{s}^{-1}$ ), and pool temperature ( $35\text{-}95\text{ }^{\circ}\text{C}$ ).

The non-condensable gas drives pool mixing only before steam arrives. However, the presence of non-condensable gas in steam blowdown significantly resists the mass transfer by accumulating as a layer at the steam/water interface. Therefore, several experimental works regarding the effects of non-condensable gas on DCC have been carried out. For example, Walsche and Cachard (1996) conducted experiments to analyze the condensation and mixing phenomena in PSP with the LINX facility with steam/non-condensable gas mixture injection. They performed various test cases based on the steam flow rate, fraction of non-condensable gas, blowdown pipe submergence depth in the pool and system pressure. They extracted information about temperature distribution and overall condensation rate applying heat and mass balances during blowdown. Later, Oh and Revankar (2005) performed an experimental investigation on the influence of non-condensable gas on DCC with vertical steam injection at various steam injection rates, system pressures, and non-condensable gas concentrations. Recently, Cai et al. (2016) analyzed the effect of non-condensable gas (nitrogen) on DCC in suppression pool at single steam injection rate. They studied the influence of non-condensable gas on thermal stratification, condensation behavior, and velocity field by using Particle Image Velocimetry (PIV) measurement technique and high speed camera.

### 2.1.2 Theoretical developments

Along with experimental studies, several theoretical works have been published on various aspects of steam blowdown in PSP. The comprehensive thermalhydraulic model of chugging was suggested by Sargis et al. (1978) based on the fundamental conservation laws. They found good agreement between their chugging model and small-scale experiments. Following, Brennen (1979) described a theoretical model to obtain the important parameters and frequencies pertaining to the instability in DCC in the PSPs. There are also a number of analytical models in which chugging has been reproduced numerically

Class (1978), Kowalchuk and Sonin (1978). Ali et al. (2007) expanded the proposed chugging model by Sargis et al. (1978) and analyzed the influence of non-condensable gas (air) on chugging by developing theoretical models.

Some extensive works have been performed to classify the condensation modes in regime maps. For example, Aya and Nariai (1987, 1991) comprehensively analyzed the characteristics of heat transfer of steam injection in water pool in chugging, condensation oscillation and jet region and they provided a DCC regime map based on the pressure pulse's characteristics. Lahey and Moody (1993) developed a qualitative regime map of steam DCC and examined bubble behavior based on the Rayleigh equation and on an energy balance. Liang and Griffith (1994) performed an experimental and analytical study of DCC of steam in water pool and proposed a transition criteria between steam chugging, bubbling and jetting. Petrovic de With et al. (2007) provided a three dimensional condensation regime diagram based on the available test data of steam injection in the water pool using more than three decades' data in literature. Their regime map was based on steam mass flux, pool water temperature and injector diameter, and it includes three regimes: chugging, jetting, and bubbling of the DCC. Aya and Nariai (1986) studied the occurrence of threshold of pressure oscillations caused by DCC analytically by employing the linear stability theory to high- and low-frequency components. Some additional works and the background of DCC models used in this study have been presented e.g. in the literature review by Tanskanen (2012).

### 2.1.3 Numerical studies

Numerical simulations of steam blowdown in PSP were not common before 2000. As CFD has become an increasingly applicable tool for thermal-hydraulic investigations in the field of nuclear safety analysis (Bestion, 2012), a progressive development in CFD simulations of chugging DCC in vertical vent pipes can be seen during last decade. However, the published numerical work on the DCC phenomena in the PSP with vertical air/steam blowdown is relatively scant. In the past, the volume of fluid (VOF) method of an interface tracking was quite famous for steam injection studies among researchers. For example, Meier (1999) and Liovic (2000) applied VOF method for the modelling of the upward and downward injection of a gas into a liquid pool with 2D-axisymmetric case. Later, the same method has been utilized by Meier et al. (2000) and Yadigaroglu (2004) to simulate large steam-air bubbles in a water pool without mass transfer. Subsequently, Thiele (2010) performed VOF simulations of steam injection into water pool enabling mass transfer based on temperature difference in OpenFOAM CFD code. Afterwards, Li et al. (2015a) investigated the DCC phenomena into subcooled water flow in a tee junction with low steam mass flux ( $10 \text{ kgm}^{-2}\text{s}^{-1}$ ) discharged with the VOF model and large eddy simulation (LES) approach of ANSYS FLUENT. They modelled steam condensation by employing user defined subroutines. They observed large chugging, small chugging and bubbling at the water temperature of 303.15 K, 343.15 K and 363.16 K, respectively. Also, Li et al. (2015b) conducted CFD simulations of DCC of subsonic steam injection into a subcooled water pool by using the VOF model and LES approach

of ANSYS FLUENT and studied the steam plume shapes. Li et al. (2012) performed simulations of suppression pool utilizing CFD-like lumped parameter code GOTHIC to analyze thermal stratification and pool mixing.

However, published works on the applicability of the Eulerian two-fluid approach with real phase-change modelling with CFD of steam blowdown are sparse. For example, Pättikangas et al. (2000) conducted 2D-axisymmetric simulation of the water hammer due to a steam bubble collapse by utilizing two-fluid models. Later, Tanskanen et al. (2008) performed simulations of a special case of low-Reynolds number DCC mode of the POOLEX test series of LUT by employing the Eulerian two-fluid approach of the NEPTUNE\_CFD code. Pättikangas et al. (2010) employed two-fluid models of ANSYS FLUENT CFD code to perform simulations of the PPOOLEX facility. They simulated first 100 seconds of the experiment and analyzed the DCC phenomena. However, in their work, the predicted rates of heat transfer and condensation were quite weak. In the works of Tanskanen and Jordan (2011), Tanskanen (2012) and Tanskanen et al. (2014), they presented an extensive CFD analysis of chugging phenomena in PSP by employing Eulerian two-fluid approach with heat and mass transfer. They performed simulations of chugging cases of the STB-28 case of POOLEX facility at subcooling levels of 30K, 40K and 60K. Their results demonstrated the improved capability of Eulerian two-phase CFD codes to rather successfully predict chugging DCC in a blowdown pipe-wetwell system. Further, they utilized a pattern recognition algorithm in order to extract the information of bubble size and bubble appearance frequency during the rapid chugging condensation mode. Recently, Tanskanen et al. (2015) presented a summary of their initial attempts of CFD simulations of the PPOOLEX DCC-05-4 test. Meanwhile, Pellegrini et al. (2015) carried out CFD simulations of chugging DCC of the experiment of POOLEX facility employing two-fluid Eulerian model of STAR-CCM+ CFD code and proposed a method to treat the steam/water interface with growing instabilities based on the Rayleigh-Taylor theory.

## 2.2 A brief review of condensing steam flow studies in LP turbines

Analyses of condensing steam flow both in nozzles and in turbines have been performed by numerous researchers over a century. There is vast published literature available in this field. This subsection summarizes only major studies especially on homogeneous condensation.

### 2.2.1 Experimental studies on wet-steam flows

The experiments of condensing steam flows were started a century ago. The pioneer experimental studies were mostly conducted with nozzle configurations with simple geometry and no rotating parts. The experimental work of condensation of Stodola (1915) was the first study performed with convergent-divergent (CD) nozzle. Following this, Callender (1915) and Martin (1918) studied the supersaturation effect in nozzle flows.

Some experimental studies, e.g. Rettaliata (1936), Yellott and Holland (1937), Binnie and Woods (1938) and Binnie and Green (1943), were concentrated on attaining information about the Wilson line and limiting supersaturation ratio. The works of Gyarmathy and Meyer (1965) and Gyarmathy and Lesch (1969) were quite remarkable for condensing steam flow measurements. They employed the light scattering technique to measure condensed droplet size. The earlier experimental works of Barschdorff (1971), Moore et al. (1973), Bakhtar et al. (1975) and Moses and Stein (1978) were the best-known CD nozzle experiments. Barschdorff (1971) conducted experiments on condensing flow in arc nozzle flows. Moore et al. (1973) performed measurements of the pressure distribution along the nozzle centreline with different nozzle configurations (by varying the throat height and divergence angle) and measured droplet radii by utilizing the light scattering technique. Following, Bakhtar et al. (1975) analyzed the nucleation phenomena in CD nozzle with high-pressure (pressure range 2-35 bars) steam flow. In the work of Moses and Stein (1978), they conducted nozzle tests with various operating conditions by applying static pressure and laser light scattering technique and extracted information about static pressure, nucleation and droplet growth. Succeeding these works, some major experimental studies of condensing steam flow in CD nozzles were reported by Skillings et al. (1987), Bakhtar and Zidi (1989, 1990), and Gyarmathy (2005).

However, real steam turbine flows are more complex due to highly 3D unsteady flow field in contrast to CD nozzle flows. Therefore, precise measurements of steam turbine flows are more challenging and demanding. Some researchers have performed condensing steam experiments with steam turbine cascades. For example, Bakhtar et al. (1995a,b), in which the authors performed experiments of the rotor-tip cascade. They extracted a large set of measured data of pressure distribution over blade profile, droplet size, loss and efficiency data over a range of expansion ratios and inlet supercooling levels. Afterwards, White et al. (1996) organized stationary turbine cascade experiments of condensing steam flow with test conditions and provided measurement data of pressure distribution, wetness level and droplet radii at certain locations, Schlieren profiles and normalised entropy. Furthermore, they extracted important information about loss coefficients. Some experimental works have been performed for 3D stator-rotor stage of LP turbine e.g. Wróblewski et al. (2009), Yamamoto et al. (2010), Cai et al. (2009). Nevertheless, the published experimental work on multi-stage steam turbine is quite rare. Recently, Eberle et al. (2013) and Schatz et al. (2014) presented test results of multi-stage model steam turbine in which they measured moisture level and droplet radii utilizing a light extinction method.

Many studies have been conducted to analyze the aerodynamics of the LP turbine blades. Prust and Helon (1972) presented an experimental analysis of the significance of the trailing edge geometry and thickness on the performance of the turbine stator blade. Some works have been organized to investigate the influence of blade thickness on the loss generation in LP turbines experimentally e.g. González et al. (2001), Brear et al. (2002), Sonoda et al. (2006). Senoo (2012) and Senoo and Ono (2013) demonstrated a design method for the high-reaction type supersonic turbine aerofoil. They presented the validation of CFD results and the design method against supersonic cascade wind tunnel tests. Torre et al. (2012) investigated the effect of airfoil thickness on the efficiency of LP tur-

bines experimentally in a multi-stage turbine high-speed rig. Granovskiy et al. (2014) conducted an experimental investigation of the effect of the unguided turning angle and the trailing edge shape on the profile loss of transonic high pressure turbine blades. Zhou et al. (2014) presented the effects of the blade trailing edge thickness on the profile loss of ultrahigh-lift LP turbine blades using experimental, numerical and analytical methods. However, there is no published experimental work related to the influence of the trailing edge geometry in condensing steam flows.

### 2.2.2 Theoretical and numerical developments on wet-steam flows

An accurate prediction of condensing steam flows requires correct nucleation and droplet growth modelling. Many theoretical works on condensing steam flow have been published. The works of Laplace (1806) and Thomson (1870) were the pioneer works for the CNT development. Following them, Helmholtz (1886) and Gibbs (1888) obtained fundamental equations which govern the equilibrium of thermodynamic systems. After their efforts, the famous Kelvin-Helmholtz or Gibbs-Thomson equation was developed. The works of Gibbs (1906) and Volmer and Weber (1926) were important to the comprehension of the kinetics of phase change and the evolution of nucleation theory. The CNT was formulated after the works of Farkas (1927), Becker and Doring (1935), Zeldovich (1942) and Frenkel (1946). Numerous modifications were introduced into the CNT, see e.g. Bijl (1938), Band (1939), Zeldovich (1942), Kantrowitz (1951), Kaschiev (1969) for the further development of it. The detailed information about nucleation theory development is described in McDonald (1962, 1963). As the CNT was formulated by assuming the isothermal conditions, Kantrowitz (1951) illustrated that the temperature of condensed droplet was altered during the nucleation process. He presented the modified version of CNT by introducing a non-isothermal correction.

Many researchers have worked in the development of droplet growth models for condensing steam flows in LP turbine. Hertz (1882) and Knudsen (1915) presented their works on droplet growth in wet-steam flows first. Since then, most of the development on droplet growth theory was conducted after the '60s. The droplet growth rate was obtained by Gyarmathy (1963) by heat conduction in which the droplet temperature was combined with a semi-empirical heat transfer coefficient. Following, Hill (1966) derived a droplet growth model based on the kinetic theory. Several researchers e.g. Wegener (1966), Konorski (1966), Bakhtar and Yousif (1974), Puzyrewski (1969) presented their contributions for further development of the droplet growth models for condensing steam flows. Following, Young (1982) presented a droplet growth model which was a modified version of the Gyarmathy (1963) model. Then, Gyarmathy (1982) and Young (1993) formulated a droplet growth model based on the flux matching method. Some researchers e.g. Kirkwood and Buff (1949), Oriani and Sundquist (1963), Campbell and Bakhtar (1970), Plummer and Hale (1972) conducted theoretical investigation on the influence of surface tension on droplet clusters. As the accurate estimation of flow expansion and the models of nucleation and droplet growth rates rely on precise thermodynamical properties, many works e.g. Vukalovich (1958), Young (1973), Bakhtar et al. (1975), and

Bakhtar and Piran (1979) were dedicated to the development of the equation of state (EOS) for condensing steam flows. Following, the theoretical works of Young (1988, 1992) can be mentioned. They derived the EOS for a superheated region with a large applicability range. There are numerous theoretical works available on condensing steam flow modelling, e.g. Barschdorff and Filippov (1970), Bakhtar and Tochai (1980), Moheban and Young (1984), Schnerr (1989), Guha and Young (1991, 1994), and Winkler and Schnerr (2001).

Since the '70s, many numerical studies of steam condensing flow have been published. Early numerical attempts e.g. Barschdorff (1971) and Moore et al. (1973) were limited to the 1D modelling. Later, several researchers conducted successful 2D simulations of steam condensing flows in LP turbine e.g. Bakhtar and Tochai (1980), Young (1992), White and Young (1993), Bakhtar et al. (1995c) and White et al. (1996). These works utilized an inviscid time-marching scheme with a Lagrangian tracking module for condensed droplet motion. However, as the Eulerian-Lagrangian approach for 3D non-equilibrium condensing steam flow is more demanding and expensive, Gerber and Kermani (2004) adopted an Eulerian-Eulerian approach for condensing steam flows. In the works of White and Hounslow (2000), White (2003), and Gerber and Mousavi (2006, 2007), the method of moments and quadrature method of moments were employed for condensing steam flow modelling. In present days, due to large computational power, the modelling of 3D multistage LP turbine flows is attempted by several researchers e.g. Yamamoto et al. (2010), Starzmann et al. (2011), Chandler et al. (2013), Starzmann et al. (2013b), and Grübel et al. (2014).

Nevertheless, the available numerical work on the influence of turbine blade shapes and trailing edge profiles on condensing steam flows in LP turbine is rather sparse. The influence of blade profile modification of a LP turbine rotor blade cascade by Bakhtar et al. (1995a) was numerically analyzed by Singh (2001). He tested different trailing edge profiles and blade chord lengths, and concluded that those modifications had a large impact on the amount of wetness generated. An et al. (2009) studied the effect of blade profile modification on the nucleation zone distribution and the degree of boundary layer separation in primary nucleation stage in wet steam flows. They modified the blade profiles by changing the blade curvature distribution of the profile. Their work concluded that the nucleation rate and the flow outlet angle were influenced by the blade modification.

The published work on the influence of turbulence and its modelling on the condensing steam flow is also quite limited. Only few works are available e.g. White (2000) who investigated the influence of the viscous effect on condensation within compressible boundary layers. Following, Simpson and White (2005) described that the pressure distributions and droplet sizes were influenced significantly by the growth of the boundary layer. The works of Avetissian et al. (2005) and Avetissian et al. (2008) can be mentioned as well. They investigated the influence of the turbulence on nozzle flows. Further, in the works of Patel et al. (2013, 2014) presented the analysis of turbulence modelling influence to wet-steam flow with 2D nozzles and stator turbine cascade.

## 3 Pressure suppression pool experiments

Since 2002, phenomena appearing in suppression pools have been studied in LUT as a part of several national projects. In this work, the experimental references for the analysis and the simulations have been obtained from the suppression pool test facility experiments of LUT. The selected reference cases include steam discharges within the POOLEX and PPOOLEX facilities. This chapter contains a brief description of the test facilities and the corresponding blowdown tests.

### 3.1 POOLEX experiments

The POOLEX test facility was a scaled down condensation pool facility of first generation Nordic BWRs. The main objective of the POOLEX test program was to enhance the perception of various intricate phenomena appearing in BWRs containment during steam discharge into a subcooled water pool. One of the motives for these experiments was the validation of CFD codes and corresponding models (Puustinen et al., 2013a). Figure 3.1 shows the schematic view of the POOLEX test facility of LUT. It was a cylinder shaped stainless steel pool with an open top and a conical bottom. The test facility included the Parallel Channel Test Loop (PACTEL) steam generator, the steam lines assembly, the blowdown pipe, and the water pool. The geometrical parameters of the test facility are listed in Table 3.1.

To prevent any wall condensation, the steam lines from steam source to POOLEX were thermally insulated with mineral wool. A DN200 stainless steel pipe was used as a blowdown pipe in most of the tests. Steam flow rate was measured with a rotameter (Krohne Model H250). Thermocouples were installed in the test facility for measuring steam and pool water temperatures at various locations. The test facility was equipped with pressure transducers in order to capture the pressure behaviour in the blowdown pipe, in the steam line, and at the pool bottom during the blowdown period. Windows were installed in the pool wall for high and standard speed camera observation of the interior during steam blowdown event. Additional details concerning the test facility, measurement instrumentation and data acquisition are presented by Laine and Puustinen (2006a).

#### 3.1.1 POOLEX STB-31 experiment

Originally, POOLEX STB-31 test of the POOLEX test series was performed for the CFD validation of the NEPTUNE\_CFD condensation models (Tanskanen et al., 2008). The condensation mode of the POOLEX STB-31 test was a special case corresponding to the ‘oscillatory interface condensation’ mode (Chan and Lee, 1982b) and the ‘condensation within the blowdown pipe’ mode (Lahey and Moody, 1993). During this test, the pool was filled with water having uniform temperature. An insulated DN200 stainless steel pipe (a 50 mm thick insulation layer of hard polyurethane foam) was used as a blowdown

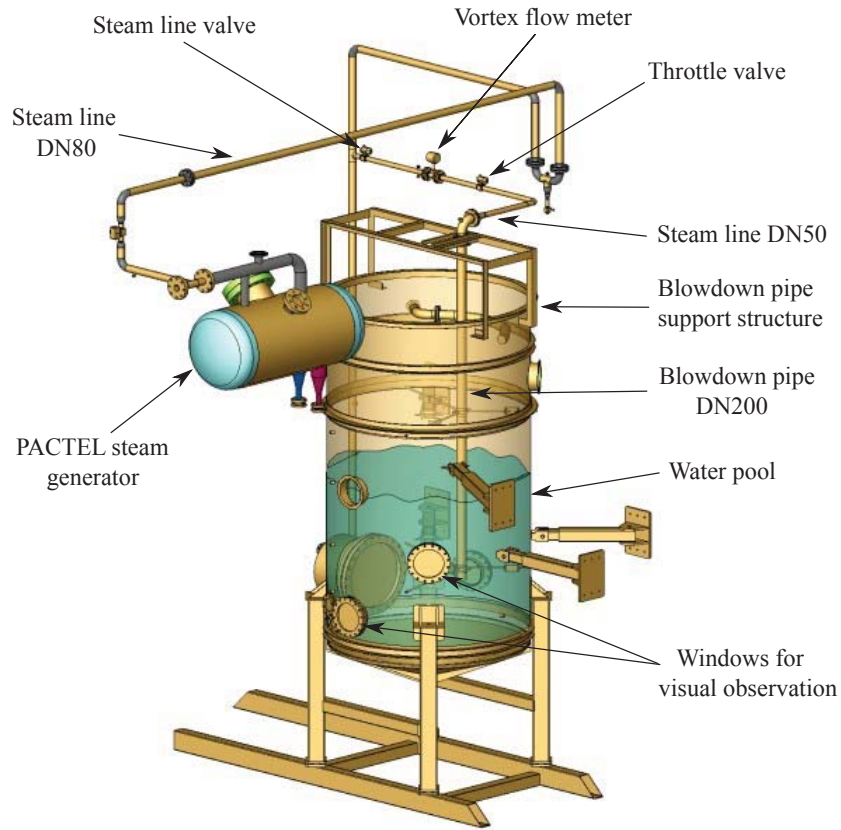


**Figure 3.1.** POOLEX test facility.

**Table 3.1.** The geometrical configuration of the POOLEX test facility.

Pool height [m]	5
Pool inner diameter [m]	2.4
Pool cross section area [m <sup>2</sup> ]	4.5
Blowdown pipe length [m]	4
Blowdown pipe diameter [m]	0.214
$A_{pipe}/A_{pool} \times 100$	0.8
Total volume of pool water [m <sup>3</sup> ]	12
Visual observation windows	5

pipe in POOLEX STB-31 test to rule out a significant wall condensation proportion of the total condensation rate. The STB-31 test conditions are listed in Table 3.2.

To prevent steam bubble formation and to keep the steam-water interface as close as

**Table 3.2.** The test parameters of the STB-31 experiment.

Initial pool water temperature [°C]	32
Initial water level in pool [m]	2.95
Blowdown pipe submergence level in pool [m]	1.81
Steam source pressure [MPa]	0.6...1.0
Steam temperature in blowdown pipe [°C]	104.35
Steam pressure in blowdown pipe [MPa]	0.119435
Steam flow rate [ $\text{g s}^{-1}$ ]	0.5...1.5

possible to the pipe outlet throughout the test, the steam mass flow rate was managed by a manual throttle valve. Figure 3.2 displays the measured data of steam mass flow rate, temperature and pressure at various locations during the POOLEX STB-31 test.

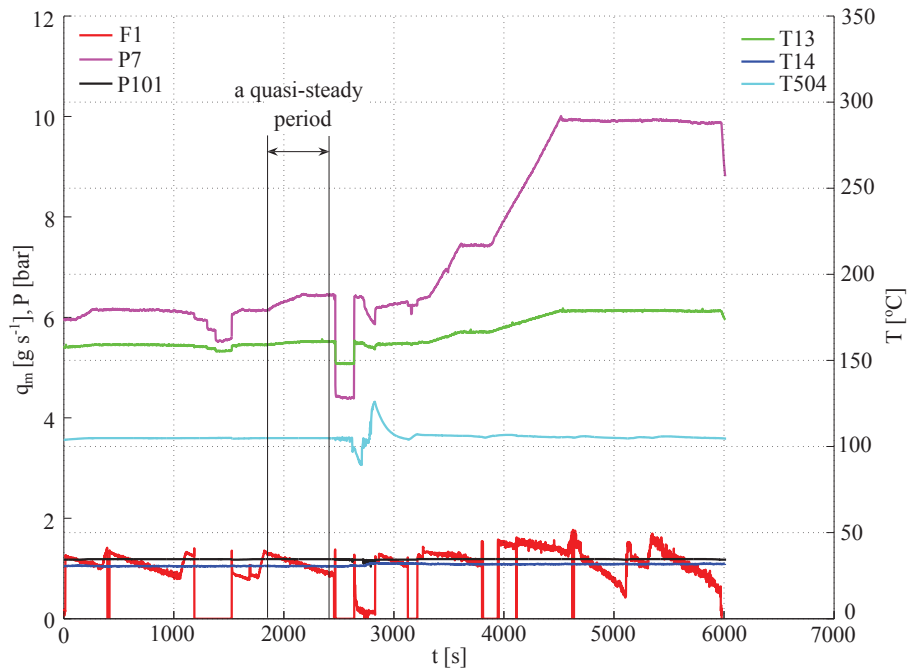


**Figure 3.2.** The measured data of the POOLEX STB-31 test (Tanskanen, 2012). Here, F1, T13, T14 and P7 indicate the volumetric flow rate in the steam line, temperature in the steam line, temperature in the pool and pressure in the steam line, respectively. These locations of instrumentation are presented in Laine and Puustinen (2006a).

During the test, it was observed that there were non-condensing bubbles escaping around the pipe lip. Accordingly, it was assumed that dissolved air was released from the pool

water, and it slowly accumulated as a layer between steam and water inside the blow-down pipe possibly having an effect on the condensation process at the steam-water interface. Therefore, it was essential to get rid of the air layer from/around the blowdown pipe mouth. This was achieved by increasing the steam flow rate at regular time periods throughout the test (e.g., during 1185...1525 s, 2455...2830 s, and 3800...3950 s). After these clearing phases, steam mass flow rate was again decreased to accomplish stable interface conditions. The corresponding video frames of stable interface, stable interface with escaping steam and strong blowdown during the POOLEX STB-31 test are shown in Figure 3.3.

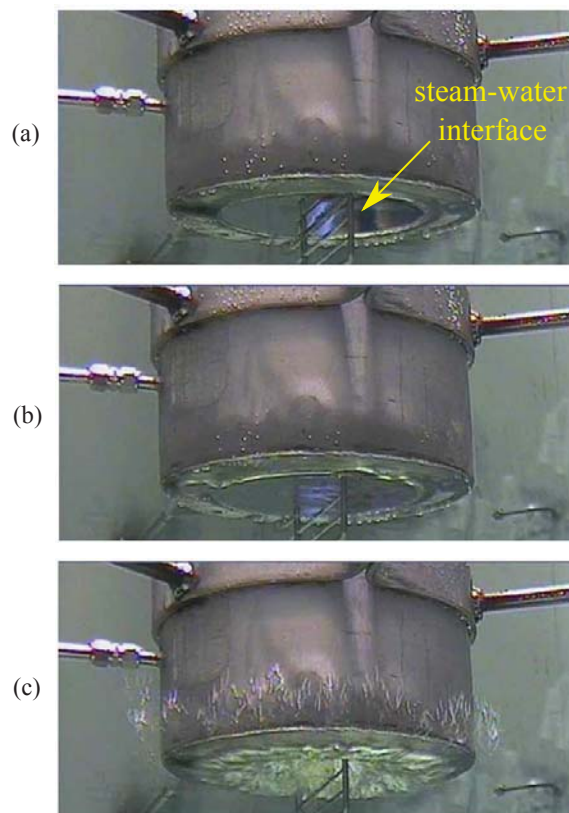


**Figure 3.3.** Instantaneous images of (a) stable interface, (b) stable interface with escaping steam/air, and (c) strong blowdown during the STB-31 POOLEX test.

As shown in Figure 3.2, there were several quasi-steady state intervals available during the experiment which were suitable for the CFD validation. A 300 s period (from 2014 s to 2314 s) from the STB-31 experiment was selected as reference for the CFD simulations (Tanskanen, 2012). Further details about POOLEX STB-31 test are presented in Publication I.

In order to estimate the non-condensables' effect on the condensation rate during the selected period of the POOLEX STB-31 experiment, Tanskanen (2012) applied the Couette flow film model by Ghiaasiaan (2008). The analysis demonstrated approximately 3–50 % higher condensation rates without the presence of non-condensable gases. The measurement error of mass flow rate exceeds that amount remarkably. However, the uncertainty of the Couette flow film analysis remained high. The calculation of total derivatives indicated that errors of one order of magnitude were possible. More details about the analysis of non-condensable gases for the POOLEX STB-31 test are described in Tanskanen (2012).

### 3.1.2 POOLEX STB-28 experiment

The POOLEX STB-28 experiment included one long-running steam blowdown. This test was aimed to investigate steam bubble formulation and its condensation at the blowdown pipe outlet as a function of pool water temperature (Laine and Puustinen, 2006b). During the blowdown, seven short time intervals in the range of 12 s to 30 s were recorded with a higher sampling rate. These sub tests were labelled from STB-28-1 to STB-28-7. During the POOLEX STB-28 test, the steam mass flow rate was kept almost constant. The STB-28 test conditions are listed in Table 3.3. Figure 3.4 shows the measured data of steam mass flow rate, temperature and pressure at various locations during the POOLEX STB-28 test.

**Table 3.3.** The test parameters of the STB-28 experiment.

Pool water temperature [°C]	47...77
Initial water level in pool [m]	3.5
Submerged level of blowdown pipe in pool [m]	2
Steam flow rate [ $\text{g s}^{-1}$ ]	300
Duration [s]	3195

A DN200 blowdown pipe was used in this test, however, the submerged part of the blowdown pipe was not thermally insulated. Therefore, the wall condensation resulting inside the submerged blowdown pipe decreased the steam mass flux. Therefore, an estimation of wall condensation at the inner surface of blowdown pipe was required. In the works of Tanskanen (2012) and Tanskanen et al. (2014), they estimated the wall condensation rate for the POOLEX STB-28 test by using the correlation of Chen et al. (1987) (Ghiaasiaan, 2008). This calculation method for wall condensation rate estimation is described in Tanskanen (2012). Figure 3.5 represents the measured values of steam mass flow rate at inlet, steam temperature and pool temperature and the estimated values of condensation rates and pipe wall temperature during the STB-28 test.

The video recording of steam blowdown event of water pool during STB-28 test was done by using both a standard video speed camera (25 fps) and a high speed video camera (500

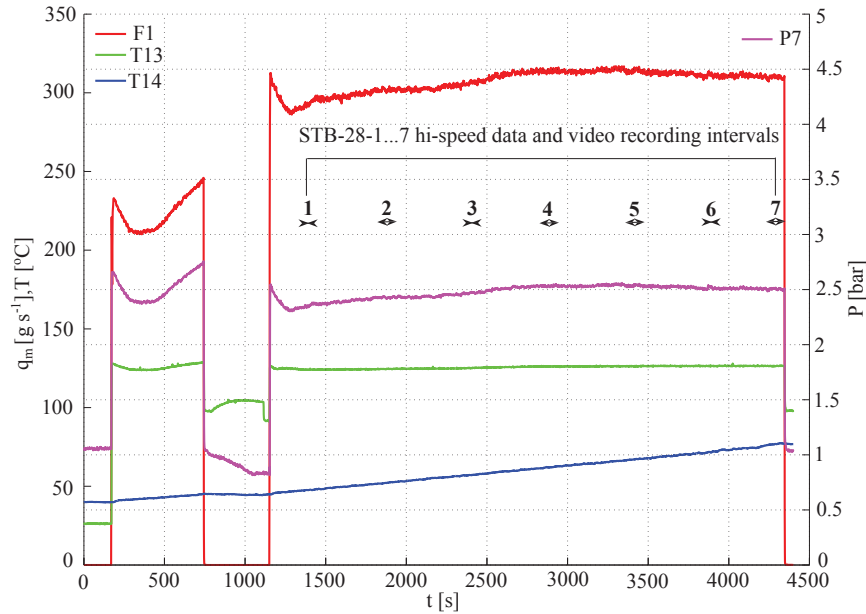


**Figure 3.4.** The measured data of the POOLEX STB-31 test (Tanskanen, 2012). Here, F1, T13, T14 and P7 indicate the volumetric flow rate in the steam line, temperature in the steam line, temperature in the pool and pressure in the steam line, respectively. These locations of instrumentation are presented in Laine and Puustinen (2006b).

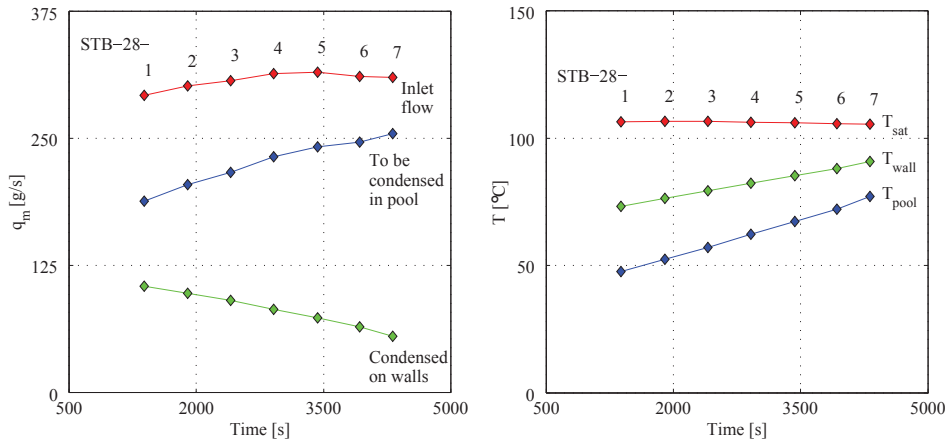


**Figure 3.5.** Estimation of wall condensation rate and wall temperatures in the STB-28 test (Tanskanen et al., 2014).

fps). The temperature and pressure were recorded via installed thermocouples and high-

frequency pressure transducers at various locations within the blowdown pipe and water pool. Also, the stress strain sensors were installed at the bottom of the pool to determine the structural loads.

The PPOOLEX STB-28 test is marked in Figure 1.3 in chapter 1 and it is categorized in the chugging condensation mode in which the steam bubbles form and rapidly collapse at the blowdown pipe outlet. Figure 3.6 displays the video frames showing typical steam bubbles resulted during the PPOOLEX STB-28 test. At the early phase of blowdown, the pool subcooling level was higher and therefore condensation rate was high, correspondingly, the steam bubbles sizes were relatively small. As the temperature of water inside the pool rose due to heat transfer, the rate of condensation decreased and consequently, the dominating steam bubble size increased gradually. The biggest bubble was resulted in the STB-28-7 test.

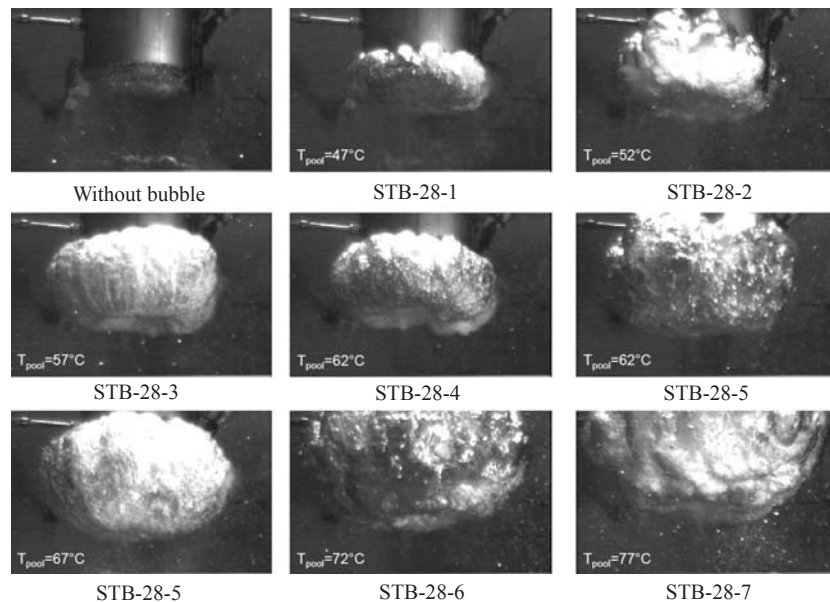


**Figure 3.6.** Typical steam bubble sizes as a function of pool water temperatures during the STB-28 test (Tanskanen et al., 2014).

### 3.2 PPOOLEX experiments

The PPOOLEX test facility of LUT is a unique technical scale experimental facility for BWR containment safety related research. The facility consists of both the drywell and wetwell (condensation pool) compartments of the containment which allows for tests of various thermalhydraulic scenarios ranging from bubble dynamics to complex interac-

tions of drywell and wetwell compartments during different types of accidents (Puustinen et al., 2006). Figure 3.7 shows the schematic view of the PPOOLEX test facility.

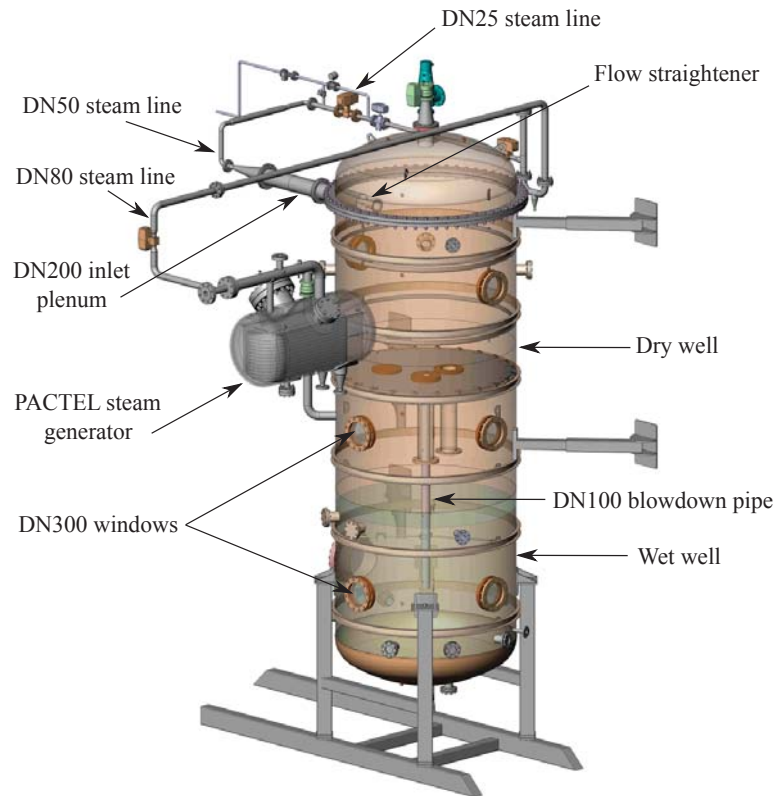


**Figure 3.7.** PPOOLEX test facility.

Several experiments have been performed with PPOOLEX facility including thermal stratification and mixing experiments, steam condensation in the drywell compartment, and effect of steam blowdown pipe outlet design and the number of blowdown pipes. More details are presented in Puustinen and Laine (2008), Puustinen et al. (2009), Laine and Puustinen (2009), Puustinen et al. (2011) and Puustinen et al. (2013b). The test facility contains an air/steam line piping, inlet plenum, drywell compartment, and a wetwell compartment (suppression pool). The total height of the test facility is 7.45 m and the inner diameter is 2.4 m. The main component of the facility is the approximately 31 m<sup>3</sup> cylindrical test vessel. The drywell compartment is thermally insulated to avoid wall condensation. The test facility is able to resist overpressure up to 4 bar and underpressure of 0.5 bar. A single or multiple blowdown pipes can be used in the PPOOLEX experiments which are positioned inside the wetwell compartment at non-axisymmetric locations. During the tests, the high-speed camera observation of the interior is possible

via the installed windows on the side walls and in the bottom segment of the wetwell compartment.

### 3.2.1 PPOOLEX DCC-05 experiment

The DCC-05 experiment was aimed to acquire test data for the validation of DCC models used in CFD codes and to obtain the multi-camera high speed video data of blowdown event to be used in the development work of pattern recognition algorithms. Unlike in the POOLEX STB-28 test, the temperature rise within the pool was minimized and the effect of different steam fluxes on the bubble size was studied in the PPOOLEX DCC-05 experiment. Also, temperature was measured in various elevations within the blowdown pipe in order to achieve the frequency and the amplitude of steam/water interface oscillations. Figure 3.8 displays the inlet steam mass flow rates during the DCC-05 experiment. The DCC-05 blowdown test is subdivided into six different steam blows viz. DCC-05-1 to DCC-05-6 according to steam mass flux.

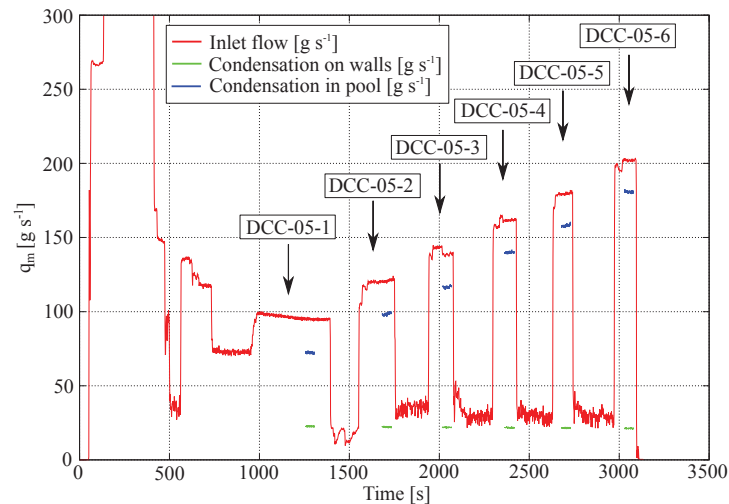


**Figure 3.8.** Six chugging blows of the DCC-05 experiment (Tanskanen et al., 2015).

Initially, the wetwell pool was filled with isothermal water. The blowdown pipe outlet was submerged in the water by approximately 1.0 m. The drywell was full of air at atmospheric pressure. During the clearing phase, part of the steam condensed on the drywell walls until the structures had heated up. After 500 seconds of the test start up, all air of the drywell compartment was displaced to the gas space of the wetwell. More details about the instrumentation and data acquisition can be found in Puustinen et al. (2013b). In this work, only PPOOLEX DCC-05-4 test was simulated. The test conditions of DCC-05-4 are listed in Table 3.4.

**Table 3.4.** The test parameters of the DCC-05-4 experiment.

Pool water temperature [ $^{\circ}\text{C}$ ]	25
Initial water level in pool [m]	3.5
Initial water temperature in pool [K]	300.7...315.6
Submerged level of blowdown pipe in pool [m]	1
Inlet steam flow rate [ $\text{kg s}^{-1}$ ]	0.1616
Drywell temperature [K]	406.8
Duration [s]	51.08

## 4 Numerical modelling

This chapter presents the details of the physical models used for DCC modelling in suppression pool and for condensing steam flows modelling in LP turbine. Throughout this work, three different CFD codes, namely OpenFOAM, ANSYS FLUENT and ANSYS CFX, were employed for CFD simulations. This chapter includes the details of governing equations, heat and mass transfer models, and interfacial area modelling used for DCC modelling. Further, the nucleation and droplet growth modelling for LP turbine flow simulations are presented. The thermodynamics properties and two-equation turbulence models used in this work are discussed in this chapter. The influence of grid refinement on the CFD results is assessed based on the GCI algorithm. This chapter discusses the utilized GCI method.

### 4.1 Physical models for DCC in suppression pool

All simulations of DCC in suppression pool were obtained by using the OpenFOAM CFD solver and compared to corresponding results of NEPTUNE\_CFD solver in which the steam-water system was simulated with the Eulerian-Eulerian two-fluid approach. In this approach, the interface between the phases is not necessarily tracked, because the existence of separate conservation equations for each phase does not require that. However, separate closure laws e.g. drag, lift, added mass forces, etc are required to close the equations and make the behaviour of smeared interface physical. Fluids share a large interface, particularly, during DCC modes appearing in a pressure suppression pool system with relatively large blowdown pipes without small orifices such as spargers during transient and accidents conditions. In this case of a large interface under phase change, the interfacial drag force and the heat/mass transfer rate are the most relevant additions needed.

#### 4.1.1 Governing equations

The equations for conservation of mass, momentum and energy for two-phase flow in OpenFOAM CFD code can be expressed as below, respectively:

$$\frac{\partial \alpha_\phi \rho_\phi}{\partial t} + \nabla \cdot (\alpha_\phi \rho_\phi \mathbf{U}_\phi) = \Gamma_\phi, \quad (4.1)$$

$$\begin{aligned} \frac{\partial \alpha_\phi \rho_\phi \mathbf{U}_\phi}{\partial t} + \nabla \cdot (\alpha_\phi \rho_\phi \mathbf{U}_\phi \mathbf{U}_\phi) + \alpha_\phi \nabla \cdot \boldsymbol{\tau}_\phi + \nabla \cdot (\alpha_\phi \rho_\phi \mathbf{R}_{\mathbf{T}\phi}) \\ = -\alpha_\phi \nabla P + \alpha_\phi \rho_\phi g + \mathbf{M}_\phi, \end{aligned} \quad (4.2)$$

$$\frac{\partial \alpha_\phi \rho_\phi H_\phi}{\partial t} + \nabla \cdot (\alpha_\phi \rho_\phi \mathbf{U}_\phi H_\phi) = \alpha_\phi \frac{\partial P}{\partial t} + \nabla \cdot (\alpha_\phi \rho_\phi D_{T,\text{eff},\phi} \nabla H_\phi) + \Gamma_\phi H_{i,\phi} + \mathbf{Q}_\phi. \quad (4.3)$$

Here,  $\phi$  stands for an arbitrary phase (further  $\phi = a$  for steam and  $\phi = b$  for water),  $\alpha_\phi$  is the phase fraction,  $\rho_\phi$  is the density, and  $\mathbf{U}_\phi$  represents the velocity of the  $\phi$  phase. In mass conservation equation, i.e. Eq. (4.1),  $\Gamma_\phi$  expresses the mass source/sink per unit volume. This source term can be defined by using a phase change model. More details about source term are discussed in chapter 4.1.2.

In momentum equation, i.e. Eq. (4.2),  $\tau_\phi$  and  $\mathbf{R}_{T\phi}$  describe the viscous stress tensor and the turbulent stress tensor, respectively. The terms on the right hand side of equation represent the forces acting on the  $\phi$  phase in the control volume, where  $\nabla P$ ,  $g$  and  $\mathbf{M}$  denote the overall pressure gradient, the gravitational force, and the interphase momentum forces, respectively. In general, the interphase momentum transfer term consists of all the interfacial forces, e.g. drag, lift, virtual mass, wall lubrication force, etc. In the present study, only the effect of drag force was considered while the other interfacial forces were omitted. In energy transport equation, i.e. Eq. (4.3),  $H_\phi$  and  $H_{i,\phi}$  are the total enthalpy and the interfacial enthalpy of the  $\phi$  phase, respectively. The term  $D_{T,\text{eff},\phi}$  indicates the phase effective thermal diffusivity.  $\mathbf{Q}_\phi$  denotes the volumetric interfacial heat transfer rate.

The interphase momentum exchange coefficient  $\mathbf{M}_{ab}$ , in Eq. (4.2) in OpenFOAM CFD code can be written as (Peltola, 2012)

$$\mathbf{M}_{ab} = \alpha_a \alpha_b \frac{3}{4} C_{D,a} \rho_b \frac{1}{d_B} |\mathbf{U}_a - \mathbf{U}_b| (\mathbf{U}_a - \mathbf{U}_b). \quad (4.4)$$

Here,  $d_B$  is the bubble diameter which was considered a constant value (i.e. 1 mm) during the simulations and  $C_D$  is the drag coefficient which was obtained using the drag correlation of Schiller and Naumann (1933), which can be written as

$$C_D = \begin{cases} \frac{24}{\text{Re}} (1 + 0.15 \text{Re}^{0.687}), & \text{if } \text{Re} \leq 1000 \\ 0.44, & \text{if } \text{Re} > 1000, \end{cases} \quad (4.5)$$

where  $\text{Re}$  is the relative Reynolds number. In the OpenFOAM simulations, the drag correlation of Schiller and Naumann (1933) was the most suitable option of the already implemented models for gas-liquid flow. Despite of its limited applicability for fully separated phases, it produces reasonable drag if the reference bubble diameter value is adjusted to a suitable value e.g. 1 mm in the suppression pool simulations.

#### 4.1.2 Phase change and heat transfer models

In this work, the phase change model was used to simulate the DCC phenomena, which describes the phase change instigated by interphase heat transfer of adjacent convective

flows. The approach is only appropriate for the change of phase without non-condensables and deals with the heat transfer processes on each side of the phase interface. The interfacial heat transfer modelling was based on the two-resistance approach, in which the heat transfer was calculated between each phase and the interface between the phases (Peltola, 2012). The heat fluxes from the interface to steam and from the interface to water were calculated from following expressions,

$$q_a = a_{ia} h_{i,a} (T_{\text{int}} - T_a) \quad (4.6)$$

$$q_b = a_{ib} h_{i,b} (T_{\text{int}} - T_b) \quad (4.7)$$

Here,  $T$  is the temperature.  $a_{ia}$  and  $a_{ib}$  stand for the interfacial area densities for steam and water, respectively. The interfacial area density was calculated from the gradient of void fraction as

$$a_{i\phi} = |\nabla a_{i\phi}|. \quad (4.8)$$

The interfacial temperature  $T_{\text{int}}$ , was set to the saturation temperature. The terms  $h_{i,a}$  and  $h_{i,b}$  represent the corresponding heat transfer coefficients of steam and water, respectively.

By imposing the total heat balance, the interface mass transfer was calculated in the simulations. The total heat flux balance was yielded by using following expressions

$$\mathbf{Q}_a = q_a - \Gamma_{i,b} H_{i,a} \quad (4.9)$$

$$\mathbf{Q}_b = q_b + \Gamma_{i,b} H_{i,b}. \quad (4.10)$$

By imposing the overall heat balance i.e.  $\mathbf{Q}_a + \mathbf{Q}_b = 0$ , the mass transfer due to the phase change at the steam-liquid interface can be calculated as

$$\Gamma_{i,b} = \frac{q_a + q_b}{H_{i,a} - H_{i,b}}. \quad (4.11)$$

In this work, the steam is in saturated state, therefore in all the simulations, the vapour phase heat transfer contribution was negligible i.e.  $q_a \approx 0$ . The heat transfer coefficient for the water phase was defined as

$$h_{i,b} = \frac{\text{Nu}_b \lambda_b}{L_T}, \quad (4.12)$$

where  $\lambda_b$  is the thermal conductivity and  $L_T$  is the characteristic length.  $\text{Nu}_b$  is the Nusselt number. Throughout this work, various Nusselt number correlations were employed for DCC simulations which are described below.

### **The Lakehal model**

The Nusselt number correlation of Lakehal (hereafter ‘LH model’) is based on the surface divergence theory of Banerjee (1990). The applicability of this model has typically

been tested for mildly sheared concurrent and countercurrent horizontal two-phase flows (Lakehal et al., 2008). The Nusselt number can be written as

$$\text{Nu}_b = Bf[\text{Re}_T^m]\text{Re}_T\text{Pr}^{1/2}. \quad (4.13)$$

Here,  $B$  is the model constant (i.e.  $B = 0.35$  for  $\text{Pr} \approx 1$  and  $B = 0.45$  for  $\text{Pr} \gg 1$ ) and the expression  $f(\text{Re}_T^m)$  can be written as

$$f[\text{Re}_T^m] = \left[ 0.3 \left( 2.83\text{Re}_T^{3/4} - 2.14\text{Re}_T^{2/3} \right) \right]^{1/4} \text{Re}_T^{-1/2}. \quad (4.14)$$

Here,  $\text{Re}_T$  denotes the turbulent Reynolds number which was determined from turbulence kinetic energy, i.e.  $k_b$ , turbulence dissipation, i.e.  $\varepsilon_b$ , and kinematic viscosity, i.e.  $\nu_b$  as

$$\text{Re}_T = \frac{k_b^2}{\nu_b \varepsilon_b}. \quad (4.15)$$

The same form of the heat transfer equation was used by the LH model as given in Eq. (4.12). The turbulent length scale, i.e.  $L_T$ , was calculated by employing the following form

$$L_T = \frac{\nu_b}{V_T} \text{Re}_T, \quad (4.16)$$

where the turbulent velocity scale, i.e.  $V_T$ , was derived from the following definition

$$V_T = (\nu_b \varepsilon_b)^{1/4} \quad (4.17)$$

### The Hughes and Duffey model

The Hughes and Duffey model (hereafter ‘HD 1 model’) is based on the surface renewal model of Hughes and Duffey (1991). The Nusselt number formulation ( $\text{Nu}_{K,b} = \frac{h_{i,b} L_K}{\lambda_b}$ ) can be defined as

$$\text{Nu}_b = \frac{2}{\sqrt{\pi}} \text{Re}_K^{1/2} \text{Pr}^{1/2}, \quad (4.18)$$

where  $\text{Re}_K$  is the Reynolds number based on Kolmogorov velocity and length scales,  $V_K$  and  $L_K$  ( $\text{Re}_K = \frac{V_K L_K}{\nu_b} \sim 1$ ):

$$V_K = (\nu_b \varepsilon_b)^{1/4} \quad \text{and} \quad L_K = \left( \frac{\nu_b^3}{\varepsilon_b} \right)^{1/4}. \quad (4.19)$$

In the NEPTUNE.CFD version of Hughes and Duffey model (hereafter ‘HD 0 model’), the Nusselt number formulation of Hughes and Duffey model in NEPTUNE.CFD can be

written as (Laviéville et al., 2006)

$$\text{Nu}_b = \frac{2}{\sqrt{\pi}} \text{Re}_T \text{Pr}^{1/2}, \quad (4.20)$$

where the turbulent scales  $V_T$  and  $L_T$  can be expressed as below:

$$V_T = C_\mu^{1/4} k_b^{1/2} \quad \text{and} \quad L_T = C_\mu^{3/4} \frac{k_b^{3/2}}{\varepsilon_b}. \quad (4.21)$$

In the NEPTUNE\_CFD HD 0 model, the  $V_T$  was limited with  $V_T = \min(|\mathbf{U}_b|, C_\mu^{1/4} k_b^{1/2})$ . However, the formulation of Eq. (4.20) using  $\text{Re}_T$  is only legitimate when the  $\text{Re} = \text{Re}_K$ . Thus, this HD 0 model seems misderived or improvised and not valid as original Hughes and Duffey model.

#### The Coste 2004 model

The Nusselt number formulation of the Coste continuous model (hereafter ‘Coste C model’) of Coste (2004) can be written as

$$\text{Nu}_b = \text{Re}_T^{7/8} \text{Pr}^{1/2}, \quad (4.22)$$

where the turbulent velocity and length scales of Coste C model can be written as below:

$$V_T = \left(\frac{2}{3} k_b\right)^{1/2} \quad \text{and} \quad L_T = L_K = \left(\frac{\nu_b^3}{\varepsilon_b}\right)^{1/4}. \quad (4.23)$$

In the Coste C model, the  $V_T$  was limited with  $V_T = \min(|\mathbf{U}_b|, (\frac{2}{3} k_b)^{1/2})$ .

#### 4.1.3 Turbulence models

The standard  $k - \varepsilon$  turbulence model of Launder and Spalding (1974) was used to solve the flow turbulence. The transport equations of the turbulent kinetic energy  $k$  and its dissipation  $\varepsilon$  can be written as follows,

$$\frac{\partial \rho_\phi k_\phi}{\partial t} + \nabla \cdot (\rho_\phi \mathbf{U}_\phi k_\phi) - \nabla \cdot \left( \left( \nu_\phi + \frac{\nu_{T,\phi}}{\sigma_k} \right) \nabla k_\phi \right) + R_{ck,\phi} \nabla k_\phi = G_\phi - \varepsilon_\phi, \quad (4.24)$$

$$\begin{aligned} \frac{\partial \rho_\phi \varepsilon_\phi}{\partial t} + \nabla \cdot (\rho_\phi \mathbf{U}_\phi \varepsilon_\phi) - \nabla \cdot \left( \left( \nu_\phi + \frac{\nu_{T,\phi}}{\sigma_\varepsilon} \right) \nabla \varepsilon_\phi \right) + R_{c\varepsilon,\phi} \nabla \varepsilon_\phi \\ = C_1 G_\phi \frac{\varepsilon_\phi}{k_\phi} - C_2 \rho_\phi \frac{\varepsilon_\phi^2}{k_\phi}. \end{aligned} \quad (4.25)$$

In Eqs. (4.24) and (4.25),  $R_{ck}$  and  $R_{c\varepsilon}$  are the volume fraction gradient fluxes. The term  $G$  is the production term of the turbulent kinetic energy which can be expressed as below

$$G_\phi = -\rho_\phi \overline{\mathbf{U}_{i\phi} \mathbf{U}_{j\phi}} \frac{\partial \mathbf{U}_{j\phi}}{\partial x_i}. \quad (4.26)$$

The turbulent viscosity  $\nu_{T,\phi}$ , was calculated as

$$\nu_{T,\phi} = C_\mu \frac{k_\phi^2}{\varepsilon_\phi}. \quad (4.27)$$

The values of model constants such as  $C_\mu$ ,  $C_1$ ,  $C_2$ ,  $\sigma_k$ ,  $\sigma_\varepsilon$  are 0.09, 1.44, 1.92, 1.0, 1.3, respectively. In the simulations of low-Reynolds number DCC case of a thermally insulated vertical blowdown pipe, the transport equations Eqs. (4.24) and (4.25) were solved for the continuous phase only i.e. liquid phase, while the ‘dispersed phase’ i.e. vapour phase, turbulent viscosity and turbulent kinetic energy were the continuous phase values scaled with the turbulence response coefficient. However, in this study, only the liquid phase turbulence was important. More details about turbulence modelling in low-Reynolds number DCC case are discussed in Publication I.

In the chugging DCC simulations of this work, the standard  $k - \varepsilon$  turbulence model proposed by Launder and Spalding (1974) (hereafter ‘Sk- $\varepsilon$ ’) and the  $k - \varepsilon$  turbulence model proposed by Lahey (2005) (hereafter ‘Lk- $\varepsilon$ ’) were used. The Lk- $\varepsilon$  model includes dispersed phase induced turbulence terms in the  $k$  and  $\varepsilon$  transport equations. Also, the Lk- $\varepsilon$  model uses modified turbulent viscosity term. More details about this model are referred in Publication III.

#### 4.1.4 Rayleigh-Taylor instability (RTI) model

In two-phase flow with phase change, accurate modelling of interface behaviour is important. Different methodologies have been used to gain the interfacial area e.g. in dispersed flows cases where the interface is small compared to the computational cell size, the Sauter mean diameter is used to calculate interfacial area. In the separated flow cases where the interface is larger and is shared by more than one computational cell, the interfacial area density is calculated from the gradient of void fraction. However, the accuracy of interfacial area density relies on the grid size related to the interfacial details. Gradient of void fraction excludes the interface alterations which are smaller in scale than the computational cells. The high accelerations in the flow field instigate interfacial instabilities

e.g. Rayleigh-Taylor instability, which increase the interfacial roughness significantly.

In this work, a model given by Pellegrini et al. (2015) to treat the surface with growing instabilities based on the Rayleigh-Taylor theory has been used. However, the chugging simulations including Rayleigh-Taylor instability are limited to NEPTUNE\_CFD simulations only.

The interfacial wave amplitude  $\eta$ , is defined as

$$\frac{d\eta}{dt} = n\eta. \quad (4.28)$$

In the work of Pellegrini et al. (2015), they derived the function  $n$  from Duff et al. (1962) and Livescu (2004), and it can be written as below

$$n = \Re \left( \sqrt{\left( Ag - \frac{\sigma \kappa^2}{\rho_b - \rho_a} \right) \kappa + \nu^2 \kappa^4 - \nu \kappa^2} \right). \quad (4.29)$$

Here,  $g$  and  $\kappa$  are the acceleration and the wave number, respectively.  $A$  is the Atwood number.

Pellegrini et al. (2015) formulated the expression for interfacial area as

$$a_{i,\text{amplified}} = \left( \frac{\kappa\eta + 1}{\pi} \right)^2 a_i, \quad (4.30)$$

where  $a_i$  is the interfacial area density (Eq. (4.8)). Here, the wave number should be maximizing the wave growth. In the work of Pellegrini et al. (2015), they simplified the calculation by employing the following definition as

$$\kappa_{\max} = \sqrt{\frac{Ag(\rho_b + \rho_a)}{3\sigma}}. \quad (4.31)$$

The amplitude of the wave was written as

$$\eta_t = \eta_{t-\Delta t} e^{n\Delta t}. \quad (4.32)$$

Pellegrini et al. (2015) employed a small value i.e.  $\eta_{t=0} = 10^{-5}$  m as an initial perturbation. The value of  $\eta$  was also limited by the cell size by using

$$\eta_t = \min(\eta_t, L). \quad (4.33)$$

Further details about Rayleigh-Taylor instability modelling are described in Publication III.

#### 4.1.5 Thermodynamics properties for DCC simulations

Thermodynamics properties are important for two-phase flow modelling with heat and mass transfer. However, due to lack of steam table availability in OpenFOAM, constant steam properties were used for saturated vapour phase in all the DCC simulations of OpenFOAM. The vapour phase was treated as perfect gas assumption. In NEPTUNE\_CFD simulations, the steam tables of CATHARE code (Laviéville et al., 2006) were used.

## 4.2 Physical models for condensing steam flows in LP turbine

The condensing steam flows consist of tiny condensed water droplets in carrier vapour phase, therefore, they are always attributed as gas-liquid two-phase flows. The CFD modelling of condensing steam flow can be categorized in three different approaches: the Eulerian-Eulerian approach, the Eulerian-Lagrangian approach and the method of moments. In the Eulerian-Eulerian approach, both continuum vapor phase and dispersed liquid phase are solved as interpenetrating continua in which the condensed droplet distribution is represented in terms of a finite number of droplet sizes (Gerber and Kermani, 2004; Dykas and Wróblewski, 2011). In the Eulerian-Lagrangian approach, the vapour phase is treated as a continuum phase in an Eulerian frame of reference, while the liquid droplet is solved as dispersed phase in the Lagrangian frame of reference in which the trajectories of each droplet are followed (Young, 1992; Gerber, 2002). In the moment method, the formation of droplets, their growth and transport are determined by a finite number of moments of the droplet size distribution. The moment-based approach estimates the heat and mass transfer between vapour and liquid phases, and this approach is considered more computationally reasonable compared to the discrete spectrum calculations (Hill, 1966; White and Hounslow, 2000).

In this work, the Eulerian-Eulerian approach has been used to model condensing steam flow, in which the mixture of carrier vapour phase and condensed liquid droplets are treated as interpenetrating continua. This chapter presents the utilized numerical models throughout this work.

### 4.2.1 Governing equations

This section summarizes the governing equations of ANSYS FLUENT only. The details concerning utilized wet-steam flow governing equations with ANSYS CFX code are described in Publication VI.

The equations for conservation of mass, momentum and energy for a mixture of vapour and liquid phases are expressed as below, respectively:

$$\frac{\partial \rho_m}{\partial t} + \nabla \cdot (\rho_m \mathbf{U}_v) = S_C, \quad (4.34)$$

$$\frac{\partial}{\partial t}(\rho_m \mathbf{U}_v) + \nabla \cdot (\rho_m \mathbf{U}_v \mathbf{U}_v) = -\nabla P + \nabla \cdot \tau_{ijm} + S_M, \quad (4.35)$$

$$\frac{\partial}{\partial t}(\rho_m H_m) + \nabla \cdot (\rho_m \mathbf{U}_v H_m) = \frac{\partial P}{\partial t} + \nabla \cdot (\Gamma_E \nabla T_m) + \nabla \cdot (\mathbf{U}_v \tau_{ijm}) + S_E. \quad (4.36)$$

Here,  $P$  is the pressure,  $\tau_{ij}$  is the stress tensor component,  $\Gamma_E$  is the effective thermal conductivity. The subscripts  $m$  and  $v$  stand for the mixture and the vapour phase, respectively. In the mass conservation equation, the source term  $S_C$  is the mass transfer caused by the condensation or evaporation. In the momentum equation,  $S_M$  is the momentum source term, which incorporates the momentum exchange between the condensed liquid droplets and the surrounding vapour, and it also includes the smaller terms resulted from the gradient of the Reynolds stress tensor. The term  $S_E$  in the energy equation indicates the energy source term which contains the interfacial heat transfer.

Additionally, two transport equations are solved together with abovementioned governing equations. The first transport equation calculates the condensed liquid phase mass-fraction  $\beta$ , and the other estimates the number of liquid droplets per unit volume  $N_d$ . These transport equations can be written as

$$\frac{\partial}{\partial t}(\rho_m \beta) + \nabla \cdot (\rho_m \mathbf{U}_v \beta) = \Gamma, \quad (4.37)$$

$$\frac{\partial}{\partial t}(\rho_m N_d) + \nabla \cdot (\rho_m \mathbf{U}_v N_d) = \rho_m I. \quad (4.38)$$

Here,  $\Gamma$  and  $I$  indicate the mass generation rate per unit volume owing to condensation or evaporation, and the nucleation rate, respectively. Although, some assumptions have been considered in the in-built wet-steam model of ANSYS FLUENT: (i) since the condensed liquid phase contains a large number of infinitesimal droplets consisting radii of the order of  $1 \mu\text{m}$  or less, the volume of the condensed liquid phase is negligible, (ii) the interactions between condensed liquid droplets are excluded, and (iii) the velocity slip between the liquid droplets and the carrier vapour phase is neglected.

#### 4.2.2 Models for nucleation and droplet growth

The condensing steam flow includes two essential phenomena: nucleation and droplet growth. The classical homogeneous nucleation theory of McDonald (1962) was used for nucleation modelling in this work. The nucleation rate was calculated by employing the following expression

$$I = \frac{q_c}{(1 + \theta)} \left( \frac{\rho_v^2}{\rho_l} \right) \sqrt{\frac{2\sigma}{M_m^3 \pi}} e^{-\left( \frac{4\pi r^2 \sigma}{3K_b T} \right)}. \quad (4.39)$$

Here,  $q_c$  is a condensation coefficient which is usually considered as unity,  $\theta$  is the non-isothermal correction function,  $K_b$  is the Boltzmann's constant, and  $M_m$  is the molecular mass of water. The  $\theta$  value has been evaluated by using the formulation of Kantrowitz (1951):

$$\theta = \frac{2(\gamma - 1)}{\gamma + 1} \left( \frac{h_{lv}}{RT} \right) \left( \frac{h_{lv}}{RT} - 0.5 \right). \quad (4.40)$$

Here,  $\gamma$  is the ratio of specific heat capacities,  $R$  is the gas constant and  $h_{lv}$  is the specific enthalpy of evaporation at pressure  $P$ .

The mass generation rate  $\Gamma$ , for liquid droplets is calculated by using the formulation of Ishizaka et al. (1995) which represents the addition of the mass generation rate for a critical-sized nucleus and the growth/demise of liquid droplets. The expression of  $\Gamma$  can be defined as

$$\Gamma = \frac{4}{3}\pi\rho_l I r_*^3 + 4\pi\rho_l N_d \bar{r}^2 \frac{\partial \bar{r}}{\partial t}, \quad (4.41)$$

where,  $r_*$  is the Kelvin-Helmholtz critical droplet radius which determines whether the droplet will grow or not and  $\bar{r}$  is the average liquid droplet radius. If the droplet radius is greater than the critical droplet radius, the droplet will grow, otherwise the droplet will evaporate. The expression of  $r_*$  can be written as below:

$$r_* = \frac{2\sigma}{\rho_l R T_v \ln S}. \quad (4.42)$$

Here,  $S$  indicates the supersaturation ratio which is calculated by the ratio of vapour pressure to the equilibrium saturation pressure as

$$S = \frac{P}{P_{\text{sat}}(T_v)}. \quad (4.43)$$

After droplet formation, condensation happens due to the growth of the generated liquid droplets. During the growth process, the subcooling of the vapour phase reduces rapidly due to released latent heat which prevents further droplet formation. There are two mechanisms incorporated in the droplet growth process in condensing steam flows: (i) mass transfer from the carrier vapour phase to condensed liquid phase and, (ii) heat transfer from liquid droplets to the vapour phase in the form of latent heat (Ishizaka et al., 1995). The growth rate of a droplet greatly relies on the rate at which heat is conducted away from the droplet (Young, 1982). In ANSYS FLUENT simulations, the droplet growth rate is estimated by the heat transfer conditions surrounding the droplet (Hill, 1966). The droplet growth model is expressed as below:

$$\frac{\partial \bar{r}}{\partial t} = \frac{P}{h_{lv}\rho_l\sqrt{2\pi RT_v}} \frac{\gamma + 1}{2\gamma} C_p (T_l - T_v), \quad (4.44)$$

The details of the droplet temperature  $T_l$ , estimation has been described by Young (1982).

In ANSYS CFX simulations, the droplet growth rate model by Gyarmathy (1976), based on Knudsen number  $K_n$ , was used. Further details about the droplet growth model are discussed in Publication VI.

### 4.2.3 Equation of state and thermodynamic properties

Since the nucleation and droplet growth phenomena are quite sensitive to the thermodynamical properties, the precise modelling of condensing steam flow requires correct thermodynamic properties of vapour in the superheated region, at the saturated line and in the two-phase region. Also, these non-equilibrium flows cannot be simulated accurately in the meta-stable region by applying the ideal-gas assumption. Therefore, the real gas model is essential to calculate steam condensing flows.

The real gas properties in ANSYS CFX simulations were computed by using the IAPWS-IF97 formulation which is based on a lookup table approach. The user has to define the appropriate range of pressure and temperature, and the number of divisions within the defined range. More details about the formulation of IAPWS-IF97 have been described by Wagner and Kruse (1998).

In ANSYS FLUENT simulations, the EOS and the thermodynamic properties for the superheated region were determined by using the formulations of Young (1988) which is the default selection in the wet-steam model of ANSYS FLUENT. The EOS for the vapour phase employs a virial form with temperature and density as the independent variables and can be expressed as

$$P_v = \rho_v R T_v (1 + B \rho_v + C \rho_v^2), \quad (4.45)$$

where,  $B$  and  $C$  represent the second and third virial coefficients, respectively. The virial coefficients can be defined as empirical functions of temperature as below:

$$B = a_1 \left(1 + \frac{T}{\alpha}\right)^{-1} + a_2 e^{\tau} \left(1 - \frac{1}{e^{\tau}}\right)^{5/2} \tau^{-1/2} + a_3 \tau, \quad (4.46)$$

$$C = a(\tau - \tau_0) e^{-\alpha\tau} + b. \quad (4.47)$$

In Eq. (4.46),  $a_1 = 0.0015$ ,  $a_2 = -0.000942$ ,  $a_3 = -0.0004882$ ,  $\alpha = 10000$ , and  $\tau = \frac{1500}{T}$ . In Eq. (4.47),  $a = 1.772$ ,  $b = 1.5 \times 10^{-6}$ ,  $\alpha = 11.16$ ,  $\tau = \frac{T}{647.286}$ , and  $\tau_0 = 0.8978$ . More details about the accuracy and applicability range of real gas formulations have been discussed by Young (1988).

In wet-steam model of ANSYS FLUENT, the estimations of saturated pressure and saturated temperature were based on the formulations of Reynolds (1979). The values of  $\rho_l$  and  $\sigma_l$  at the saturated liquid line were calculated from Reynolds (1979) and Young (1982), respectively. Other thermodynamic properties, e.g.  $C_{p_l}$ ,  $\mu_l$  and  $\lambda_l$  at the saturated liquid line, were determined from the formulations of Eckert and Drake (1972).

The conservation equations of wet-steam model of ANSYS FLUENT utilised the mixture properties of the vapour and liquid phases. These mixture properties were defined by using the mixing law as below:

$$\phi_m = \phi_l \beta + (1 - \beta) \phi_v. \quad (4.48)$$

Here,  $\phi$  denotes  $h$ ,  $s$ ,  $C_p$ ,  $C_v$ ,  $\mu$ , and  $\lambda$  which indicate the specific enthalpy, the entropy, the specific heat at a constant pressure, the specific heat at a constant volume, the dynamic viscosity and the thermal conductivity, respectively.

#### 4.2.4 Turbulence models

In the present work, Reynolds-averaged two-equation turbulence models viz. the standard  $k$ - $\varepsilon$  turbulence model of Launder and Spalding (1974) and the shear stress transport (SST)  $k$ - $\omega$  turbulence model of Menter (1994) were employed for modelling the flow turbulence. In LP turbine flows, most of the liquid phase mass concentration consists of a very large number of submicron size droplets (Guha, 1995). Therefore, it could be assumed that the condensed droplets have no direct influence on the flow turbulence, and therefore, in this work, the direct influence of the condensed liquid droplets on the vapour phase turbulence was not investigated. Although, there exist an indirect influence through the velocity field introduced to the turbulence models. The turbulence in the vapour phase does have an influence on the dispersion of the liquid droplets. Owing to both small sizes and mass concentrations of liquid droplets, the transport equations of turbulence models were treated for the mixture of the vapour and liquid phases.

The transport equations of the turbulence kinetic energy  $k$ , and its specific rate of dissipation  $\omega$ , for SST  $k$ - $\omega$  turbulence model, for the mixture of vapour and liquid phases can be expressed in the following form, respectively,

$$\frac{\partial}{\partial t}(\rho_m k) + \nabla \cdot (\rho_m \mathbf{U}_v k) = \nabla \cdot \left[ \left( \mu_m + \frac{\mu_{Tm}}{\sigma_k} \right) \nabla k \right] + \tilde{G}_k - Y_k + S_k, \quad (4.49)$$

$$\frac{\partial}{\partial t}(\rho_m \omega) + \nabla \cdot (\rho_m \mathbf{U}_v \omega) = \nabla \cdot \left[ \left( \mu_m + \frac{\mu_{Tm}}{\sigma_\omega} \right) \nabla \omega \right] + G_\omega - Y_\omega + D_\omega + S_\omega, \quad (4.50)$$

where,  $Y_k$  and  $Y_\omega$  represent the dissipation of  $k$  and  $\omega$  due to turbulence, respectively, and  $D_\omega$  defines the cross-diffusion term.  $S_k$  and  $S_\omega$  refer to the source terms of turbulent equations, and  $\tilde{G}_k$  and  $G_\omega$  indicate the generation of turbulence kinetic energy and its specific dissipation rate due to mean velocity gradients, respectively. The term  $\tilde{G}_k$  is calculated as follows:

$$\tilde{G}_k = \min(G_k, 10\rho_m\beta^*k\omega), \quad (4.51)$$

where  $\beta^*$  is the model constant and  $G_k$  is the production term.

In Eqs. (4.49) and (4.50),  $\mu_{Tm}$  represents the turbulent viscosity which is written as below:

$$\mu_{Tm} = \frac{\rho_m k}{\omega} \frac{1}{\max\left[\frac{1}{\alpha^*}, \frac{S_1 F_2}{\alpha_1 \omega}\right]}, \quad (4.52)$$

where,  $\alpha^*$  is the damping coefficient,  $\alpha_1$  is the model constant,  $S_1$  is the strain rate magnitude, and  $F_2$  is the blending function. More details about the auxiliary relations, closure coefficients and model constants are presented in Menter (1994).

In wet-steam flows, the rate of collisions of liquid droplets on flow turbulence is important. In the work of Zaichik et al. (2003), they presented the statistical mechanical models of the geometrical collision rate due to the particle turbulence interaction. In their approach, the particle density was considered much higher than that of the carrier phase. Moreover, the dispersed particle diameter was assumed to be of the order of or less than the Kolmogorov length scale (Zaichik et al., 2003). Their analytical model provides the collision rate which describes the particle interaction contribution to the carrier phase turbulent eddies. In this work, the influence of turbulence modelling on condensing steam flow was studied. For this purpose, both the SST  $k$ - $\omega$  and the standard  $k$ - $\varepsilon$  turbulence models were modified. The modifications were based on the work of Avetissian et al. (2005, 2008), in which the modulation of turbulence kinetic energy due to condensed liquid droplets has been established via source terms additions to the turbulence models. The modifications of Avetissian et al. (2005, 2008) were originally based on the analytical model of (Zaichik et al., 2003). The liquid droplets in the flow introduce an additional turbulent kinetic energy and its dissipation to the flow via the acceleration/deceleration of the droplets. The addition of source terms alters the turbulent viscosity and the Reynolds stresses. Therefore, the momentum and energy transport equations should have some influence. Also, the formulation of turbulent viscosity was modified by including an additional multiplier term which incorporates the turbulence production to dissipation ratio, and the Rotta constant  $C_1$ . The modified turbulent viscosity term can be written as below:

$$\mu_{Tm} = \frac{\rho_m k}{\omega} \frac{1}{\max\left[\frac{1}{\alpha^*}, \frac{S_1 F_2}{\alpha_1 \omega}\right]} \frac{C_1}{C_1 + \left[\frac{\bar{G}_k}{\omega \beta^* k} - 1\right]}. \quad (4.53)$$

The source term  $S_k$ , in Eq. (4.49), defines the inclusion of turbulent kinetic energy due to the liquid mass generation and the droplet response time. The term  $S_k$  can be written as

$$S_k = \frac{4M}{\tau_p} (1 - f_u) k, \quad (4.54)$$

where,  $M$  indicates the liquid mass. The term  $\tau_p$  defines the droplet response time and can be written as below:

$$\tau_p = \frac{2\bar{r}^2 \rho_l}{9\mu_v}. \quad (4.55)$$

The  $f_u$  in Eq. (4.54) represents the coefficient of the droplet response to fluid velocity fluctuations. The formulation of  $f_u$  was adopted from Zaichik et al. (2003) and can be expressed as below:

$$f_u = \frac{2 \left( \frac{\tau_p}{T_L} \right) + \left( \frac{\tau_T}{T_L} \right)^2}{2 \left( \frac{\tau_p}{T_L} \right) + 2 \left( \frac{\tau_p}{T_L} \right)^2 + \left( \frac{\tau_T}{T_L} \right)^2}. \quad (4.56)$$

Here,  $T_L$  refers to the Lagrangian integral time microscale of fluctuations of velocity which was obtained as:

$$T_L = \frac{C_\mu^{\frac{1}{2}}}{\omega \beta^*}. \quad (4.57)$$

The term  $\tau_T$  in Eq. (4.56) indicates the Taylor time microscale of velocity fluctuations which describes the time of interaction of particles in small-scale turbulent motion and can be written as

$$\tau_T = \left( \frac{2 \text{Re}_\lambda}{15^{\frac{1}{2}} a_0} \right)^{\frac{1}{2}} \left( \frac{\mu_m}{\rho_m \omega \beta^* k} \right)^{\frac{1}{2}}. \quad (4.58)$$

Here,  $\text{Re}_\lambda$  refers the turbulent Reynolds number which was based on the Taylor microscale and can be calculated as below:

$$\text{Re}_\lambda = \left( \frac{20k\rho_m}{3\omega\beta^*\mu_m} \right)^{\frac{1}{2}}. \quad (4.59)$$

The source term  $S_\omega$ , in Eq. (4.50) indicates the modulation of turbulent dissipation through liquid droplets.  $S_\omega$  is proportional to  $S_k$ , which can be defined as below:

$$S_\omega = C_{2\varepsilon} \omega \beta^* S_k. \quad (4.60)$$

The standard  $k$ - $\varepsilon$  turbulence model was also modified by adding the modulation of turbulence kinetic energy and its dissipation due to liquid droplets through source terms. Also, the definition of turbulent viscosity was altered by production to dissipation ratio likewise in the modified SST  $k$ - $\omega$  model. The transport equations of standard  $k$ - $\varepsilon$  turbulence model and corresponding modifications in them are presented in Publication IV. All these modifications in the turbulence models were implemented to CFD codes by employing user defined subroutines.

### 4.3 Grid convergence error

It is fact that there exit some inherent inaccuracies in any CFD simulation of any continuum problem and these inaccuracies are present due to many reasons. In literature, various approaches have been proposed by researchers in order to determine the present

uncertainty in CFD simulations. There are several sources of errors or uncertainty in calculations; namely modelling errors, truncation error, discretization error, iteration and rounding errors, etc. Among all of them, the discretization errors are considered the prime source of numerical errors, which describe the difference between the exact solution of the governing equations and the discretized system in a CFD code (Pletcher et al., 2012). These errors are resulted from numerical algorithms, the grid structure and/or quantity, boundary conditions, etc. The grid structure and size within the computational domain have some impact on the prediction of complex flow structures, such as the boundary layers, the von Karman vortex street, secondary flows, shock waves (Montomoli et al., 2015) as well as at the fluid interfaces which govern the transfer processes between the fluids. Therefore, a special importance has been given to the grid generation phase in order to select the suitable grid size and its distribution within the computational domain, grid orthogonality, aspect ratio, grid singularities and zonal boundary interfaces. Some researchers, for example, Roache (1994, 1997, 1998) and Celik (1993), have proposed techniques to investigate the errors resulting from the number of grid points called the GCI method. In this work, the GCI method presented by Celik et al. (2008) was used. This method is based on the Richardson extrapolation technique given by Richardson and Gaunt (1927), in which multiple numerical solutions are calculated by adjusting a computational grid size and are then utilised to extrapolate a more accurate solution.

The GCI was assessed by employing a relative error measure of flow parameters between the selected computational grids. The relative error was evaluated by using the formula

$$e_a^{nm} = \left| \frac{\phi_n - \phi_m}{\phi_m} \right|. \quad (4.61)$$

Here,  $\phi$  indicates the selected flow parameter, e.g. subscripts  $n$  and  $m$  denote the selected grid indices. An extrapolated relative error can be estimated from the extrapolated value  $\phi_{\text{ext}}^{nm}$ , and the flow property as below:

$$e_{\text{ext}}^{nm} = \left| \frac{\phi_{\text{ext}}^{nm} - \phi_n}{\phi_{\text{ext}}^{nm}} \right|, \quad (4.62)$$

where the extrapolated value  $\phi_{\text{ext}}^{nm}$ , was calculated as

$$\phi_{\text{ext}}^{nm} = \frac{r_{nm}^p \phi_m - \phi_i}{r_{ij}^p - 1}, \quad (4.63)$$

where  $r_{nm}$  represents the grid refinement factor which was calculated from the ratio of corresponding grid sizes of  $n$ th and  $m$ th grid as below:

$$r_{nm} = \left( \frac{h_n}{h_m} \right)^{\frac{1}{2}}. \quad (4.64)$$

Here,  $h_n$  and  $h_m$  are the corresponding grid sizes of the  $n$ th and  $m$ th grids, respectively.

In Eq. (4.63),  $p$  indicates the order of the discretisation method. The representative grid size can be obtained from the following expression:

$$h = \frac{1}{N} \sum_{i=1}^N (\Delta A_i). \quad (4.65)$$

Here,  $\Delta A_i$  represents the area of the  $i$ th cell, and  $N$  denotes to the number of total cells in the corresponding computational grid. The GCI value was calculated using following expression (Roache, 1994):

$$\text{GCI}^{nm} = F_s \frac{e_a^{nm}}{r_{nm}^p - 1}, \quad (4.66)$$

where  $F_s$  is the safety factor 1.25. This value of the safety factor was selected based on the experiences obtained by applying GCI to many situations (Roache, 1994).

More details of the procedure to estimate the discretization error can be found in Celik et al. (2008). The adaptive time stepping was applied in the GCI simulations with  $\text{CFL} \leq 1$ . Further, the simulations of nozzle and LP turbine were conducted with steady state consideration. Although, GCI does not care, correctness of a simulation requires  $\text{CFL} \leq 1$ .

## 5 Computational models and simulation strategies

In this work, different steam blowdown tests of the open-top wetwell facility POOLEX and the drywell-wetwell suppression pool facility PPOOLEX were simulated. Further in this work, different nozzles, a stator turbine cascade and a 3D stator-rotor stage of an LP turbine were modelled. This chapter contains the details of the computational grids, corresponding case set-ups and main solver settings for the DCC simulations for the suppression pool and the condensing steam flow in the LP turbine. Commercial grid generators i.e. GAMBIT and Pointwise were used for computational grid generation.

### 5.1 CFD models of pressure suppression pool

#### 5.1.1 Geometrical details and grid generation

In this work, both 2D and 3D simulations of the DCC mode of PSP tests were performed.

##### CFD grid for STB-31 test

All the simulations of the STB-31 test were conducted with the 2D-axisymmetric CFD model. Only a  $1^\circ$  sector of the POOLEX pool was modelled. Therefore, a grid of hexahedral cells was generated by rotating a quadrilateral grid to contain a single cell thickness in respect to z-axis. Figure 5.1 shows the 2D-axisymmetric grid of the POOLEX pool for the STB-31 test simulations. In the axisymmetric model, the blowdown pipe was transferred to the centerline i.e. axis of the pool. The height of the computational domain was set to 2.63 m. By using this height, the initial surface of water could be set on the upper edge of the domain. Moreover, the lower conical part of the test vessel was truncated off at 0.8 m from the mouth of the blowdown pipe. These simplifications should have negligible effect on the results in the STB-31 case.

In the case of the STB-31 test, the location of the steam-water interface was almost stationary at the blowdown pipe mouth. Therefore, the grid was more refined near the pipe mouth. A grid independence study was performed considering four different grids, i.e., Grid A (2500 cells), Grid B (6270 cells), Grid C (14014 cells), and Grid D (20940 cells) (Figure 5.2). The minimum cell sizes in the refined region of Grid A, B, C and D were circa  $0.1 \times 6$  mm,  $0.03 \times 3$  mm,  $0.006 \times 0.6$  mm and  $0.001 \times 0.2$  mm, in vertical and horizontal directions, respectively. In the STB-31 test, the inlet steam mass flow rate was very small. Therefore, the velocities within the calculation domain remained low. The wall function approach of  $k - \epsilon$  turbulence model ( $y^+ > 30$  preferred) would lead to a notably coarse calculation grid relative to the interface and condensation modelling. However, in the simulations with incompressible two-phase solver of OpenFOAM, the wall treatment was not applied. In order to capture interfacial details, the grid densities near the blowdown pipe wall were refined and their corresponding  $y^+$  values were  $y^+_{\text{Grid A}} \approx 5.3$ ,  $y^+_{\text{Grid B}} \approx 1.9$ ,  $y^+_{\text{Grid C}} \approx 0.6$  and  $y^+_{\text{Grid D}} \approx 0.1$  of which first two

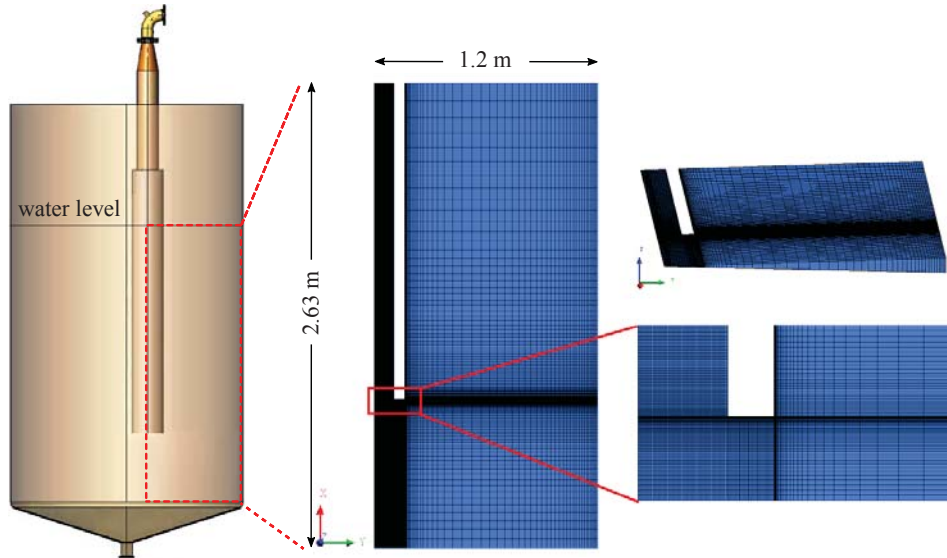


**Figure 5.1.** 2D-axisymmetric grid for the POOLEX STB-31 simulations.

may not be best suited for up to wall solution. The study of the grid refinement influence on the CFD simulations of DCC phenomena was conducted by using the GCI method using these grids.

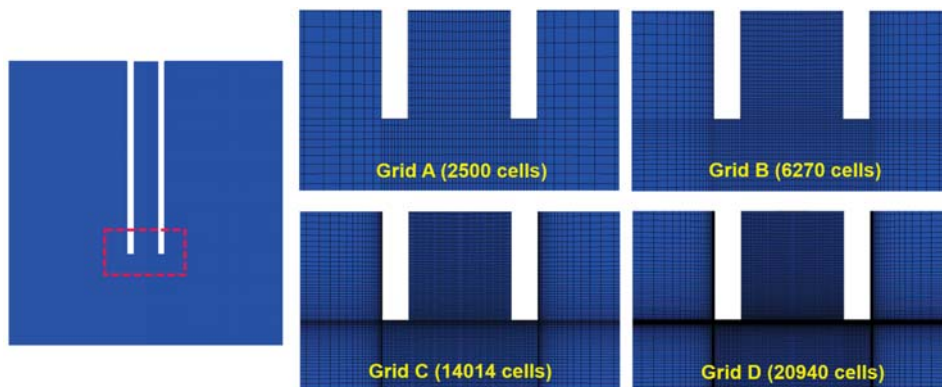


**Figure 5.2.** Different grid resolutions around the blowdown pipe in the POOLEX STB-31 simulations.

### CFD grid for STB-28 test

In preliminary chugging simulation try-outs, a spherical curvilinear grid around the blow-down pipe exit was used. This grid was the same as used in previous work by Taniskanen (2012). However, those simulations of 2D-axisymmetric spherical curvilinear grid encountered some convergence problems with OpenFOAM. Therefore, a new 2D-axisymmetric grid was generated without the curvilinear approach (Figure 5.3). The grid was generated with same manner as the STB-31 grid, but this time the bottom cone of the pool was preserved. Also, the blowdown pipe was modelled in full length.

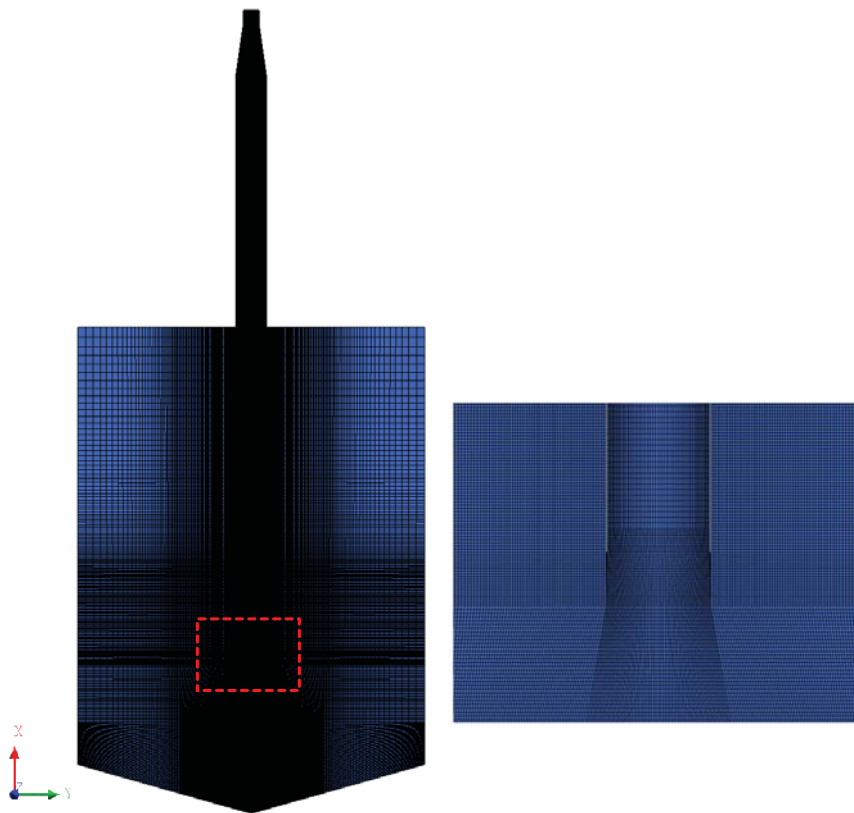


Figure 5.3. 2D-axisymmetric grid for the POOLEX STB-28 simulations.

In rapid flow DCC rate simulations, the interface area increase can be significant due to the acceleration by pressure decrease and chugging motion of the interface. In order to capture the details of interfacial movements, the computational grid was refined towards the inner wall of the blowdown pipe, around the mouth of the blowdown pipe and around the pool bottom. The grid sensitivity study was performed with four different grid resolutions i.e. Grid A (9000 cells), Grid B (18600 cells), Grid C (45600 cells), and Grid D

(120000 cells). The smallest cell sizes in the refined region of Grid A, B, C and D were circa  $6 \times 15$  mm,  $4 \times 12$  mm,  $2 \times 5$  mm and  $0.1 \times 8$  mm, respectively.

However, as a whole, the discharge of steam into condensation pool is a 3D event. The shape of the bubbles around blowdown pipe outlet and the shape of the steam-water interface inside the blowdown pipe after a bubble collapse could not be captured exactly with an axisymmetric approach (Tanskanen, 2012). Therefore, a 3D grid was generated for POOLEX simulations. Figure 5.4 shows the 3D grid. The grid contains 302796 hexahedral cells. In order to confirm the shape of erupting ellipsoidal bubbles, a spherical curvilinear grid around the blowdown pipe mouth was generated. The grid size around the mouth of the blowdown pipe is approximately  $5 \times 5$  mm. This is the same grid which was used previously in the preliminary NEPTUNE\_CFD simulations by Tanskanen (2012).

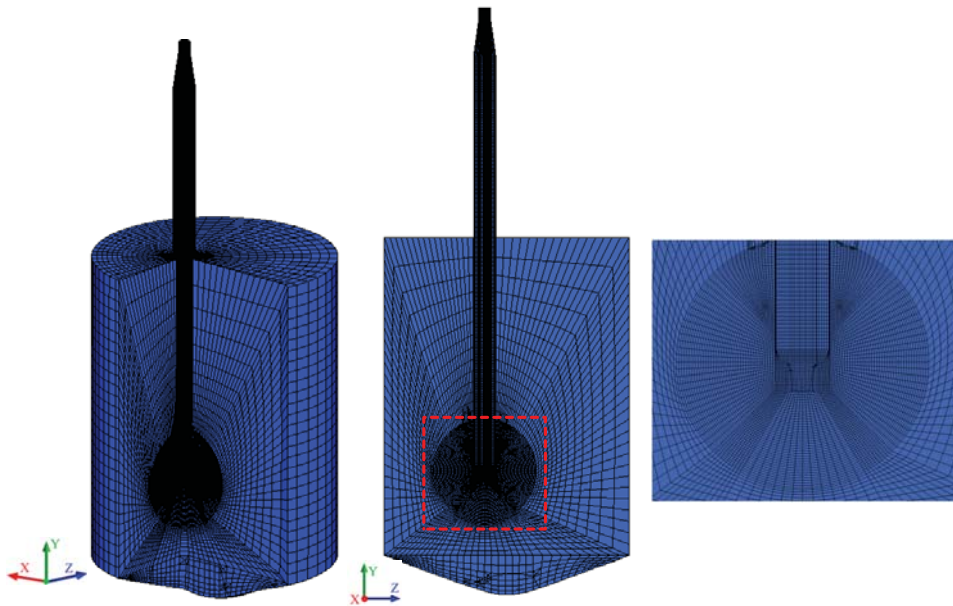
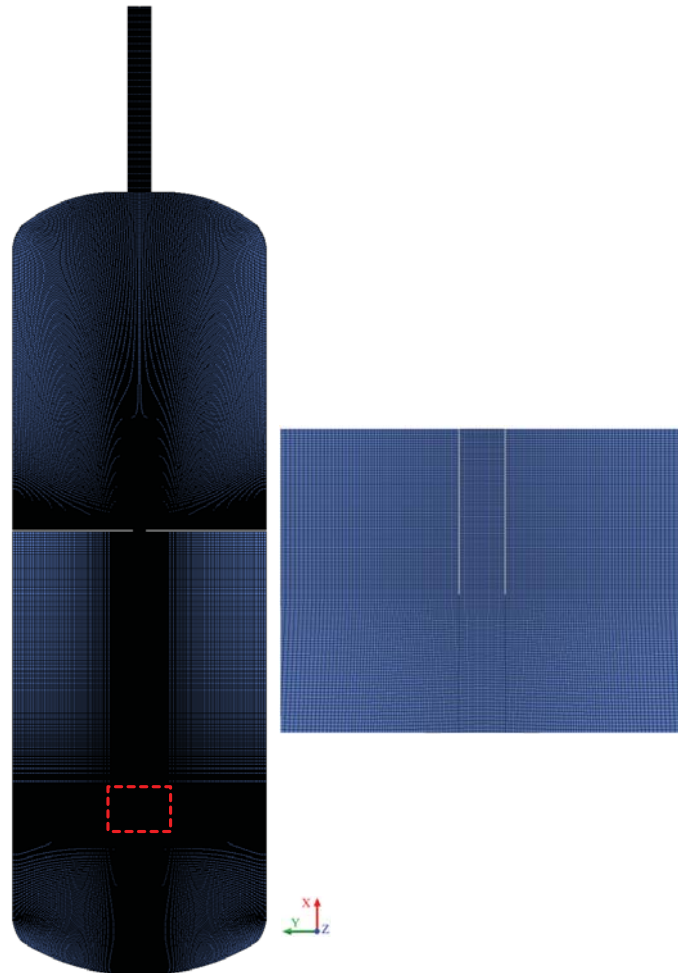


Figure 5.4. 3D grid for the POOLEX STB-28 simulations.

#### CFD grid for DCC-05 test

Due to the large volumes of both drywell and wetwell in PPOOLEX, the 3D PPOOLEX model requires a huge number of cells even with a coarser grid resolution in it which makes the 3D simulations of DCC-05 test computationally time consuming (Tanskanen et al., 2015). Additionally, the adaptive time stepping of OpenFOAM leads to a very small time step size which has a significant influence on the simulation progress. Therefore, in this work, only 2D-axisymmetric simulations of PPOOLEX DCC-05 were performed. Figure 5.5 shows the computational grid for 2D-axisymmetric simulations of the DCC-05-4 test.



**Figure 5.5.** 2D-axisymmetric grid for the PPOOLEX DCC-05-4 simulations.

The 2D-axisymmetric geometry contained a  $1^\circ$  sector of the PPOOLEX pool. The main simplification in the PPOOLEX 2D-axisymmetric grid was to place the blowdown pipe to the centre axis of the facility and to relocate the inlet plenum to the top of the dry well. However, the other dimensions, i.e. volumes of different parts of the pool, were preserved. Due to the large size of the wetwell and the relatively low inlet velocity, the inlet plenum re-location towards the blowdown pipe did not have a significant effect on the phenomena in the wetwell (Tanskanen et al., 2016). Concerning the blowdown pipe relocation, the 2D simplification lost the likely asymmetric field of pool liquid circulation and asymmetric bubble shapes, as well. However, the effect of these simplifications was assumed small due to the short samples simulated i.e. pool mixing remained weak, and

due to the mainly symmetric bubbles which were observed when the DN100 blowdown pipe was used in the experiment. The grid density should be good enough in the rapid condensation simulations in order to compute the gradient of the volume fraction that represents the bubble interface well. The grid was refined inside the blowdown pipe and around the pipe tip region with a  $5 \times 5$  mm cell size. The grid contained 72000 hexahedral computational cells. This grid was suitable for standard wall functions approach. Other grid resolutions were not simulated with OpenFOAM simulations, but a denser grid with  $1 \times 1$  mm cell size was tested with NEPTUNE\_CFD. More details about the denser grid selection for NEPTUNE\_CFD simulations are discussed in Publication III.

### 5.1.2 Simulation set-up

#### Simulation set-up for STB-31 test

All the simulations of the STB-31 test were performed by setting the initial volume fraction of steam to unity in the blowdown pipe and zero elsewhere. Thus, steam/water interface location was exactly at the tip of the blowdown pipe. In the simulations, the initialization of pressure and temperature fields of the steam corresponded to the STB-31 test conditions (see Table 2 in Publication I). The water pressure in the computational domain was initialised by using hydrostatic pressure. As the STB-31 test was performed with open-top wetwell facility, the upper boundary of water surface in the simulations was set to the atmospheric pressure of 0.10287 MPa. A velocity boundary condition was imposed for steam at the blowdown pipe inlet. Based on a quasi-steady period in the STB-31 test, the steam inlet velocity was fixed to  $0.043 \text{ m s}^{-1}$  which corresponded to the mass flow rate of  $1.0594 \text{ g s}^{-1}$ . In all simulations, the steam was assumed to be at the saturated state ( $T_a = T_{\text{sat}}$ ). The pool walls were considered to be adiabatic and no-slip boundary conditions were imposed on all the wall surfaces. Also, the effect of non-condensable gases was excluded from the CFD simulations. All simulations were performed with the incompressible two-phase flow solver of the OpenFOAM 1.7.1. An upwind discretization scheme was applied for the phase volume fraction, the phase velocities, and the turbulent kinetic energy and its dissipation rate. The fixed time step size of  $10^{-4} \text{ s}$  was used. The CFD simulations of the STB-31 case were performed with the HD 0 model and the LH model in order to compare the OpenFOAM and the corresponding NEPTUNE\_CFD results. However, the HD 1 model was not applied in this mild DCC case. Further details about the OpenFOAM simulation set-up and the corresponding NEPTUNE\_CFD set-up are described in Publication I.

#### Simulation set-up for STB-28 test

Basing on the experimental data of the STB-28 case, the initial location of the steam/water interface inside the pipe was unknown. Tanskanen and Jordan (2011) tested and analyzed different steam/water interface initializations for STB-28 POOLEX test simulations. By analyzing the speed of steam jet penetration into a water pool from the available high-

speed video material of the STB-28-4 test, they assumed that the initial level of interface should be 0.76 m inside the blowdown pipe at  $t = 0$  s. Based on this, all 2D and 3D simulations of the STB-28 case in this work were done by assuming the initial steam/water interface location at 0.76 m inside the blowdown pipe. The volume fraction and interface were initialized accordingly. The liquid surface of pool as the upper boundary of the computational domain was fixed to the atmospheric pressure of 0.1022 MPa. The pool liquid volume was initialized by using hydrostatic pressure. The liquid phase heat transfer in the STB-28 POOLEX test simulations was solved by employing the LH model, the HD 1 model and the Coste C model. The vapour phase was assumed to be approximately at the saturated state ( $T_a = T_{\text{sat}}$ ) and the vapour side heat transfer was assumed negligible. The pool walls were considered to be adiabatic and a no-slip boundary condition was imposed at all the wall surfaces.

In this work, three subtests of the STB-28 POOLEX experiment series i.e. STB-28-1, STB-28-4 and STB-28-7 were simulated. These tests indicate three different pool sub-cooling levels. Modelling wall condensation of these steam blowdown cases in OpenFOAM simulations could be an additional challenge. For the sake of simplicity, the wall condensation modelling was not considered in this study. Tanskanen (2012) estimated the total amount of wall condensation analytically for STB-28 POOLEX tests by employing the correlation of Chen et al. (1987) (see Figure 3.5). The estimated wall condensate amount was removed from the inlet mass flow rate in order to compensate for its effect on the available steam mass flux in the blowdown pipe based on his estimation. A velocity boundary condition was applied for the vapour phase at the blowdown pipe inlet. The inlet velocity was set based on the wall condensation corrected mass flow rates for each case. The temperature fields of the vapour and the initial liquid temperatures in liquid pool domain were set according to the test conditions. Table 5.1 includes the details of the selected subtest conditions where the vapour mass flow rates and corresponding velocities are the wall condensate corrected values.

**Table 5.1.** Details about POOLEX STB-28 POOLEX test cases.

Case	Vapour temp. [K]	Liquid temp. [K]	$\Delta T$ [K]	Mass flow rate [kg s <sup>-1</sup> ]	Vapour velo. [m s <sup>-1</sup> ]
STB-28-1	379.7	320.8	$\approx 60$	0.188	26.58
STB-28-4	379.1	340.5	$\approx 40$	0.238	34.32
STB-28-7	378.7	350.4	$\approx 30$	0.255	37.18

Adaptive time stepping (with the limit of  $\text{Max } \Delta t = 10^{-4}$ ) was applied with maximum Courant-Friedrichs-Lewy (CFL) criterion ( $\text{Max CFL} \leq 1$ ). The phase volume fraction, the phase velocities, and the turbulent kinetic energy and its dissipation rate were solved based on the second order central difference scheme. In all simulations, most of the fields were converged to the value of the normalized root mean square (RMS) residual of  $10^{-5}$ .

### Simulation set-up for DCC-05 test

In the simulations of the DCC-05-4 test, the liquid phase heat transfer was calculated by applying the HD 1 model and the Coste C model. As the vapour phase was considered to be in saturated state ( $T_a = T_{sat}$ ), the vapour side heat transfer was considered negligible. Most of the simulations of DCC-05-4 test were conducted by initializing the location of the steam/water interface at the elevation of 1.8 m corresponding to the water level in the pool inside the blowdown pipe. Some cases were also conducted with different steam/water interface initialization near blowdown pipe outlet in order to study the influence of interface initialization on chugging DCC. All the walls of the domain were set to the adiabatic conditions. Also a no-slip boundary condition was applied at all the wall surfaces. Figure 5.6 presents the temperature and pressure fields at  $t=0$  s of the DCC-05-4 simulation.

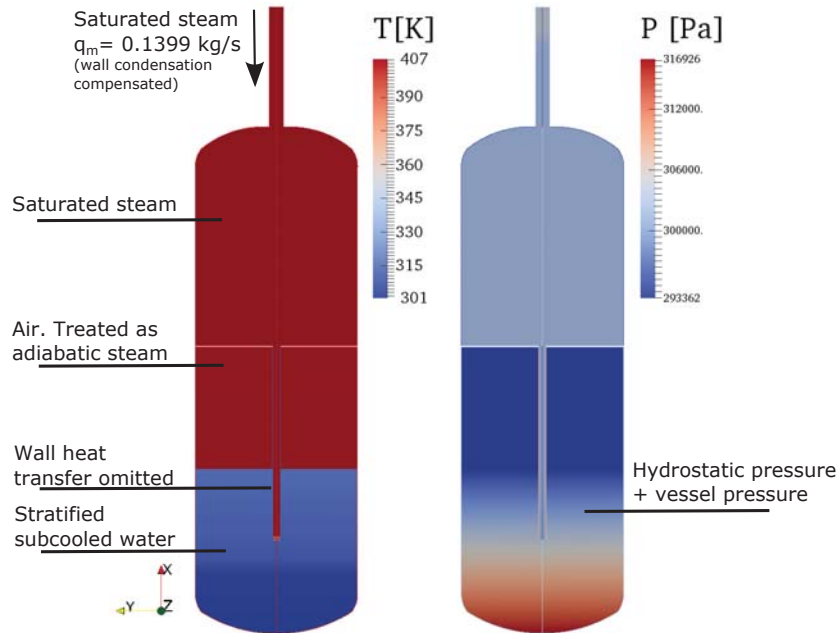


**Figure 5.6.** Initial temperature and pressure fields in the simulations of the PPOOLEX DCC-05-4 case.

The wall condensation was not simulated in PPOOLEX simulations and therefore the estimated amount of wall condensation was deduced from the inlet mass flow rate. The initial and boundary parameters for the simulation of the case are listed in Table 5.2.

Simulations were performed with the adaptive time stepping (with the limit of  $\text{Max } \Delta t = 10^{-4}$  and with  $\text{Max CFL} \leq 1$ ). Initial time step size was set to  $10^{-4}$  s. The normalized

**Table 5.2.** Initial and boundary conditions of PPOOLEX DCC-05-4 simulation.

Maximum simulation duration	10 s (test sample in OpenFOAM)
Initial interface level in pipe	0.042 m or 1.03 m (above pipe outlet)
Water level in pool	1.03 m (above pipe outlet)
Initial drywell pressure	301310 Pa
Initial wetwell gas space pressure	293370 Pa
$T_{\text{sat}}$ in drywell	406.8 K
T in wetwell gas space	313.7 - 330 K
T in wetwell liquid	300.7 - 315.6 K (stratified)
T in water plug in pipe	374.3 - 405.6 K
Actual inlet mass flow rate	+ 0.1616 kg s <sup>-1</sup> (mean)
Wall condensation estimation	- 0.0217 kg s <sup>-1</sup> (based on Chen et al. (1987))
Reduced inlet mass flow rate	+ 0.1399 kg s <sup>-1</sup> (inlet BC.)
Inlet temperature	429.2 K

RMS residuals in the order of  $10^{-5}$  or lower were used as convergence criteria for all the simulated cases of the DCC-05-4 test of OpenFOAM. The OpenFOAM simulation results of the DCC-05-4 test were compared with the NEPTUNE\_CFD results. More details about the DCC-05-4 test simulation set-ups and the DCC model and other selections for both OpenFOAM and NEPTUNE\_CFD are discussed in Publication III.

## 5.2 CFD models of wet-steam flows

In this work, different well-known CD nozzle configurations, a stationary cascade of turbine blades and a stator-rotor stage of an LP turbine have been modelled for validation purposes. This chapter presents the geometrical details of the computational models, grid generation and boundary conditions.

### 5.2.1 Geometrical details and grid generation

There are several nozzle experiments available in the literature. In this work, the nozzles of Barschdorff (1971), Moore et al. (1973) and Moses and Stein (1978) were simulated. These nozzles have been used for various validation purposes by researchers. The details of the selected nozzle configurations, the boundary condition and the corresponding grid selection are listed in Table 5.3.

**Table 5.3.** Details about the nozzle cases, the boundary condition and the corresponding grid selection.

Case	Expansion rate [ $s^{-1}$ ]	Throat height [mm]	Inlet condition	Grid details	Average $y^+$
Barschdorff nozzle	-	60	$P_{01} = 78390$ Pa $T_{01} = 380.55$ K	$N_x = 370$ $N_y = 100$	3.5
Moore nozzle A	3160	63	$P_{01} = 25000$ Pa $T_{01} = 354.6$ K	$N_x = 755$ $N_y = 54$	5
Moses and Stein nozzle (case-203)	6500	10	$P_{01} = 35800$ Pa $T_{01} = 363.3$ K	$N_x = 430$ $N_y = 150$	12

For all nozzle cases, the outlet boundary condition was considered as the supersonic flow condition. A no-slip adiabatic wall boundary condition was applied to the walls of the domain. In order to achieve an optimal  $y^+$  value, the grid density was fine enough near the wall surfaces to solve the boundary layer precisely for all cases. All the simulations of nozzle cases have been performed by using the standard wall functions. Further, in the nozzle throat and in the region of rapid condensation, the grid was refined to resolve the nucleation and droplet growth processes accurately.

Further, the stationary steam turbine stator cascade of White et al. (1996) was modelled in this work. The White cascade is the planar stator cascade of the fifth stage stator blade from the six-stage LP cylinder of a 660 MW steam turbine. The schematic of the stator blade arrangements is shown in Figure 5.7 (a). Originally, in the experiments of White et al. (1996), there were four stator vanes. However, in this work, simulations were conducted both with a single passage and also with two passages of the experimental facility by applying a periodic boundary condition in the corresponding direction. The blade pitch was 87.59 mm, the blade chord was 137.51 mm and the blade stagger angle was  $45.32^\circ$ . The blade height was 152 mm. In the test series of White et al. (1996), they performed experiments of condensing steam flow with various inlet superheat levels and with moist steam at inlet. Details of all modelled cases of the White cascade are described in Table 5.4.

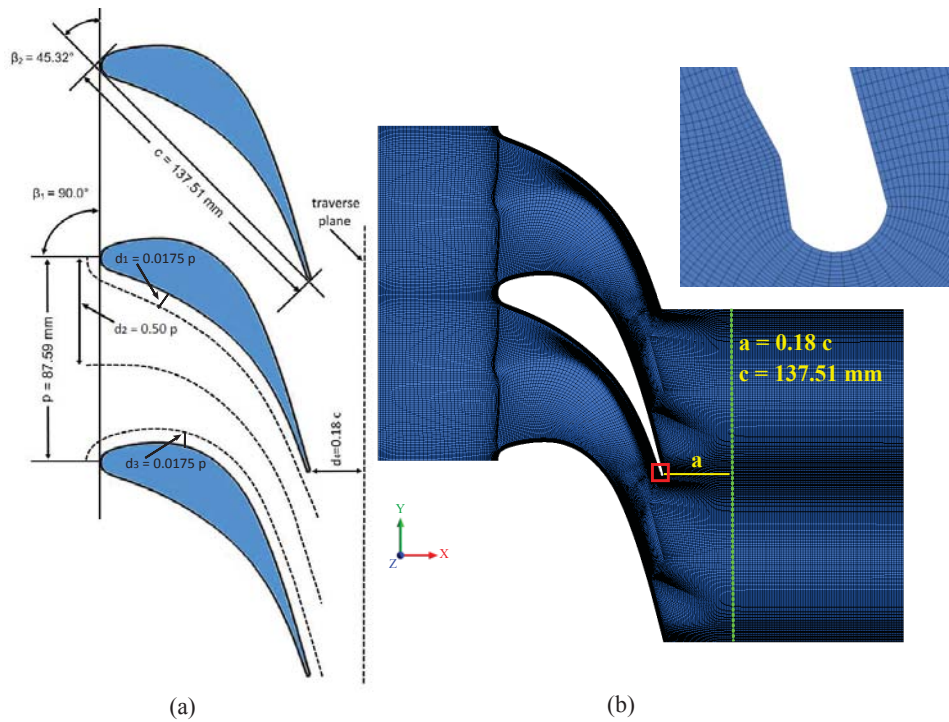


**Figure 5.7.** (a) The schematic of the LP turbine stator blade of White et al. (1996) experiments, and (b) the computational grid in the domain (Grid B). The dotted lines indicate the locations where the CFD data were obtained,

**Table 5.4.** Details of test conditions for the turbine cascade cases of White et al. (1996).

Test No.	Upstream stagnation conditions			Downstream conditions	
	Pressure $P_{01}$ [Pa]	Temperature $T_{01}$ [K]	Superheat $\Delta T_{01}$ [K]	Static pressure (mean) $P_2$ [Pa]	Isentropic Mach No. $M_{2s}$
L1	40300	354.0	4.5	16300	1.24
L2	40900	354.0	4.0	19400	1.11
L3	41700	357.5	7.5	20600	1.08
W1	41900	350.0	wet ( $\sim 1.6\%$ )	17800	1.20
H3	41400	376.0	26.0	19400	1.10

Corresponding to the experimental data of White et al. (1996), the pressure inlet and pressure outlet boundary conditions were applied at the domain inlet and outlet, respectively. At the blade surfaces, a no-slip adiabatic wall boundary condition was specified. The inflow angle was fixed to  $0^\circ$  for all cases.

In all cases, a non-uniform structured grid was generated in the computational domain. O-grid was generated around the blade surfaces to resolve the boundary layers (Figure 5.7 (b)). A grid was more refined around the leading and trailing edges of the stator blade. Different grid resolutions were tested for stator cascade simulations. Further details about the grid are shown in Publication IV.

Further, in present work, the influence of blade shape modification on the condensing steam flow was studied. For this purpose, the LP turbine stator blade of White et al. (1996) was chosen and several modifications were applied to the blade profile. Figure 5.8 displays the modified blade shapes.

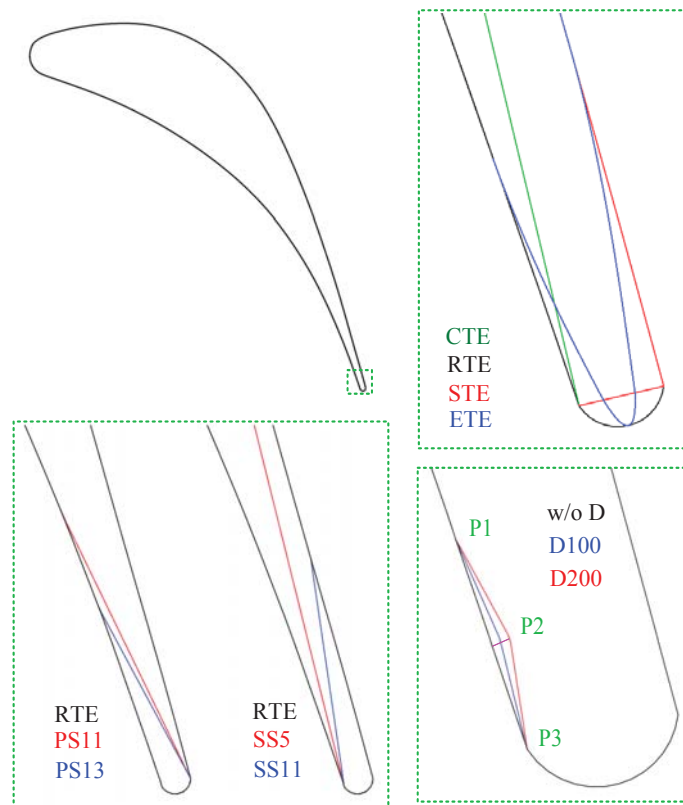


**Figure 5.8.** Modifications to the stator blade shape.

An exact information about blade trailing edge shape is not available in White et al. (1996), however, visually, it seems that the original blade had sharp trailing edge shape.

In this work, the square trailing edge (STE) shape represents the original blade shape. For generating the semicircular trailing edge (RTE), both the pressure and suction surfaces of the blade were combined by considering a semicircular curve. In the case of conic trailing edge (CTE), the pressure surface and the suction surface of the blade were joined by tapering the suction surface only. The angle between the pressure surface and the suction surface was  $8^\circ$  in the CTE shape. The elliptic trailing edge (ETE) shape was generated by tapering the pressure surface and the suction surface of the blade. Only 3.2% and 2.8% of the total length of the pressure and suction surfaces were tapered, respectively, for the ETE shape. As a result, the blade chord was reduced by approx. 0.54% in the ETE shape. The trailing edge thickness of RTE, STE and ETE was approx. 1.61 mm, 1.61 mm and 0.60 mm, respectively. Because the blade surfaces of CTE were joined by tapering, the trailing edge thickness was 0 mm. Further, the throat width was same for the CTE, RTE and STE profiles which was approx. 27.33 mm. In the ETE profile, both blade surfaces were tapered slightly and therefore, it had marginally larger throat width (approx. 27.78 mm) than the CTE, RTE and STE profiles.

The influence of a pressure side dimple close to the trailing edge is also examined following its successful implementation close to the trailing edge of a transonic gas turbine blade by Sonoda et al. (2006). Although their work was dealing with air, the positive influence on lowering the aerodynamic losses by the manipulation of trailing edge shock pattern and the relatively easy manufacturing of the shape modification gives a motivation to extend the method to steam turbine flows. In this work, the dimple profiles were generated on the pressure side of the blade. Two dimple shapes of  $100\ \mu\text{m}$  (D100) and  $200\ \mu\text{m}$  (D200) were tested. Only 1.94% of the total length of the pressure surface on blade trailing edge was changed by the dimple addition. The D100 and D200 profiles were generated from the RTE profile. Therefore, both profiles had approx. 1.61 mm trailing edge thickness.

Further, in this work, the influence of blade tapering was conducted by considering different blade surface tapering. In Figure 5.8, PS and SS indicate the cases of blade pressure surface tapering and blade suction surface tapering, respectively, where 5, 11 and 13 refer to the angle between the pressure surface and the suction surface after tapering. In the cases of PS11 and PS13, a total of 11.86% and 7.38% of the length of the pressure surface were tapered, respectively. While in the SS5 and SS11 cases, a total of 23.37% and 7.60% of the length of the suction surface were tapered, respectively. In all blade tapering cases, the blade surfaces were merged by a semicircular trailing edge. The trailing edge thickness of PS11, PS13, SS5 and SS11 was approx. 0.021 mm, 0.026 mm, 0.005 mm and 0.010 mm, respectively. For the SS5 and SS11 profiles, only suction surface was tapered. Thus, both the profiles had approx. 27.33 mm throat width which is similar to the RTE profile. Due to pressure surface tapering, the throat width was changed for both the cases. The PS11 profile had approx. 28.89 mm throat width while the PS13 profile had approx. 28.91 mm throat width.

A 3D stator-rotor stage of a LP turbine was designed to analyze the influence of turbulence modelling on wet-steam flow. The geometry of it was not based solely on any real LP turbine stage. Figure 5.9 (a) displays the schematic of the computational domain. In

this stage design, the stator geometry of White et al. (1996) was chosen as a stator blade while the rotor blade was selected by assuming 25% of reaction at mid span. The whole stage steam expansion ration was about 4. The axial gap between the stator and rotor was considered to be 40% of the axial chord of the stator. The stator blade row consisted of 30 blades while the rotor blade row included 31 blades. The stator blade and the rotor blade diameters were 836.42 mm and 886.94 mm, respectively at 50% span. For the sake of simplicity, the blade profiles of stator and rotor were designed with a constant radial thickness without any twisting. Only single passage of stator and rotor was simulated applying a periodic boundary condition in the circumferential direction. Further, the stage was designed excluding rotor tip clearance to remove the influence of tip swirls on the flow. More details about the computational domain are given in Publication VI.

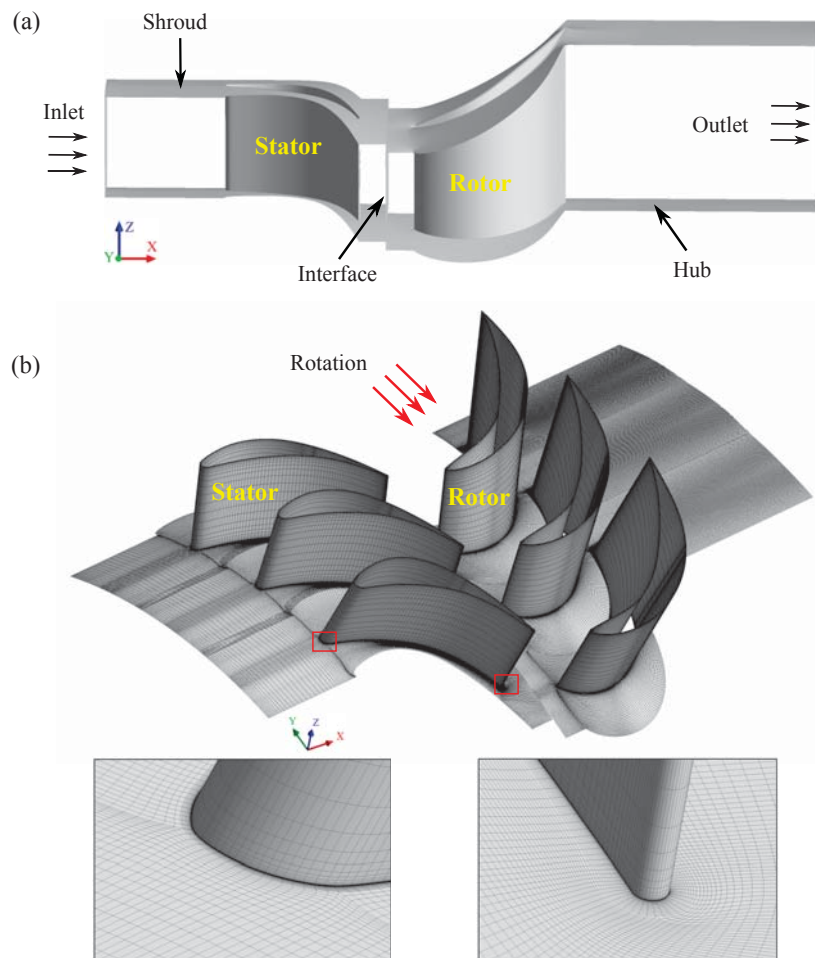


**Figure 5.9.** (a) The schematic of a 3D LP turbine computational model, and (b) the computational grid.

Based on the previous simulated cases of a 2D stator domain and GCI analysis, a sufficiently fine grid was generated. Around the blade surfaces, an O-type grid was used to resolve boundary layers. Also, grid density was fine around the leading and trailing edges of the stator and rotor blades (Figure 5.9 (b)). There were about 2870000 hexahedral computational cells in the computational domain. Further detail about grid is discussed in Publication VI.

### 5.2.2 Simulation set-up

All the simulations of CD nozzles, stator cascade and LP turbine stage were conducted with steady state conditions. In the ANSYS FLUENT simulations, the solution method of flow solving algorithm was based on the explicit density based coupled solver. The density-based explicit solver of ANSYS FLUENT uses full approximation storage (FAS) multigrid methodology. The spatial discretization was based on the second order upwind scheme. The scheme of Roe (1986) was employed to estimate the convective fluxes. All the 2D stator cascade simulations with the standard  $k-\varepsilon$  and modified standard  $k-\varepsilon$  turbulence models were performed with the enhanced wall treatment to solve boundary layer flow. Further information on the simulation set-up is discussed in Publications IV and V.

The simulations of 3D LP turbine stage were performed only with steady state assumption. Therefore, a mixing plane was used as an interface between the stator and the rotor domain. The mixing plane assumption averages the flow properties at the interface in the circumferential direction both at the outlet of stator domain and at the inlet of rotor domain. The advection was solved with a high resolution scheme. High resolution methods were used for volume fraction, turbulence models and energy equations. An in-built automatic wall treatment approach of ANSYS CFX was used for all simulations. This approach enables an automatic switching from a low-Reynolds number formulation to a wall function treatment based on grid density close to the wall surfaces of the domain (ANSYS Inc., 2016). More details are listed in Publication VI.



## 6 Analysis of CFD results of pressure suppression pool

### 6.1 Results of POOLEX STB-31 experiment

Before modelling very rapid and complex steam chugging or other DCC modes with high condensation rates, it was essential to first analyse the performance of the implemented models in OpenFOAM two-phase solver for relatively mild DCC case modelling. For this purpose, the POOLEX STB-31 steam blowdown test was chosen. This POOLEX test was related to the steam condensation case of a thermally insulated vertical blowdown pipe with a relatively large diameter and low steam mass flux. Therefore, this special case was the best starting point for CFD simulations with phase change due to its mild condensation rates. Previously, this POOLEX STB-31 steam blowdown test was used by Tanskanen (2012) for the DCC models validation for the NEPTUNE\_CFD and TransAT CFD codes.

#### 6.1.1 Grid independence study

Firstly, the effect of the computational grid size on DCC phenomena was analyzed with four different grid densities. The selected grids are discussed in detail in chapter 5.1.1. For the grid study, the interfacial heat transfer between steam and water was modeled by using the LH model. Figure 6.1 shows a closer view of steam volume fraction field around the blowdown pipe mouth predicted with different grids. Noticeable differences are observed between different grid density results. The coarser grids A and B resulted in visibly more smeared interface profile compared to the other grids. More steam leaves the interface as rising bubbles in the coarser grid cases as well. As the grid refined, the interface profile became sharper. The finest grid i.e. Grid D produced the sharpest interface profile.

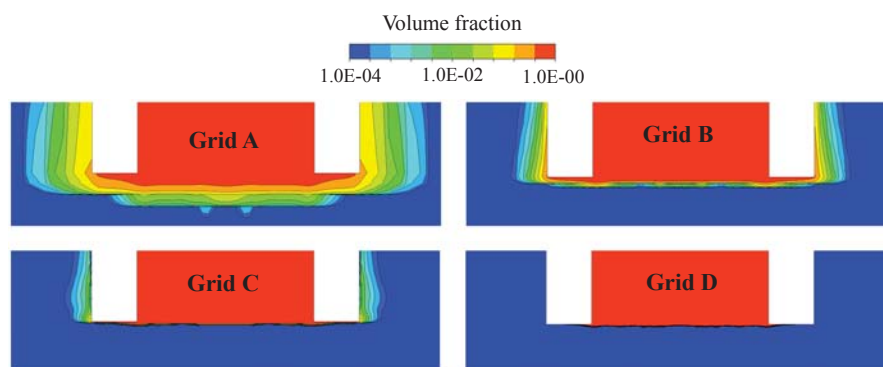


**Figure 6.1.** Volume fraction fields by different grids near blowdown pipe mouth in a 2D-axisymmetric OpenFOAM simulation of the POOLEX STB-31 test by using the LH model.

Further, after observing these qualitative differences in the results, it was essential to investigate the influence of grid density to the convergence of the DCC phenomena. The instantaneous condensation rate can usually not be measured in blowdown experiments at all. However, in the POOLEX STB-31 test, the inlet steam mass flow rate was regulated to prevent steam bubble formation and to keep the steam/water interface location as close as possible to the blowdown pipe outlet. Hence, it could be assumed that the injected steam mass flow rate was almost equal to the condensation mass flow rate itself and therefore, based on this assumption, it was possible to compare the test and simulation results of the DCC rates. Figure 6.2 presents the predicted condensation mass flow rate, the condensation mass flux, and the total interfacial area with different grids. The CFD results are compared to the measured data of the POOLEX STB-31 test. The mass flow rate measurement error range was  $\pm 1.3 \text{ g s}^{-1}$  in the test.

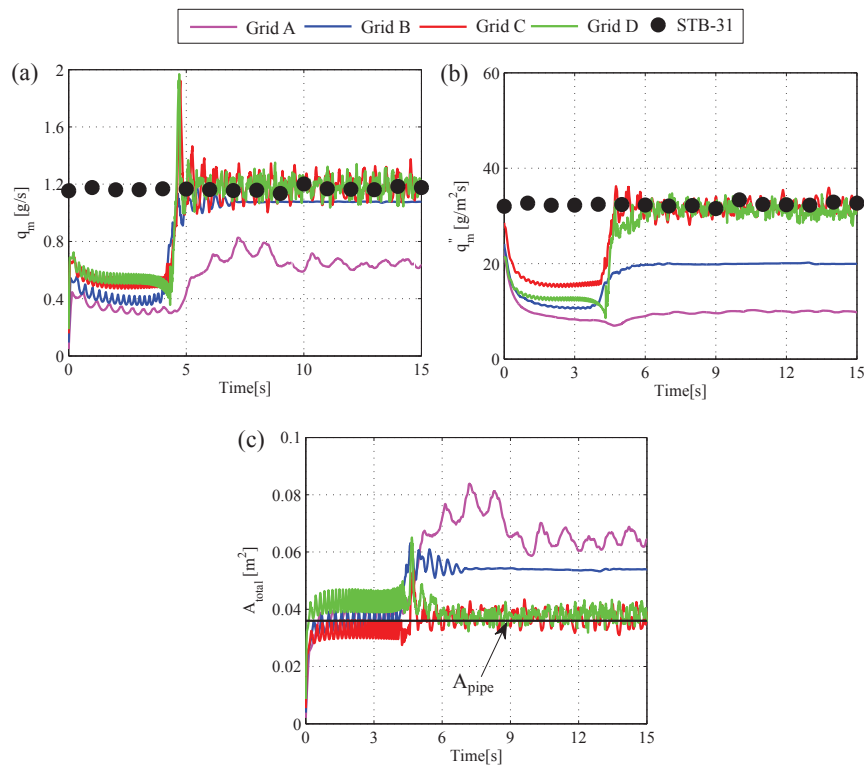


**Figure 6.2.** (a) Condensation mass flow rate, (b) condensation mass flux, and (c) total interfacial area by the LH model using OpenFOAM versus the POOLEX STB-31 experimental data (STB-31).  $A_{\text{pipe}}$  indicates the cross-sectional area of the blowdown pipe outlet in the POOLEX STB-31 test thus excluding the thick wall area of the pipe lip.

In the grid influence study calculations, the steam/water interface was initialized 5 cm inside the blowdown pipe outlet at  $t = 0$  s. The steam/water interface started to approach to the blowdown pipe mouth as simulation time elapsed and it took about 5 s of simulation time to attain the blowdown pipe mouth. Therefore, the DCC rate was lower than the STB-31 inlet flow rate at the prior stage of the simulations as shown in Figure 6.2 for all the cases. The coarsest grid yielded weaker DCC rate than the others. As the grid density increased, the predicted condensation mass flow rate reached the measured value. Grid C and Grid D predicted relatively similar and accurate results of the condensation mass flow rate. However, the condensation mass flow rate included the effect of interface area fluctuations during the simulations. Because the interfacial area changes due to the interface fluctuation, that had an effect on the total condensation rate. Therefore, it was essential to also calculate the interfacial mass fluxes (Figure 6.2(b)) by dividing the total condensation mass flow rates by the total interfacial areas. The coarser grids i.e. Grid A and Grid B, underpredicted the condensation mass flux considerably, while Grid C and Grid D predicted the condensation mass flux very close to the measurements. As the steam/water interface profile was almost stable at blowdown pipe outlet in the test, the interfacial area should be close to the cross-sectional area of pipe outlet. The averaged total interfacial areas are shown in Figure 6.2(c). Due to the too low condensation mass fluxes with the coarser grids, total interfacial area increased because of pressure build up. As a result, Grid A and Grid B overpredicted the total interfacial area. In the cases of Grid C and Grid D, the predicted total interfacial areas were very near the blowdown pipe cross-sectional area and both grid resolutions yielded quite good results.

Further, the GCI method was used to calculate the discretization error for the CFD simulations with selected grid refinements. For this purpose, the time averaged values of the total condensation mass flow rate and the total interfacial area were used for all selected grids. More details on the GCI analysis can be found in Publication II. Figure 6.3 shows the estimated grid discretisation errors.

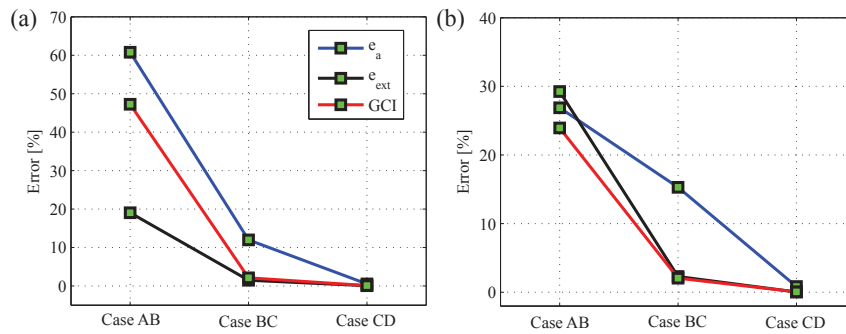


**Figure 6.3.** Estimated relative error (i.e.,  $e_a$ ), extrapolated relative error (i.e.,  $e_{ext}$ ) and GCI values for (a) condensation mass flow rate, and (b) total interfacial area for successive grid refinements for POOLEX STB-31 simulations using the LH model.

Here, the Cases AB, BC and CD indicate the grid refinements from Grid A to B, Grid B to C, and Grid C to D, respectively. It is apparent that the calculated relative error (i.e.,  $e_a$ ) decreased as the grid density increased. Further, the successive grid refinements decreased both the extrapolated relative error (i.e.,  $e_{ext}$ ), and the GCI value for both the properties as well. It can be seen that the grid refinement from Grid C to Grid D yielded a negligible discretization numerical error of less than 0.1 %. Additionally, the asymptotic range of convergence (i.e. Eq. (4.66)) was calculated. For the grid group of A, B and C, the asymptotic range of convergence for total condensation mass flow rate and total interfacial area were 1.045 and 1.092, respectively, and for the grid group of B, C and D, the asymptotic range of convergence for total condensation mass flow rate and total interfacial area were 1.006 and 1.002, respectively. The asymptotic range of convergence for the corresponding grid groups are approximately unity, which indicates that the achieved numerical solution is well within the asymptotic range of convergence. Based on this analysis, the finest grid, Grid D was used for the further calculations.

### 6.1.2 Comparison of CFD results

In this work, two DCC models viz. the HD 0 model and the LH model were employed to calculate an interfacial heat transfer between steam and water. Further, the OpenFOAM POOLEX STB-31 case results were compared with the previously simulated results of the NEPTUNE.CFD code and with some preliminary results of the TransAT code by

Tanskanen (2012). Development of volume fraction fields of steam and corresponding condensation mass flux in the blowdown pipe predicted by the HD 0 model are displayed in Figure 6.4. Like in the early simulations by Tanskanen et al. (2008), the HD 0 model yielded a too high condensation rate and as a result, steam condensed quickly and the steam/water interface began to move upwards inside the blowdown pipe as the simulation progressed. The applied velocity boundary condition for steam injection failed to maintain the steam volume in the pipe and therefore, after 8 s of simulation the interface reached the inlet.

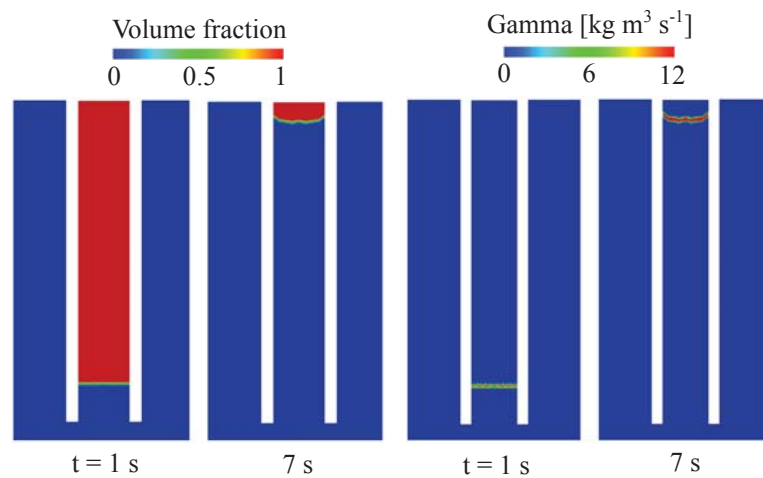


**Figure 6.4.** Instantaneous fields of the steam volume fraction and corresponding condensation mass flux in a 2D-axisymmetric OpenFOAM simulation of the POOLEX STB-31 experiment using the HD 0 model.

Figure 6.5 shows the corresponding fields of the steam volume fraction and the condensation mass flux near the blowdown pipe mouth predicted by the LH model. It can be seen that the steam/water interface in the LH model was located at the blowdown pipe mouth throughout the simulation. However, a weak oscillatory motion of the steam/water interface was observed in the simulation. A 2D-axisymmetric model may invoke axisymmetric waves which can be different from the ones occurring in real and 3D conditions. As the possible mechanical vibrations of the system during steam blowdown were not modelled in the CFD simulations, the oscillating wavy interfacial motion appeared likely due to the total DCC rate. The oscillation occurs probably due to the fact that the DCC rate in the smooth free surface area could be lower than the amount of injected steam, which forces the steam to spread onto the wall of the pipe lip where the condensation rate increases again temporarily due to the increase of turbulence and increase in the interfacial area as well. The 2D-axisymmetric geometry enhances this effect. The cycle started again after the excess steam was condensed near the pipe lip.

Further, the qualitative behaviour of the OpenFOAM results was analyzed with the NEPTUNE\_CFD simulation. Figure 6.6 compares the contours of steam volume fraction,

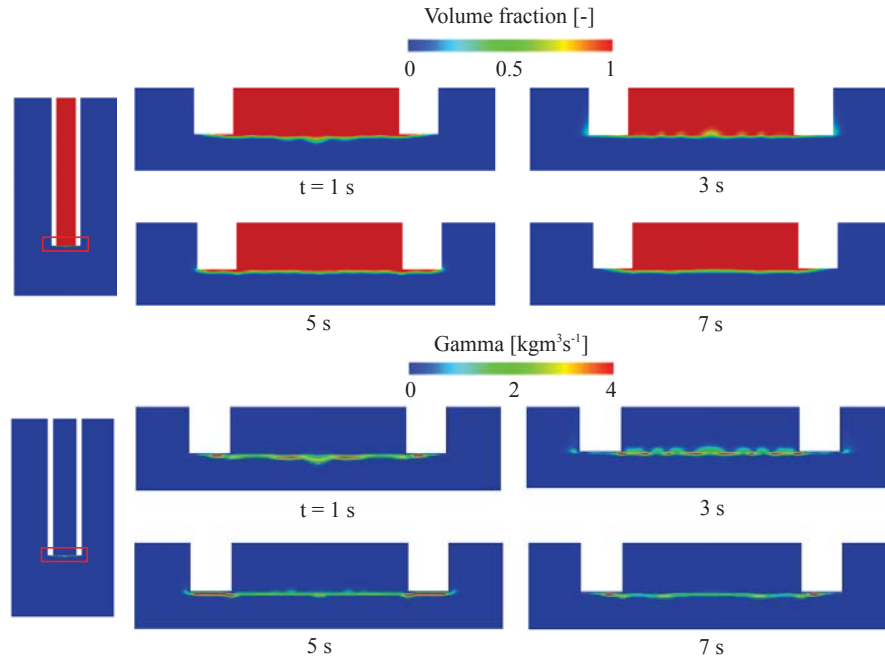


**Figure 6.5.** Instantaneous fields of the steam volume fraction and corresponding condensation mass flux in a 2D-axisymmetric OpenFOAM simulation of the POOLEX STB-31 experiment using the LH model.

turbulent kinetic energy weighted by volume fraction of water phase and the velocity weighted by volume fraction of the steam in OpenFOAM and NEPTUNE\_CFD predicted by the LH model. As a reference, the instantaneous video frames of stable interface (left) and strong blowdown (right) during the POOLEX STB-31 test are presented together.

It can be seen that both CFD solvers predicted the profile of the steam/water interface well. However, the NEPTUNE\_CFD simulation predicted less oscillatory motion of the steam/water interface compared to the OpenFOAM simulation. In the OpenFOAM case, some residual bubble escape was resulted around the pipe mouth. Therefore, the turbulence kinetic energy and further the DCC rate at the outer surface and at the lip area of the pipe appeared to be higher than in the NEPTUNE\_CFD case. However, the higher interfacial turbulence kinetic energy in the NEPTUNE\_CFD case indicates that there are differences in the modelling of interfacial turbulence between the codes as well (see Publication I for further details). In both codes, the standard  $k-\varepsilon$  turbulence model and standard no-slip boundary conditions may have yielded local mispredictions in the near wall turbulence values. In the NEPTUNE\_CFD case, a higher interfacial turbulence may reduce the amount of escaping steam around the pipe lip therefore reducing the turbulence on the lip wall region as well.

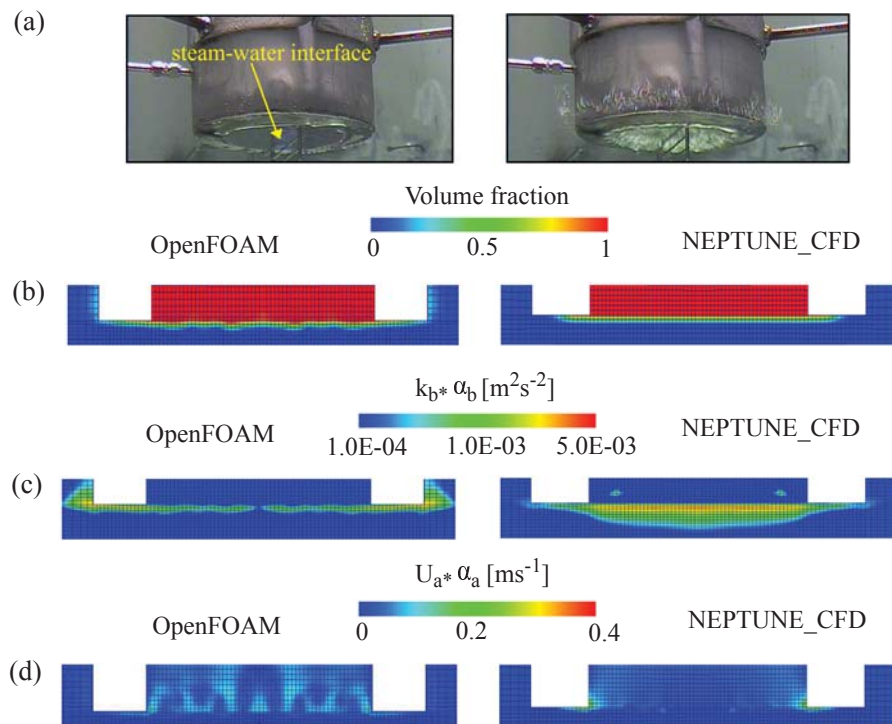


**Figure 6.6.** (a) Instantaneous video frames of stable steam/water interface (left) and strong blow-down of steam (right) during POOLEX STB-31 test, (b) contours of the steam volume fraction, (c) the water phase turbulence kinetic energy times phase fraction of water, and (d) the steam phase velocity times phase fraction of steam near blowdown pipe mouth in 2D-axisymmetric simulations of the POOLEX STB-31 test with the OpenFOAM and NEPTUNE\_CFD using the LH model.

Further, the quantitative assessment of CFD results for both DCC models for both codes were conducted. Figure 6.7 shows results of the condensation mass flow rates, condensation mass flux and total interfacial areas predicted by the HD 0 and the LH DCC models with both CFD codes.

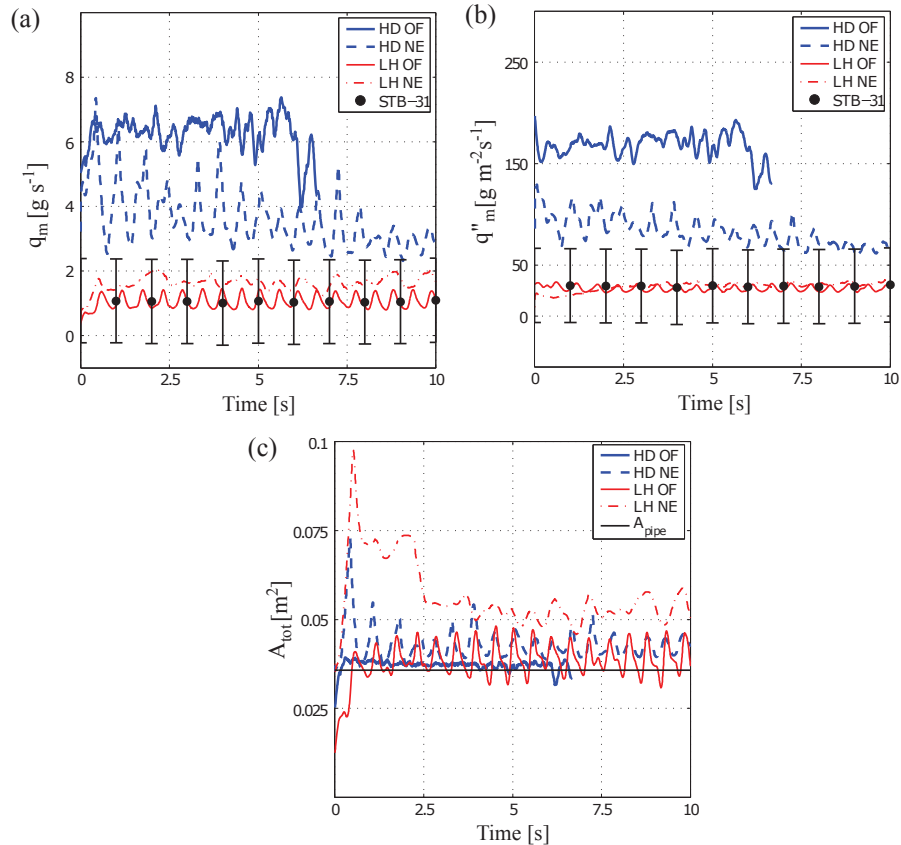


**Figure 6.7.** Averaged (a) condensation mass flow rate, (b) condensation mass flux and (c) total interfacial area predictions of the HD 0 and the LH models using OpenFOAM (OF) and NEPTUNE\_CFD (NE) versus the POOLEX STB-31 experimental data (STB-31). Data is averaged applying a moving average of 0.25 s by using the Savitzky-Golay filtering in MATLAB (Orfanidis, 1996).  $A_{pipe}$  indicates the cross-sectional area of the blowdown pipe outlet in the POOLEX STB-31 test thus excluding the thick wall area of the pipe lip.

All simulation data was averaged by applying a moving average of 0.25 s by using the Savitzky-Golay filtering in MATLAB (Orfanidis, 1996). Further, the measured steam mass flow rate and corresponding measurement error range are displayed. The effect of non-condensable gases was not included in the presented measurement results for the sake of simplicity. The estimated effect of non-condensable gases was small but it con-

tained high uncertainties. Thus, it was excluded from this study and the results presented. Further details on non-condensable gases' effect are discussed in Publication I.

Results show that the HD 0 model overestimated the condensation mass flow rate notably with both CFD codes while the LH model predicted the condensation mass flow rate nearly to the measured values. However, there were some differences in the simulation set-ups between the codes, e.g. the NEPTUNE\_CFD simulations were carried out by employing pressure boundary conditions at inlet and steam tables of CATHARE, whereas the OpenFOAM simulations were conducted by applying velocity inlet boundary condition and fixed steam properties due to lack of steam tables. These differences resulted in slightly different interfacial behaviour which could be one probable reason for the 50 % overestimation in the DCC rate for the LH model predicted by NEPTUNE\_CFD compared to the OpenFOAM and measurements. The results of averaged condensation mass flux shows that the HD 0 model in NEPTUNE\_CFD overestimated the condensation mass flux about 100 – 200 % while in OpenFOAM overpredicted it strongly around 600 %. The steam/water interface retreated into the blowdown pipe in OpenFOAM simulation with the HD 0 model. The LH model predicted the condensation mass flux very close to the assumed values of the STB-31 test with both of the CFD codes.

For the averaged total interfacial areas, it can be seen that in the HD 0 case with NEPTUNE\_CFD and in the LH case with OpenFOAM, the total interfacial area was quite near the blowdown pipe cross-sectional area as the interface profile was very stable and oscillated only moderately. In the NEPTUNE\_CFD case, this was resulted due to the hydrostatically well suited pressure inlet boundary condition which maintained the interface location to the pipe mouth regardless of the unsuited DCC rate. In the OpenFOAM case, the velocity boundary condition matched well to the DCC rate prediction by the LH model. However, in the case of the LH model of NEPTUNE\_CFD, the condensation mass flow rate was higher due to interface expansion regardless of the pressure boundary condition. As shown previously, the higher condensation rate in the HD 0 case of OpenFOAM collapsed the steam volume within the blowdown pipe. During the slow collapse, the total interfacial area in the HD 0 case of OpenFOAM was almost constant and near the blowdown pipe cross-sectional area. More results are presented and discussed in Publication I.

The significance of reference bubble diameter in large interface drag modelling was analyzed assuming various diameters with OpenFOAM. For this purpose, the POOLEX STB-31 case was chosen. Achieved results are presented in Publication II. Also, the sensitivity of subcooling rate on the DCC phenomenon was studied with different pool temperatures and relatively low steam injection rate. Publication II refers the results of this study.

The presented analysis demonstrated that the OpenFOAM simulation results corresponded well to the NEPTUNE\_CFD results. Based on that, it can be concluded that the two-phase CFD solver of OpenFOAM is capable to model DCC phenomena of the special mildly sheared interfacial DCC steam blowdown test of POOLEX.

## 6.2 Results of POOLEX STB-28 experiment

After modelling the POOLEX STB-31 test case with the incompressible two-phase solver of OpenFOAM, simulations were performed for the POOLEX STB-28 test case. All the OpenFOAM simulations of the POOLEX STB-28 test were performed with the  $Lk-\epsilon$  turbulence model. In the POOLEX STB-28 test, the steam injection rate was higher and corresponded therefore to the ‘chugging and oscillatory condensation’ mode (Lahey and Moody, 1993) and the ‘external chug with encapsulating bubble and external chug with detached bubble’ mode (Chan and Lee, 1982a).

The performance of incompressible two-phase flow solver of OpenFOAM for chugging simulations was compared to the compressible two-phase solver of OpenFOAM and the numerical results of NEPTUNE\_CFD simulations by Tanskanen (2012) and Tanskanen et al. (2014). Figure 6.8 compares the predicted volume fraction fields of steam in the 2D-axisymmetric OpenFOAM simulations with the incompressible and compressible solvers, and with the NEPTUNE\_CFD results. Results show that the early phase of the simulation with the incompressible solver was promising as the initial hyperboloid jet condensed quite rapidly. Following that, a toroidal bubble was formed at the pipe mouth. However, the size of the bubble was relatively large and it persisted oscillating at the blowdown pipe outlet never totally collapsing. This indicates that the condensation rate was high enough to condense steam before any bubbles detached upwards in the pool. However, the condensation rate was too weak to provoke chugging. In contrast, the compressible solver of OpenFOAM predicted high enough condensation rates to instigate chugging. In the beginning of the all simulations, the pool water was stagnant, thus the turbulence level was relatively weak. As the heat transfer model was based on the turbulence properties, the condensation rates were low. As a consequence, the size of the steam bubble was larger in the initial stages of the simulations. After the initial steam bubbles collapsed, the steam/water interface retreated inside the blowdown pipe in the upward direction. Subsequently, the steam pressure in the blowdown pipe was adequately favourable to prevent the upward motion of the interface and it started to push the steam/water interface downward again. Further, this chugging cycle continued again from bubble formation to rapid collapse as shown in Figure 1.4. Increased turbulence kinetic energy and chugging motion maintaining it steadied the chugging frequency and bubble sizes to certain values. The compressible flow solver of OpenFOAM yielded qualitatively good results of chugging which are comparable to the previous NEPTUNE\_CFD simulations.

Figure 6.9 shows the total condensation mass flow rate and condensation mass flux predicted with the incompressible and compressible solvers in the 2D-axisymmetric OpenFOAM simulations and they are compared to the NEPTUNE\_CFD results.

It is apparent that in chugging simulations the DCC rates were higher compared to the inlet steam flow rate as they should. However, the incompressible solver yielded relatively constant and lower condensation rate than the compressible solvers. The rate of condensation was clearly higher in OpenFOAM simulations. The OpenFOAM simulations were conducted without steam tables. Further, the main differences between the

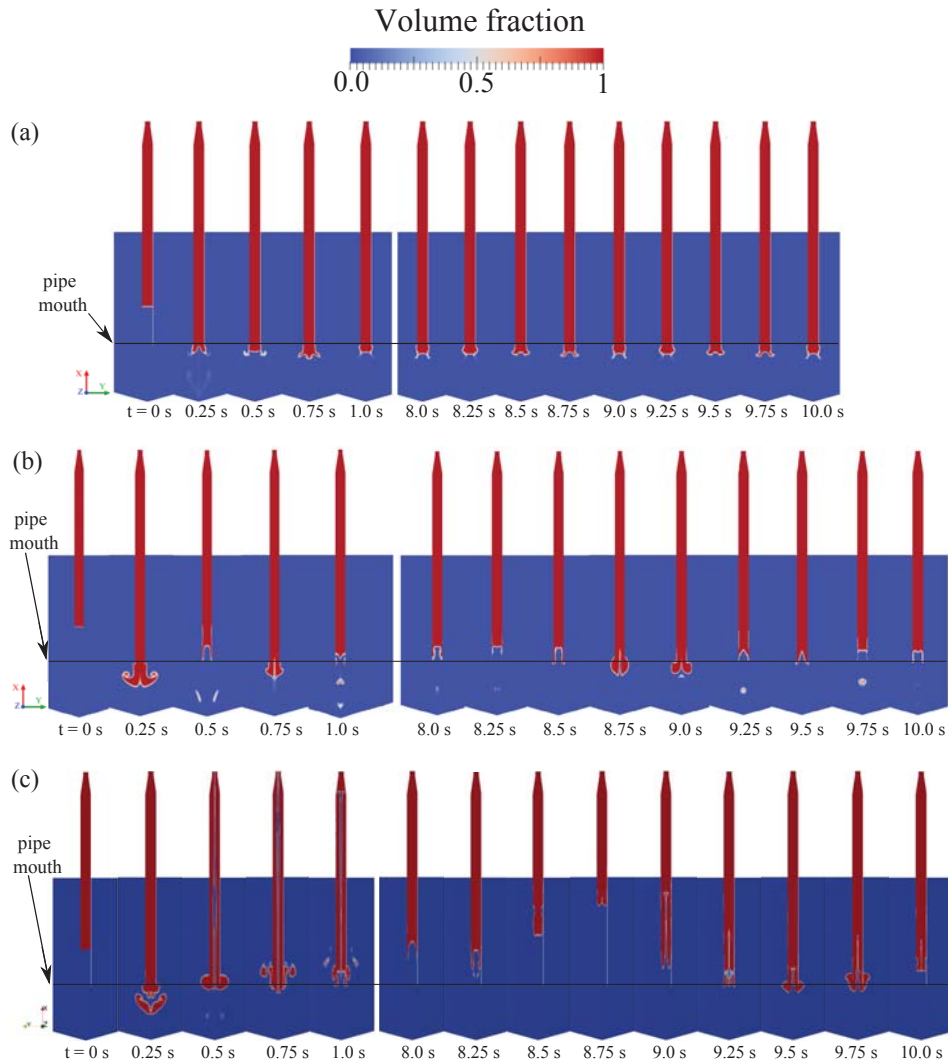


**Figure 6.8.** Contours of volume fraction of steam in the 2D-axisymmetric simulations of the POOLEX STB-28-4 experiment using the HD 1 model with (a) incompressible two-phase solver of OpenFOAM, (b) compressible two-phase solver of OpenFOAM, and (c) compressible two-phase solver of NEPTUNE.CFD using the HD 0 model with steam tables.

NEPTUNE.CFD and OpenFOAM simulations were the DCC model, the interfacial drag and turbulence modelling. These could be the reasons for differences between the NEPTUNE.CFD and OpenFOAM results. The DCC rate was higher in OpenFOAM simulation than in the NEPTUNE.CFD simulations due to a higher interfacial area. As a result, the condensation mass flux was decreased in OpenFOAM simulations compared to the NEPTUNE.CFD simulations. However, the compressible solver yielded good results

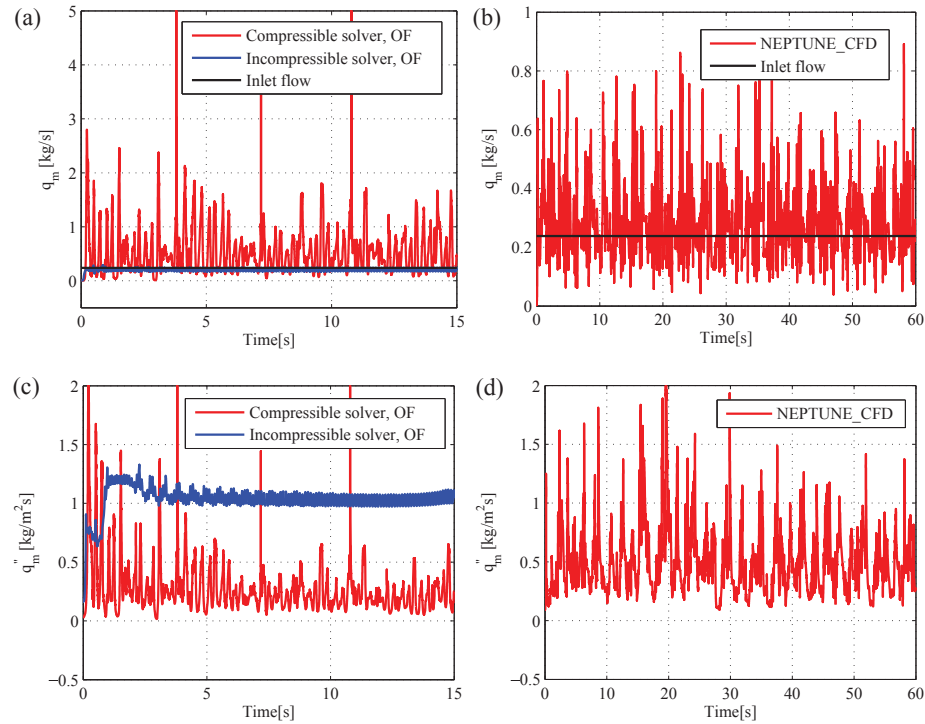


**Figure 6.9.** Condensation mass flow rates (a) in OpenFOAM and (b) in NEPTUNE\_CFD, and condensation mass flux (c) in OpenFOAM and (d) in NEPTUNE\_CFD in the 2D-axisymmetric simulations of the POOLEX STB-28-4 experiment. The OpenFOAM simulations were performed using the HD 1 model and NEPTUNE\_CFD simulations were conducted with the HD 0 model.

along with the NEPTUNE\_CFD simulations. Results show that the incompressible solver was unable to solve the rapid pressure/density variation of steam blowdown simulations which is likely necessitated to simulate chugging phenomena. Based on these results, it can be concluded that the incompressible solver is inadequate for chugging simulations.

### 6.2.1 Influence of grid on chugging

In the simulation of the chugging phenomenon, steam/water interface is of prime interest as it is governed by the transfer processes in the vapour and liquid regions around the interface. As the grid density in the domain defines the accuracy of steam/water interface, it is interesting to study the dependency of the chugging phenomenon on the computational grid density. In the present work, the influence of the computational grid density on the results was studied by employing four grid resolutions. For this analysis, the POOLEX STB-28-4 case was chosen and the HD 1 model was used for interfacial heat transfer modelling. Figure 6.10 displays the results predicted with different grids. Results show that all four grids resulted in high condensation mass flow rates and were able to condense all injected steam. High peaks in condensation mass flow rate were observed with denser grids. The total interfacial area was increased as grid resolution was increased. Grid D predicted significantly higher interfacial area than the other grids. However, chugging simulations with a much denser grid experienced some convergence issues. Some differences were noticed for condensation mass flux prediction between grids (Figure 6.11). In the later part of the simulation, the poor resolution grids yielded slightly higher condensation mass flux per area, while the increased interfacial area in the denser grids decreased condensation mass flux. Base on these results, it can be concluded that the interfacial details and, later on, details due to the Rayleigh-Taylor and other instabilities could be possible to capture with better grids.

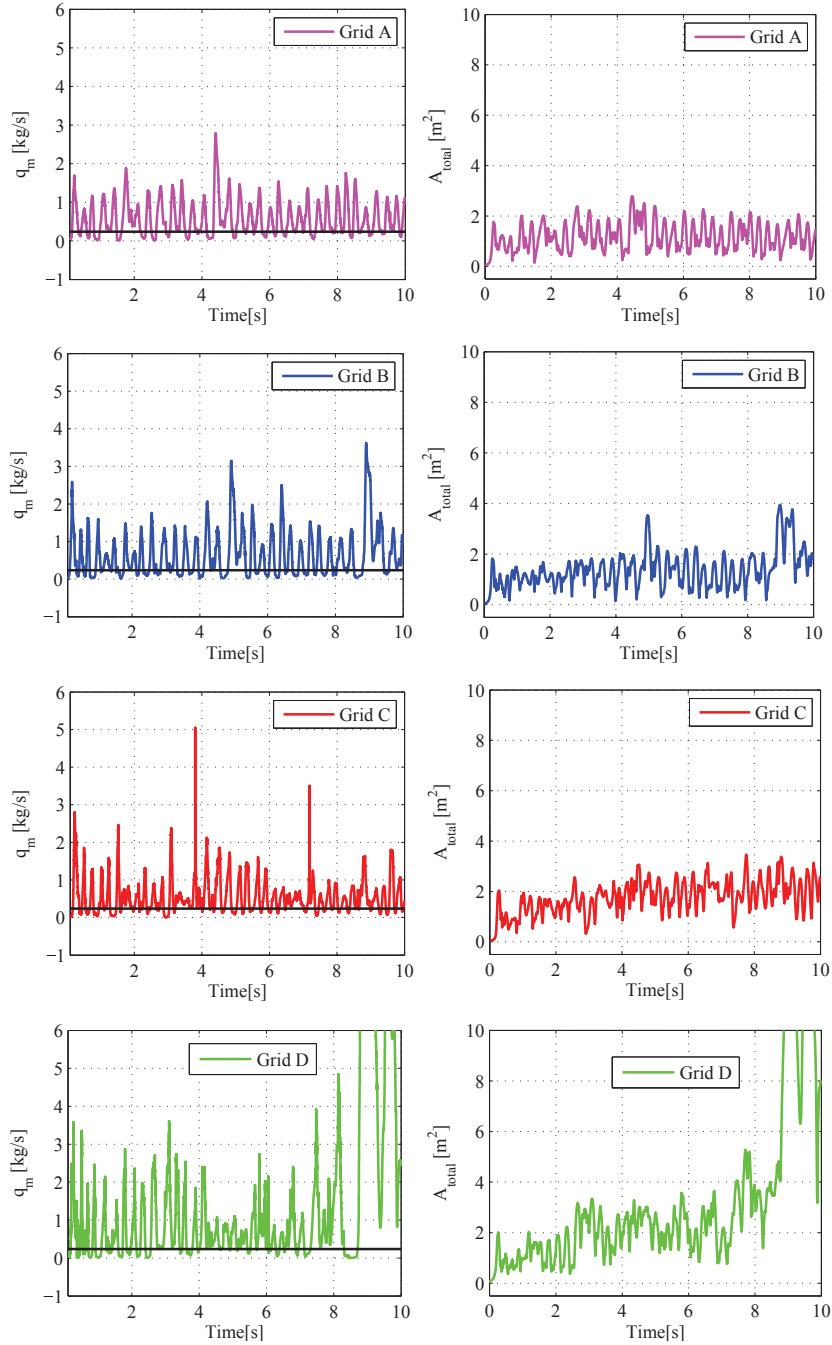


**Figure 6.10.** Condensation mass flow rate and interfacial area in 2D-axisymmetric OpenFOAM simulations of the POOLEX STB-28-4 experiment predicted by different grid resolutions by using the HD 1 model. The black solid line indicates the inlet flow.

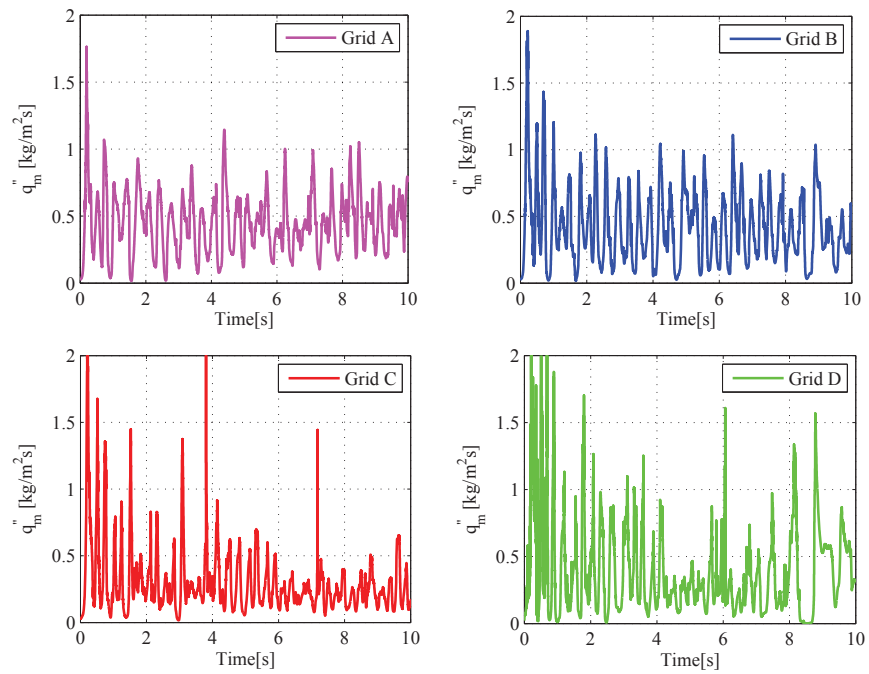


**Figure 6.11.** Condensation mass flux in 2D-axisymmetric OpenFOAM simulations of the POOLEX STB-28-4 experiment predicted by different grid resolutions by using the HD 1 model.

Turbulence properties predicted by different grids are presented in Figures 6.12 and 6.13. For all grid cases, very mild initial turbulence level was assumed in the pool water. As simulation time elapsed, a gradual increment resulted in pool water turbulence due to pool mixing. All the grids predicted fairly high turbulence kinetic energy which maintained DCC rates in the simulations (Figure 6.10) as the HD 1 DCC model is dependent on the turbulence. However, the denser grids viz. Grid C and Grid D predicted slightly higher turbulence kinetic energy and its dissipation rate than the coarser grids i.e. Grid A and B.

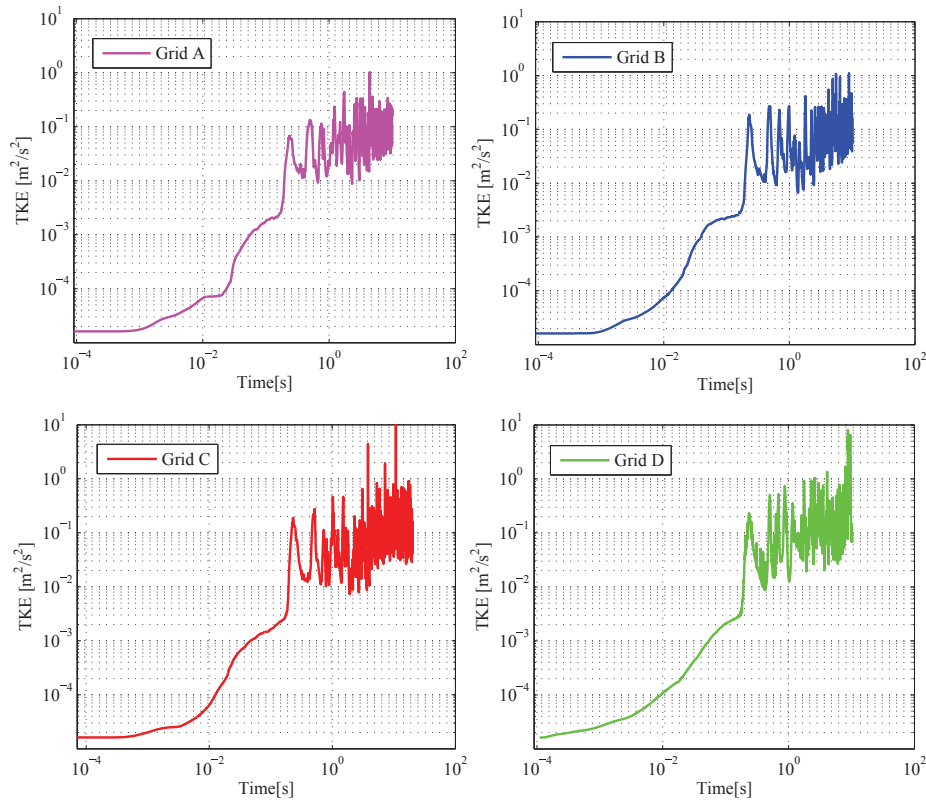


**Figure 6.12.** Volume averaged turbulence kinetic energy of the liquid phase in 2D-axisymmetric OpenFOAM simulations of the POOLEX STB-28-4 experiment predicted by different grid resolutions by using the HD 1 model.

Further, the GCI method by Celik et al. (2008) was employed in order to analyze the discretization error for the CFD results with the chosen computational grids. The GCI analysis was assessed with the time average values of condensation mass flow rate and total interfacial area. Figure 6.14 presents the measures of the estimated and extrapolated relative errors and the GCI values. The presented GCI analysis demonstrates that the relative error was reduced from Case AB to BC. However, there was a significant increment

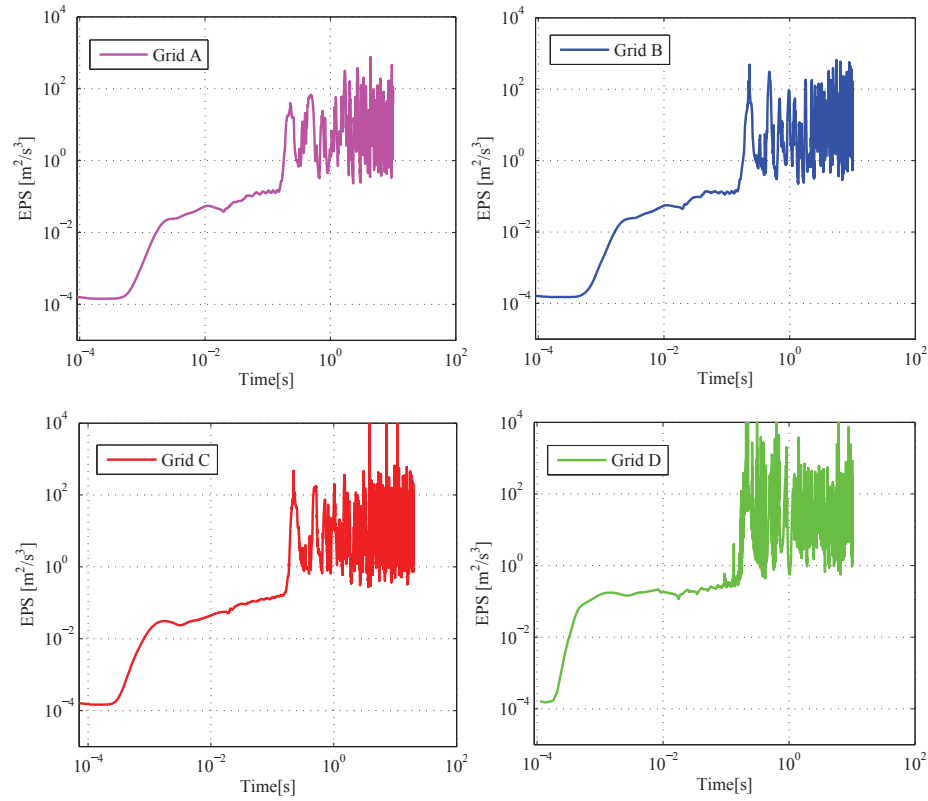


**Figure 6.13.** Volume averaged dissipation rate of turbulence kinetic energy of the liquid phase in 2D-axisymmetric OpenFOAM simulations of the POOLEX STB-28-4 experiment predicted by different grid resolutions by using the HD 1 model.

in relative error from Case BC to CD which indicates that refinement from Grid C to Grid D produced large differences both in condensation mass flow rate and in interfacial area. Similar behaviour also resulted for the extrapolated relative error, however the error increment was not as high. The GCI measure was almost trivial for Case BC for both properties. Based on this GCI study, it seems that the finest grid resolution used in these simulations was not suitable for POOLEX-STB-28 simulations. Grid C was employed for further simulations in order to be on safe side and because the DCC rate was already high. The divergence between the Grid C and D can be occurred due to the activation of interfacial instability phenomena or due to the change in the applicability of the turbulence model.

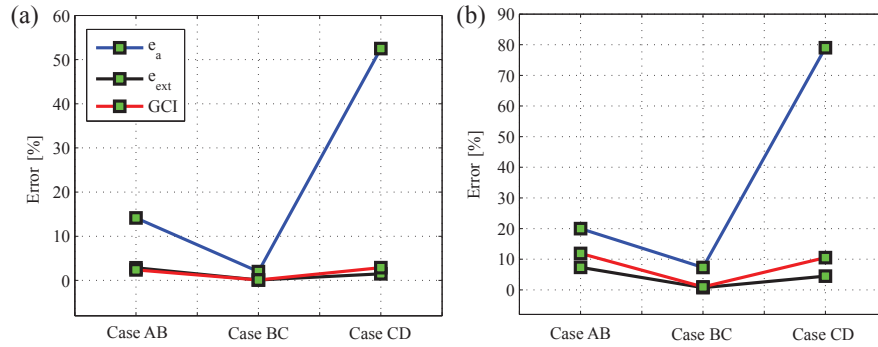
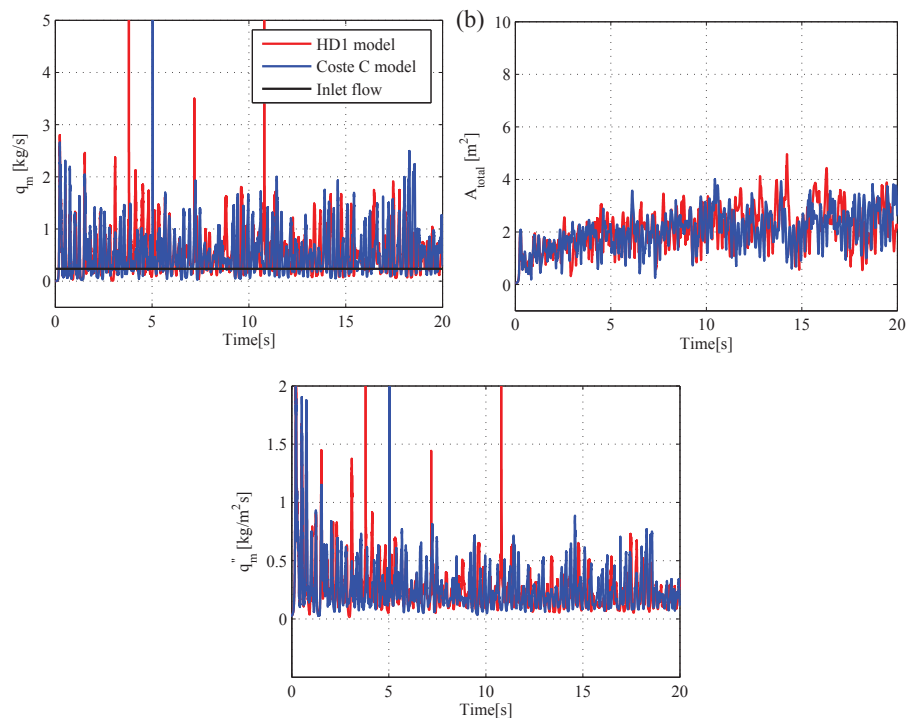


**Figure 6.14.** Estimated relative error (i.e.,  $e_a$ ), extrapolated relative error (i.e.,  $e_{ext}$ ) and GCI values for (a) condensation mass flow rate, and (b) total interfacial area for successive grid refinements for POOLEX STB-28-4 2D-axisymmetric simulations by using the HD 1 model in OpenFOAM. The Cases AB, BC and CD express the grid refinements from Grid A to B, Grid B to C, and Grid C to D, respectively.

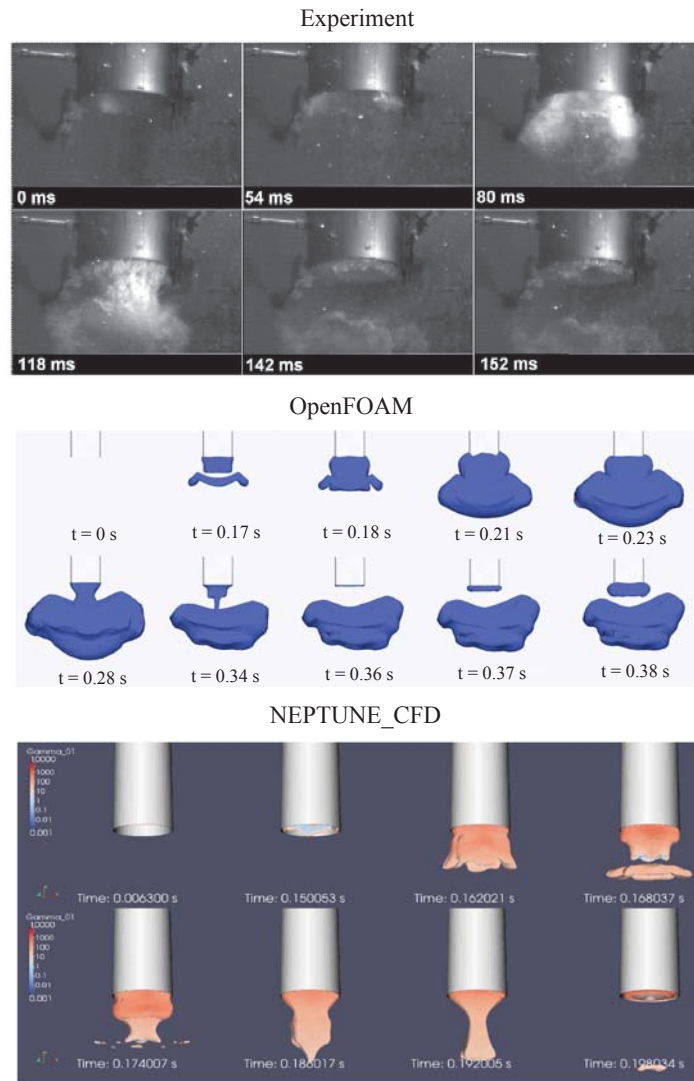
### 6.2.2 Influence of DCC model on chugging

Further, the chugging simulations were performed by employing other DCC models i.e. the Coste C model and the LH model, and the results were compared with the HD 1 model. Figure 6.15 shows the results of 2D-axisymmetric simulations with HD 1 and Coste C models. The HD 1 and the Coste C models predicted comparatively similar results for condensation mass flow rate, interfacial area and condensation mass flux. In both cases, the injected steam was condensed within the pool and both the models were able to predict a high enough DCC rate to provoke chugging.

Further, the POOLEX STB-28-4 case was simulated with the 3D computational model for the total simulation time span of 10 s. Figure 6.16 displays the event of initial steam jet penetration in the POOLEX STB-28-4 test and the instantaneous contours of OpenFOAM simulations. The previously simulated results of 3D NEPTUNE\_CFD case by Tanskanen (2012) are shown as well. In the beginning, the steam/water interface was inside the blow-down pipe. As the steam mass flux increased, the interface moved downwards inside the blowdown pipe and a steam bubble was formed at the pipe outlet. In the OpenFOAM simulation, the size of the initial bubble was larger than in the experiments and the NEPTUNE\_CFD simulations. Also, the bubble remained a little longer and it travelled further towards the pool bottom.

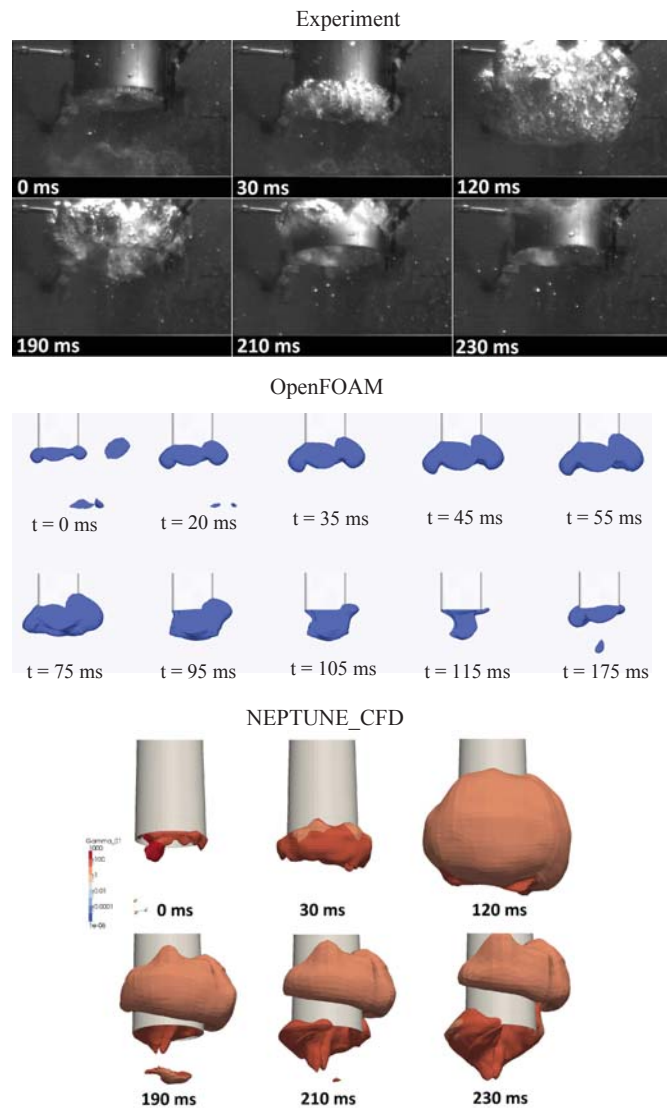


**Figure 6.15.** (a) Condensation mass flow rate, (b) interfacial area, and (c) condensation mass flux predicted by the HD 1 model and the Coste C model in 2D-axisymmetric OpenFOAM simulations of the POOLEX STB-28-4 experiment.



**Figure 6.16.** Photographs of the initial steam jet penetration into the pool in the POOLEX STB-28-4 test, and corresponding results of the 3D OpenFOAM simulation conducted with the HD 1 model and the 3D NEPTUNE\_CFD simulation by Tanskanen (2012) conducted with the HD 0 model.

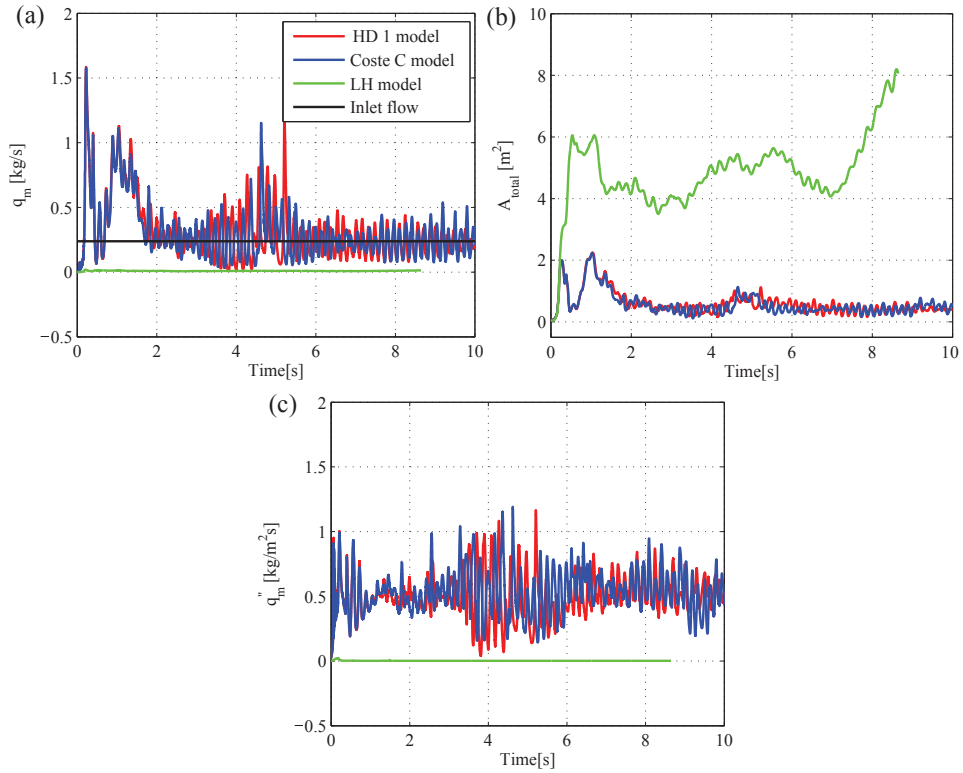
Figure 6.17 shows the inflating and collapsing steam bubble in the POOLEX STB-28-4 test, and the corresponding results of the 3D OpenFOAM and the NEPTUNE\_CFD simulations.



**Figure 6.17.** Photographs of the inflating and collapsing steam bubble into the pool in the POOLEX STB-28-4 test, and corresponding results of the 3D OpenFOAM simulation conducted with the HD 1 model and the 3D NEPTUNE\_CFD simulation by Tanskanen (2012) conducted with the HD 0 model.

The steam bubble inflated around the blowdown pipe mouth in the test and in the NEPTUNE\_CFD simulations. Subsequently, it detached from the pipe mouth and moved in the upward direction. In the OpenFOAM simulation, steam bubble formed around the blowdown pipe mouth and condensed there. However, the bubble collapse times for both codes are visually rather similar. Also, the bubble shape in the OpenFOAM simulation differed slightly from the bubble shape in the NEPTUNE\_CFD simulation. In the NEPTUNE\_CFD simulations, either the SIMMER drag model by Kondo et al. (1992) or the 'large interface' (LI) drag model by Coste et al. (2008) was used, while in OpenFOAM simulation, the Schiller-Naumann drag model by Schiller and Naumann (1933) was used. The difference in the results between the CFD codes could be assigned to the differences in compressibility treatment, the interfacial drag modelling and turbulence models. However, possible suitability issues of the used 3D grid for the OpenFOAM solver can be a likely reason for this discrepancy in DCC rate between the codes. The spherical curvilinear design of the grid yielded some less orthogonal cells that OpenFOAM tolerates poorly compared to NEPTUNE\_CFD. Some artificial forces could be generated in OpenFOAM in that case.

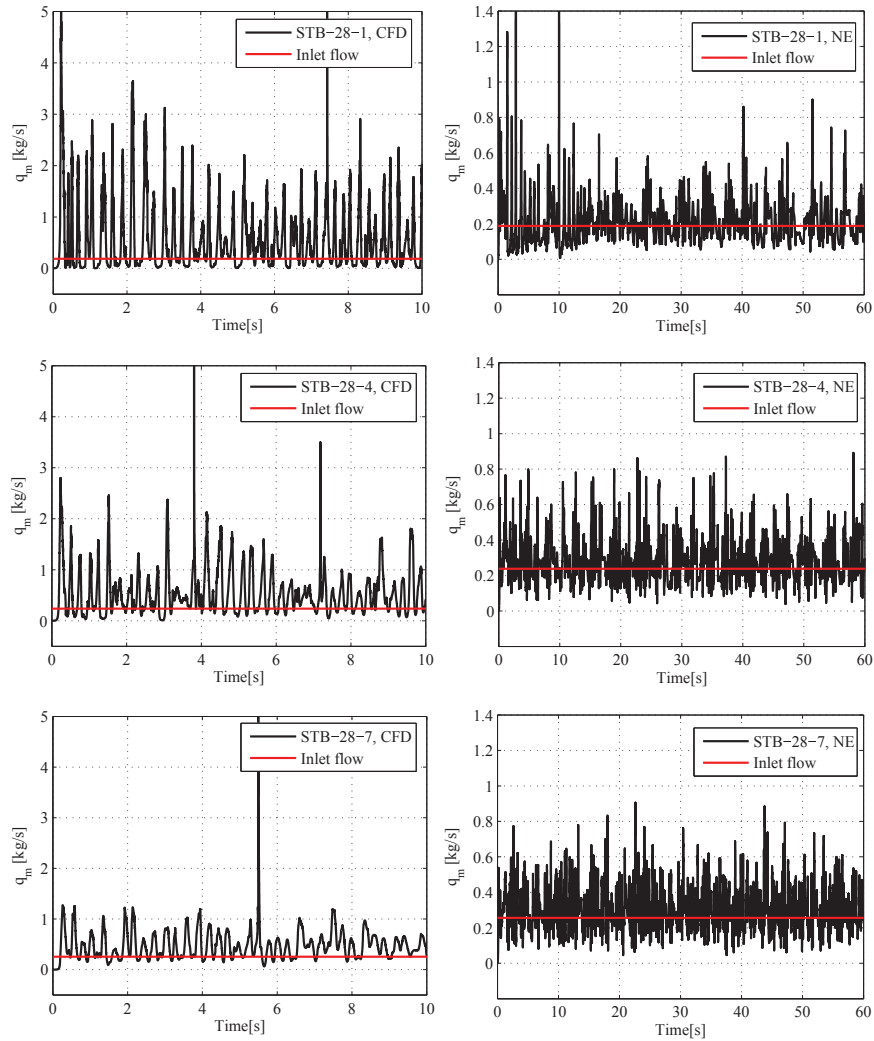
Further, different DCC models were employed for the 3D chugging simulations. Figure 6.18 displays the total condensation mass flow rate, interfacial area, and corresponding condensation mass flux of the 3D STB-28-4 simulation using OpenFOAM. It can be seen that the LH model predicted a too low condensation rate. As a result, a large amount of injected steam escaped without condensing which increased the interfacial area significantly (Figure 6.18 (b)). The LH model failed to model chugging phenomena in the POOLEX simulations. The results of the HD 1 model and the Coste C model demonstrate that the DCC rates were higher. Accordingly, the complete and oscillating steam condensation occurs within the domain. However, in the case of 3D simulations, the frequencies of oscillations in the condensation mass flow rate, interfacial area and condensation mass flux are different than in the 2D-axisymmetric simulations. 2D-axisymmetric CFD model yields axisymmetric surface structures that are not physically as representative as in the 3D simulations e.g. any interfacial wrinkle has an amplified effect on the DCC rate and on the interfacial area in 2D. Both the HD 1 model and the Coste C model yielded good results in the 3D POOLEX STB-28-4 case.



**Figure 6.18.** Volume averaged (a) condensation mass flow rate, (b) interfacial area, and (c) condensation mass flux predicted by the HD 1 model, the Coste C model and the LH model in 3D OpenFOAM simulations of the POOLEX STB-28-4 experiment.

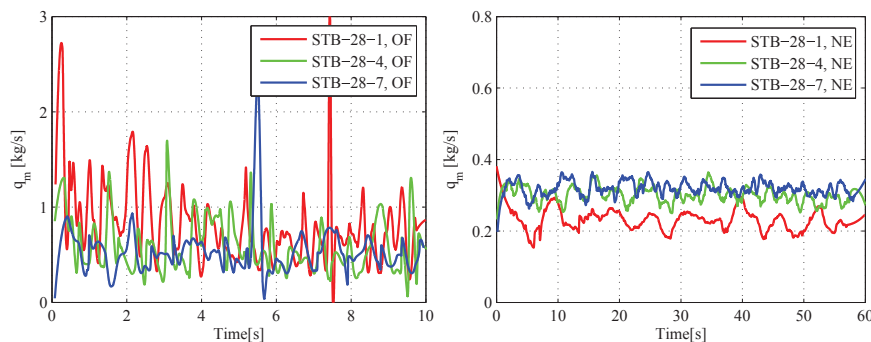
### 6.2.3 Influence of subcooling rate on chugging

In this work, three sub tests of POOLEX STB-28 viz. STB-28-1, STB-28-4 and STB-28-7 were simulated. Figure 6.19 shows the predicted DCC rates of the POOLEX STB-28-1, 4, and 7 in the 2D-axisymmetric OpenFOAM simulations. These sub tests STB-28-1, STB-28-4 and STB-28-7 refer the different subcooling levels of 60 K, 40 K and 30 K, respectively. The NEPTUNE\_CFD results are shown as well for the corresponding cases. It can be seen that the condensation mass flow rate was highest in the STB-28-1 case due to cold pool water. As the pool water temperature increased due to heat transfer, the DCC rate was reduced being lowest in the case of STB-28-7. The DCC rate was higher in the OpenFOAM simulations than in the NEPTUNE\_CFD simulations for all cases.



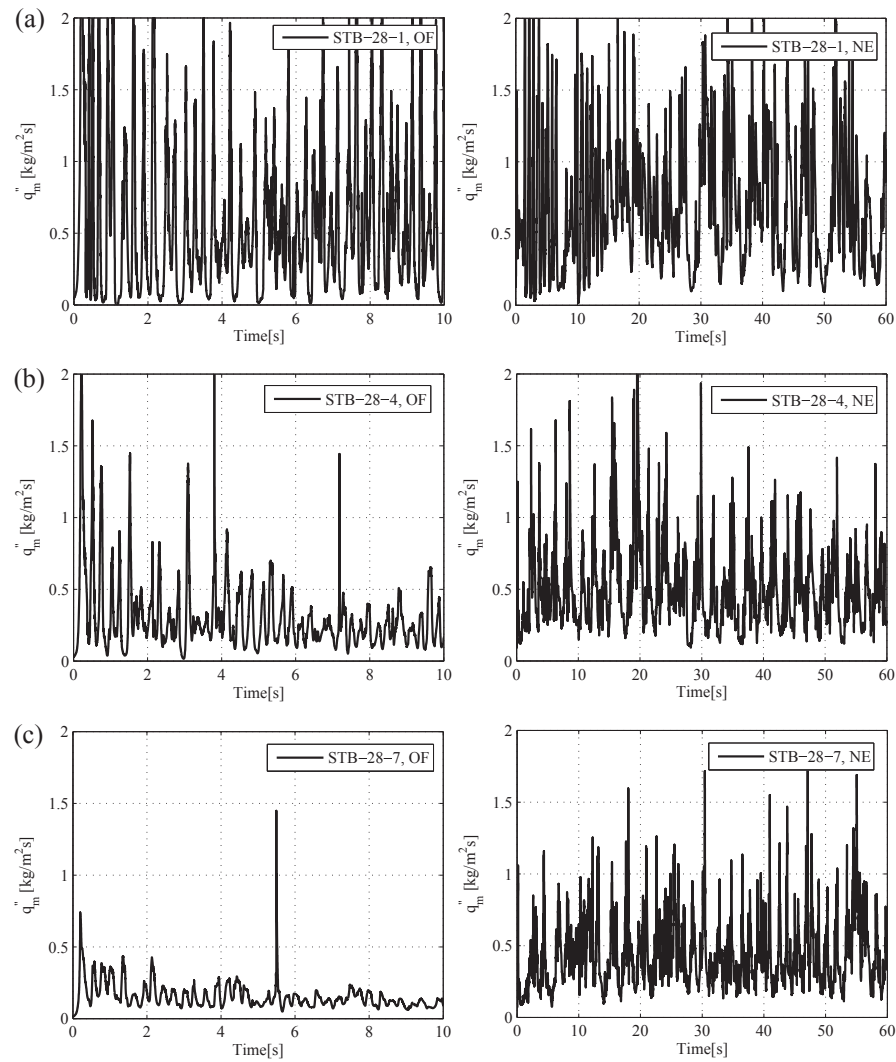
**Figure 6.19.** Results of condensation mass flow rate in the 2D-axisymmetric OpenFOAM simulations of POOLEX (a) STB-28-1, (b) STB-28-4, and (c) STB-28-7 experiments predicted by the HD 1 model and in comparison with the corresponding NEPTUNE.CFD simulations by Tanskanen et al. (2014) with the HD 0 model.

Further, an averaged condensation mass flow rate was obtained for all the cases. Figure 6.20 shows a comparison between the codes. In the short simulation sample of OpenFOAM, the averaged condensation rate was maximum for the STB-28-1 case and it gradually decreased as the pool subcooling level was decreased. However, in the long simulation run of the NEPTUNE\_CFD case, the averaged condensation mass flux was lower in the case of STB-28-1. The lower DCC rate was the result of the lesser inlet flow rate in the STB-28-1 due to considerable deduction of wall condensate. As a result, internal chugging occurred and therefore the large interfacial area which appears in external chugging was absent in the STB-28-1 case.

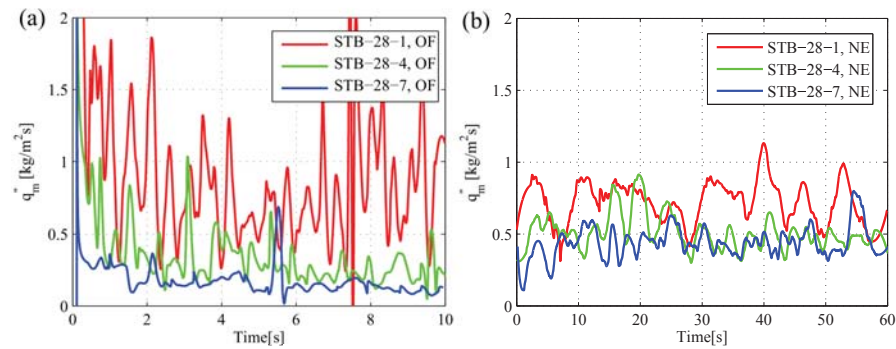


**Figure 6.20.** Results of averaged condensation mass flow rate in the 2D-axisymmetric OpenFOAM simulations of POOLEX (a) STB-28-1, (b) STB-28-4, and (c) STB-28-7 experiments predicted by the HD 1 model and in comparison with the corresponding NEPTUNE\_CFD simulations with the HD 0 model. The data is averaged by employing the Savitzky-Golay filtering (moving average of 60,000 points) in MATLAB (Orfanidis, 1996).

The total condensation mass flux and the averaged condensation mass flux are compared in Figures 6.21 and 6.22, respectively. It is apparent that the highest condensation mass flux was observed in the STB-28-1 due to the highest subcooling level and due to lower interfacial area. Despite the large differences in total condensation mass flow rates, the condensation mass fluxes in OpenFOAM simulations were not much higher than those in NEPTUNE\_CFD simulations. This could be explained, as the total interfacial area in OpenFOAM simulations was higher than in the NEPTUNE\_CFD simulations. Overall, the compressible two-phase solver of OpenFOAM was able to produce chugging in all 2D-axisymmetric simulated cases of the POOLEX test.

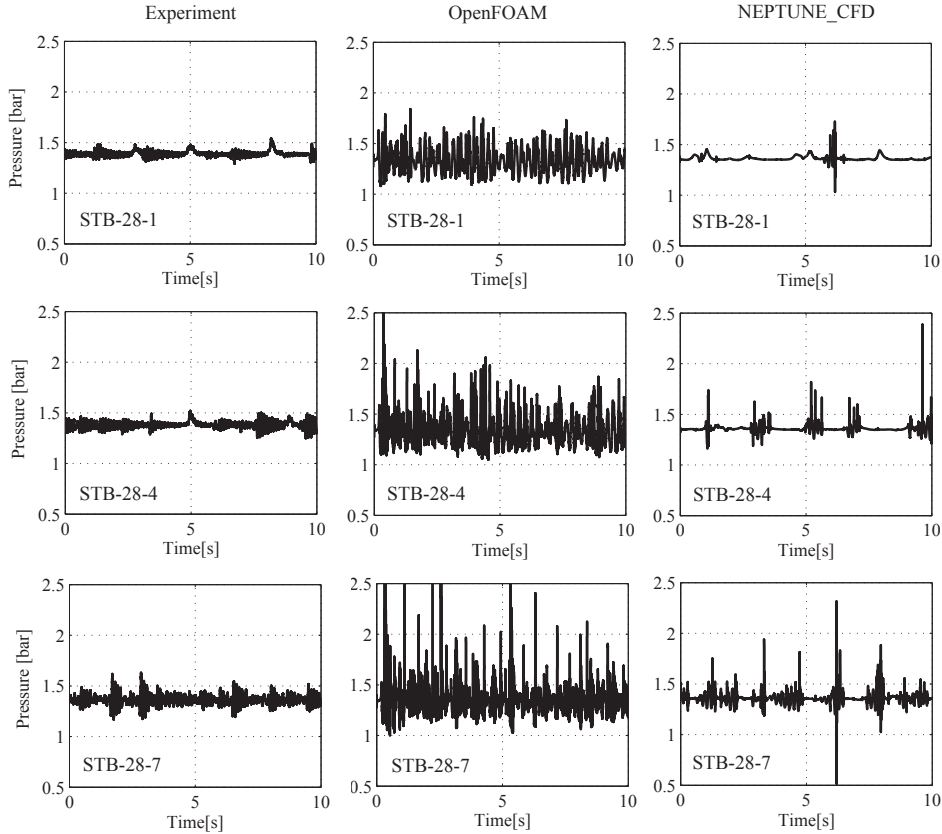


**Figure 6.21.** Results of condensation mass flux in the 2D-axisymmetric OpenFOAM simulations of POOLEX (a) STB-28-1, (b) STB-28-4, and (c) STB-28-7 experiments predicted by the HD 1 model and in comparison with the corresponding NEPTUNE.CFD simulations by Tanskanen et al. (2014) with the HD 0 model.



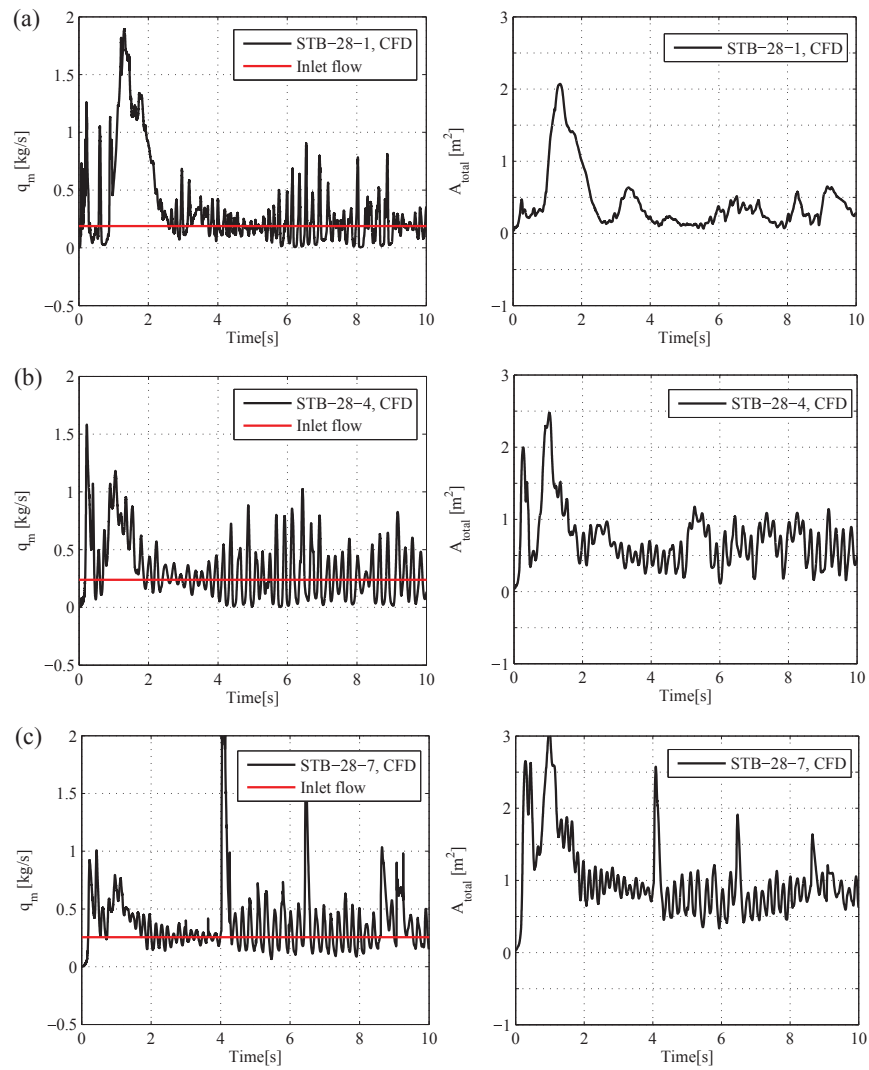
**Figure 6.22.** Results of averaged condensation mass flux in the 2D-axisymmetric OpenFOAM simulations of POOLEX (a) STB-28-1, (b) STB-28-4, and (c) STB-28-7 experiments predicted by the HD 1 model and in comparison with the corresponding NEPTUNE\_CFD simulations by Tanskanen et al. (2014) with the HD 0 model. The data is averaged by employing the Savitzky-Golay filtering (moving average of 60,000 points) in MATLAB (Orfanidis, 1996).

Figure 6.23 shows the recorded pressures in the tests and in the CFD simulations. Results indicate that the pressure pulse magnitudes increased as the pool subcooling level decreased. The fact that the simulations were performed with the 2D-axisymmetric CFD model which intensified the pressure behaviour in the pool, could be one obvious reason for differences between the modelled and the measured pressure values. Further, in simulations, the pool was rigid and thus unable to incorporate pressure fluctuations. Therefore, the predicted pressures of all the simulations were notably higher than the measured ones. There were some differences between the results of the CFD codes. In OpenFOAM simulations, more external chugging resulted than the NEPTUNE\_CFD simulations, and therefore bubble collapses. Thus, the overall frequency of the pressure data at pool bottom in OpenFOAM simulations was higher than in the NEPTUNE\_CFD simulations. Unfortunately, data probing was missing in OpenFOAM 3D simulations. Thus, high frequency pressure data cannot be presented here.



**Figure 6.23.** Recorded pressure data of pool water in the POOLEX STB-28-1, 4, and 7 experiments, and in the corresponding 2D-axisymmetric OpenFOAM with the HD 1 model and NEPTUNE\_CFD simulations with the HD 0 model. The data were recorded at the bottom of the pool beneath the blowdown pipe.

Further, the POOLEX STB-28-1, 4 and 7 cases were simulated with the 3D computational model and the corresponding results are presented in Figures 6.24 and 6.25. The total interfacial area increased as pool subcooling decreased. The STB-28-7 case had the lowest subcooling among the other selected STB-28 cases. In the early phase of the 3D simulation of the STB-28-7 case, the DCC rate was weaker. As simulation progressed, pool mixing was increased and subsequently the DCC rate grew. Both DCC rate and condensation mass flux in the 3D simulations are smaller than in the 2D simulations. As shown previously, the total interfacial area is larger in the 2D simulations than in the 3D simulations. The differences between 2D and 3D results are probable because 2D amplifies the effect of local high DCC points on the interface.



**Figure 6.24.** Results of condensation mass flow rate and interfacial area in the 3D OpenFOAM simulations of POOLEX (a) STB-28-1, (b) STB-28-4, and (c) STB-28-7 experiments predicted by the HD 1 model.

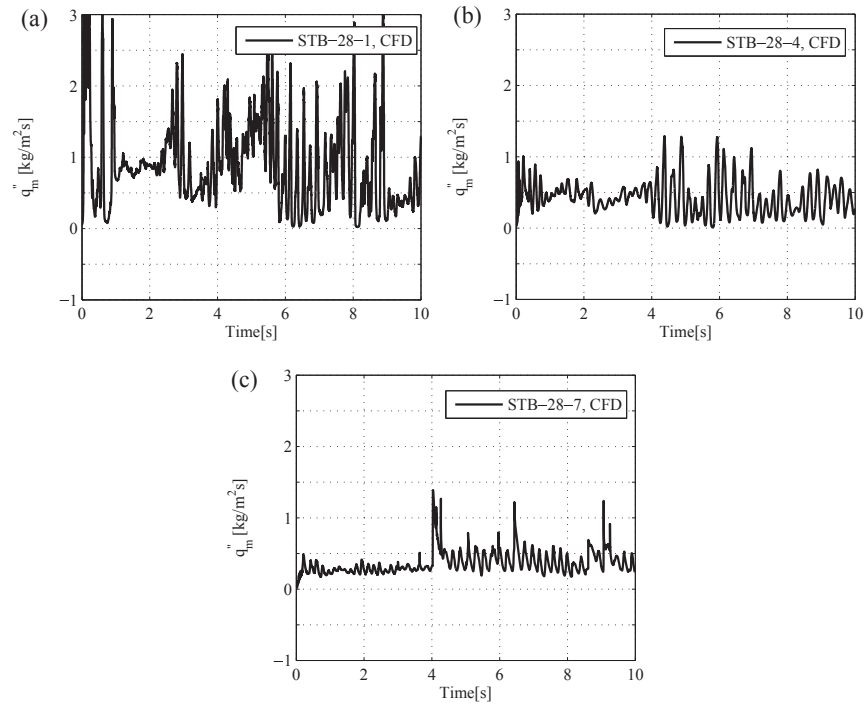


**Figure 6.25.** Results of condensation mass flux in the 3D OpenFOAM simulations of POOLEX (a) STB-28-1, (b) STB-28-4, and (c) STB-28-7 experiments predicted by the HD 1 model.

The Fast Fourier Transform (FFT) analysis of pressure data on pool bottom in the experiment distinguished best the 10 Hz eigenmode of the pool bottom deformation due to the vertical motion of pool water mass, leaving the chugging frequencies less distinguishable (Tanskanen, 2012). Regardless of that, 1 Hz chugging frequency, recognized by Tanskanen (2012), could be found there. The FFT analysis of 2D NEPTUNE\_CFD pressure data showed the nearest maximums below and around the 1 Hz chugging rate, and a clearly separate maximum near 6 Hz, which would correspond the motion of locally oscillating interface. The FFT of corresponding 2D OpenFOAM data showed more peaks between 1 Hz and 3 Hz, which confirms that along with the higher DCC rate, the chugging rate was higher in the OpenFOAM simulations as well (Figure 6.26).

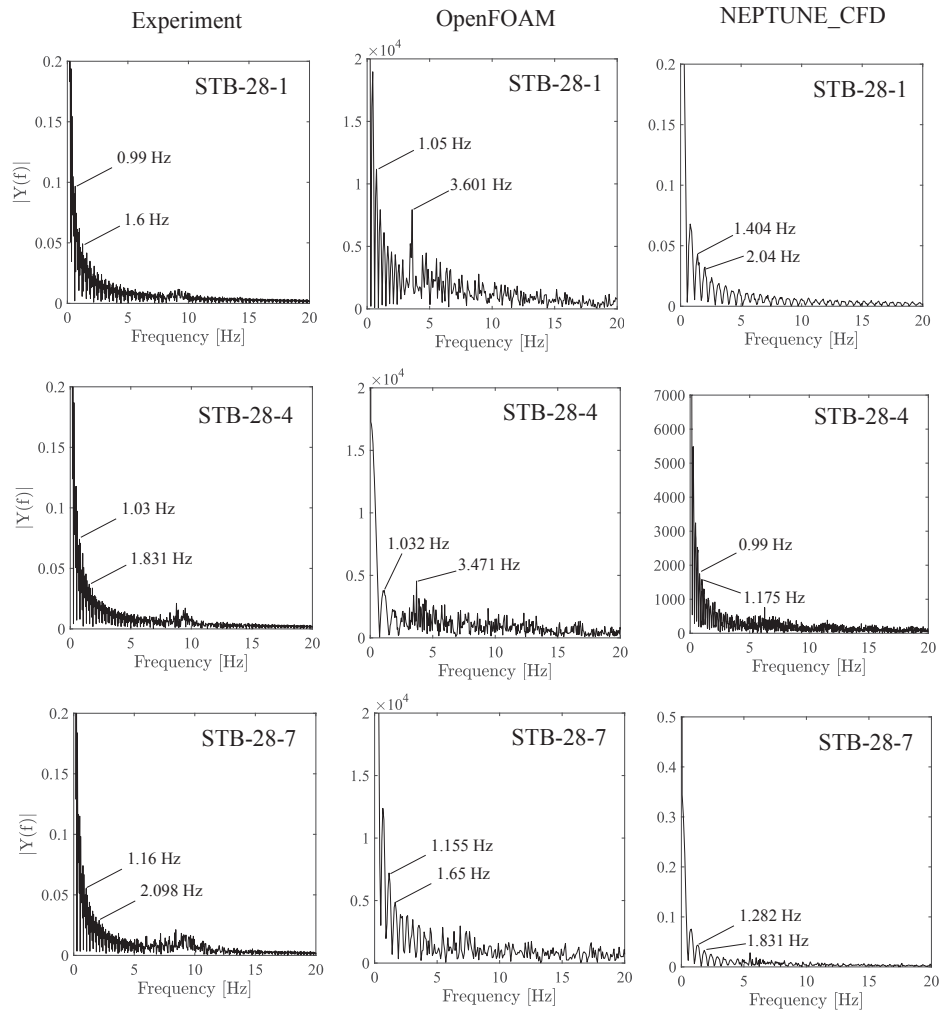
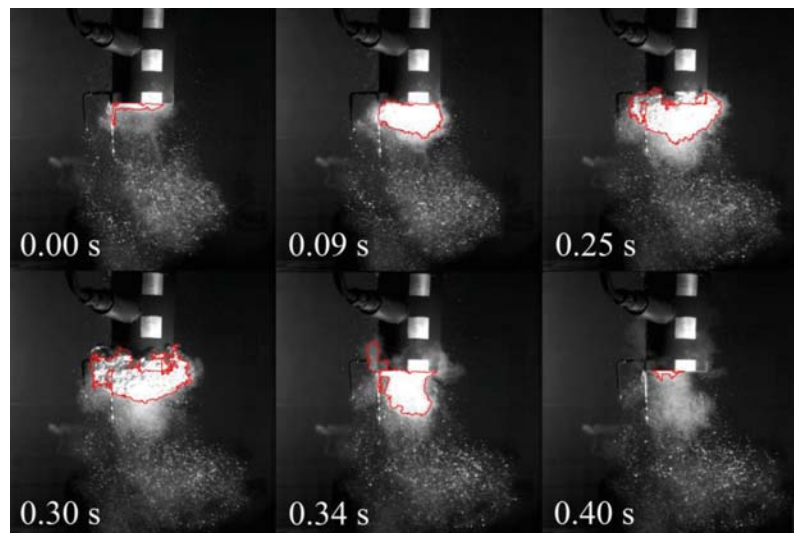


**Figure 6.26.** FFT from pressure data of pool water in the POOLEX STB-28-1, 4, and 7 experiments, and in the corresponding 2D-axisymmetric OpenFOAM with the HD 1 model and NEPTUNE\_CFD simulations with the HD 0 model.

### 6.3 Results of PPOOLEX DCC-05 experiment

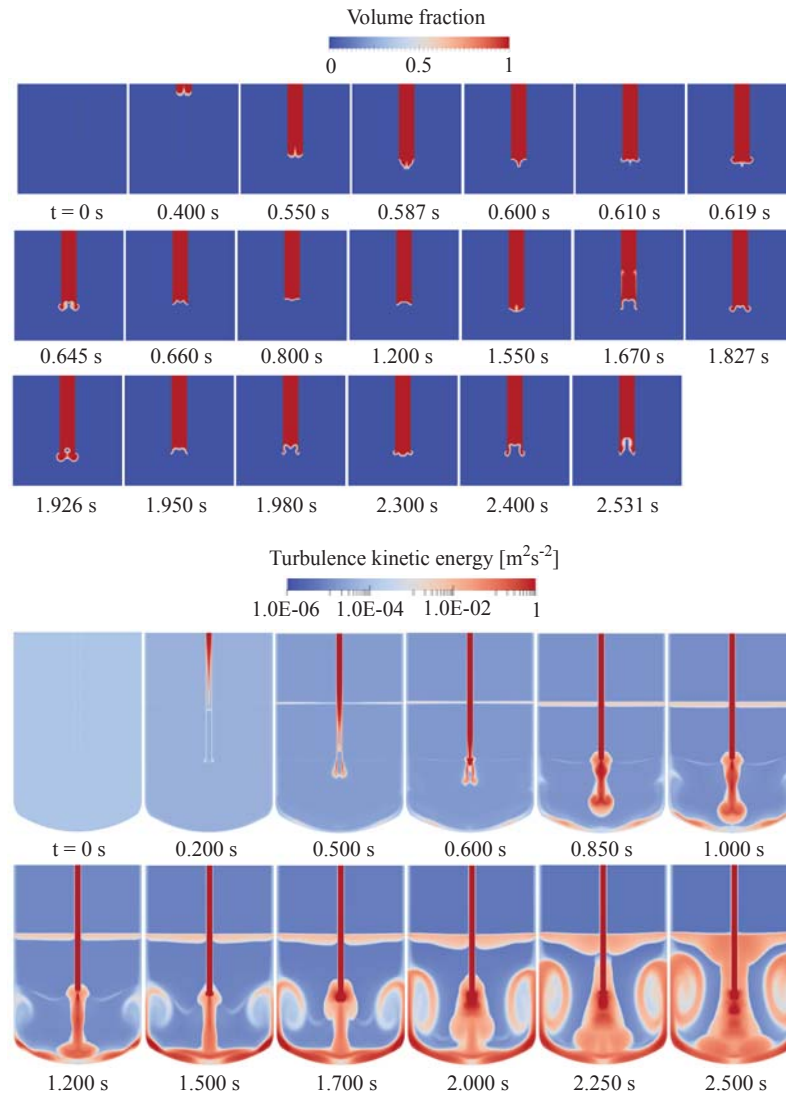
Further, the simulations of PPOOLEX DCC-05 experiment were performed for short time span by employing the compressible two-phase solver of OpenFOAM. In OpenFOAM, a 10 s simulation run with the 2D-axisymmetric PPOOLEX geometry took 4.8 days with 1 core, while the same run with the whole 3D PPOOLEX geometry could take approx. 22.3 days with 12 cores. The dense grid 3D simulations are computationally even more expensive. However, numerical problems in 3D simulations seem to be worse, which make required 15-60 s transients practically slower than core count would permit. 2D simulations allow rapid testing of implemented models which is the practical reason for numerous 2D cases. Among the DCC-05 PPOOLEX experiments, the test number 4 i.e. DCC-05-4 was modelled. As the DCC-05 blowdown test was classified as a chugging condensation mode case (see Figure 1.3), the most suitable DCC models i.e. the HD 1 model and the Coste C model were utilized for the simulations.

Figure 6.27 displays the captured frames showing the bubble growth and its collapse in the PPOOLEX DCC-05-4 experiment. The information about the formation and break up of bubbles can be extracted by visual observation using a suitable pattern recognition algorithm. Tanskanen (2012) proposed a pattern recognition technique with which chugging DCC was studied indirectly from the recorded video material of the PPOOLEX tests. For the DCC-05 PPOOLEX experiments, the preliminary version of the pattern recognition algorithm was improved by Hujala (2013). More details are presented in Publication III.



**Figure 6.27.** Photographs of bubble growth and its collapse in the PPOOLEX DCC-05-4 experiment. The red lines indicate the bubble boundaries recognized by the pattern recognition algorithm.

Figure 6.28 displays the instantaneous volume fraction contours of steam and turbulence kinetic energy fields in a 2D-axisymmetric OpenFOAM simulation.

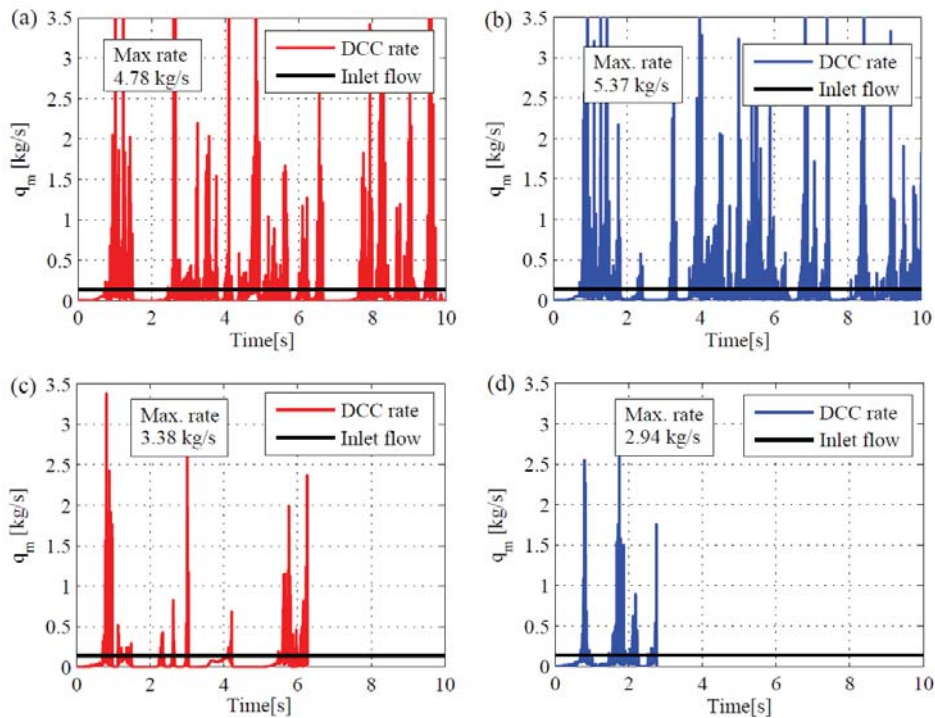


**Figure 6.28.** Instantaneous (a) volume fraction fields of steam and (b) turbulence kinetic energy in the 2D-axisymmetric OpenFOAM simulation of the PPOOLEX DCC-05-4 experiment predicted by the HD 1 model.

It can be seen that injected steam formed bubbles which condensed rapidly. However, the DCC rate was not as high as in the POOLEX cases to provoke as a strong chugging. Highly turbulent trail was generated when the water was pushed towards the bottom of

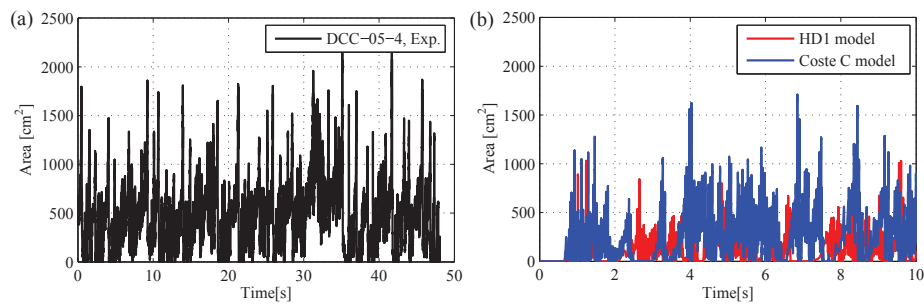
the pool by steam during initial blowdown. As time elapsed, the turbulence kinetic energy was increased further around the blowdown pipe and pool bottom. The turbulence development corresponded well with the early observations of Tanskanen (2012) from the STB-28 simulations, in which the turbulent mixing processes maintained the turbulence level in the pool water sustaining certain DCC rate.

Figure 6.29 shows the DCC rates in the 2D-axisymmetric OpenFOAM simulation of the PPOOLEX DCC-05-4 experiment predicted by the HD 1 model and the Coste C model. Both the models used in the simulations are proportional to the velocity scale relative to the near interface turbulence kinetic energy or dissipation rate. As the Lk- $\epsilon$  model yielded more turbulence kinetic energy than the Sk- $\epsilon$  model, the condensation rates were much higher in both DCC model cases of HD1 and Coste C with the Lk- $\epsilon$  model than in the corresponding OpenFOAM simulations with the Sk- $\epsilon$  model. As a result, bubbles collapsed and chugging occurred. The OpenFOAM results of DCC-05-4 test are compared to and discussed together with the NEPTUNE.CFD results in Publication III.



**Figure 6.29.** Results of condensation mass flow rate predicted by (a) the HD 1 model with the Lk- $\epsilon$  model, (b) the Coste C model with the Lk- $\epsilon$  model, (c) the HD 1 model with the Sk- $\epsilon$  model and (d) the Coste C model with the Sk- $\epsilon$  model in the 2D-axisymmetric OpenFOAM simulations of PPOOLEX DCC-05-4 experiment.

As the instantaneous condensation rate can not be measured reliably in steam blowdown experiments, other information of the characteristic phenomena e.g. size of the bubble and its collapse rate, and chugging frequency could be extracted from the available video material of the test. This information can be utilized for CFD validation purposes if the corresponding characteristic can be acquired from the CFD field data as well. The interfacial area and the bubble volume in the DCC-05-4 test were extracted by using the pattern recognition method. The volume of the bubbles was calculated by using bubble boundary data and numerical integration. More details about this methodology are presented in Hujala et al. (2014) and in Publication III. Figures 6.30 and 6.31 display the recognized interfacial area and bubble volume in the PPOOLEX DCC-05-4 experiment, respectively.



**Figure 6.30.** The recognized interfacial area in (a) the PPOOLEX DCC-05-4 experiment and (b) in a 2D-axisymmetric OpenFOAM simulation of the PPOOLEX DCC-05-4 experiment predicted by the HD 1 model and the Coste C model.

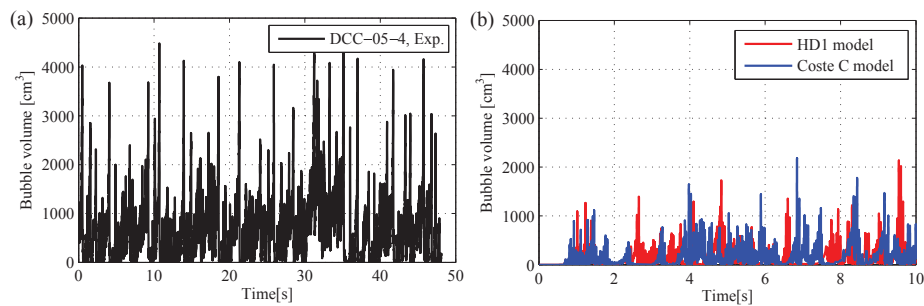


**Figure 6.31.** The recognized bubble volume in (a) the PPOOLEX DCC-05-4 experiment and (b) in a 2D-axisymmetric OpenFOAM simulation of the PPOOLEX DCC-05-4 experiment predicted by the HD 1 model and the Coste C model.

The predicted values of the interfacial area and bubble volume in 2D-axisymmetric OpenFOAM simulations are presented as well. In simulations, the interfacial area and bubble volume data were gathered in the box around and below the blowdown pipe mouth. The

size of the box was big enough to confine the bubbles throughout the simulation. As presented in Figure 6.29, the condensation mass flow rates are high in both models, and as a result persistently high condensation occurs which in turn prevents bubble growth around the blowdown pipe. Therefore, the interfacial area and bubble size remain small compared to the experiment.

FFT was used to estimate the frequency of chugging motion from the recognized bubble volume obtained with pattern recognition and from the CFD data. The FFT works best for purely periodic signals, therefore power spectrum of the volume data with peaks occurring at uneven time intervals tends to give multiple spikes with nearly equal frequencies. Figure 6.32 displays the FFT from the recognized bubble volume in the DCC-05-4 experiment and in the OpenFOAM simulations. It can be seen that the chugging frequencies are around 2 Hz in the PPOOLEX DCC-05-5 experiment. In the simulations with the Lk- $\epsilon$  turbulence model in OpenFOAM, some indications of chugging frequencies from the experiment in the range of 0.5-3.3 Hz were observed, but the most significant 20 Hz oscillation did not correspond to the test at all. On the other hand, in the simulations with the Sk- $\epsilon$  turbulence model, the chugging frequencies of 0.5-2.5 Hz were noticed. However, all the OpenFOAM cases predicted noticeable strong 25 Hz of interface oscillations. A rapid natural interface oscillation of 50 Hz was seen in the test, but not clearly in the OpenFOAM simulations. Generally, the OpenFOAM simulations predicted a higher chugging frequency than the experiments and the NEPTUNE.CFD simulations. This could be anticipated, because the DCC rate is also much higher.

Further, an example of the Coste C model results of PPOOLEX-DCC-05-4 case with NEPTUNE.CFD are presented in Figure 6.33 which shows the DCC rate and bubble size results, and the corresponding power spectrum of bubble size. It can be seen that the bubble volume was always bigger than zero which indicated chugging was missing. Although the condensation rate was occasionally higher than the inlet steam flow rate, that was just the result of the increase in the size of the inflating bubble and not due to the interface ripping induced by rapid condensation. However, the condensation rate was too weak to provoke actual chugging motion. The FFT of the recognized bubble volume shows that the 0.5-3.3 Hz peaks and also the rapid interface oscillation of 50 Hz seen in the experiment are absent.

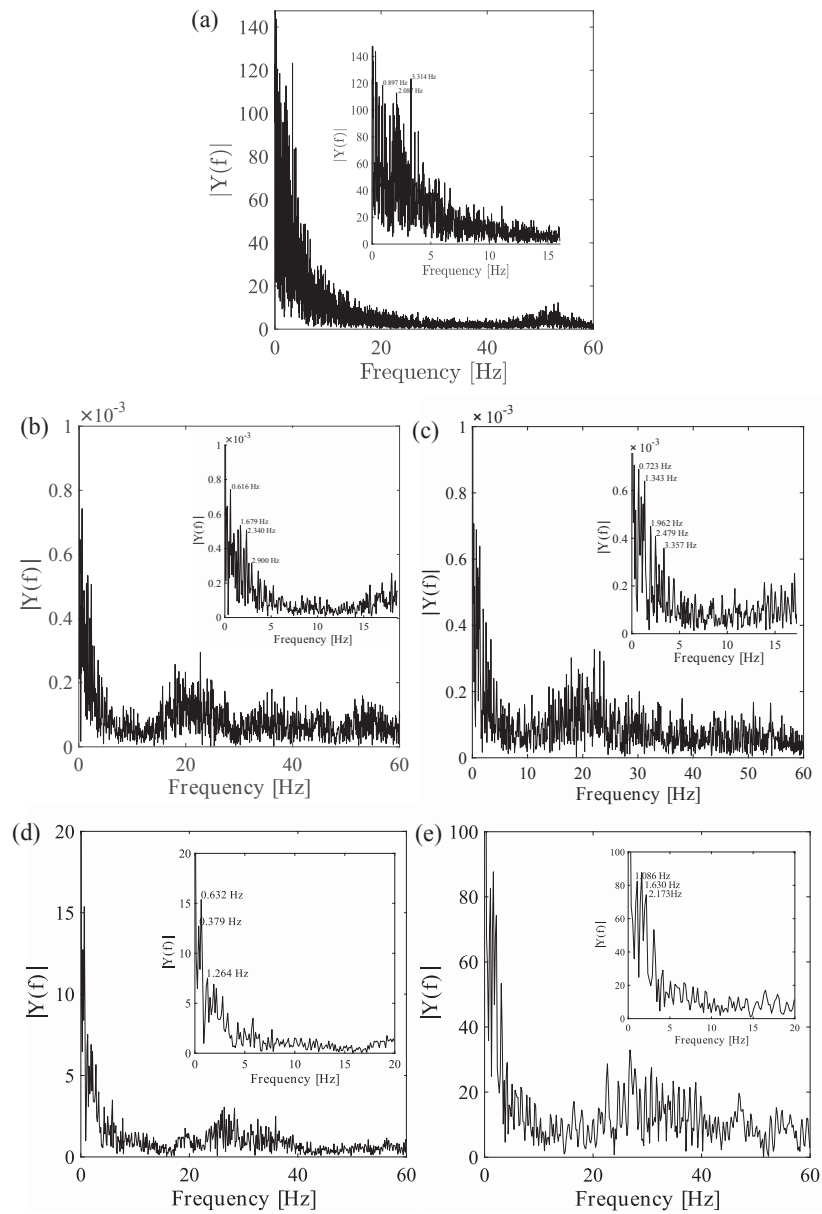


**Figure 6.32.** FFT from the recognized bubble volume in (a) the DCC-05-4 experiment and in a 2D-axisymmetric OpenFOAM simulation of the PPOOLEX DCC-05-4 experiment predicted by (b) the HD 1 model with the Lk- $\epsilon$  model, (c) the Coste C model with the Lk- $\epsilon$  model, (d) the HD 1 model with the Sk- $\epsilon$  model and (e) the Coste C model with the Sk- $\epsilon$  model.

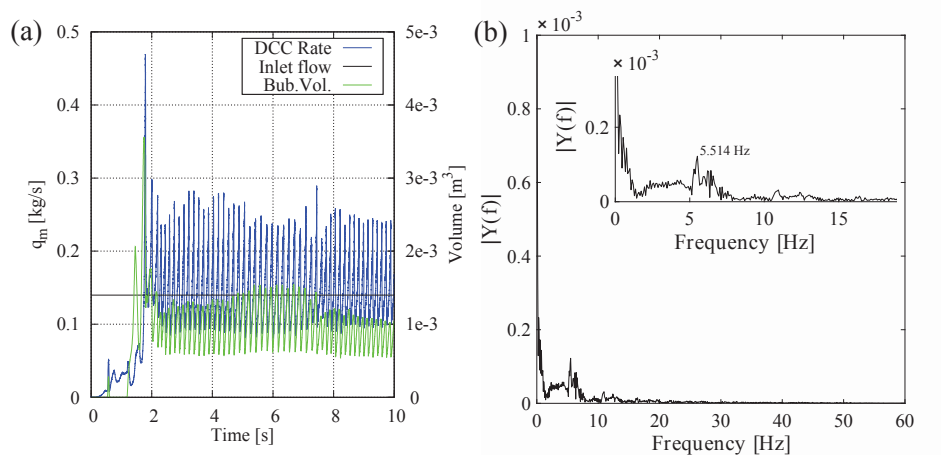


**Figure 6.33.** (a) Condensation mass flow rate and bubble volume, and (b) corresponding FFT from the recognized bubble volume in a 2D-axisymmetric NEPTUNE\_CFD simulation of the PPOOLEX DCC-05-4 experiment predicted by the Coste C model. This simulation refers the CASE1 in Publication III, see Table 3 in Publication III for further details.

After the poor NEPTUNE\_CFD results, the Rayleigh-Taylor instability was included in the same simulated case by using the Pellegrini et al. (2015) model. The results are presented in Figure 6.34. It can be seen that with the Rayleigh-Taylor instability modelling, chugging occurred. The enlarged interfacial area increased the condensation rate in the simulations, which in turn led to interface collapse and consequently the cyclic process continued. The predicted power spectrum of bubble volume is quite close to the experimental result. Both the chugging frequencies of 1-3 Hz and a distinguishable rapid interface oscillation of 50 Hz were noticed in the NEPTUNE\_CFD simulations as in the experiment (Figure 6.32). The 50 Hz was due to the fluctuation/flickering of this size bubble interface at its natural frequency of oscillation before it collapses completely. (Brennen, 2014; Leighton, 1994). The presence of that frequency in the simulations indicate that the interfacial area and condensation rate had been predicted well.

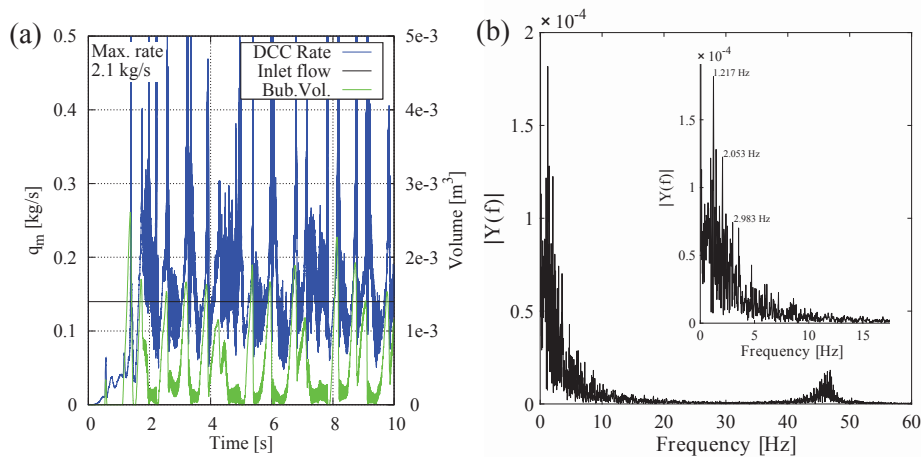


**Figure 6.34.** (a) Condensation mass flow rate and bubble volume, and (b) corresponding FFT from the recognized bubble volume in a 2D-axisymmetric NEPTUNE\_CFD simulation of the PPOOLEX DCC-05-4 experiment predicted by the Coste C model with Rayleigh-Taylor instability. This simulation refers to CASE7 in Publication III, see Table 3 in Publication III for further details.

In rapid DCC simulations, the interface area increase can be significant due to the acceleration by pressure decrease and the chugging motion of the interface. In simulations, interfacial instabilities can be captured increasingly better by increasing the grid resolution to over the critical wave lengths of invoking instabilities, e.g. the Rayleigh-Taylor instability at first, then the Kelvin-Helmholtz instability on the waves generated by the Rayleigh-Taylor one etc.. Therefore, a denser grid resolution of  $1 \times 1$  mm cell size inside the blowdown pipe and around the pipe tip region was used without Rayleigh-Taylor instability modelling in NEPTUNE\_CFD. Figure 6.35 compares the predicted interfacial area with the denser grid resolution ( $1 \times 1$  mm cell size) without Rayleigh-Taylor instability modelling, and with the coarser grid resolution with Rayleigh-Taylor instability

modelling. It can be seen that the increase of grid resolution yielded more the interfacial ripples despite of missing surface tension modelling i.e. without robust interface tracking. Missing surface tension modelling can be seen in the dense grid cases as departing water mist streaks near the interface. However, the increased amount of less smeared interface curvatures dominate more likely in DCC, because  $|\nabla a_i|$  of mist is low. However, in these NEPTUNE\_CFD simulations the large interface drag model of Coste et al. (2008) includes the calculation of tangential shear at the interface.

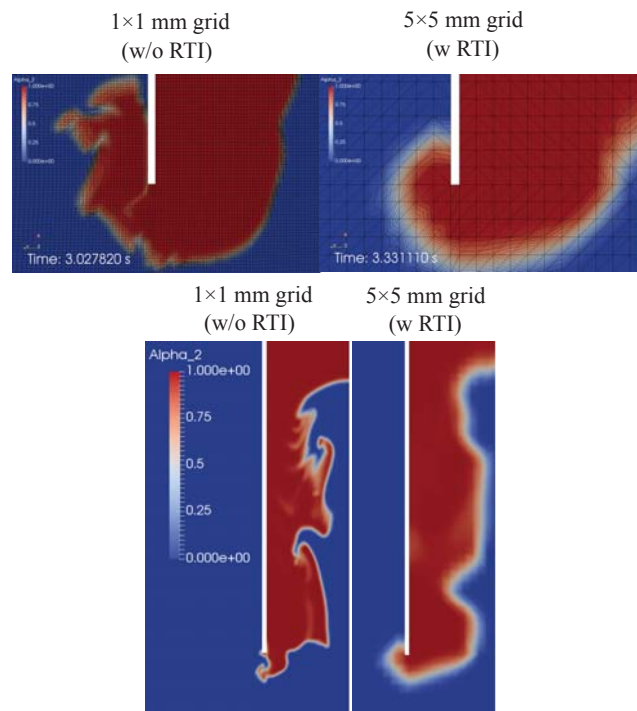


**Figure 6.35.** Instantaneous steam volume fraction near blowdown pipe predicted with the denser grid resolution ( $1 \times 1$  mm) without RTI modelling and with the coarser grid resolution ( $1 \times 1$  mm) with RTI modelling. This simulation refers the CASE6 and CASE7 in Publication III, see Table 3 in Publication III for further details.

Figure 6.36 shows that the denser grid was able to capture the critical wave length of the Rayleigh-Taylor instability calculated from the recognized interface acceleration in the experiment. Further, it predicted accurate results of the chugging frequencies. However, denser grids are not always favourable for the simulations of large-scale engineering applications. Therefore, a Rayleigh-Taylor instability is a good option for large-scale suppression pool simulations.

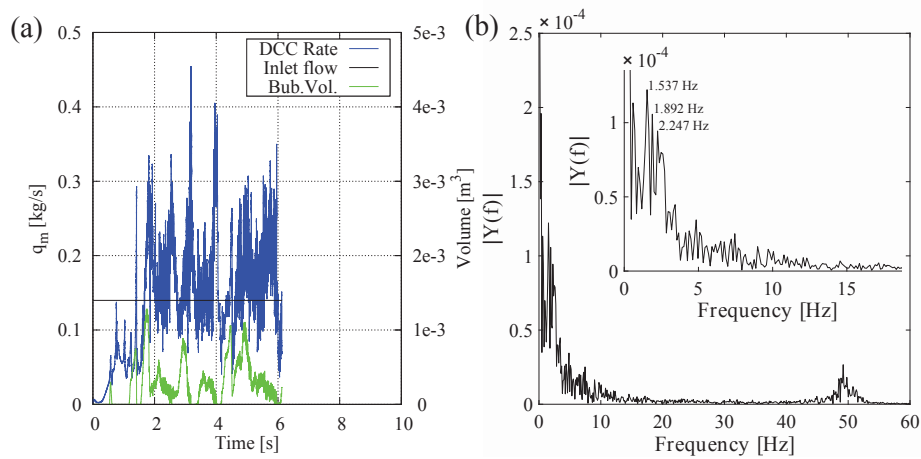


**Figure 6.36.** (a) Condensation mass flow rate and bubble volume, and (b) corresponding FFT from the recognized bubble volume in a 2D-axisymmetric NEPTUNE\_CFD simulation of the PPOOLEX DCC-05-4 experiment predicted by the Coste C model with finer grid resolution. This simulation refers to CASE6 in Publication III, see Table 3 in Publication III for further details.

Further, Publication III discusses other key modelling issues concerning the chugging DCC mode of PPOOLEX DCC-05-4 test e.g. the performance of different condensation models, the effects of turbulence modeling, interfacial momentum transfer, geometry effects and interface initialization.



## 7 CFD simulation results of wet-steam flows

### 7.1 Analysis of turbine blade shape influence on condensing steam flows

The nature of turbomachinery flows and variation in them rely on boundary conditions and local flow fields. A slight modification in the blade design could yield a significant influence on the whole flow field. Particularly, in LP turbine flows, the expansion of steam and condensation phenomena depend on both the flow passage shape and the operating conditions. The condensation process is rather sensitive to the blade shape and thickness. As the shape and the size of the blades influences the pressure fields, it could be expected that the blade shapes should have significant impact on the entire condensation process and corresponding loss mechanism. In this work, the quantification of the influence of local geometrical details including blade trailing edge shapes, modification in blade shape by surface tapering and inclusion of dimple profile at blade surface on the flow expansion and condensation phenomena is studied. The numerical simulations were performed with ANSYS FLUENT, in which the two-phase vapour-liquid mixture was modelled adopting the Eulerian-Eulerian approach. Flow turbulence was modeled by the modified SST  $k-\omega$  (MSST  $k-\omega$ ) turbulence model. The performance of the MSST  $k-\omega$  turbulence model is presented in Publication VI and in Patel et al. (2014). White et al. (1996) measured various parameters of condensing steam flow and extracted a large set of data such as pressure distribution along the blade surface, droplet size, Schlieren photograph, distribution of static pressure, wetness fraction and normalised entropy at the traverse plane located at the flow downstream. For the analysis of blade shape influence on condensing steam flows, the low inlet superheat experimental case L1 of White et al. (1996) was chosen.

Firstly, the influence of grid density on CFD simulations of condensing steam flow was performed. The GCI algorithm was used as well. Figure 7.1 presents the details about grid discretization error. The error was calculated for the static pressure, velocity, and wetness fraction. An averaged value of each selected parameter was taken at the pitchwise traverse position which was at 50 mm downstream of the blade trailing edge. Three grid resolutions i.e. Grid A (40970 cells) over Grid B (76554 cells) to Grid C (103582 cells) were studied. It can be seen that the relative error was smaller for all parameters. The extrapolated relative error was decreased with grid refinements. However, slightly more error was noted for wetness fraction. The GCI value for the successive grid refinements (i.e., Case A to Case B) has been reduced for all three variables. However, very little reduction was observed in all errors for wetness fraction with grid refinements. The GCI values indicate that the grid refinement from Grid B to C yielded a minimal numerical error. Based on these results, an intermediate grid (i.e., Grid B) could be the optimal selection for the rest of the study. Further results are presented in Publication IV.

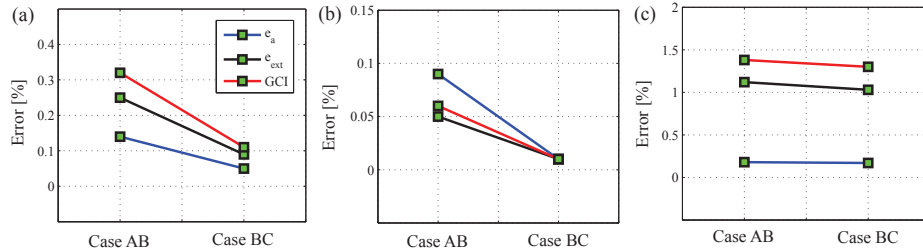


**Figure 7.1.** Estimated relative error (i.e.,  $e_a$ ), extrapolated relative error (i.e.,  $e_{ext}$ ) and GCI values for (a) static pressure, (b) velocity, and (c) wetness fraction for successive grid refinements for L1 case simulations. Here, Case A and Case B indicate the refinements of grids from Grid A to B and Grid B to C, respectively.

### 7.1.1 Effect of blade trailing edge shape

In this work, four different trailing edge shapes were modelled. More details on trailing edge shapes are described in chapter 5.2. Figures 7.2, 7.3 and 7.4 compare the predicted static pressure, expansion rate and Mach number fields with different trailing edge profiles. It can be observed that the pressure distribution on the pressure surface of the blade with the CTE, RTE and STE were quite similar. However, little variation was observed in the predicted pressure gradient on the suction side near the trailing edge. The results of the pressure distribution around the blade surfaces estimated with the CTE, RTE and STE are compared and discussed in Publication V. The trailing edge shape modification influenced the distribution of pressure the most near to the trailing edge and in the flow downstream. Due to suction surface tapering, the static pressure in the CTE profile was affected at the rear part of the suction surface. The expansion rate differs through the blade passage, being quite low at the entrance and exceedingly high in the vicinity of the throat. Typically, in steam turbines, expansion rates are in the order of  $10^3$  to  $10^4 \text{s}^{-1}$ . It may reach up to  $10^6 \text{s}^{-1}$  or more near blade pressure surfaces and within trailing edge expansion fans White and Young (2008). Among all trailing edge shapes, the ETE profile yielded the highest expansion rate (in the order of  $10^5 \text{s}^{-1}$ ) around the trailing edge region. Some variation has been noticed in the Mach number distribution among different trailing edge shapes. In the case of CTE profile, the flow area was enlarged near the rear part of trailing edge likely due to the suction surface tapering. Also, in the ETE case, the flow area was modified slightly due to modification. The Mach number was higher in the cases of CTE and ETE profiles possibly due to the pressure drop.

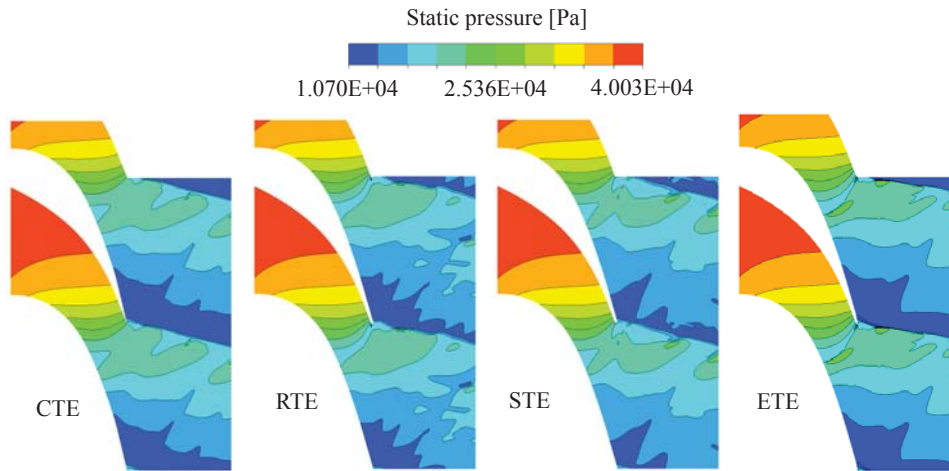


Figure 7.2. Predicted contours of the static pressure with different trailing edge shapes.

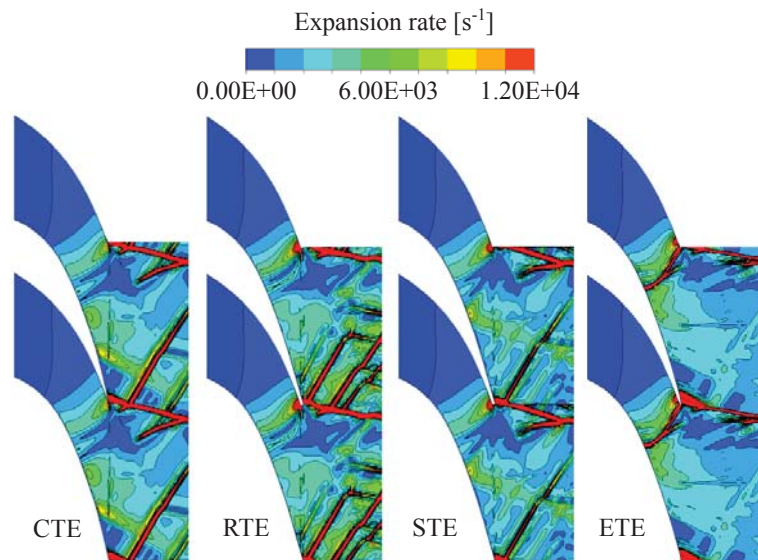
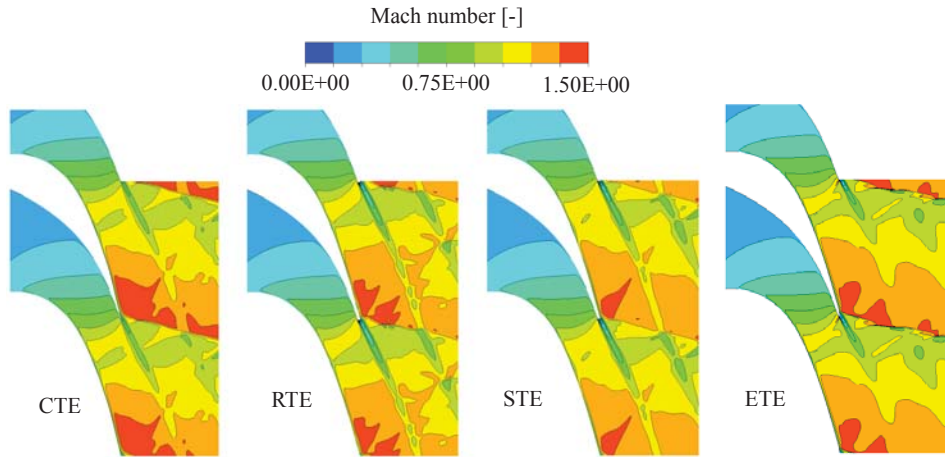
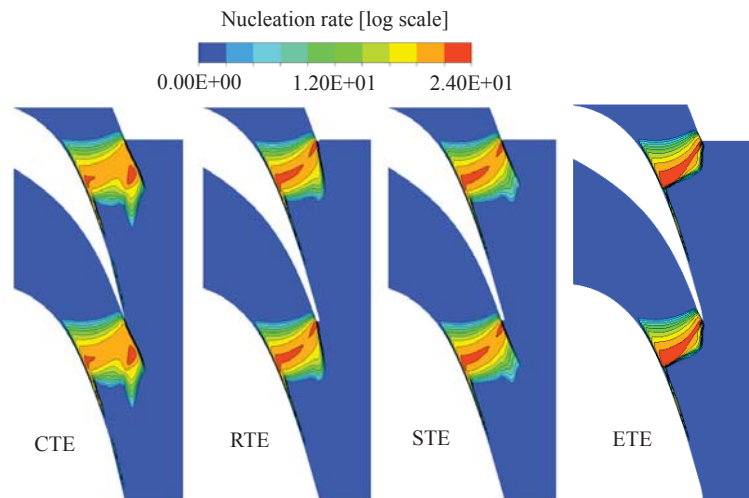


Figure 7.3. Predicted contours of the flow expansion rate with different trailing edge shapes.



**Figure 7.4.** Predicted contours of the Mach number with different trailing edge shapes.

As the process of nucleation and growth rate are dependent on the pressure distribution and expansion rate (White et al., 1996), it could be anticipated that trailing edge shapes could influence on the overall nucleation and droplet growth processes. The predicted contours of the nucleation rate are presented in Figure 7.5.



**Figure 7.5.** Predicted contours of the nucleation rate with different trailing edge shapes.

It can be seen that the nucleation zone was wider in the mid-pitch of the blade passage and the rate of nucleation was reasonably low. The nucleation rate was quite high near the suction surface and at the trailing edge of the pressure surface likely due to the rapid acceleration and consequent high subcooling. In the CTE profile, the nucleation profile

was wider than in the other cases. It was also slightly stretched to the downstream due to expanded flow area after tapering. As the expansion was highest in the ETE case, the subcooling level was maximum and as a result, the nucleation rate was also the highest. However, the nucleation region in the ETE case was narrower than in the others.

The differences in pressure and velocity fields around the blade trailing edge affect the nucleation process and therefore, the droplet number distribution can be influenced. Owing to the rapid deflection of flow at the pressure surface near the trailing edge where the rate of formation of liquid droplet nuclei is maximum, the droplet number in the blade wake is higher than in the mainstream. The distinct nucleation rates determine total number of droplets through distinct droplet growth rates. Figure 7.6 compares the predicted results of droplets per unit volume at traverse plane which was positioned at the position of one fourth axial chord length away from the trailing edge in axial flow direction (Figure 5.9). It can be seen that the ETE shape yielded the maximum number of droplets among the cases likely due to the highest nucleation rate. The smallest number of droplets were observed in the CTE profile.

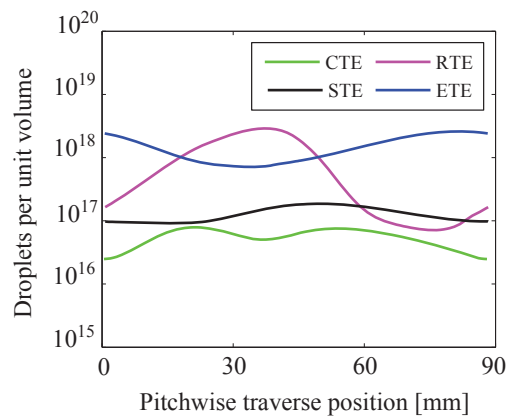


**Figure 7.6.** Predicted results of droplets per unit volume with different trailing edge shapes.

Figure 7.7 shows the contours of droplets average radius predicted by various trailing edge shapes. The distribution of the droplet radius relies mainly on the number of droplets generated. The number of droplets is smaller in the mid-pitch region. Consequently, for all the cases, the droplet size is bigger in the downstream of the mid-pitch region. Further, near the suction surface, nucleation occurs in the region where the expansion rate is high/rapid resulting in an enormous number of tiny droplets. As a result, the droplet size is smaller compared to the mid-pitch region. The blade wakes are warmer due to highly viscous effects after the trailing edge and they cool down due to mixing with the adjacent flow. Thus, the droplet growth was prevented in the wakes. Accordingly, the average droplet radius is lower in the blade wakes for all the cases. The CTE profile yielded the highest droplet radius. On the other hand, the ETE profile predicted the smallest droplet

size because of the large number of droplets per unit volume.

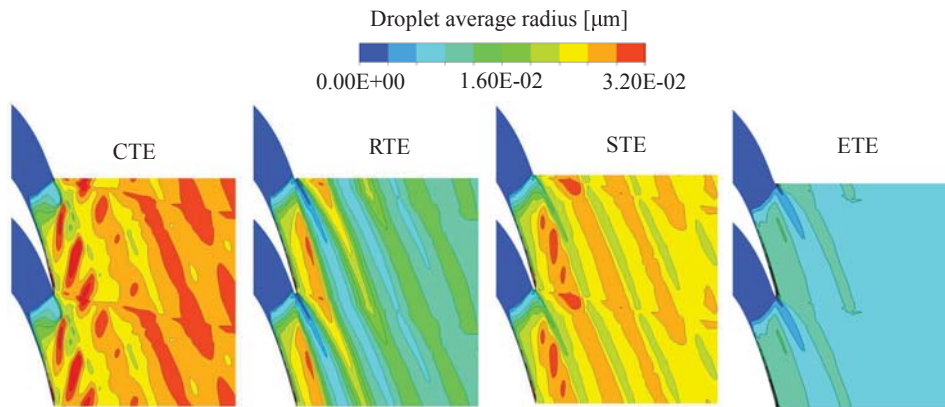


**Figure 7.7.** Predicted contours of droplet average radius with different trailing edge shapes.

It is obvious that the liquid phase generation is sensitive enough to the local rate of change of the pressure in the flow field. Therefore, it could be expected that the wetness fraction prediction would be altered due to distinct trailing edge shapes. Figure 7.8 displays the average wetness fractions yielded by the different trailing edge profiles.

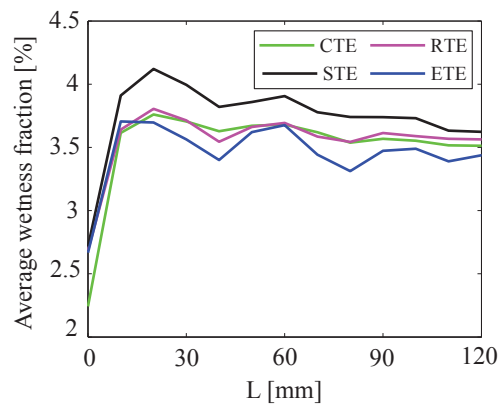


**Figure 7.8.** Predicted results of the average wetness fraction at downstream of the cascade with different trailing edge shapes. L is the distance from the trailing edge of the blade.

The wetness fraction was averaged on traverse planes at various axial locations on downstream of the blade. For all profiles, the wetness fraction was decreased gradually towards the flow downstream. The STE profile predicted a higher wetness fraction than the other cases, while the ETE profile estimated lowest wetness. Further results were compared with the available experimental data of White et al. (1996) and are presented in Publication V.

The losses in turbomachinery are estimated based on entropy rise. The entropy generation in turbomachinery flows results from three main processes: (i) viscous friction either in boundary layers or in free shear layers, (ii) heat transfer across temperature variations, and (iii) non-equilibrium processes in very rapid expansions or in shock waves (Denton, 1993). The rates of local entropy generation are notably high in wake regions of a blade, at the edges of separated regions and in vortices. These are the regions where the shearing rates are considerably high. It would be anticipated that the trailing edge shapes should have some influence on the entropy generation and subsequently on loss mechanism. The predicted contours of entropy generation with different trailing edge shapes are presented in Figure 7.9. The STE shape predicted highest entropy generation likely due to a stronger wake region compared to the other shapes. Also, the RTE profile yielded high entropy generation. Due to the most narrow wake region, the CTE shape predicted the lowest entropy generation, particularly in the blade wake. The ETE profile predicted the lowest entropy production of the examined four trailing edge shapes.

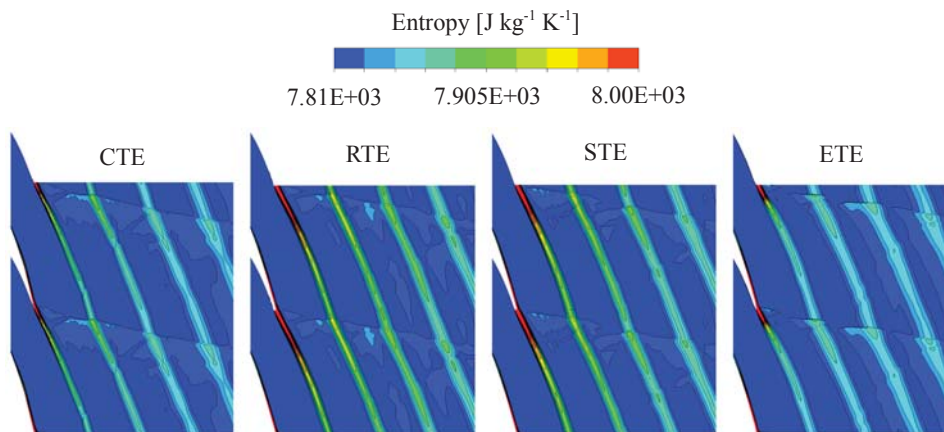


**Figure 7.9.** Predicted contours of entropy generation with different trailing edge shapes.

Further, the loss generation which results due to the irreversible heat and mass transfer during the condensation process in different trailing edge shapes is studied by calculating the Markov energy loss coefficient based on entropy increase. In the work of White et al. (1996), they obtained Markov energy loss coefficient for all test cases. Therefore, it was possible to compare the numerical and the measured loss data. The Markov energy loss

coefficient was calculated based on the following definition:

$$\zeta = \frac{T_2 \cdot \Delta s}{0.5u_2^2}. \quad (7.1)$$

White et al. (1996) divided the Markov energy loss coefficients in three components: (i) shockwave plus wetness loss which was calculated from the mass-averaged values across a section of the traverse plane, excluding the wake regions, (ii) viscous loss which was calculated by subtracting the shockwave and wetness loss from the mass-averaged loss across the entire pitch at the traverse plane and (iii) mixing loss which was calculated by subtracting the total mass-averaged loss at the traverse plane from the fully mixed-out loss. The predicted losses for different trailing edge shapes are compared with the experimental losses by White et al. (1996) in Figure 7.10.

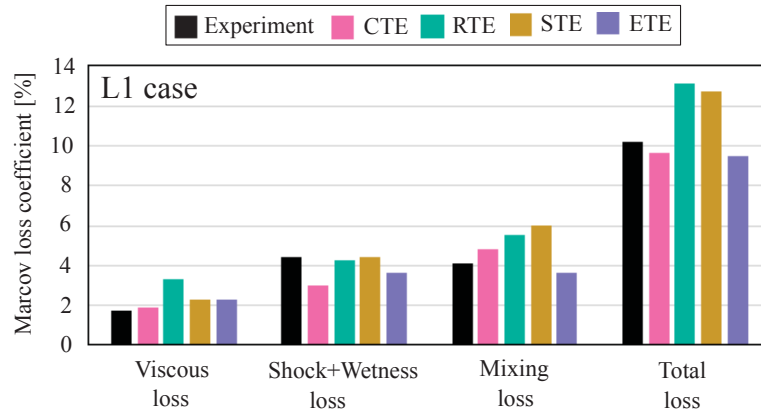


**Figure 7.10.** Predicted Markov loss coefficients with different trailing edge shapes compared with the experiments by White et al. (1996)

The viscous loss measure depends on boundary layers (Boyce, 2012). In the L1 case of White et al. (1996), the pressure side shock merged with the condensation shock and it contributed to the boundary layer on suction side on the adjoining blade. In the case of RTE, the pressure side shock had a higher intensity than other shapes (see density gradients contours in Publication V). Therefore, the RTE shape yielded the highest viscous loss compared to the other shapes. The CTE shape predicted a lesser shock plus wetness loss compared to other cases. The RTE and STE shapes yielded almost identical values of shock plus wetness losses. The combined action of shock and expansion waves, and viscous forces causes a gradual transition from the nonuniform flow condition in the trailing edge plane to the uniform conditions far downstream, which generate mixing loss. The mixing loss depends on the blade wake and external flow conditions. If entropy generation is higher it directly contributes to the mixing loss. The RTE and the STE shapes predicted higher entropy generation than the others (Figure 7.9). Consequently, the mixing losses were higher in those two cases. It can be seen that the ETE shape predicted the smallest

value for mixing loss which is lower than the experimental ones likely due to the lower entropy production. The total loss is the addition of viscous loss, shock plus wetness loss, and mixing loss. The RTE and STE profiles yielded notably higher total loss. Of all the trailing edge shapes, the ETE shape predicted the smallest total loss, which is mainly attributed to low mixing loss. The ETE profile predicted approximately 7% less total loss than to the experiment. Further, the influence of trailing edge shape was studied with the H3 case of White et al. (1996). The H3 case is the high inlet superheat case which had  $\Delta T_{01} = 26.0$  K. Results revealed that even in the high inlet superheat case of LP turbine, blade trailing edge shape influenced on overall loss generation. The results of the loss analysis study of the H3 case are discussed in Publication V.

### 7.1.2 Effect of dimple pattern on blade surface

In this work, two dimple profiles i.e. D100 and D200 were modelled (see Figure 5.8), in order to understand how the expected changes in trailing edge shock pattern and boundary layer interaction affect the condensation phenomena. The steam turbine stator cascade of White et al. (1996) with a semicircular trailing edge was chosen as the base profile. It can be expected based on Sonoda et al. (2006) that the pressure distribution is affected after the dimple inclusion. Figures 7.11, 7.12 and 7.13 show the predicted pressure and Mach number on the blade surfaces, and contours of pressure and Mach number distribution in the flow passage, respectively. Here 'w/o D' notation indicates the base profile case without dimple. It can be seen that the pressure distribution was affected by the dimple inclusion.

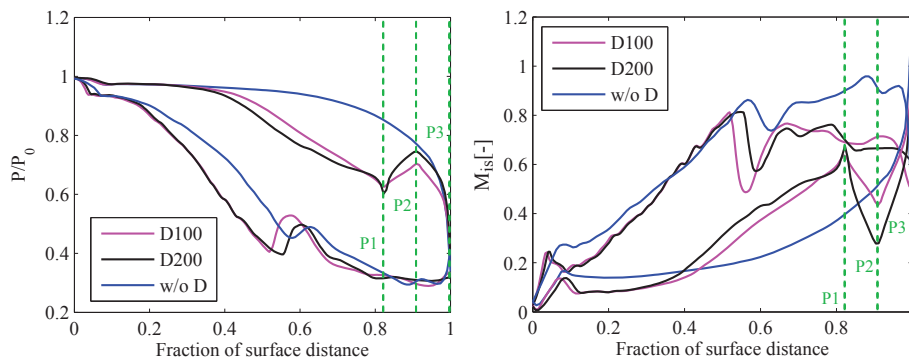


**Figure 7.11.** Blade surface pressure and isentropic Mach number distributions predicted with and without dimple profiles.

At the pressure surface, the pressure drop was interrupted at point P1 which indicates the beginning of the dimple profile (Figure 5.8). The pressure increased from point P1 to point P2 where point P2 indicates the peak location of the dimple. The pressure increment was higher in the D200 case due to a larger dimple and a larger change in the area.

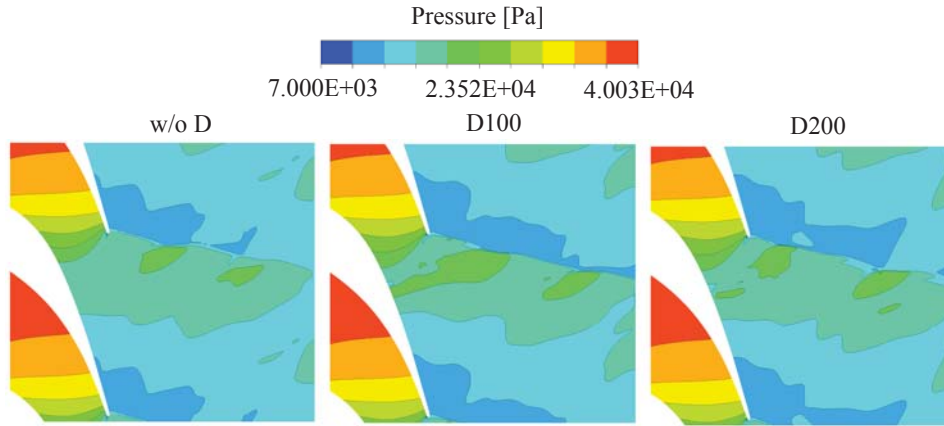


**Figure 7.12.** Predicted contours of static pressure with and without dimple profiles.

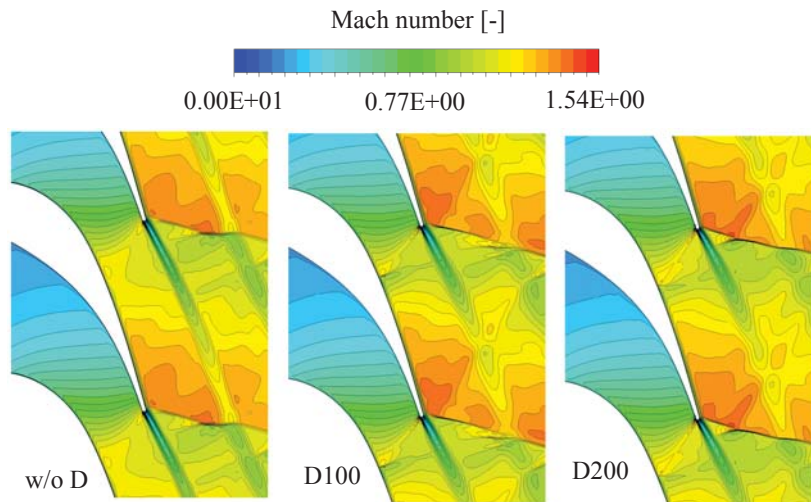
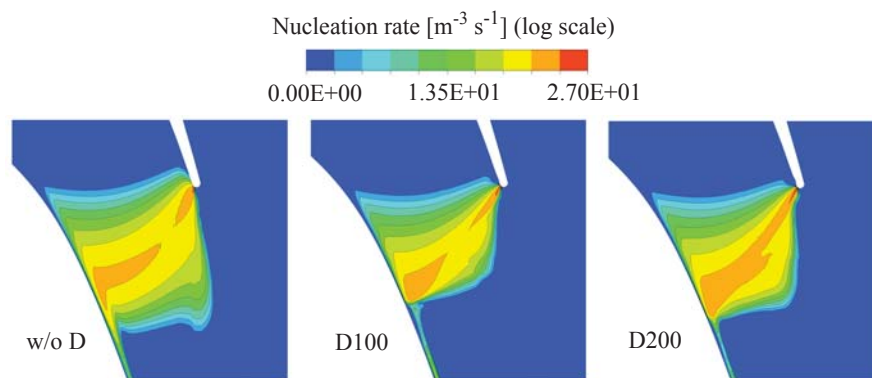


**Figure 7.13.** Predicted contours of the Mach number with and without dimple profiles.

Subsequently, the pressure dropped after point P2. In transonic flows, the flow structure in the trailing edge region of the blade is intricate which includes the expansion waves, flow separation, base flow region and free-shear wake. Near trailing edge, the pressure surface and suction surface flows separate and form free-shear layers. At the separation points, the flow accelerates and the expansion waves generate. After the base region, the pressure surface and suction surface flows meet and turn in a common flow direction. As a result, two shockwaves generate. For both dimple profiles, a strong shock wave was generated from the trailing edge of the blade and it impinged onto the suction side which influenced the boundary layer transition on it. The flow expansion was altered and the Wilson point was changed, and the location of condensation distribution was changed for D100 and

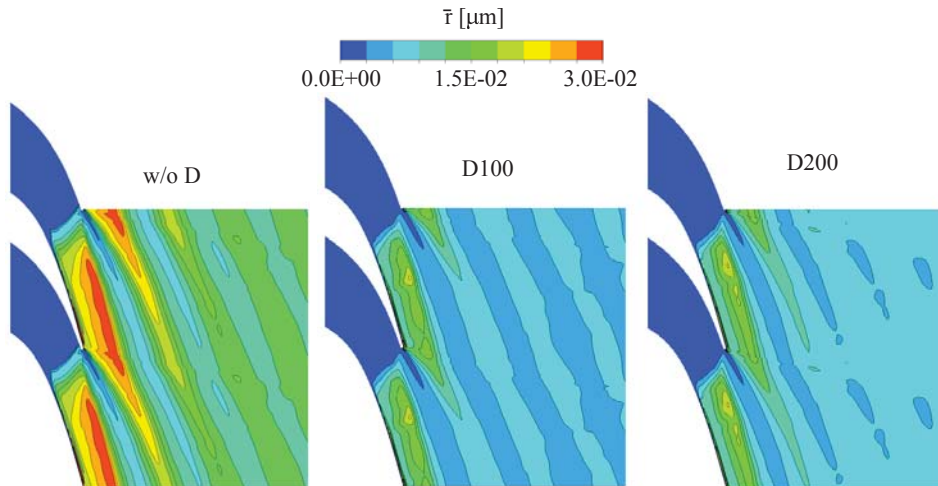
D200. After dimple inclusion, the blade surface pressure ratio was decreased compared to the base profile without a dimple even in the upstream of the throat and the condensation process was forwarded to the flow upstream. However, the addition of a larger dimple, i.e. case D200, caused the condensation process to extend more downstream compared to case D100. Moreover, the intensity of the condensation disturbance was marginally higher in the case D100. It can be seen that the Mach number was decreased in the dimple area for both cases. However, the decrement was maximum for the D200 case at point P2. The highest expansion was resulted in the case of D200 near the trailing edge. As a result, slightly higher Mach number was observed in the case of D200 likely due to the pressure drop.

Figure 7.14 shows the nucleation rate predicted with and without dimple profiles. It can be observed that the nucleation rate was increased with the dimple feature and a narrowed region of nucleation was estimated for the profile with the added dimple than for the base profile. Further, the nucleation region was larger in the D200 case than in the D100 case in mid-pitch. Thus, the droplet growth rate should be delayed in the D200 case.



**Figure 7.14.** Predicted contours of the nucleation rate with and without dimple profiles.

Figure 7.15 and 7.16 compare the droplet average radii and wetness fraction, respectively. It can be seen that the D100 case yielded overall smaller droplet average radius than the D200 case. Apparently, the base profile without dimple predicted the largest droplets. The wetness fraction is higher in the downstream of the blade passage. Flow temperature is raised in the blade wake regions owing to mixing which prevents wetness generation. Slight increment in the wetness fraction was observed in the dimple cases compared to the base profile. However, at the outlet of the domain, all three cases yielded nearly identical wetness distribution.



**Figure 7.15.** Predicted contours of the droplet average radius with and without dimple profiles.

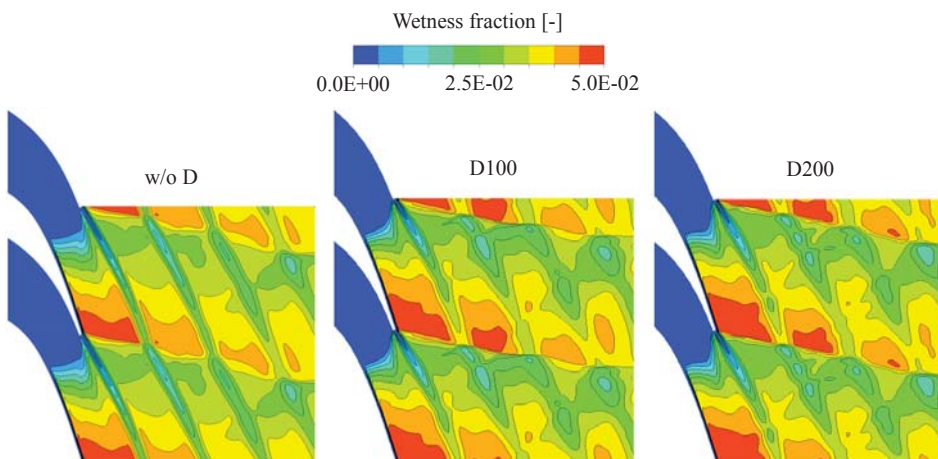


**Figure 7.16.** Predicted contours of the wetness fraction with and without dimple profiles.

The predicted contours of density gradients are displayed in Figure 7.17. Results show that the flow was expanded around the trailing edge. The base profile yielded slightly large separation zone in the region of the trailing edge than the dimple cases and therefore, it had the strongest wake region (Figure 7.13). After the dimple inclusion on the pressure side of the blade, the pressure side shock strength was increased. The maximum strength was observed in the D100 case. In dimple cases, the shock impinged on the suction surface of the succeeding blade and reflected towards the mid-passage. The strength of the reflected shock was visibly higher for the D100 case than the D200. The D200 case yielded a smaller Mach number in the dimple compared to the D100 case. This may also

explain the differences in the strength of the reflection. In all cases, some reflections were spotted from the downstream.

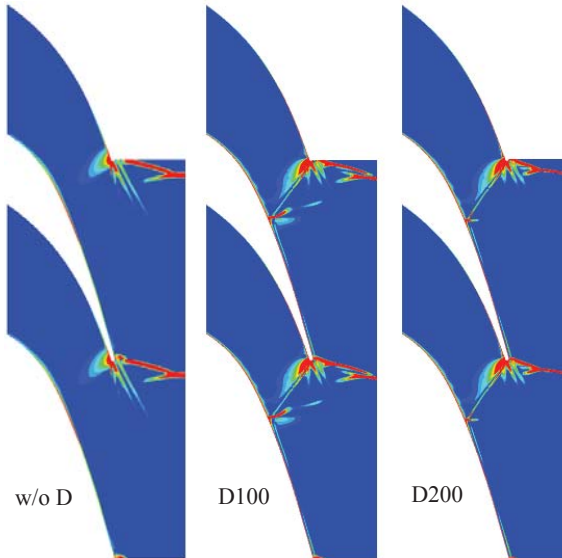


**Figure 7.17.** Predicted contours of the density gradients with and without dimple profiles.

Figure 7.18 shows the contours of entropy generation. The entropy generation was highest in the base profile case likely due to stronger wake region. Entropy generation was observed to be slightly higher in the D200 case than in the D100 case.

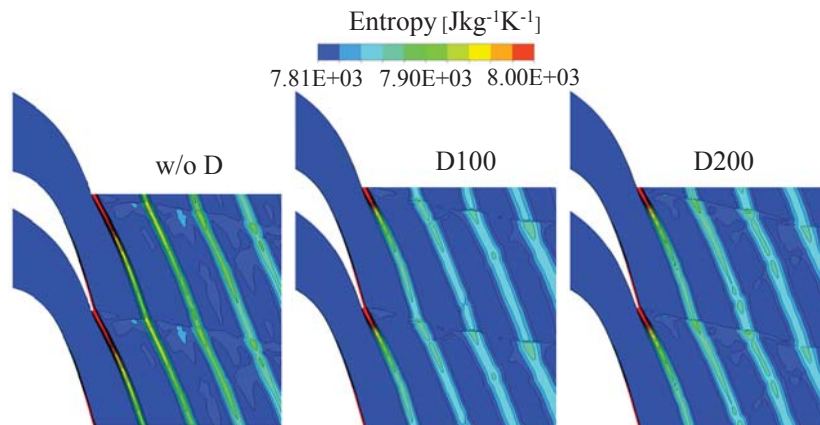


**Figure 7.18.** Predicted contours of the entropy generation with and without dimple profiles.

Further, the Markov loss coefficients were calculated using the same definitions discussed

previously. Figure 7.19 compares the predicted losses for all the cases. After including a dimple, some cutback was observed in the losses. Slight decrement was noted in the viscous loss after dimple addition likely due to lesser separation zone. The D100 case yielded the lowest value of viscous loss. The strength of wake was reduced in the D100 and D200 cases compared to the base profile case (Figure 7.17). Accordingly, the overall value of shock plus wetness loss was lessened for the dimple cases. A slight reduction was observed in the mixing loss for the D100 and D200 cases due to lesser entropy generation compared to the base profile case. The total loss measure was reduced in the dimple profile cases. The D100 case yielded approximately 8% less total loss than the base profile.

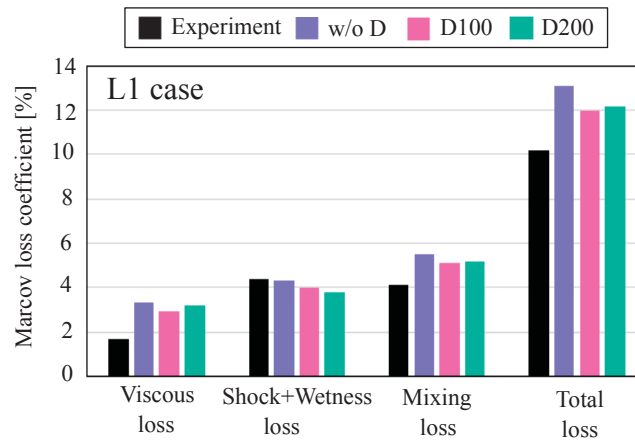


Figure 7.19. Predicted Markov loss coefficients with and without dimple profiles.

### 7.1.3 Effect of blade surface tapering

Further, the influence of the blade surface tapering on condensing flow field and on the corresponding loss generation was studied. For this purpose, both the pressure surface and the suction surface of the blade were modified via tapering. In all the cases, the pressure surface and suction surface of the blade were merged by a semicircular arc. Further details about blade tapering are presented in chapter 5.2.1.

#### 7.1.3.1 Pressure surface tapering

Due to the pressure surface tapering, the throat width of the blade passage was increased slightly. Figure 7.20 compares the contours of nucleation rate, droplet radius and density gradients predicted with and without pressure tapering. After pressure side tapering, the nucleation rate was increased particularly in the mid-pitch of the blade passage. In the case of PS13, the rate of nucleation was slightly higher than in the PS11 case. After

pressure surface tapering, the droplet radius was decreased. However, in the downstream, the overall droplet sizes were slightly larger for the tapered cases. The average droplet radius was lower for the PS13 case than the PS11 case. After the blade tapering, the separation zone was reduced in the region of the trailing edge. As a result, the PS11 and PS13 cases yielded small wake region. Also, the pressure side shock strength was decreased slightly in the PS11 and PS13 cases. Some reflections were resulted on the suction surface after blade tapering.

After pressure side blade tapering, the entropy generation was decreased due to smaller wake region (Figure 7.21). The entropy was marginally higher for the PS13 case than the PS11, both in the wake and in the downstream of the blade. Thus, it could be possible to have some influence on the loss generation.

The Markov loss coefficients were calculated and are presented in Figure 7.22. The viscous loss was smaller for the PS11 case than the base profile without tapering, possibly due to weak pressure side shock. The shock plus wetness loss was reduced with the tapered blade. Due to higher entropy generation, the PS13 case estimated a higher mixing loss than the PS11 case. The overall loss measure was reduced approximately 30% and 8% with the PS11 and PS13 cases compared to the base profile, respectively.

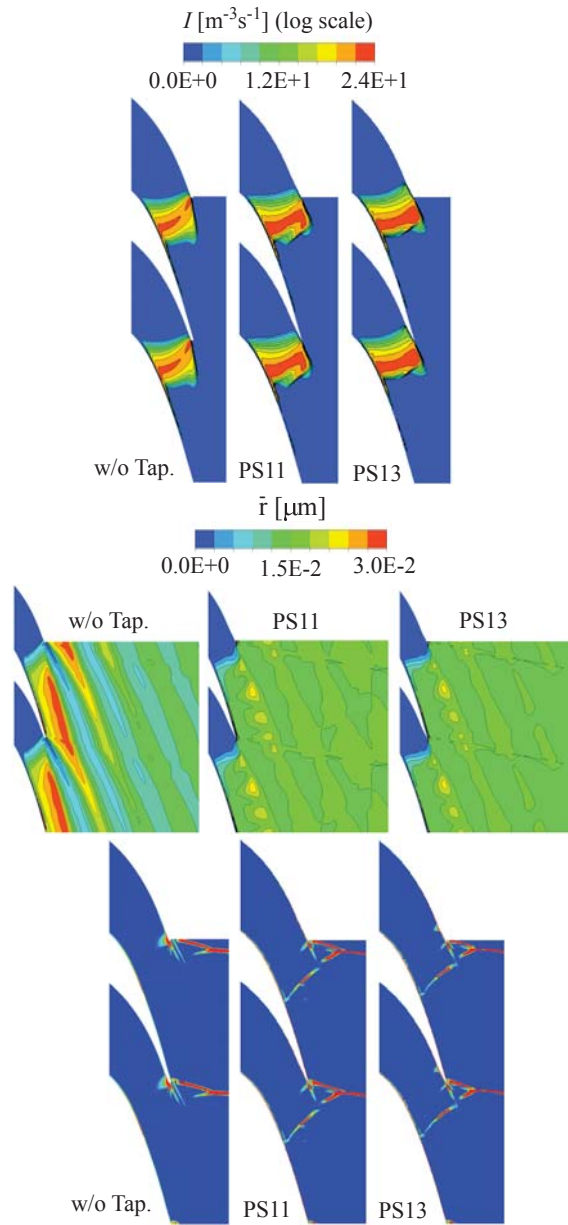


**Figure 7.20.** Predicted contours of the nucleation rate, droplet average radius and density gradients with and without pressure surface tapering.

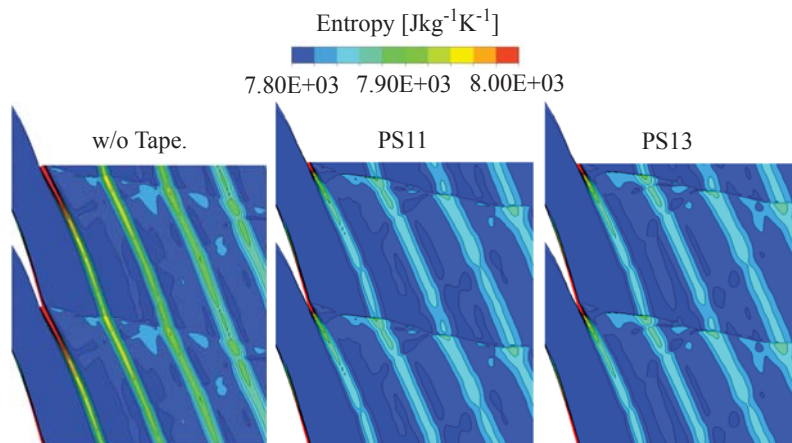


**Figure 7.21.** Predicted contours of the the entropy generation with and without pressure surface tapering.

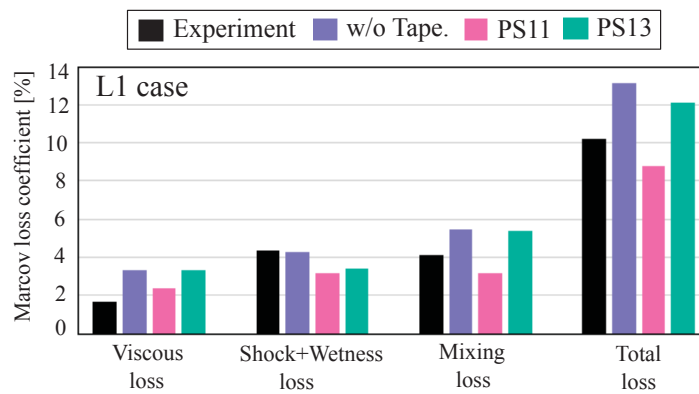


**Figure 7.22.** Predicted Markov loss coefficients with and without pressure surface tapering.

### 7.1.3.2 Suction surface tapering

Further, two cases of suction surface tapering viz. SS5 and SS11 were modelled. The original blade passage throat size and location remained the same after suction side tapering. The predicted contours for suction side tapering are compared with the base profile without tapering in Figure 7.23. It can be observed that the nucleation rate was increased and the nucleation region was extended slightly downstream due to expanded flow area after tapering. Also, the nucleation region became narrower after blade surface tapering. As a result, droplet sizes were affected. The droplet sizes for the SS5 and SS11 were smaller than for the base profile. Also, the droplet sizes were slightly bigger in the suction side tapering cases compared to the pressure side tapering cases. The strength of pressure side shockwave was lesser for the SS5 and SS11 case. Some additional reflections were generated from the suction surface. Also, a shock wave was observed at the position from where the suction surface was tapered.

Further, Figures 7.24 and 7.25 compare the entropy generation contours and calculated loss coefficients for cases with and without suction surface tapering, respectively. The entropy generation was reduced with suction side tapering due to smaller wake. Visibly, the entropy production was higher in the SS11 case than in the SS5 case due to flow deflection and mixing. The viscous loss was decreased in the tapered blade cases compared to the base profile. The shock plus wetness loss was reduced after blade modification. However, the SS11 case predicted a higher value of shock plus wetness loss than the SS5 case. Mixing loss was decreased in the SS5 and SS11 cases likely due to a lower entropy generation. The SS5 and SS11 cases predicted approximately 30% and 24% less overall loss generation compared to the base profile case without tapering, respectively.

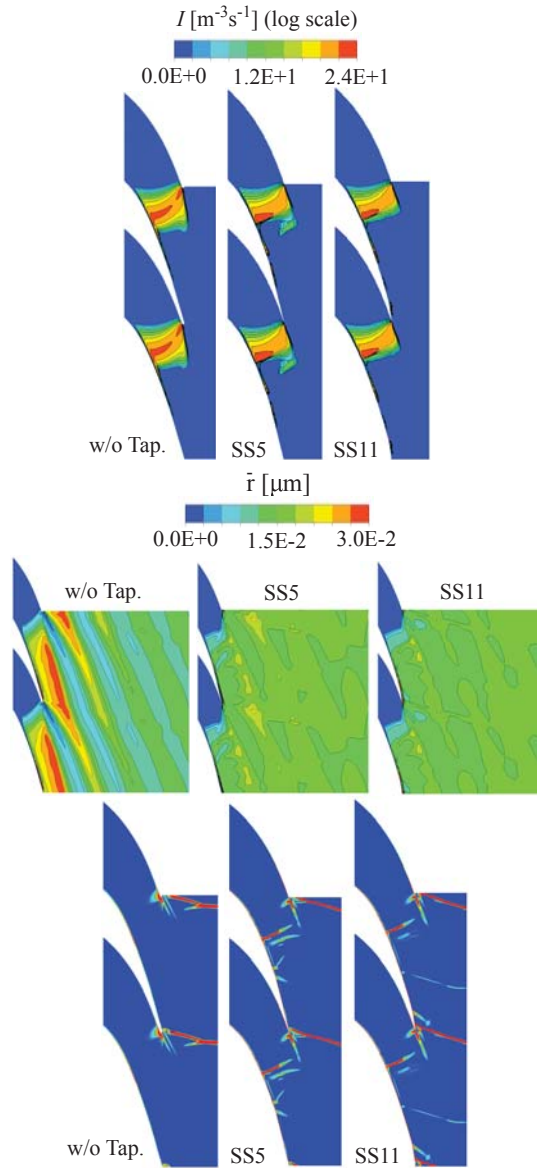


**Figure 7.23.** Predicted contours of the nucleation rate, droplet average radius and density gradients with and without suction surface tapering.

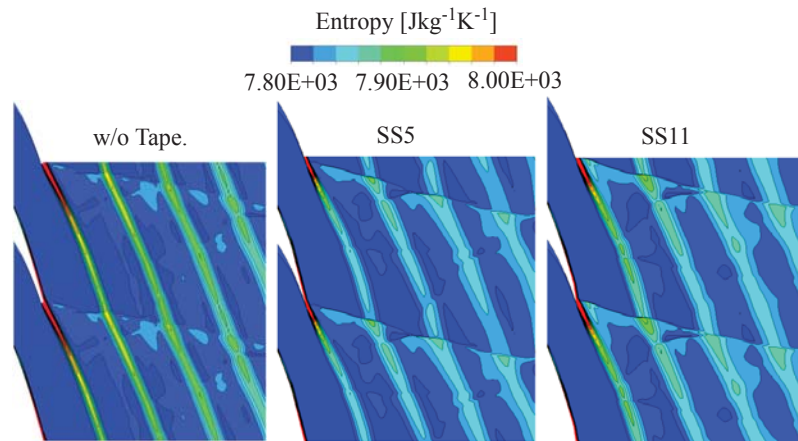


**Figure 7.24.** Predicted contours of the the entropy generation with and without suction surface tapering.

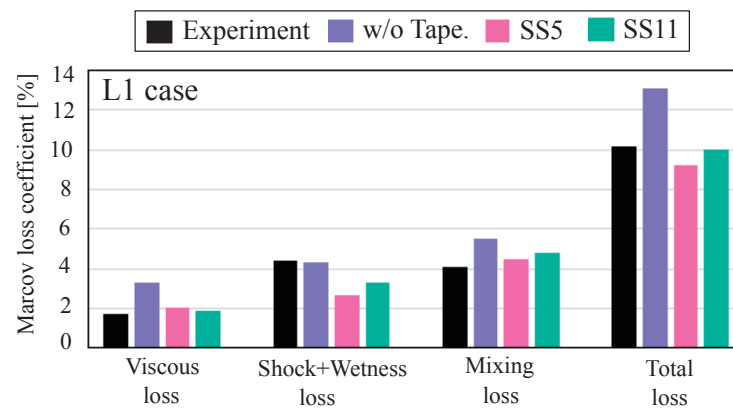


**Figure 7.25.** Predicted Markov loss coefficients with and without suction surface tapering.

## 7.2 Analysis of turbulence modelling influence on condensing steam flows

The correctness of transport phenomena prediction relies strongly on an accurate turbulence estimation. In the case of condensing steam flows in LP turbine, precise modelling of turbulence is important, because turbulence plays a major role in the possible deposition of fine/coarser liquid droplets on the blade surfaces, in flow boundary layers and in shockwave regions.

The flow turbulence intensity is a significant property which affects the entire flow field as well flow transition. Therefore, the impact of freestream inlet turbulence intensity on the condensation was studied in this work. The influence of inlet turbulence level on the condensing steam flow was studied with the nozzle of Barschdorff (1971). The boundary conditions of this case were discussed in chapter 5. For this study, four inlet turbulence levels namely  $\chi = 0.02, 0.05, 0.1, \text{ and } 0.2$  were used. For this purpose, the standard  $k-\varepsilon$  (Sk- $\varepsilon$ ) turbulence model was applied. All the simulations were performed with an adequately fine grid to acquire a grid independent results.

Figure 7.26 shows the predicted results of pressure ratio, droplet number and mean droplet radius at various inlet turbulence levels. These data were extracted at the nozzle center-line where 0 axial distance denotes the throat of the nozzle. The turbulence intensity is proportional to the turbulent kinetic energy and dissipation rate. Therefore, it is apparent that a greater value of turbulence intensity enlarges viscous dissipation in the flow field and, as a result, the flow expansion could have some influence. The mild level of inlet turbulence increased the flow expansion (Figure 7.26(a)). The nucleation rate was enlarged moderately to the downstream with the increased level of turbulence because of lesser expansion. Therefore, the wetness fraction was reduced in the case of highest turbulence level. The corresponding results of subcooling, nucleation rate and wetness fraction are presented in Publication IV. Figures 7.26(b) and (c) indicate that the droplet number was decreased, while the droplet radius was increased as the inlet freestream turbulence intensity level was increased. The droplets grow by delivering latent heat to the steam, and as a consequence, the steam pressure and temperature suddenly increase which is known as condensation disturbance. It is expected that if the droplet number is larger, the droplets release considerably more latent heat. Thus, the predicted condensation disturbance is the highest in the case of  $\chi = 0.02$ .

Further, the influence of turbulence modelling was studied by modifying the Sk- $\varepsilon$  turbulence model. Additional source terms were added to the Sk- $\varepsilon$  turbulence model. Further, the turbulent viscosity formulation was modified. The results of model modifications influence on turbulence variables, turbulent viscosity and Reynolds stress are discussed in Publication IV.

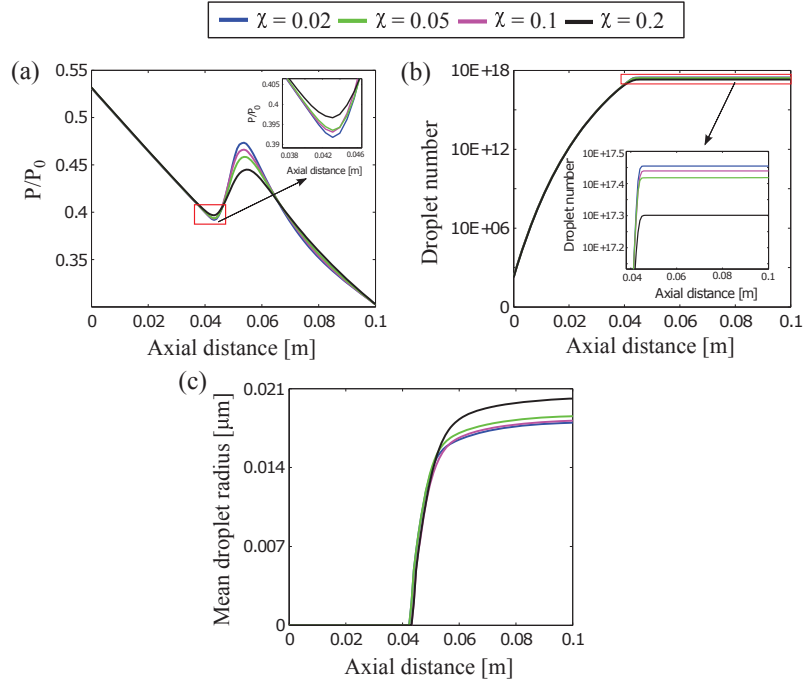


**Figure 7.26.** (a) Pressure ratio, (b) droplet number and (c) mean droplet radius along the nozzle centreline.

The performance of modified Sk- $\varepsilon$  (MSk- $\varepsilon$ ) turbulence model was assessed with the inviscid calculation and the Sk- $\varepsilon$  turbulence model and results are presented in Figure 7.27. Based on the available measured data of pressure at nozzle centreline of Barschdorff (1971), the MSk- $\varepsilon$  model predicted correct pressure distribution including condensation disturbance location and intensity. The Sk- $\varepsilon$  model failed to predict the exact location of condensation disturbance. However, the inviscid calculation predicted stronger condensation disturbance than the other cases and this increment in the pressure rise was prompted because of the excessive latent heat released via liquid droplets. In the case of MSk- $\varepsilon$  model, the increased viscous dissipation affected the flow temperature through energy source, which influenced the heat transfer rates and therefore, the condensation process was extended to the downstream of the nozzle (Figure 7.27 (b)). Further, the inviscid calculation and the MSk- $\varepsilon$  model predicted a higher number of droplets than the Sk- $\varepsilon$  model (Figure 7.27 (c)). This was due to a higher nucleation rate. As shown in Figure 7.27 (d), the Sk- $\varepsilon$  model yielded maximum droplet radius compared to the others due to a greater growth rate. The wetness generation location in the MSk- $\varepsilon$  model case was marginally altered to the downstream of the nozzle and a slight reduction in wetness fraction was noted. The results are presented in Publication IV.

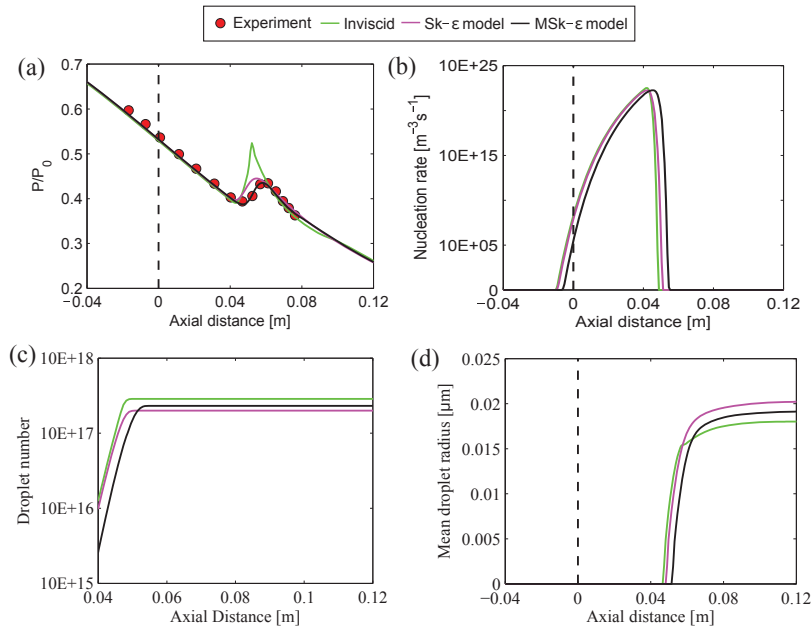


**Figure 7.27.** (a) Pressure ratio, (b) nucleation rate, (c) droplet number, and (d) droplet average radius along the nozzle centreline. The black dashed vertical line at the axial distance of  $x = 0$  indicates the nozzle throat.

Further, the MSk- $\varepsilon$  model was applied to the simulations of the steam turbine stator cascade by White et al. (1996) and its performance was analyzed with the inviscid calculation and Sk- $\varepsilon$  model. In this work, numerical results are analyzed both qualitatively and quantitatively together with the experimental data by White et al. (1996). Three low inlet superheat test cases namely L1, L2 and L3, one high inlet superheat case i.e. H3, and one wet inlet case i.e. W1, were simulated in this work. Figure 7.28 shows the comparison between the predicted pressure distribution along the stator blade surfaces and the measured data for the L1 and H3 cases.

The results show that both the turbulence models and an inviscid calculation yielded good trends of pressure side pressure distribution, while some differences were noted for the suction side pressure distribution for the L1 case. The Sk- $\varepsilon$  model failed to predict condensation disturbance. The Sk- $\varepsilon$  model calculated lesser subcooling level than the modified turbulence model and therefore, it predicted a smaller droplet number which reduced the amount of latent heat released to the steam. The MSk- $\varepsilon$  model predicted both the location and the intensity of the condensation disturbance accurately. The inviscid calculation was able to predict the condensation disturbance, however, the position was shifted to the flow upstream. In the H3 case, due to a higher level of superheat, condensation

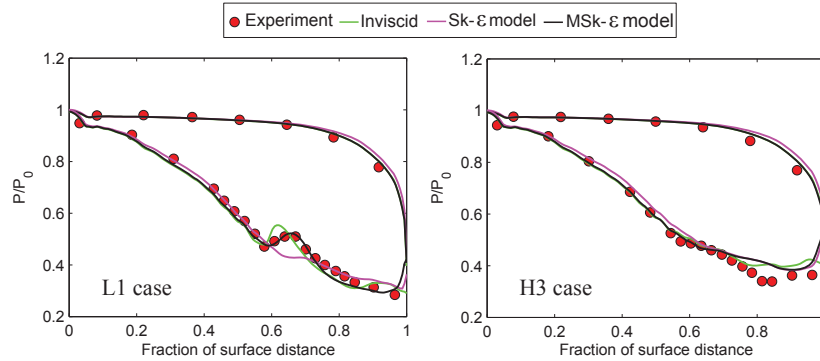


**Figure 7.28.** Blade surface pressure distribution for the L1 and H3 cases of White et al. (1996).

was absent. Thus, the condensation disturbance did not appear on the surface pressure distributions. However, the pressure rise near to the trailing edge in the experimental data resulted because of the reflections from the upper tailboard during the test by White et al. (1996). A relatively good correspondence was observed between the CFD results and the test results. The details of other test cases and corresponding results of the pressure distribution are discussed in Publication IV.

Figure 7.29 shows the comparison between the predicted results and the measured data of the mean droplet size, static pressure distribution, wetness fraction, and normalized entropy for the L1 case. These data were extracted at the traverse plane at the flow downstream (see Figure 5.7). The droplet radius distribution shows that the droplets are bigger specially in the downstream of mid-pitch region because of lower expansion rate (Figure 7.29 (a)). The nucleation appears near the suction surface which generates a large number of fine liquid droplets. Hence, in the regions from 35 mm to 45 mm and from 115 mm to 125 mm, the droplet size is smaller than in the mid-pitch region. The Sk- $\epsilon$  model predicted a larger droplet radius than the others, whereas the MSk- $\epsilon$  model yielded marginally smaller droplets because of a higher number of droplets. Both the turbulence models and the inviscid calculation predicted quite similar pressure profiles at the traverse plane. In the wakes, the temperature is higher due to mixing. As a result, the wetness fraction is smaller in these regions where wakes flow passes the traverse plane. Further, the tests of White et al. (1996) were carried out with three flow passages. Therefore, it is rather difficult to attain an exact periodicity in the flow downstream by modelling one/two flow passages. Nevertheless, the numerical simulations were performed by employing periodic boundary conditions. Therefore, some variations were noted in the results of the second passage. Overall, the MSk- $\epsilon$  model predicted better results of wetness fraction than the others. Further, the Sk- $\epsilon$  model predicted good trends of the non-dimensional entropy distribution except in regions where the wake flow crosses the traverse plane (Figure 7.29 (d)). On the other side, the MSk- $\epsilon$  model estimated maximum entropy compared to the others, specially in the wake region of the blade, likely due to the higher turbulent dissipation in that region, which raised the entropy generation.

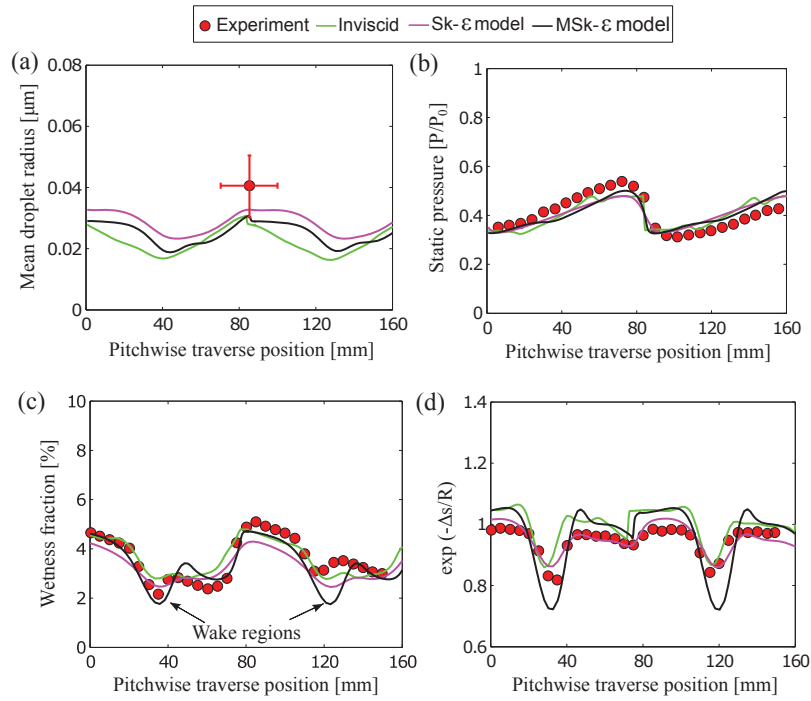


**Figure 7.29.** (a) Mean droplet radius, (b) static pressure, (c) wetness fraction, and (d) non-dimensional entropy for the L1 case of White et al. (1996).

Further, the simulated density gradients are compared with the experimental Schlieren photograph of L1 case by White et al. (1996) in Figure 7.30. It can be seen that the Sk- $\epsilon$  model failed to predict the  $S_c$  shock. Also, due to the lack of viscous effect, the inviscid calculation estimated a thinner  $S_s$  shock than the others. In the case of MSK- $\epsilon$  model, the higher viscous dissipation enhanced the entropy generation at the blade trailing edge and it thickened the profile of  $S_s$  shock. Overall, the MSK- $\epsilon$  model produced good results for the shockwave patterns.

As discussed before, the rates of entropy generation are considerable in blade wakes, at separated regions and in vortices. However, due to strong mixing in these regions, the flow turbulence is high. Therefore, it is apparent that precise information on loss generation requires accurate turbulence modelling. Publication IV shows the results concerning the influence of turbulence modelling on entropy generation prediction. The assessment of turbulence modelling was conducted by comparing the predicted and measured losses. For this purpose, the Markov loss coefficients were calculated using the same definitions discussed previously for all simulated cases of stator cascade. All loss components were calculated for L1 and H3 cases and the results are presented in Figure 7.31

As shown in previous results, the  $S_p$  shock merges with the  $S_c$  shock which thicken the

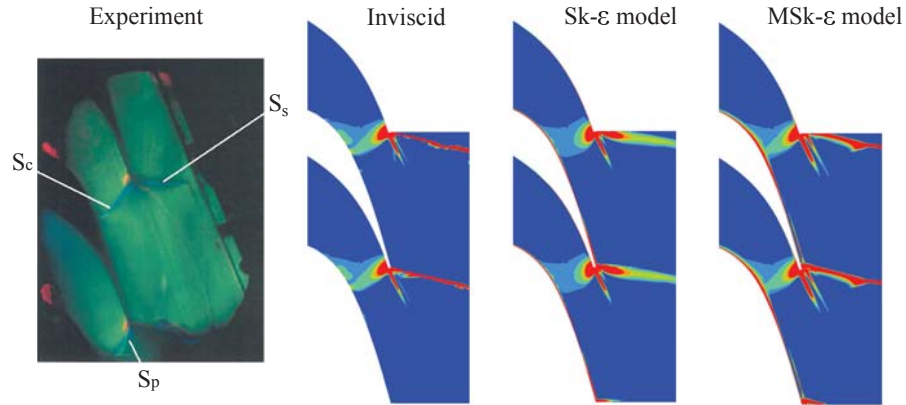


**Figure 7.30.** The predicted density gradients of the inviscid, the Sk- $\epsilon$  model, and the MSk- $\epsilon$  model compared with a reproduced picture of the experimental Schlieren photograph of L1 case in White et al. (1996). Here,  $S_c$  is condensation shock,  $S_p$  is pressure side shock, and  $S_s$  is suction side shock.

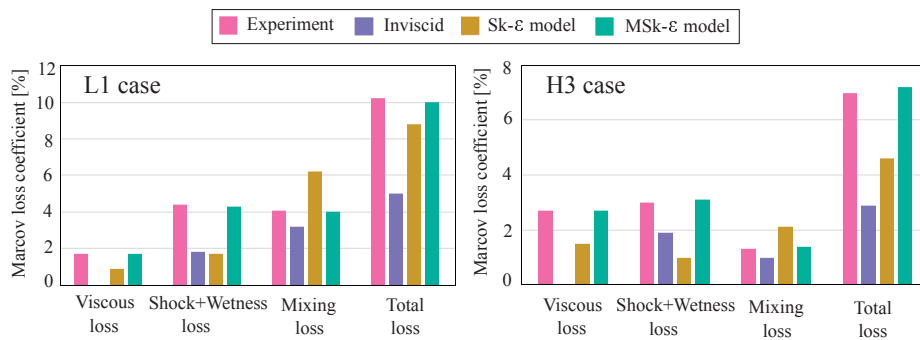


**Figure 7.31.** Predicted Markov loss coefficients compared with the experiments by White et al. (1996). Here, the total loss is the sum of viscous loss, shock plus wetness loss, and mixing loss.

suction side boundary layer onto the suction side of the adjacent blade and as a result the viscous loss increases. In the case of the Sk- $\epsilon$  model, the strength of the  $S_p$  shock was comparatively weaker for the L1 and H3 cases. Thus, the Sk- $\epsilon$  model predicted a lower value of viscous loss for both cases. For the MSk- $\epsilon$  model, the intensity of the  $S_p$  shock was good and increased viscous dissipation improved the entropy generation and, as a result, it predicted a higher viscous loss than the Sk- $\epsilon$  model. The MSk- $\epsilon$  model's prediction for the shock plus wetness loss was in better agreement with the experimental values for L1 and H3 cases than the others. As due to lack of boundary layer effect in inviscid simulation, the measure of mixing loss yielded by inviscid calculation are lesser for both cases. In contrast, the Sk- $\epsilon$  model overpredicted (more than 50%) the mixing loss due to a higher value of the turbulent viscosity which induced the higher entropy generation in the mid-passage at downstream (see corresponding results in Publication

IV). The MSk- $\varepsilon$  model predicted accurate values of mixing loss for both cases. Overall, both the inviscid simulation and the Sk- $\varepsilon$  model underpredicted total loss, while the MSk- $\varepsilon$  model yielded precise loss information for both cases.

In LP turbine, because of the stator and rotor blade rows' alternation, the flow field is highly turbulent. The wake of the preceding blade rows enter to the succeeding rotor blades where the flow accelerates and rotates. In such a situation, correct turbulence modelling is required to gain accurate flow information. In this work, the influence of turbulence modelling was studied with 3D LP turbine stage. For non-equilibrium LP turbine flow analysis, ANSYS CFX has been used by many researchers e.g. Gerber and Mousavi (2007), Grübel et al. (2014). Moreover, based on the personal user experiences, it was observed that ANSYS CFX was the most suitable option for 3D LP turbine stator-rotor stage simulations due to good convergence, relative speed and robustness. Therefore, all the 3D stator-rotor stage calculations were conducted with ANSYS CFX. However, the analysis of turbulence modelling influence in this work was limited to the steady state flow conditions. For this study, the MSST k- $\omega$  model was used. The model was implemented in the ANSYS CFX solver by using user defined subroutines. However, there was no measured data available for the utilized 3D stage as it did not corresponded to a real turbine geometry. Therefore, the achieved results of the MSST k- $\omega$  model were analyzed together with the SST k- $\omega$  model only. Firstly, an appraisal of both turbulence models was performed in ANSYS CFX with the CD nozzles of Moore et al. (1973) and Moses and Stein (1978), and the steam turbine stator cascade of White et al. (1996). The achieved results are described in Publication VI.

Figure 7.32 presents the contours of the turbulent kinetic energy at 10% span and 90% span of the stage. It is obvious that turbulent kinetic energy is higher in the wake region of the blades due to strong mixing. Also, due to rotor blade curvature, the flow deflection was notable at the leading edge of the pressure side of the rotor blade. At 90% span, a separation bubble was formed which enhanced flow mixing and thus, the turbulent kinetic energy was higher in the mid passage of the rotor. The formation of separation bubble is presented in the streamline contours in Publication VI. Due to enlarged viscous dissipation, the MSST k- $\omega$  model predicted lesser turbulent kinetic energy than the SST k- $\omega$  model in the rotor downstream.

The contours of the flow expansion rate for the SST k- $\omega$  model and the MSST k- $\omega$  model are compared in Figure 7.33. In the case of MSST k- $\omega$  model, the increased viscous dissipation reduces the Reynolds stresses. Thus, the shear effect is decreased, which influences the flow parameters. It is apparent that the MSST k- $\omega$  model predicted a higher flow expansion rate.

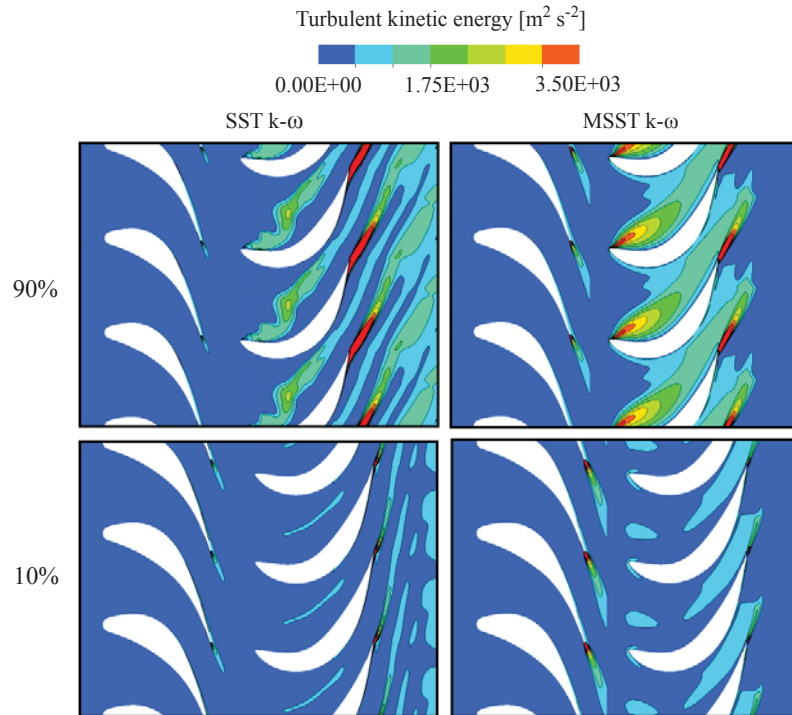


**Figure 7.32.** Predicted contours of the turbulence kinetic energy with the SST  $k-\omega$  and the MSST  $k-\omega$  turbulence models at 10% and 90% spanwise planes.

The nucleation and growth processes are quite dependent on the expansion rate. Figure 7.34 compares the nucleation rate contours for both the turbulence models. The strength of nucleation is decreased from the hub to the shroud surfaces of the stator. At 90% span, the nucleation region was dispersed uniformly at rotor inlet. The modified model predicted a wider nucleation region than the SST  $k-\omega$  model and the nucleation region was also moved marginally downstream. Moreover, secondary nucleation was observed in the rotor passage. This occurred because the subcooling level was too weak to gain thermal equilibrium. The MSST  $k-\omega$  model yielded a larger secondary nucleation zone than the SST  $k-\omega$  model. More results are discussed in Publication VI.

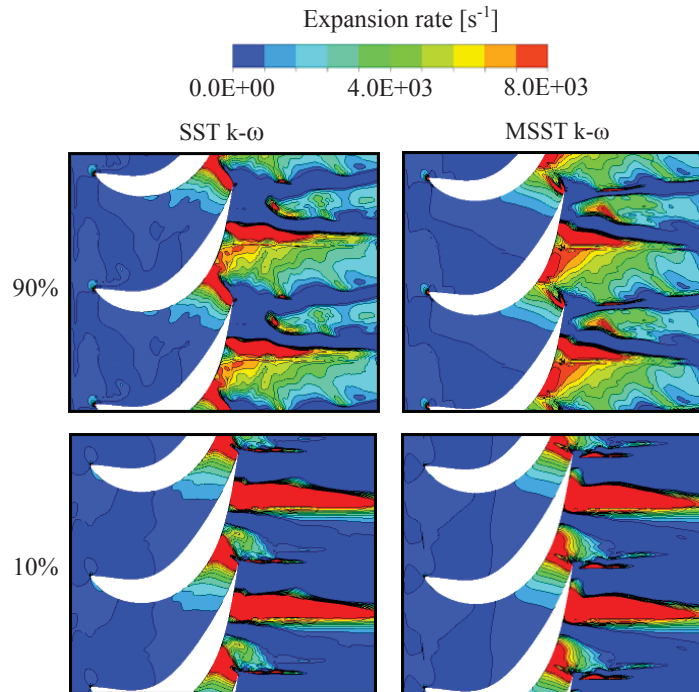


**Figure 7.33.** Predicted contours of the flow expansion rate of rotor with the SST  $k-\omega$  and the MSST  $k-\omega$  turbulence models at 10% and 90% spanwise planes.

The predicted droplet number at normalized pitchwise distance are compared for both the models in Figure 7.35. Due to the higher nucleation rate, the number of droplets at 10% span is larger than at 50% and at 90% span at the stator exit. It is apparent that a relatively large number of droplets were present at the outlet. The growth rate is delayed in the case of MSST  $k-\omega$  model due to larger nucleation region. As a result, the MSST  $k-\omega$  model yielded a lower number of droplets than the SST  $k-\omega$  model. Therefore, the MSST  $k-\omega$  model yielded larger droplet average radius than the SST  $k-\omega$  model. Further, the MSST  $k-\omega$  model predicted lesser wetness fraction than the SST  $k-\omega$  model. The results of average droplet radius and wetness fraction are presented and discussed in detail in Publication VI.

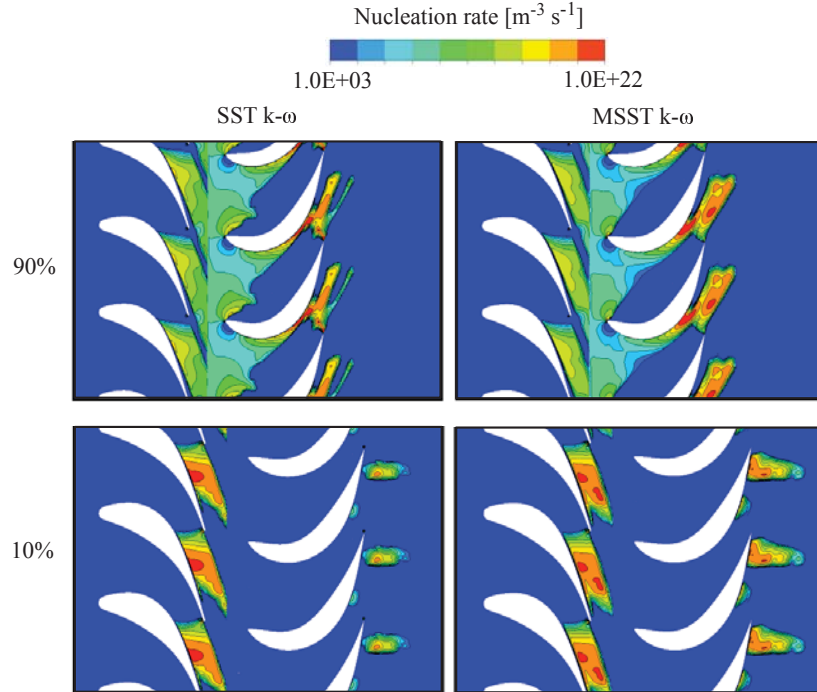


**Figure 7.34.** Predicted contours of the nucleation rate with the SST  $k-\omega$  and the MSST  $k-\omega$  turbulence models at 10% and 90% spanwise planes.

Further, the influence of turbulence modelling in 3D turbine stage was analyzed by extracting loss measure induced by condensation. For this purpose, the viscous loss and shockwave plus wetness loss were calculated by employing the definition of White et al. (1996) from CFD results and presented in Figure 7.36. The loss coefficients were obtained by applying the circumferential average at different spans along the traverse plane in which the plane was positioned at 25% axial chord length from the rotor trailing edge in the axial direction. Due to higher entropy generation, the SST  $k-\omega$  model yielded more viscous loss at 10% and 50% span surfaces than the MSST  $k-\omega$  model. The corresponding entropy contours are presented in Publication VI. However, at 90% span, the MSST  $k-\omega$  model predicted higher viscous loss due to considerable viscous dissipation particularly at the edges of the separated region after the trailing edge of rotor. Subsequently, the MSST  $k-\omega$  model yielded lesser wetness fraction due to increased viscous dissipation. Therefore, the measure of shock plus wetness loss for the MSST  $k-\omega$  model was reduced for all span surfaces.

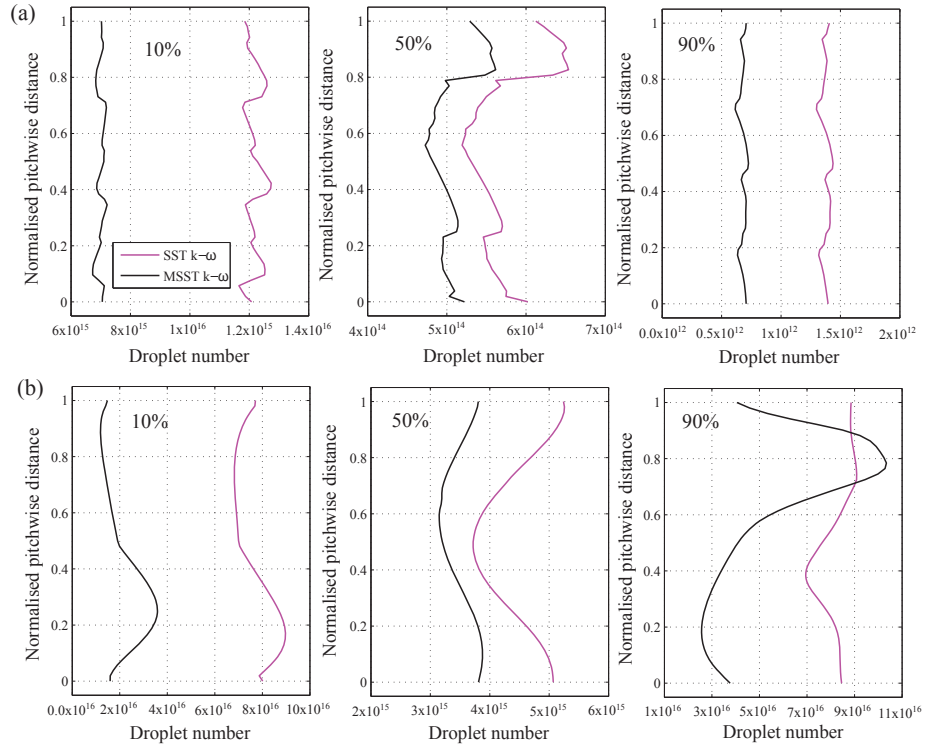


**Figure 7.35.** Predicted droplet numbers with the SST  $k-\omega$  and the MSST  $k-\omega$  turbulence models (a) at the stator exit and (b) outlet.

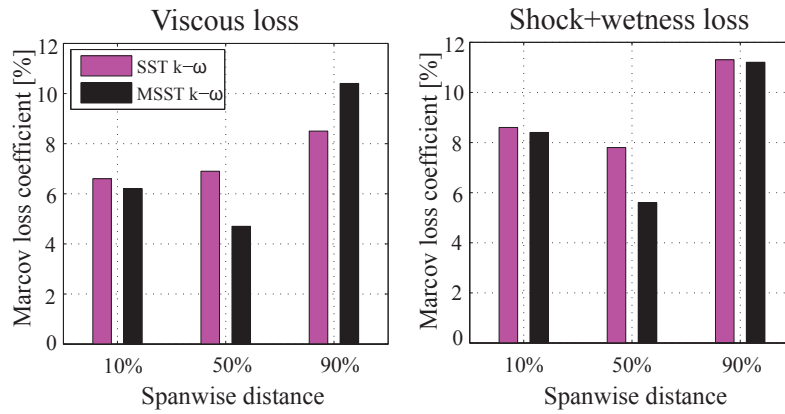


**Figure 7.36.** Predicted Markov loss coefficients with the SST  $k-\omega$  and the MSST  $k-\omega$  turbulence models.



## 8 Conclusions and Suggestions for Future Research

The design and performance analysis of nuclear power plant safety systems and key components of power generation cycle requires experiments and simulation models that are able to capture accurately thermal hydraulic nonequilibrium flow phenomena.

This thesis addresses steam condensation in Boiling Water Reactor's (BWRs) pressure suppression pool (PSP) and in low-pressure (LP) steam turbines. The heat sink function of PSP relies on the direct contact condensation (DCC) that limits the containment over-pressurisation and mixes the suppression pool inventory maximising its capacity as a heat sink. In LP steam turbines, the droplet formation due to condensation causes additional losses, blade erosion and corrosion problems which directly affect the overall component efficiency.

This chapter presents conclusions of computational fluid dynamics (CFD) simulations of this work and provides suggestions for future research in the subject areas.

### 8.1 Conclusions

#### 8.1.1 Direct contact condensation modelling of pressure suppression pool tests

The Eulerian-Eulerian two-fluid approach was applied to model steam blowdown tests of the open pool test facility (POOLEX) and the pressurizing drywell-wetwell suppression pool facility (PPOOLEX) of Lappeenranta University of Technology. For this purpose, two CFD codes, OpenFOAM and NEPTUNE\_CFD were used. Throughout this work, four different DCC models from the literature were employed to model interfacial heat transfer. The turbulence was solved by using the standard  $k-\varepsilon$  turbulence model of Launder and Spalding (1974) ( $Sk-\varepsilon$ ) and the  $k-\varepsilon$  model of Lahey (2005) ( $Lk-\varepsilon$ ). The influence of computational grid on direct contact condensation was studied by varying grid density in the computational domains. The grid convergence index (GCI) method was used to assess discretization error.

The open pool test POOLEX STB-31 was modelled to verify basic functionality of the OpenFOAM solver. The STB-31 case has low turbulence and an almost steady DCC interface. Interfacial heat transfer was simulated with the same models as used in the previous NEPTUNE\_CFD simulations. OpenFOAM reproduced well the STB-31 test, NEPTUNE\_CFD and TransAT results, demonstrating that the combination of DCC model of Lakehal et al. (2008) (LH) and the  $Sk-\varepsilon$  turbulence model of Launder and Spalding (1974) predicts the quantitative DCC rate and qualitative phenomena well, while the DCC model of Laviéville et al. (2006) (HD 0) overestimates the DCC rate significantly.

The GCI analysis showed that near-interface grid size of 0.001 mm (vertical)  $\times$  0.2 mm (horizontal) led to the grid convergence of the DCC rate and interfacial area in of the STB-31 case. That resolution locked the interface to the location seen in the test and

provided the most correct interfacial area. The desired resolution was higher than assumed in the previous NEPTUNE\_CFD simulations. The OpenFOAM simulations employed an incompressible two-phase solver whereas all the NEPTUNE\_CFD simulations have been carried out with compressible flow solver and steam tables.

The first NEPTUNE\_CFD results of chugging were obtained using the open pool POOLEX test STB-28 as a reference. Thus that case was chosen for the first OpenFOAM simulations as well. The POOLEX STB-28 test series corresponds to the high turbulence, unstable and rough interface chugging DCC mode. Decreasing pool subcooling during the test was expected due to high energy input and demonstrated by high-speed video data of increasing bubble sizes. The DCC models of Hughes and Duffey (1991) (HD 1), Coste (2004) (Coste C) and Lakehal et al. (2008) were employed in the chugging simulations. Both incompressible and compressible two-phase solvers of the OpenFOAM code were tested, but only the Lk- $\epsilon$  turbulence model turned out to be numerically stable with the code version used. NEPTUNE\_CFD cases were carried out with compressible solver, steam tables and the Sk- $\epsilon$  model.

The incompressible OpenFOAM solver was unable to predict correctly pressure during chugging and therefore, the steam bubble around the blowdown pipe outlet never collapsed totally, as it should have. Missing chugging led to too low DCC rate because too low predicted turbulence and interfacial area. The compressible OpenFOAM solver enabled chugging in the cases of Hughes and Duffey (1991) and Coste (2004) models. The Lakehal et al. (2008) model failed to produce the chugging due to its very low DCC rate prediction. The DCC rate was higher with more subcooling, as expected. As pool temperature increased, the condensation rate decreased, larger bubbles appeared, and the pressure pulse magnitudes rose. These results are in agreement with the NEPTUNE\_CFD results.

However, the Lk- $\epsilon$  turbulence model of OpenFOAM simulations yielded significantly higher turbulence kinetic energy than the Sk- $\epsilon$  turbulence model of NEPTUNE\_CFD simulations. As a result, the DCC rates in these OpenFOAM cases were notably higher, and the bubbles collapse was more frequent than in the NEPTUNE\_CFD simulations. The Fast Fourier Transform (FFT) of OpenFOAM pressure data showed more peaks between 1 Hz and 3 Hz than in the experiment and in the NEPTUNE\_CFD simulations. It appears that Lk- $\epsilon$  turbulence production is too high for large interface simulations such as the chugging.

The GCI study of the OpenFOAM STB-28 chugging simulations showed that the grid convergence would be reached when grid size decreases to 2 mm  $\times$  5 mm. It was seen that the total interfacial area increased clearly with increasing grid resolution, but turbulence kinetic energy increased only slightly. Based on later PPOOLEX DCC-05 NEPTUNE\_CFD simulations, it is possible that more details due to the Rayleigh-Taylor and other instabilities are actually captured with higher resolution grids even without interface tracking CFD models. This would explain the GCI divergence after the '5 mm' turning point, which is near the critical interfacial wavelength calculated for the PPOOLEX DCC-05 case. It can be concluded that certain grid density is needed to resolve the interfacial

heat and mass transfer, but the user should determine carefully whether he is operating with the interfacial instability modelling system or with the interfacial instability resolving system.

Pressurizing drywell-wetwell PPOOLEX facility represents a BWR suppression pool containment better than open-top pools and the facility is better instrumented than the previous POOLEX system. Comprehensive pattern recognition and FFT analysis results of PPOOLEX DCC-05-4 subtest are available, which made the NEPTUNE\_CFD and OpenFOAM simulations easier to compare to the test.

In a simulation of the DCC-05-4 test, two bubble oscillation frequencies should be visible together, the 0.5-3.3 Hz for chugging and 50 Hz natural oscillation ranges of the condensing bubble. Chugging did indeed occur in OpenFOAM simulations of the DCC-05-4 case with the Lk- $\varepsilon$  model, but at a far too high frequency in the 20 Hz range. This confirms that the Lk- $\varepsilon$  turbulence production was too high to be physically realistic.

The OpenFOAM simulations with the Sk- $\varepsilon$  turbulence model produced better chugging frequencies 0.5-2.5 Hz, but 25 Hz interface oscillation was seen instead of 50 Hz. The NEPTUNE\_CFD simulations with the Sk- $\varepsilon$  turbulence model failed to produce chugging with any of the tested DCC models, showing only the 5.5 Hz oscillation of a persistent bubble. Compressible flow solvers and the grid of 5 mm cell resolution was used in the above-mentioned simulations. Missing chugging or natural frequencies of the condensing bubble indicates that the interfacial area modelling was insufficient in these cases because the result was quite insensitive to any other model changes.

In NEPTUNE\_CFD simulations, the presence of drywell tends to prevent the appearance of chugging, in contrast to cases without such a pressure reserve i.e. STB-28. The Rayleigh-Taylor Interfacial area model of Pellegrini et al. (2015) (RTI) was implemented in the NEPTUNE\_CFD and tested with the same 5 mm grid. Chugging appeared in the cases where the DCC condensation rate would be nevertheless a high e.g model of Coste (2004) succeeded but the model of Hughes and Duffey (1991) failed.

The compressible flow solution with the model combination of Coste C, RTI, Coste Large Interface drag model and Sk- $\varepsilon$  turbulence model resulted in two coexisting frequency ranges 1.2-3 Hz and 47 Hz, which are remarkably near the experimental results. In order to test if the same result would be achieved without the RTI model, a dense 1 mm grid was tested with otherwise same models. The result was as good yielding frequencies 1.5-2.2 Hz and 48 Hz, but more interfacial details were visible in the volume fraction fields. The denser grids are not often suitable for large-scale engineering applications simulations, and therefore, the Rayleigh-Taylor instability modelling would be a good alternative for full-scale 3D suppression pool simulations in future.

### 8.1.2 Condensation modelling of LP turbine flows

This work was partially focussed on non-equilibrium condensing steam flow modelling in LP steam turbines by adopting the Eulerian-Eulerian approach. The mixture of steam and

condensed water droplets was solved with the compressible Reynolds-averaged Navier-Stokes equations. The classical homogeneous nucleation theory of McDonald (1962) was used for nucleation modelling. For this purpose, ANSYS FLUENT and ANSYS CFX CFD codes were utilized. The vapour thermodynamic properties are significant for correct prediction of non-equilibrium condensing steam flows. Thus, the vapour properties were estimated by using the real gas equation of state of Young (1988) and the IAPWS-IF97 formulation (Wagner and Kruse, 1998).

In this work, condensing steam flow fields of convergent-divergent nozzles, a stationary cascade of turbine blades and the 3D stator-rotor stage were investigated. The achieved CFD results were discussed together with available test data of condensing steam flows in the literature. For validation purposes, the Markov loss coefficients were extracted from the simulations by using the definitions of White et al. (1996).

The influence of local geometrical details including blade trailing edge shapes, blade shape modification via blade surface tapering, and dimple inclusion on condensation phenomena was analyzed. For this purpose, four different trailing edge shapes i.e. conic trailing edge, semicircular trailing edge, square trailing edge, and elliptic trailing edge were chosen. The presented results revealed that the flow expansion was affected notably by the different trailing edge shapes. As a result, the nucleation, droplet growth processes and other key features of wet-steam flows were altered. The highest nucleation rate was observed in the elliptic trailing edge case due to highest expansion and, thus, it yielded the smallest average droplet radius among all cases. Both the round and square trailing edge cases had strong wake regions which raised the rate of entropy generation and predicted the higher total loss. Results revealed that the elliptic trailing shape yielded the lowest loss generation among all the cases and it predicted about 7% less total loss compared with the experiment.

Two dimple shapes of 100  $\mu\text{m}$  (D100) and 200  $\mu\text{m}$  (D200) were generated on the pressure surface of the turbine blade. After including dimple profiles on the turbine blade, the Wilson point was altered and the location of condensation disturbance was changed. The rate of nucleation was increased and more droplets were generated which released more latent heat to the vapour phase. As a result, the intensity of condensation disturbance was increased with dimple inclusion. An additional shock wave was resulted both in the D100 and the D200 cases which impinged onto the suction side. The dimple profiles affected on the entropy generation in the blade wake and downstream of the flow. Results demonstrated that blade profiles including dimple features reduced the overall loss particularly the D100 case yielded about 8% lesser total loss compared to the base profile without dimple case.

The blade pressure surface tapering and suction surface tapering were done generating different angles between the pressure and the suction surfaces. Results revealed that the nucleation rate was increased and droplet average radius was decreased after pressure side tapering. The entropy generation was decreased with pressure side tapering which lessened the overall loss. The shock plus wetness loss was reduced about 20-25% with the tapered blade compared to the base profile without tapering. The pressure surface tapered

blade with  $11^\circ$  angle reduced the total loss approximately 30% than the base profile. The suction surface tapered blades predicted approximately 24-30% lesser overall loss generation compared to the base profile without tapering case. Based on the presented results, it can be concluded that the blade profile and their trailing edge shape selection have a vital role in the entire condensation process and corresponding loss generation in LP turbine flows.

The accurate modelling of both wall-bounded shear layers and free shear layers is important to solve turbomachinery flows precisely. In particular, the turbulence modelling is crucial in order to correctly predict the turbulent cascade process which involves the deformation and stretching of eddies and their corresponding dissipation. For LP turbine flow modelling, turbulence modelling is required to investigate the processes of mass, momentum and heat transfer both around the solid surfaces and in core flow passages. Also, an adequate droplet deposition modelling in wet-steam flow requires the turbulence to be correctly modelled.

In this work, the effect of inlet turbulence level on non-equilibrium homogeneously condensing steam flow was examined. The analysis showed that the intensity of condensation disturbance was inversely proportional to the freestream turbulence level at the inlet. Thus, the processes of liquid droplet nuclei formation and droplet growth were influenced. The results illustrated that the overall moisture level was increased in the case of lower inlet turbulence level.

Further, the influence of turbulence modelling on condensing steam flow was studied by modifying turbulence models. For this purpose, the two-equation turbulence models i.e. the  $Sk-\varepsilon$  and the shear stress transport  $k-\omega$  (SST  $k-\omega$ ) turbulence models were chosen and modified. In the modified turbulence models, source terms were added which defined the modulation of turbulence kinetic energy and its dissipation rate/specific dissipation rate due to liquid droplets. The standard turbulent viscosity was modified via production to dissipation ratio multiplier. The presented results showed that the inviscid calculation, and the  $Sk-\varepsilon$  and the SST  $k-\omega$  turbulence models were poor for condensing steam flow modelling. It was seen that the overall viscous dissipation was increased notably by the addition of source terms and with the modified turbulent viscosity formulation. As a result, the flow temperature was influenced via energy sources. Thus, the heat transfer phenomena were affected in the flow which influenced on the condensation process. The flow expansion was altered in modified turbulence models. Subsequently, the subcooling level rose because of increased flow expansion. Accordingly, the nucleation rate was increased which generated more liquid droplets. These droplets raised the rate of latent heat release to the vapour phase. The modified turbulence models yielded condensation disturbance information with better accuracy than the non-modified turbulence models. Further, the losses predicted by the modified turbulence models corresponded well with the measured losses. It can be concluded that the modified turbulence models are capable to model condensing steam flow correctly.

## 8.2 Future suggestions

Based on the presented analysis, some suggestions for further research on these applications can be made as below.

- The Rayleigh-Taylor instability model predicted good results of chugging DCC mode. The implementation of Rayleigh-Taylor instability model in OpenFOAM two-phase flow solver is ongoing. The applicability of Rayleigh-Taylor instability modelling should be tested with 3D simulations. Further, some efforts could be placed on turbulence model validation especially for large interface cases. The 3D DCC modelling could be validated further with other blowdown pipe geometries or with spargers.
- Well validated implementation of steam tables in OpenFOAM two-phase solver could be very valuable for any thermal-hydraulics simulations.
- The current work of blade shape influence on condensation was restricted to only 2D simulations. Thus, it would be anticipated that 3D analysis of blade shape effects can be performed. The outcome of 3D CFD simulations concerning the blade shape influence on condensing steam flow in LP turbine would be worthwhile for turbine manufacturers in blade shape optimisation process. Further, in multi-stage turbine flows, the stator-rotor interaction and wake-chopping greatly influence the entire condensation process and entropy generation. As entropy generation dominantly relies of blade shapes, it would be interesting to analyze the impact of blade shape on wake-chopping in multi-stage steam turbine.
- Concerning steam turbines, it would be fascinating to model multi-stage steam turbine or last stages of LP turbine and to analyze the flow phenomena including the turbulence modelling role.
- Several experimental studies have been performed hitherto. Nevertheless, still the existing experimental facilities and the measured data of LP turbine flows are very limited worldwide. Thus, the comprehensive measurement of non-equilibrium condensing steam flows of LP turbine are very essential to enhance the understanding of these complex flow phenomena and to validate the models.

## References

- Ali, S. M., Verma, V., and Ghosh, A. K. (2007). Analytical thermal hydraulic model for oscillatory condensation of steam in presence of air. *Nuclear Engineering and Design*, 237:2025–2039.
- An, L., Wang, Z., and Han, Z. (2009). Numerical study and control method of interaction of nucleation and boundary layer separation in condensing flow. *Front. Energy Power Eng. China*, Vol. 3 (3):254–261.
- ANSYS Inc. (2016). *ANSYS CFX Theory Guide*. Release 16.0, Canonsburg, Pennsylvania.
- Arinobu, M. (1980). Studies on the dynamic phenomena caused by steam condensation in water. In *in: Proc. of ANS-ASME-NRC Int. Topical Meeting on Nuclear Reactor Thermal Hydraulics, Saratoga Springs, New York, pp. 293-302*.
- Aust, E. and Seeliger, D. (1982). Pool dynamics and dynamic loads in pressure suppression containment systems. *Transactions of the American Nuclear Society*, 41:696–699.
- Avetissian, A. R., Philippov, G. A., and Zaichik, L. I. (2005). The effect of turbulence on spontaneously condensing wet-steam flow. *Nucl. Eng. Des.*, Vol. 235:1215–1223.
- Avetissian, A. R., Philippov, G. A., and Zaichik, L. I. (2008). Effects of turbulence and inlet moisture on two-phase spontaneously condensing flows in transonic nozzles. *Int. J. Heat Mass Transfer*, Vol. 51:4195–4203.
- Aya, I., Kobayashi, M., and Nariyai, H. (1983). Pressure and fluid oscillations in vent system due to steam condensation, (ii) high-frequency component of pressure oscillations in vent tubes under at chugging and condensation oscillation. *J. Nucl. Sci. Tech.*, 20 (3):213–227.
- Aya, I. and Nariyai, H. (1985). Chugging phenomenon induced by steam condensation into pool water (amplitude and frequency of fluid oscillation). *Heat Transfer-Japanese Research*, Vol. 14 (4):26–43.
- Aya, I. and Nariyai, H. (1986). Occurrence treshold of pressure oscillations induced by steam condensation in pool water. *Bulletin of JSME*, 29/235:2131–2137.
- Aya, I. and Nariyai, H. (1987). Boundaries between regimes of pressure oscillation induced by steam condensation in pressure suppression containment. *Nucl. Eng. Des.*, 99:31–40.
- Aya, I. and Nariyai, H. (1991). Evaluation of heat-transfer coefficient at directcontact condensation of cold water and steam. *Nucl. Eng. Des.*, 131:17–24.
- Aya, I., Nariyai, H., and Kobayashi, M. (1980). Pressure and fluid oscillations in vent system due to steam condensation (i), experimental results and analysis model for chugging. *Nucl. Sci. Tech.*, Vol. 17 (7):499–515.

- Bakhtar, F., Ebrahimi, M., and Bamkole, B. (1995a). On the performance of a cascade of turbine rotor tip section blading in nucleating steam, part 2: wake traverses. *Proc. Inst. Mech. Eng. Part C: J. Mech. Eng. Sci.*, Vol. 209:169–177.
- Bakhtar, F., Ebrahimi, M., and Webb, R. (1995b). On the performance of a cascade of turbine rotor tip section blading in nucleating steam, part 1: surface pressure distributions. *Proc. Inst. Mech. Eng. Part C: J. Mech. Eng. Sci.*, Vol. 209:115–124.
- Bakhtar, F., Mahpeykar, M. R., and Abbas, K. K. (1995c). An investigation of nucleating flows of steam in a cascade of turbine blading-theoretical treatment. *ASME J. Fluids Eng.*, Vol. 117:138–144.
- Bakhtar, F. and Piran, M. (1979). Thermodynamic properties of supercooled steam. *Int. J. Heat & Fluid Flow*, Vol. 1 (2):53–62.
- Bakhtar, F., Ryley, D., Tubman, K., and Young, J. (1975). Nucleation studies in flowing high pressure steam. *Inst. Mech. Eng.*, Vol. 189:427–436.
- Bakhtar, F. and Tochai, M. T. M. (1980). An investigation of two-dimensional flows of nucleating and wet steam by the time-marching method. *Int. J. Heat Fluid Flow*, Vol. 2:5–18.
- Bakhtar, F. and Yousif, F. H. (1974). The behaviour of wet steam after disruption by a shock wave. In *Inst. Chem. Engrs. Symposium on Multi-Phase Flow Systems. Univ. of Strathclyde*.
- Bakhtar, F. and Zidi, K. (1989). Nucleation phenomena in flowing high-pressure steam: experimental results. *Proc. Inst. Mech. Eng.*, Vol. 203:195–200.
- Bakhtar, F. and Zidi, K. (1990). Nucleation phenomena in flowing high-pressure steam, part, 2: theoretical analysis. *Proc. Inst. Mech. Eng.*, Vol. 204:233–242.
- Band, W. (1939). Dissociation treatment of condensation of water vapour. *J. Chem. Phys.*, Vol.7:324.
- Banerjee, S. (1990). Turbulence structure and transport mechanisms at interfaces. In *9th International Heat Transfer Conference, Keynote Lectures*.
- Barschdorff, D. (1971). Verlauf der Zustandsgrossen und gasdynamische Zusammenhaenge der spontanen Kondensation reinen Wasserdampfes in Lavalduesen. *Forsch. Ingenieurwes*, Vol. 37:146–157.
- Barschdorff, D. and Filippov, G. (1970). Analysis of special conditions of the work of laval nozzles with local heat supply. *Heat Transfer - Soviet Research*, Vol. 2:76–87.
- Baumann, K. (1912). Some recent developments in large steam turbine practice. *J. Inst. Elec. Engrs.*, Vol. 48:768–877.

- Becker, R. and Doring, W. (1935). Kinetische behandlung der keimbildung in ubersetzten dampfen. *Ann. d. Phys.*, Vol. 24:719–752.
- Bestion, D. (2012). Applicability of two-phase CFD to nuclear reactor thermalhydraulics and elaboration of best practice guidelines. *Nucl. Eng. Des.*, 253:311–321.
- Bijl, A. (1938). *Discontinuities in the Energy and Specific Heats*. PhD thesis, University of Leiden, Germany.
- Binnie, A. M. and Green, J. R. (1943). An electrical detector of condensation in high velocity steam. *Proc. Roy. SOCA.*, Vol. 181:134.
- Binnie, A. M. and Woods, M. W. (1938). The pressure distribution in a convergent–divergent steam nozzle. *Proc. Inst. Mech. Eng.*, Vol. 138:229–266.
- Bosdas, I. (2016). *Time Resolved Flow Field and Droplet Measurements in Wet Steam Turbine Flows*. PhD thesis, Dissertation, ETH Zurich.
- Boyce, M. P. (2012). *Gas Turbine Engineering Handbook*. Elsevier, fourth edition edition.
- Brear, M. J., Hodson, H. P., and Harvey, N. W. (2002). Pressure surface separations in low pressure turbines: Part 1 of 2-midspan behaviour. *J. Turbomachinery*, Vol. 124:393–405.
- Brennen, C. (1979). A linear dynamics analysis of vent condensation stability. *J. Fluids Eng.*, pages 63–71.
- Brennen, C. (2014). *Cavitation and Bubble Dynamics*. 1st edn. Cambridge University Press. ISBN 978-1-107-64476-2.
- Cai, J., Jo, B., Erkan, N., and Okamoto, K. (2016). Effect of non-condensable gas on thermal stratification and flow patterns in suppression pool. *Nucl. Eng. Des.*, 300:117–126.
- Cai, X., Niu, F., Ning, T., Wu, G., and Song, Y. (2009). An investigation of wet steam flow in a 300 mw direct air-cooling steam turbine. part 1: measurement principles, probe, and wetness. *Proc. Inst. Mech. Engrs., Part A J. Power and Energy*, Vol. 223:625–634.
- Callender, H. L. (1915). On the steady flow of steam through a nozzle or throttle. *Proc. Inst. Mech. Engrs.*, pages 53–77.
- Campbell, B. and Bakhtar, F. (1970). Condensation phenomena in high speed flow of steam. *Proc. Instn. Mech. Engrs.*, Vol. 185:395–404.
- Celik, I. (1993). Numerical uncertainty in fluid flow calculations: Needs for future research. *ASME. J. Fluids Eng.*, Vol. 115 (2):194–195.
- Celik, I. B., Ghia, U., Roache, P. J., Freitas, C. J., Coleman, H., and Raad, P. E. (2008). Procedure for estimation and reporting of discretization error in cfd applications. *J. Fluids Eng.*, Vol. 130 (7), 078001:1–4.

- Chan, C. and Lee, C. (1982a). A regime map for direct contact condensation. *Int. J. Multiphase Flow*, 8(1):11–20.
- Chan, C. and Lee, C. (1982b). A regime map for direct contact condensation. *Int. J. Multiphase Flow*, 8(1):11–20.
- Chandler, K., White, A. J., and Young, J. B. (2013). Non-equilibrium wet-steam calculations of unsteady low-pressure turbine flows. *Proc. IMechE, Part A: J Power and Energy*, Vol. 228:143–152.
- Chen, C.-L. and Dhir, V. K. (1982). Hydrodynamics of a bubble formed at vent pipe exit. *Int. J. Multiphase Flow*, 8/2:147–163.
- Chen, S., Gerner, F., and Tien, C. (1987). General film condensation correlations. *Exp. Heat Transfer*, 1:93–107.
- Cho, S., Song, C. H., Chung, H. J., Chun, S. Y., and Chung, M. K. (2001). Multiple-hole effect on the performance of a sparger during direct contact condensation of steam. *KSME International Journal*, 15 (4):482–491.
- Chuang, T. H. (1977). Mark iii one-third area scale submerged structure tests. [bwr]. Technical report, General Electric Co., San Jose, CA (USA). Boiling Water Reactor Systems Dept.
- Class, G. (1978). Theoretical investigation of pressure pulse development during steam condensation in the pressure reducing system of boiling water reactors. Computer program KONDAS NUREG/ TR-0028, Translation of Report KFK 2487 of Society of Nuclear Research, Karlsruhe, Germany by the U. S. Nuclear Regulatory Commission.
- Coste, P. (2004). Computational simulation of multi-d liquid-vapor thermal shock with condensation. In *Proceedings of ICMF'04, Yokohama, Japan, May 30 - June 4*.
- Coste, P., Pouvreau, J., Laviéville, J., and Boucker, M. (2008). Status of a two-phase cfd approach to the pts issue. In *XCFD4NRS, Grenoble, France*.
- Denton, J. D. (1993). The 1993 igti scholar lecture: Loss mechanisms in turbomachines. *ASME J. Turbomachinery*, 115 (4):621–656.
- Duff, R., Harlow, F., and Hirt, C. (1962). Effects of diffusion on interface instability between gases. *Physics of fluids*, 5(4):417–425.
- Dykas, S. and Wróblewski, W. (2011). Single- and two-fluid models for steam condensing flow modeling. *Int. J. Multiphase Flow*, Vol. 37 (9):1245–1253.
- Eberle, T., Schatz, M., Starzmann, J., Gr'ubel, M., and Casey, M. (2013). Experimental study of the effects of temperature variation on droplet size and wetness fraction in a low pressure model steam turbine. *Proc. Inst. Mech. Eng., Part A J. Power and Energy*, Vol. 228:97–106.

- Eckert, E. R. G. and Drake, R. M. (1972). *Analysis of Heat and Mass Transfer*. McGraw-Hill Co.
- Farkas, L. (1927). Keimbildungsgeschwindigkeit in übersättigten dampfen. *Z. Phys. Chem.*, Vol. 125:236–242.
- Frenkel, J. (1946). *Kinetic Theory of Liquids*. Oxford University Press, New York.
- Gerber, A. (2002). Two-phase eulerian/lagrangian model for nucleating steam flow. *ASME J. Fluids Eng.*, Vol. 124:465–475.
- Gerber, A. G. and Kermani, M. J. (2004). A pressure based Eulerian-Eulerian multi-phase model for non-equilibrium condensation in transonic steam flow. *Int. J. Heat Mass Transfer*, Vol. 44:2217–2231.
- Gerber, A. G. and Mousavi, A. (2006). Application of quadrature method of moments to the polydispersed droplet spectrum in transonic steam flows with primary and secondary nucleation. *Applied Mathematical Modelling*, Vol. 31:1518–1533.
- Gerber, A. G. and Mousavi, A. (2007). Representing polydispersed droplet behavior in nucleating steam flow. *J. Fluids Eng.*, Vol. 129:1404–1414.
- Ghiaasiaan, S. (2008). *Two-Phase Flow, Boiling, and Condensation in Conventional and Miniature Systems*. Cambridge University Press, New York, ISBN 978-0-521-88276-7, 1 edition.
- Gibbs, J. (1906). *Scientific Papers*. Vol. 1. Longmans Green, London.
- Gibbs, J. W. (1888). On the equilibrium of heterogeneous surfaces. In *Collected Papers (Thermodynamics)*, Longmans, London,.
- González, P., Ulizar, I., Vázquez, R., and Hodson, H. P. (2001). Pressure and suction surfaces redesign for high lift low pressure turbines. *J. Turbomachinery*, Vol. 124 (2):161–166.
- Grafton, W. A., McIntyre, T. R., and Ross, M. A. (1977). Mark ii pressure suppression test program, phase ii and iii tests. Technical report, General Electric Co., San Jose, CA (USA). Boiling Water Reactor Projects Dept.
- Granovskiy, A., Kostege, M., and Vassiliev, V. (2014). Effect of unguided turning angle and trailing edge shape on cooled blade loss. In *Proc. of ASME Turbo Expo, GT2014-26215, Düsseldorf, Germany, June 16-20, 1-14*.
- Grübel, M., Starzmann, J., Schatz, M., Eberle, T., Vogt, D. M., and Sieverding, F. (2014). Two-phase flow modeling and measurements in low-pressure turbines: Part 1 — numerical validation of wet steam models and turbine modeling. *J. Eng. Gas Turbines Power*, Vol. 137(4):042602–042602–11.

- Guha, A. (1995). *Two-phase Flows with Phase Transition*. In VKI Lecture Series 1995-06, von Karman Institute for Fluid Dynamics, Belgium, 1-110.
- Guha, A. and Young, J. B. (1991). Time marching prediction of unsteady condensation phenomena due to supercritical heat addition. In *Turbomachinery : Latest Developments in a Changing Scene, London IMechE, C423/057, 167-173*.
- Guha, A. and Young, J. B. (1994). The effects of flow unsteadiness on the homogeneous nucleation of water droplets in steam turbines. *Phil. Trans. Royal Soc., Series A*, Vol. 349:445–472.
- Gulawani, S. S., Dahikar, S. K., Mathpati, C. S., Joshi, J. B., Shah, M. S., RamaPrasad, C. S., and Shukla, D. S. (2009). Analysis of flow pattern and heat transfer in direct contact condensation. *Chem. Eng. Sci.*, 64:1719–1738.
- Gyarmathy, G. (1963). On the rate of growth of small liquid drop in a supersaturated atmosphere. *Z. Angew. Math. Phys.*, Vol. 14:280.
- Gyarmathy, G. (1976). *Condensation in flowing steam*. A von Karman Institute Book on Two-Phase Steam Flow in Turbines and Separators, Hemisphere, London, pp. 127-189.
- Gyarmathy, G. (1982). The spherical droplet in gaseous carrier streams: Review and synthesis. *Multiphase Science and Technology*, Vol. 1:99–279.
- Gyarmathy, G. (2005). Nucleation of steam in high-pressure nozzle experiments. In *Proc. of 6th European Conference on Turbomachinery, Lille, France, March 7-11, 458-469*.
- Gyarmathy, G. and Lesch, F. (1969). Fog droplet observations in a laval nozzle and in an experimental turbine. *Proc. Inst. Mech. Eng.*, Vol. 184:29.
- Gyarmathy, G. and Meyer, H. (1965). Spontane kondensation. *V.D.I. Forschungsheft*, page 508.
- Hart, J., Slegers, W. J. M., de Boer, S. L., Huggenberger, M., Jimenez, J. L., Gonzalez, J. L. M.-C., and Puigjaner, F. R. (2001). TEPSS-Technology enhancement for passive safety systems. *Nuclear Engineering and Design*, 209/1-3:243–252.
- Helmholtz, R. (1886). Untersuchungen über dämpfe und nebel, besonders über solche von losungen. *Ann. d. Phys.*, Vol. 27:508.
- Hertz, H. (1882). *Ann. Phys.*, Vol. 17:177.
- Hill, P. G. (1966). Condensation of water vapour during supersonic expansion in nozzles. *J. Fluid Mech.*, Vol. 25 (3):593–620.
- Hong, S. J., Park, G. C., Cho, S., and Song, C. H. (2012). Condensation dynamics of submerged steam jet in subcooled water. *Int. J. Multiphase Flow*, 39:66–77.

- Hughes, E. D. and Duffey, R. B. (1991). Direct contact condensation and momentum transfer in turbulent separated flows. *Int. J. Multiphase Flow*, 17(5):599–619.
- Hujala, E. (2013). Evaluation of bubble formation and break up in suppression pools by using pattern recognition methods. Master thesis, Lappeenranta University of Technology, LUT Energy, Lappeenranta, Finland.
- Hujala, E., Tanskanen, V., and Puustinen, M. (2014). Progress in the development of Pattern Recognition algorithm for the PPOOLEX video data, SAFIR/EXCOP Research report 3/2013. SAFIR Research Report EXCOP 3/2013, Nuclear Engineering, Lappeenranta University of Technology.
- IEA (2016). International energy outlook 2016. *U.S. Energy Information Administration, WASHINGTON DC 20585, DOE/EIA-0484(2016)(PDF):1–290.*
- Ishizaka, K., Ikohagi, T., and Daiguji, D. (1995). A high-resolution numerical method for transonic nonequilibrium condensation flows through a steam turbine cascade. In *Proc. of 6th International Symposium on Computational Fluid Dynamics*, 479-484.
- Kang, H. S. and Song, C. H. (2008). CFD analysis for thermal mixing in a subcooled water tank under a high steam mass flux discharge condition. *Nucl. Eng. Des.*, 238:492–501.
- Kantrowitz, A. (1951). Nucleation in very rapid vapour expansions. *J. Chem. Phys.*, Vol. 19:1097–1100.
- Kaschiev, D. (1969). Solution of the non-steady state problem in nucleation kinetics. *Surface Science*, Vol. 14:209–220.
- Kennedy, W., McGovern, D., Maraschin, R., and Wolfe, K. (1978). Rigid and flexible vent header testing in the quarter scale test facility. mark i containment program, task 5. 3. 3. Technical report, Acurex Corp., Mountain View, CA. (USA). Alternate Energy Div.
- Kerney, J., Feath, G. M., and Olson, D. R. (1972). Penetration characteristics of a submerged steam jet. *AIChE J.*, 18/3:584–553.
- Kim, Y. S., Park, J. B. W., and Song, C. H. (2004). Investigation of the steam-water direct contact condensation heat transfer coefficients using interfacial transport model. *Int. Commun. Heat Mass Transfer*, 31:397–408.
- Kirkwood, J. G. and Buff, E. P. (1949). The statistical mechanical theory of surface tension. *J. Chem. Phys.*, Vol. 17:338.
- Knudsen, M. (1915). *Ann. Phys.*, Vol. 47:697.
- Kondo, S., Tobita, Y., Morita, K., and Shirakawa, N. (1992). SIMMERIII : An advanced computer program for LMFBR severe accident analysis. In *In: Proceedings of the International Conference on Design and Safety of Advanced Nuclear Power Plants (ANP'92), Tokyo, Japan, October.*

- Konorski, A. (1966). *Pr. Inst. Maszyn Przeplywowych (in Polish)*, Vol. 29-31:27–30.
- Kowalchuk, W. and Sonin, A. A. (1978). A model for condensation oscillations in a vertical pipe discharging steam into a subcooled water pool. Computer program KONDAS NUREG/ TR-0028, NRC Report.
- Kukita, Y., Namatame, K., and Shiba, M. (1984). Loca air-injection loads in bwr mark ii pressure suppression containment systems. *Nuclear Engineering and Design*, 77/2:117–129.
- Kukita, Y., Namatame, K., Takeshita, I., and Shiba, M. (1987). Loca steam condensation loads in bwr mark ii pressure suppression containment system. *Nu*, 102/2:225–228.
- Lahey, R. (2005). The simulation of multidimensional multiphase flows. *Nucl. Eng. & Design*, 235:1043–1060.
- Lahey, R. and Moody, F. (1993). *The Thermal-Hydraulics of a Boiling Water Reactor*. American Nuclear Society, 2 edition.
- Laine, J. and Puustinen, M. (2005). Condensation pool experiments with steam using dn200 blowdown pipe. NKS-111 ISBN 87-7893-171-1, Lappeenranta University of Technology.
- Laine, J. and Puustinen, M. (2006a). Condensation pool experiments with steam using insulated dn200 blowdown pipe. Research report poolex 3/2005, Lappeenranta University of Technology.
- Laine, J. and Puustinen, M. (2006b). Steam blowdown experiments on chugging. Research report poolex 2/2005, Lappeenranta University of Technology.
- Laine, J. and Puustinen, M. (2009). PPOOLEX experiments on wall condensation. Research report condex 3/2008, Lappeenranta University of Technology.
- Laine, J., Puustinen, M., and Räsänen, A. (2015). Ppoolex experiments with a sparger. Excop 1/2014, Lappeenranta University of Technology.
- Lakehal, D., M.Fulgosi, and G.Yadigaroglu (2008). DNS of Condensing Stratified Steam Water Flow. *ASME J. Heat Transfer*, 130:021501–10.
- Laplace, P. (1806). *Traite de Méchanique Celeste*. Vol. 4. Coucier, Paris.
- Launder, B. E. and Spalding, D. B. (1974). The numerical computation of turbulent flows. *Comput. Methods Appl. Mech. Eng.*, Vol. 3:269–289.
- Laviéville, J., Quémérais, E., Mimouni, S., Boucker, M., and Méchitoua, N. (2006). NEPTUNE\_CFD v1.0 theory manual. Technical report, EDF.
- Leighton, T. (1994). *The Acoustic Bubble*. Academic Press. ISBN 978-0-12-441920-9.

- Li, H., Villanueva, W., and Kudinov, P. (2012). Effective momentum and heat flux models for simulation of stratification and mixing in a large pool of water. Nks report nks-266, NKS, Nordic nuclear safety research. ISBN 978-87-7893-339-3.
- Li, S. Q., Wang, P., and Lu, T. (2015a). CFD based approach for modeling steam-water direct contact condensation in subcooled water flow in a tee junction. *Prog. Nucl. Energy*, 85:729–746.
- Li, S. Q., Wang, P., and Lu, T. (2015b). Numerical simulation of direct contact condensation of subsonic steam injected in a water pool using vof method and les turbulence model. *Prog. Nucl. Energy*, 78:201–215.
- Liang, K. and Griffith, P. (1994). Experimental and analytical study of direct contact condensation of steam in water. *Nucl. Eng. Des.*, 147:425–435.
- Liovic, P. (2000). *Numerical modelling of top-submerged gas injection*. PhD thesis, Doctoral dissertation, University of Melbourne, Melbourne, Australia.
- Livescu, D. (2004). Compressibility effects on the rayleigh-taylor instability growth between immiscible fluids. *Physics of Fluids*, 16 (1):118–127.
- Marks, J. S. and Andeen, G. B. (1979). Chugging and condensation oscillation. In *Proceedings of 18th National Heat Transfer Conference, San Diego, California*.
- Martin, H. M. (1918). A new theory of the steam turbine. *Engineering*, Vol. 106:1–3, 53–55, 107–108, 161–162, 189–191, 245–246.
- McDonald, J. E. (1962). Homogeneous nucleation of vapour condensation. I - Thermodynamic aspects. *Am. J. Physics*, Vol. 30:870–877.
- McDonald, J. E. (1963). Homogeneous nucleation of vapour condensation. II - kinetic aspects. *Am. J. Physics*, Vol. 31:31–41.
- McIntyre, T. R., Myers, L. L., Torbeck, J. E., and Booker, R. J. (1975). Mark iii confirmatory test program: one third scale, three vent air tests. Technical report, General Electric Co., San Jose, Calif. (USA). Boiling Water Reactor Systems Dept.
- McIntyre, T. R., Ross, M. A., and Myers, L. L. (1976). Mark ii pressure suppression test program: Phase i tests. [bwr]. Technical report, General Electric Co., San Jose, CA. (USA). Boiling Water Reactor Systems Dept.
- Meier, M. (1999). *Numerical and experimental study of large steam-air bubbles injected in a water pool*. PhD thesis, ETH, Swiss Federal Institute of Technology, Zurich. DISS. ETH No. 13091.
- Meier, M., Andreani, M., and Yadigaroglu, G. (1998). Experimental study of large steam-air bubbles condensing in a suppression pool. In *IMECA'98, ASME, Anaheim*.

- Meier, M., Yadigaroglu, G., and Andreani, M. (2000). Numerical and experimental study of large steam-air bubbles injected in a water pool. *Nucl. Sci. Eng.*, 136:363–375.
- Menter, F. R. (1994). Two-equation eddy-viscosity turbulence models for engineering applications. *AIAA Journal*, Vol. 32 (8):1598–1605.
- Moheban, M. and Young, J. B. (1984). A time marching method for the calculation of blade-blade non-equilibrium wet steam flows in turbine cascades. In *Inst. Mech. Engrs., Conf. on Comp. Methods in Turbomach., C76/84*, 89.
- Montomoli, F., Carnevale, M., D’Ammaro, A., Massini, M., and Salvadori, S. (2015). Limitations in turbomachinery cfd. In *Uncertainty Quantification in Computational Fluid Dynamics and Aircraft Engines*, SpringerBriefs in Applied Sciences and Technology, pages 21–32. Springer International Publishing.
- Moore, M. J., Walters, P. T., Crane, R. I., and Davidson, B. J. (1973). Predicting the fog drop size in wet steam turbines. In *Wet Steam 4 Conference, Institute of Mechanical Engineers (UK), University of Warwick, paper C37/73*.
- Moses, C. A. and Stein, G. D. (1978). On the growth of steam droplets formed in a Laval nozzle using both static pressure and light scattering measurements. *J. Fluids Eng.*, Vol. 100:311–322.
- Nariai, H. and Aya, I. (1986). Fluid and pressure oscillations occurring at direct contact condensation of steam flow with cold water. *Nucl. Eng. Des.*, 95:35–45.
- NEA (2015). Nuclear energy: Combating climate change.
- Norman, T. L. and Revankar, S. T. (2010). Jet-plume condensation of steam-air mixtures in subcooled water, part 1: Experiments. *Nucl. Eng. Des.*, 240:524–532.
- Oh, S. and Revankar, S. T. (2005). Effect of noncondensable gas in a vertical tube condenser. *Nucl. Eng. Des.*, 235:1699–1712.
- Orfanidis, S. J. (1996). *Introduction to Signal Processing*. Prentice-Hall, 1st edition. ISBN 9780132091725.
- Oriani, R. A. and Sundquist, B. E. (1963). Emendations to nucleation theory and the homogeneous nucleation of water from vapour. *J. Chem. Phys.*, Vol. 38:2082–2089.
- Park, C. K., Song, C. H., and Jun, H. G. (2007). Experimental investigation of the steam condensation phenomena due to a multi-hole sparger. *J. Nuc. Sci. Tech.*, 44 (4):548–557.
- Patel, G., Tanskanen, V., Hujala, E., and Hyvärinen, J. (2016). Direct contact condensation modeling in pressure suppression pool system (SI: NURES SAFE 2016). *Nucl. Eng. Des.*, xx (in press):xx–xx.

- Patel, Y., Patel, G., and Turunen-Saaresti, T. (2013). The effect of turbulence and real gas models on the two phase spontaneously condensing flows in nozzle. In *Proc. of ASME Turbo Expo, GT2013-94778, San Antonio, USA, June 3-7, 1-7*.
- Patel, Y., Turunen-Saaresti, T., Patel, G., and Grönman, A. (2014). Numerical investigation of turbulence modelling on condensing steam flows in turbine cascade. In *Proc. of ASME Turbo Expo, GT2014-26307, Düsseldorf, Germany, June 16-20, 1-14*.
- Pättikangas, T., Niemi, J., Laine, J., Puustinen, M., and Purhonen, H. (2010). CFD modelling of condensation of vapour in the pressurized PPOOLEX facility. In *CFD for Nuclear Reactor Safety Applications (CFD4NRS-3) Workshop, Bethesda, MD, USA, 14-16 September 2010*, page 12.
- Pättikangas, T., Raussi, P., Pokela, H., and Huttunen, M. (2000). Two-dimensional CFD simulation of water hammer in a pool. Technical report, VTT Energy, Finland.
- Pellegrini, M., Araneo, L., H. Ninokata, M. R., Naitoh, M., and Achilli, A. (2016). Suppression pool testing at the siet laboratory: experimental investigation of critical phenomena expected in the fukushima daiichi suppression chamber. *J. Nucl. Sci. Tech.*, 53 (5):614–629.
- Pellegrini, M., Naitoh, M., Josey, C., and Baglietto, E. (2015). Modeling of rayleigh-taylor instability for steam direct contact condensation. In *The 16th International Topical Meeting on Nuclear Reactor Thermal Hydraulics (NURETH-16), Chicago, IL, August 30-September 4*, page 15.
- Peltola, J. (2012). twophasenufoam v0.3. Technical report, VTT.
- Petrovic de With, A., Calay, R. K., and de With, G. (2007). Three-dimensional condensation regime diagram for direct contact condensation of steam injected into water. *Int.J.Heat Mass Transfer*, 50:1762–1770.
- Pletcher, R. H., Tannehill, J. C., and Anderson, D. (2012). *Computational Fluid Mechanics and Heat Transfer*. CRC Press, Taylor & Francis Group, Boca Raton, third edition edition.
- Plummer, P. L. M. and Hale, B. N. (1972). Molecular model for pre-nucleation water clusters. *J. Chem. Phys.*, Vol. 56 (9):4329–4334.
- Prust, H. W. and Helon, R. M. (1972). Effect of trailing-edge geometry and thickness on the performance of certain turbine stator blading. Technical report, Lewis Research Center, National Aeronautics and Space Administration, Washington, D. C. 20546.
- Puustinen, M., Kyrki-Rajamäki, R., Tanskanen, V., Räsänen, A., Purhonen, H., Riikonen, V., Laine, J., and Hujala, E. (2013a). BWR suppression pool studies with POOLEX and PPOOLEX test facilities at LUT. In *The 15th International Topical Meeting on Nuclear Thermal Hydraulics (NURETH-15), Pisa, Italy, 12-17 May 2013*.

- Puustinen, M. and Laine, J. (2008). Characterizing experiments with the PPOOLEX facility. Research report condex 1/2007, Lappeenranta University of Technology.
- Puustinen, M., Laine, J., and Räsänen, A. (2009). PPOOLEX experiments on thermal stratification and mixing. Research report condex 1/2008, Lappeenranta University of Technology.
- Puustinen, M., Laine, J., and Räsänen, A. (2011). Multiple blowdown pipe experiments with the ppoollex facility. Research report condex 2/2010, Lappeenranta University of Technology.
- Puustinen, M., Laine, J., Räsänen, A., and Hujala, E. (2013b). Chugging test with dn100 blowdown pipe in the ppoollex facility. Research report poollex 2/2005, Lappeenranta University of Technology.
- Puustinen, M., Partanen, H., Räsänen, A., and Purhonen, H. (2006). PPOOLEX facility description. Research report poollex 2/2006, Lappeenranta University of Technology.
- Puzyrewski, R. (1969). *Pr.Inst. Maszyn Przepływowych (in Polish)*, Vol. 47.
- Rassame, S., Griffiths, M., Yang, J., Ju, P., Sharma, S., Hibiki, T., and Ishii, M. (2015). Experimental investigation of void distribution in suppression pool over the duration of a loss of coolant accident using steam-water two-phase mixture. *Annals of Nuclear Energy*, 75:570–580.
- Retталиата, T. (1936). Undercolling in steam nozzles. *Trans. A.S.M.E.*, Vol. 58:599.
- Reynolds, W. C. (1979). *Thermodynamic properties in SI: Graphs, Tables, and Computational Equations for 40 Substances*. Department of mechanical Engineering, Stanford University.
- Richardson, L. F. and Gaunt, J. A. (1927). The deferred approach to the limit. *Philos. Trans. Roy. Soc. London. Ser. A.*, Vol. 226:299–361.
- Roache, P. J. (1994). Perspective: A method for uniform reporting of grid refinement studies. *J. Fluids Eng.*, Vol. 116:405–413.
- Roache, P. J. (1997). Quantification of uncertainty in computational fluid dynamics. *Annual Review of Fluid Mechanics*, Vol. 29:123–160.
- Roache, P. J. (1998). Verification of codes and calculations. *AIAA Journal*, Vol. 36 (5):696–702.
- Roe, P. L. (1986). Characteristic based schemes for the Euler equations. *Annual Review of Fluid Mechanics*, Vol. 18:337–365.
- Sargis, D. A., Stuhmiller, J. H., and Wang, S. S. (1978). A fundamental thermalhydraulic model to predict steam chugging phenomena. Technical report, Electric Power Research Institute.

- Schatz, M., Eberle, T., Grübel, M., Starzmann, J., Vogt, D. M., and Sürken, N. (2014). Two-phase flow modeling and measurements in low-pressure turbines: Part 2 — turbine wetness measurement and comparison to cfd-predictions. *J. Eng. Gas Turbines Power*, Vol. 137(4):042603–042603–9.
- Schiller, L. and Naumann, A. (1933). Über die grundlegenden Berechnungen bei der Schwerkraftbereitung. *Z. Verein Deutscher Ing.*, 77:318–320.
- Schnerr, G. H. (1989). Two-dimensional transonic flow with energy supplied by homogeneous condensation: Onset condition and two-dimensional structure of steady laval nozzle flow. *Experiments in Fluids*, Vol. 7:145–156.
- Senoo, S. (2012). Development of design method for supersonic turbine aerofoils near the tip of long blades in steam turbines part 1: Overall configuration. In *Proc. of ASME Turbo Expo, Copenhagen, Denmark, June 11-15, 1-11*.
- Senoo, S. and Ono, H. (2013). Development of design method for supersonic turbine aerofoils near the tip of long blades in steam turbines part 2: Configuration details and validation. In *Proc. of ASME Turbo Expo, San Antonio, Texas, USA, June 3-7, 1-12*.
- Seong, H. J., Hee, C. N., and Mayinger, F. (2000). Measurement of heat transfer coefficients for direct contact condensation in core makeup tanks using holographic interferometer. *Nucl. Eng. Des.*, 199:75–83.
- Simpson, D. A. and White, A. J. (2005). Viscous and unsteadyflow calculations of condensing steam in nozzles. *Int. J. Heat and Fluid Flow*, Vol. 26 (1):71–79.
- Singh, U. (2001). A study of the effects of geometrical changes on wetness in low pressure steam turbine. In *The 4th European Conference on Turbomachinery, Firenze, Italy, pp. 823-841*.
- Skillings, S., Walters, P., and Moore, M. (1987). A study of supercritical heat addition as potential loss mechanism in condensing steam turbines. In *Int. Mech. Engrs., Intl. Conf. on Turbomachinery, Cambridge, C259/87, 125-134*.
- Smith, B. L. (2007). A numerical investigation of three-dimensional flows in large volumes in the context of passive containment cooling in BWRs. *Nuclear Engineering and Design*, 237/11:1175–1184.
- Sonoda, T., Arima, T., Olhofer, M., Sendhoff, B., Kost, F., and Giess, P. A. (2006). A study of advanced high-loaded transonic turbine airfoils. *J. Turbomachinery*, Vol. 128 (4):650–657.
- Starzmann, J., Casey, M. V., and Mayer, J. F. (2013a). *Water Droplet Flow Paths and Droplet Deposition in Low Pressure Steam Turbines*, chapter IV, pages pp. 351–365. Springer Berlin Heidelberg.

- Starzmann, J., Kaluza, P., Casey, M. V., and Sieverding, F. (2013b). On kinematic relaxation and deposition of water droplets in the last stages of low pressure steam turbines. In *Proc. of ASME Turbo Expo, San Antonio, Texas, USA, June 3-7, 1-12*.
- Starzmann, J., Schatz, M., Casey, M. V., Mayer, J. F., and Sieverding, F. (2011). Modelling and validation of wet steam flow in a low pressure steam turbine. In *Proc. ASME Turbo Expo, GT2011-45, Vancouver, Canada, June 6-10, 1-12*.
- Stodola, A. (1915). Undercooling of steam in nozzles. *Engineering*, pages 643–646.
- Tanskanen, V. (2012). *CFD modelling of direct contact condensation in suppression pools by applying condensation models of separated flow*. Acta Universitatis Lappeenrantaensis 472, Lappeenranta University of Technology. ISBN 978-952-265-221-8, ISBN 978-952-265-222-5 (PDF), ISSN 1456-4491.
- Tanskanen, V., Hujala, E., and Puustinen, M. (2016). Numerical simulation of PPOOLEX chugging case with a Rayleigh-Taylor instability model for interfacial area (the report being written now), SAFIR/INSTAB Research report 4/2015. SAFIR Research Report CONDEX 3/2010, Nuclear Engineering, Lappeenranta University of Technology.
- Tanskanen, V. and Jordan, A. (2011). 3D CFD simulation of STB-28 steam discharge experiment. SAFIR Research Report CONDEX 3/2010, Lappeenranta University of Technology.
- Tanskanen, V., Jordan, A., Puustinen, M., and Kyrki-Rajamäki, R. (2014). CFD simulation and pattern recognition analysis of the chugging condensation regime. *Annals of Nuclear Energy*, 66:133–143.
- Tanskanen, V., Lakehal, D., and Puustinen, M. (2008). Validation of Direct Contact Condensation CFD Models Against Condensation Pool Experiments. In *XCFD4NRS, Grenoble, France*.
- Tanskanen, V., Patel, G., Puustinen, M., Hujala, E., Kyrki-Rajamäki, R., and Hyvärinen, J. (2015). CFD modelling of chugging condensation regime of BWR suppression pool experiments. In *16th International Meeting on Nuclear Reactor Thermal Hydraulics (NURETH-16), Chicago, IL, August 30 - September 4 2015*, page 12.
- Thiele, R. (2010). Modeling of direct contact condensation with openfoam. Master thesis, KTH, Royal Institute of Technology, Division of Nuclear Reactor Technology, Royal Institute of Technology, Stockholm, Sweden. ISSN 0280-316X.
- Thomson, W. (1870). On the equilibrium of vapour at a curved surface of a liquid. *Proc. Royal Society*, Vol. 7:63–68.
- Torre, D., Vázquez, R., Armañanzas, L., Partida, F., and García-Valdecasas., G. (2012). The effect of airfoil thickness on the efficiency of lp turbines. In *Proc. of ASME Turbo Expo, GT2012-68556, Copenhagen, Denmark, June 11-15, pp. 1-10*.

- TVO (2008). Nuclear power plant units olkiluoto 1 and olkiluoto 2.
- Varzaly, A. M., Grafton, W. A., Chang, H., and Mitchell, M. K. (1977). Mark iii confirmatory test program:  $1/\sqrt{3}$  scale condensation and stratification phenomena, test series 5807. Technical report, General Electric Co., San Jose, Calif. (USA). Boiling Water Reactor Systems Dept.
- Volmer, M. and Weber, A. (1926). Keimbildung in übersättigten gebilden. *Z. Phys. Chem.*, Vol. 119:227–301.
- Vukalovich, M. P. (1958). *Thermodynamic Properties of Water and Steam*. Mashgis, Moscow.
- Wagner, W. and Kruse, A. (1998). *The Industrial Standard IAPWS-IF97: Properties of Water and Steam*. Springer, Berlin.
- Walsche, C. D. and Cachard, F. D. (1996). Experimental investigation of condensation and mixing during venting of a steam/non-condensable gas mixture into a pressure-suppression pool. Technical report, IAEA Report, pp. 53–61.
- Wegener, P. P. (1966). *Gas dynamics of expansion flows with condensation and homogeneous nucleation of water vapour; Nonequilibrium Flows, Part 1*. Marcel Dekker, New York.
- White, A. (2000). Numerical investigation of condensing steam flow in boundary layers. *Int. J. Heat and Fluid Flow*, Vol. 21:727–734.
- White, A. (2003). A comparison of modeling methods for polydispersed wet-steam flow. *Int. J. Numer. Meth. Eng.*, Vol. 57:819–834.
- White, A. J. and Hounslow, M. J. (2000). Modelling droplet size distributions in polydispersed wet-steam flows. *Int. J. Heat Mass Transfer*, Vol. 43:1873–1884.
- White, A. J. and Young, J. B. (1993). Time-marching method for the prediction of two-dimensional unsteady flows of condensing steam. *AIAA J. Propulsion and Power*, Vol. 9 (4):579–587.
- White, A. J. and Young, J. B. (2008). Transient calculations of nucleation and droplet growth for wet-steam expansions. In *ICPWS XV, Berlin, Germany, September 8-11, pp. 1-8*.
- White, A. J., Young, J. B., and Walters, P. T. (1996). Experimental validation of condensing flow theory for a stationary cascade of steam turbine blade. *Philos. Trans. Roy. Soc. London.*, Vol. A 354:59–88.
- Wikdahl, C. E. (2007). Marvikenreaktorn - ett industripolitiskt utvecklingsprojekt i otakt med tiden. Technical Report SKI Rapport 2007:18, SKI.

- Winkler, G. and Schnerr, G. H. (2001). Nucleating unsteady flows in low pressure steam turbine stages. In *Proc. 4th European Conf. on Turbomachinery, Fluid Dynamics and Thermodynamics, Firenze, Italy*, 793-802.
- Wróblewski, W., Dykas, S., Gardzilewicz, A., and Kolovratnik, M. (2009). Numerical and experimental investigations of steam condensation in lp part of a large power turbine. *J. Fluids Eng.*, Vol. 131.
- Wu, X. Z., Yan, J. J., Shao, S. F., Cao, Y., and Liu, J. P. (2007). Experimental study on the condensation of supersonic steam jet submerged in quiescent subcooled water: steam plume shape and heat transfer. *Int. Journal of Multiphase Flow*, 33/12:1296–1307.
- Yadigaroglu, G. (2004). Computational Fluid Dynamics for nuclear applications: from CFD to multi-scale CMFD. *Nucl. Eng. Des.*, 235:153–164.
- Yamamoto, S., Sasao, Y., Kato, H., Satsuki, H., Ooyama, H., and Ishizaka, K. (2010). Numerical and experimental investigation of unsteady 3-d wet-steam flows through two-stage stator-rotor cascade channels. In *Proc. ASME Turbo Expo, GT2010-22796, Glasgow, UK, June 14-18, 1-9*.
- Yellott, J. I. and Holland, C. K. (1937). The condensation of flowing steam - condensation in diverging nozzles. *Engineering*, Vol. 143:647–703.
- Youn, D. H., Ko, K. B., Lee, Y. Y., Kim, M. H., Bae, Y. Y., and Park, J. K. (2003). The direct contact condensation of steam in a pool at low mass flux. *Nuclear Science and Technology*, 40/10:881–885.
- Young, J. B. (1973). *Nucleation in High Pressure Steam and Flow in Turbines*. PhD thesis, University of Birmingham.
- Young, J. B. (1982). The spontaneous condensation of steam in supersonic nozzles. *Physico Chemical Hydrodynamics*, Vol. 3:57–82.
- Young, J. B. (1988). An equation of state for steam for turbomachinery and other flow calculations. *J. of Eng. for Gas Turbines and Power*, Vol. 110:1–7.
- Young, J. B. (1992). Two-Dimensional nonequilibrium wet steam calculations for nozzles and turbine cascades. *ASME J. Turbomachinery*, Vol. 114:569–579.
- Young, J. B. (1993). The condensation and evaporation of liquid droplets at arbitrary knudsen number in the presence of an inert gas. *Int. J. Heat Mass Transfer*, Vol. 36:2941–2956.
- Zaichik, L., Simonin, O., and Alipchenkov, V. (2003). Two statistical models for predicting collision rates of inertial particles in homogeneous isotropic turbulence. *Phys. Fluids*, Vol. 15:2995–3005.
- Zeldovich, J. (1942). Theory of the formation of a new phase. *J. Expl. Theoret. Physics*, Vol. 12:525.

- 
- Zhou, C., Hodson, H., and Himmel, C. (2014). The effects of trailing edge thickness on the losses of ultrahigh lift low pressure turbine blades. *J. Turbomach.*, Vol. 136 (8):081011–1–9.



# Publication I

Patel, G., Tanskanen, V., and Kyrki-Rajamäki, R. (2014).  
**Numerical modelling of low-Reynolds number direct contact  
condensation in a suppression pool test facility**

Annals of Nuclear Energy  
Vol. 71, pp. 376-387

© Elsevier, 2014

Reprinted with permission from the publisher





Contents lists available at ScienceDirect

## Annals of Nuclear Energy

journal homepage: [www.elsevier.com/locate/anucene](http://www.elsevier.com/locate/anucene)

## Numerical modelling of low-Reynolds number direct contact condensation in a suppression pool test facility



G. Patel\*, V. Tanskanen, R. Kyrki-Rajamäki

Laboratory of Nuclear Engineering, LUT Energy, School of Technology, Lappeenranta University of Technology (LUT), PO Box 20, FIN-53851 Lappeenranta, Finland

## ARTICLE INFO

## Article history:

Received 29 October 2013  
 Received in revised form 10 April 2014  
 Accepted 14 April 2014  
 Available online 13 May 2014

## Keywords:

Two-phase flow  
 Condensation  
 CFD  
 Suppression pool

## ABSTRACT

In the safety pressure suppression pool systems of Boiling Water Reactors (BWRs), the condensation rate has to be maintained high enough in order to fulfill their safety function. A major part of this condensation occurs as direct contact condensation (DCC), which governs different modes varying from vigorous chugging of collapsing bubbles to mild condensation on almost flat steam–water interface. This paper discusses the Computational Fluid Dynamics (CFD) simulations of the latter, low-Reynolds number weak condensation regime. The numerical simulations were performed with two CFD codes, NEPTUNE\_CFD and OpenFOAM, in which the DCC phenomenon was modelled by using the Eulerian two-fluid approach of interpenetrating continua without interfacial tracking. The interfacial heat transfer between steam and water was modelled by using the DCC models based on the surface renewal and the surface divergence theories. Flow turbulence was solved by employing the standard  $k-\epsilon$  turbulence model. The CFD results of this study were validated against the test results of the POOLEX facility of Lappeenranta University of Technology. In the reference test STB-31, the condensation phenomena were limited to only occur on a stable steam–water interface by very low steam mass flux applied and thermal insulation of the blow-down pipe. The simulation results demonstrated that the surface divergence model predicted the condensation phenomena quite accurately both qualitatively and quantitatively while the surface renewal model overestimated it strongly.

© 2014 Elsevier Ltd. All rights reserved.

## 1. Introduction

Direct contact condensation (DCC) occurs when saturated vapour contacts and condenses on a sub-cooled liquid interface directly. The behaviour of this interface is of prime interest as it is governed by the transfer processes in the vapour and liquid regions around the interface. DCC has a fundamental importance in a variety of industrial applications such as boilers, propulsion systems, condensers, steam jet injectors, direct contact feedwater heaters, as well as in nuclear reactor systems e.g., the pressure suppression system of Boiling Water Reactors (BWRs) and the rapid depressurization system of current Pressurized Water Reactors (PWRs) (Chan and Lee, 1982; Song et al., 2012; Coste et al., 2012). The main design purpose of a pressure suppression pool in BWRs is to mitigate the threats of containment overpressurization and fission product releases. It is one of the key systems during a loss of coolant accident (LOCA) or safety valve actuation, which provides a large pressure and heat sink by condensing steam into a denser volume of water and absorbing the energy discharged

from a reactor vessel (Lahey and Moody, 1993). The steam discharge into sub-cooled water is connected with hydrodynamic and thermodynamic issues like bubble dynamics, thermal stratification, mixing, steam condensation within water pool, within ducts, and at wall surfaces, etc. Injected steam interacts with pool water by heat transfer, rapid condensation and momentum exchange which induces hydrodynamic loads to the pool structures. Therefore, detailed analysis of steam blowdown phenomena either by experiments or with numerical simulations has a great importance from the nuclear reactor safety point of view.

To enhance the knowledge about the complicated physics of steam blowdown events in water pool, comprehensive studies have been made by numerous researchers on the air/steam discharge into sub-cooled water. Several experimental studies with suppression pool have been reported in the literature by various injection systems both with horizontal and vertical blowdown pipes. Although the DCC phenomena include similar condensation modes in horizontal, vertical, and nozzle type steam injections, the geometry itself and different injectors like spargers make the steam–water interface structures in horizontal and nozzle systems much different from the typical large diameter vertical pipe systems of General Electric's MARK I and MARK II, and Nordic

\* Corresponding author. Tel.: +358 40 152 9413; fax: +358 5 621 63 99.  
 E-mail address: [Giteshkumar.Patel@lut.fi](mailto:Giteshkumar.Patel@lut.fi) (G. Patel).

ASEA-Atom type BWR's (Kang and Song, 2008; Gulawani et al., 2009). In the past, some major experimental studies have been done on various aspects with vertical blowdown pipes. For example, significant experiments have been organized in the Marviken facility to analyse the pressure suppression principle for a MARK II type containment during 1972–1981 (Wikdahl, 2007). These experiments were focused on the dynamic processes of the condensation as well. McIntyre et al. (1976) and Grafton et al. (1977) conducted suppression pool experiments with a single vertical pipe to analyse the pool responses in LOCA situations. Kennedy et al. (1978) performed experiments of MARK I suppression pool with a 1/4 scale facility to test the effect of the rigidity of the blowdown pipe header on the pressure impact loads. Aust and Seeliger (1982) conducted suppression pool tests which emphasized the mitigation of dynamic loads by pipe design. Moreover, vertical blowdown pipe experiments with air have been conducted by Chen and Dhir (1982) to develop a theoretical model for bubble growth at the pipe exit. Chan and Lee (1982) organized experiments by varying steam mass fluxes and pool temperatures to develop a condensation regime map. Later on, smaller scale blowdown experiments were performed by Meier et al. (1998) and Meier (1999) with a transparent tank using steam and non-condensables to analyse the effect of pipe length and compressibility of the gas in piping on the bubble size, shape, and frequency. Later on suppression pool experiments have been done with the PANDA and LINX experimental facilities, in which, the PANDA facility was utilized to study passive containment cooling systems and the interaction between the various systems components during long-term cooling (Smith, 2007) and the LINX facility was aimed to study condensation, mixing, the effect of non-condensable gases and stratification in suppression pools (Hart et al., 2001). Extensive experimental work has been done by Puustinen et al. (2013) focusing on several BWR containment related issues such as dynamics loading of pool structures, thermal stratifications and mixing, wall condensation, and behaviour of parallel blowdown pipes.

In the field of nuclear safety analysis, Computational Fluid Dynamics (CFD) has become an increasingly applicable tool for thermohydraulic investigations (Bestion, 2012). However, published work on the numerical simulations of the DCC phenomena in the pressure suppression pool with vertical air/steam blowdown cases is rather sparse. For example Meier et al. (2000) and Yadigaroglu (2004) utilized piecewise linear interface construction-volume of fluid (PLIC-VOF) method to simulate large steam-air bubbles in a water pool without mass transfer. Also Thiele (2010) conducted VOF simulations with mass transfer based on temperature difference. Pättikangas et al. (2010) performed 2D-axisymmetric CFD simulation of the water hammer due to a steam bubble collapse by utilizing two-fluid models. Tanskanen et al. (2008) utilized the NEPTUNE\_CFD code to model a low DCC rate case with different inlet boundary conditions. Tanskanen (2012) continued that work and conducted also an analysis of chugging phenomena by means of Eulerian simulations with heat and mass transfer.

Before modelling very rapid and complex steam chugging or other DCC modes with high condensation rate, it is essential to analyse the performance of available DCC models to calculate the condensation phenomena. The present work is related to the steam condensation case of a thermally insulated vertical blowdown pipe with a relatively large diameter and low steam mass flux. The modelled DCC mode in the present work is a special case corresponds to the 'oscillatory interface condensation' mode (Chan and Lee, 1982) and the 'condensation within the blowdown pipe' mode (Lahey and Moody, 1993). This special case is a simple starting point for CFD simulations with phase change due to its mild condensation rates. The DCC phenomena of steam–water system are solved by the Eulerian two-fluid approach. The interfacial heat transfer

between steam and water phases is calculated using two different DCC models. The numerical results are partially validated with the steam blowdown test 'STB-31' of Laine and Puustinen (2006) conducted with the condensation pool test facility POOLEX of Lappeenranta University of Technology (LUT).

## 2. POOLEX STB-31 experiment

The main objective of the POOLEX test program was to enhance the understanding and to grow the fidelity in the assessment of various complex phenomena in BWR's containment during steam discharge into sub-cooled water pool. Moreover, these experiments were aimed to establish a high-grade database for different validation purposes of CFD codes and corresponding models (Puustinen et al., 2013). A schematic view of the POOLEX test facility is shown in Fig. 1. It was a cylinder shaped stainless steel pool with an open top and a conical bottom. The test facility consisted of the steam generator, the steam lines assembly, the blowdown pipe, and the water pool.

The steam generators of the Parallel Channel Test Loop (PACTEL) facility (Tuunanen et al., 1998) were used as a steam source during the test. The maximum operating pressures on the primary and the secondary sides of the PACTEL facility are 8.0 MPa and 4.6 MPa, respectively. The maximum electrical heating power of the PACTEL core simulator available for steam production is 1 MW. The steam lines from PACTEL to POOLEX facility were thermally insulated with mineral wool to prevent steam from condensing before being conveyed to the blowdown pipe. A DN200 stainless steel pipe was used as a blowdown pipe, and its lower end was submerged in the water pool. In the STB-31 test, the blowdown pipe was insulated with a 50 mm thick layer of hard polyurethane foam to prevent wall condensation. The total volume of pool water was approximately 12 m<sup>3</sup>. The test facility was equipped with thermocouples for measuring steam and pool water temperatures. To capture the pressure behaviour in the blowdown pipe, in the steam line, and at the pool bottom, the pressure transducers were installed. Steam flow rate was measured with a rotameter (Krohne Model H250). Visual observation of the interior was possible through circular windows installed in the pool wall. Additional details pertaining to the measurement instrumentation and data acquisition have been given by Laine and Puustinen (2006). The geometrical parameters of the test facility are listed in Table 1.

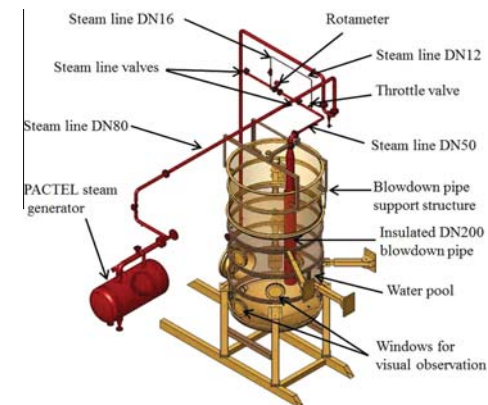


Fig. 1. POOLEX test facility (Laine and Puustinen, 2006).

**Table 1**

The geometrical configuration of the POOLEX test facility (Laine and Puustinen, 2006).

Pool height [m]	5
Pool inner diameter [m]	2.4
Pool cross section area [m <sup>2</sup> ]	4.5
Blowdown pipe length [m]	4
Blowdown pipe diameter [m]	0.214
$A_{\text{pipe}}/A_{\text{pool}} \times 100$	0.8
Visual observation windows	5

**Table 2**

The test parameters of the STB-31 experiment (Laine and Puustinen, 2006).

Initial pool water temperature [°C]	32
Initial water level in pool [m]	2.95
Steam source pressure [MPa]	0.6–1.0
Steam temperature in blowdown pipe [°C]	104.35
Steam pressure in blowdown pipe [MPa]	0.119435
Steam flow rate [gs <sup>-1</sup> ]	0.5–1.5
Duration [s]	6000

An experiment labeled as STB-31 was selected as the CFD validation case of this study. During the STB-31 test, the pool was filled with isothermal water. The steam mass flow rate was controlled by using a manual throttle valve throughout the test to prevent steam bubble formation and to keep the steam–water interface as close as possible to the pipe outlet. Although the steam–water interface was almost smooth during the quasi-steady periods in the test, some very low amplitude oscillation was observed in the video samples from these periods. The oscillation could have originated from possible minor mechanical vibrations of the facility or from the condensation phenomena itself. During the experiment, there were several quasi-steady state intervals suitable for the CFD validation. The experimental conditions of the STB-31 test are specified in Table 2.

During the STB-31 test, it was seen that there were non-condensing bubbles escaping around the pipe lip. Thus it was assumed that dissolved air was released from the pool water, and it slowly accumulated as a layer between steam and water inside the blowdown pipe possibly having an effect on the condensation process at the steam–water interface. It was essential to remove the air layer from the blowdown pipe. This was done by increasing the steam flow rate at regular time periods (e.g., during 1185–1525 s, 2455–2830 s, and 3800–3950 s). After air was blown out from the pipe, steam mass flow rate was decreased to attain stable interface conditions again. Fig. 2(a)–(c) shows video frames of stable interface, stable interface with escaping steam and strong blowdown during the STB-31 POOLEX test, respectively.

The Couette flow film model of Ghiaasiaan (2008) was applied to produce an estimation of the non-condensables effect on the condensation rate during the selected period of the experiment (Tanskanen, 2012). The analysis was based on the air and steam partial pressures derived from the measured temperatures and the total pressure at the outlet of the pipe. The model provided an alternative condensation rate for each measured mass flow rate value. These scaled-up values represented the optimal condensation rates without the presence of non-condensable gases. The analysis indicated approximately 3–50% higher condensation rates without the presence of non-condensable gases. The measurement error of mass flow rate exceeds that amount remarkably. However, the uncertainty of the analysis remained high. Calculation of total derivatives indicated that errors of one order of magnitude are possible. The analysis of non-condensable gases in the STB-31 case has been discussed more in Tanskanen (2012).

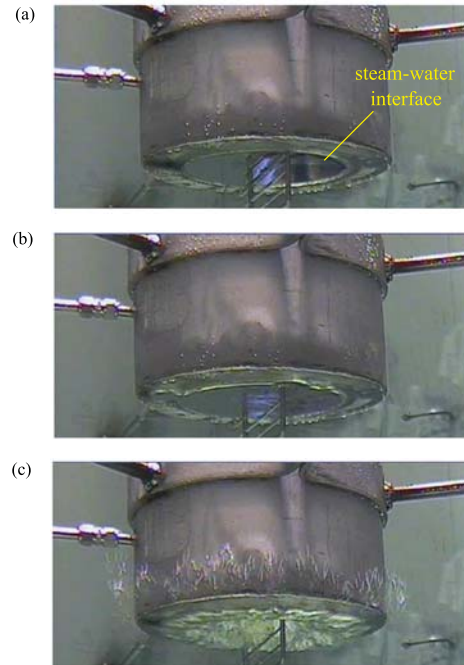


Fig. 2. Instantaneous images of (a) stable interface, (b) stable interface with escaping steam, and (c) strong blowdown during the STB-31 POOLEX test (Laine and Puustinen, 2006).

### 3. Numerical methodology

In this work, low-Reynolds number DCC was modelled with OpenFOAM CFD code and the results were compared to previous NEPTUNE\_CFD results. Eulerian two-fluid approach was used in the both codes. In Eulerian 2-phase modelling, the interface between the phases is not necessarily tracked, because the existence of separate conservation equations for each phase does not require that. However, separate closure laws (e.g., drag, lift and added mass forces) are needed to close the equations and make the behaviour of smeared interface physical. In this case of a large interface under phase change, the interfacial drag force and the heat/mass transfer rate are the most relevant additions needed. These models can be implemented typically by using source terms (mass, momentum, heat) that are activated by certain volume fraction conditions i.e., only near the interface. There are workarounds e.g., LI3C model of Coste et al. (2008) also, in which the interface region is recognized more accurately making possible to apply the source terms more precisely to the correct phase and to the suitable distances from the interface.

In this study, the traditional source term approach was used due to its availability in the both of codes. Schiller and Naumann (1933) drag coefficient was used in the drag models of the both codes i.e., weighting the coefficient by the product of volume fractions in the OpenFOAM and according the SIMMER model (Laviéville et al., 2006) in the NEPTUNE\_CFD. The heat and mass transfer source terms were limited to the interfacial region by

the interfacial area density i.e., the gradient of volume fraction. Only the liquid phase heat transfer was taken into account due to its dominance. Thus a heat transfer correlation for the heat source term was needed only for the liquid phase. The interfacial heat transfer was modelled using the DCC models of Hughes and Duffey (1991) (HD) and Lakehal et al. (2008) (LH). The standard k- $\epsilon$  turbulence model of Launder and Sharma (1974) was employed for modelling the flow turbulence.

### 3.1. Governing equations

The details about two-phase flow models utilized in this work with NEPTUNE\_CFD code can be found in Laviéville et al. (2006). This section summarizes the governing equations of mass, momentum, and energy conservation regarding the OpenFOAM simulations (Peltola, 2012).

#### 3.1.1. Mass conservation equation

The mass continuity equation describes the mass flux ratio into and out of a control volume and accumulation into a corresponding control volume. The fundamental form of the equation for two-phase flows is written as

$$\frac{\partial \alpha_\phi \rho_\phi}{\partial t} + \nabla \cdot (\alpha_\phi \rho_\phi \mathbf{U}_\phi) = \Gamma_\phi. \quad (1)$$

Here  $\phi$  stands for an arbitrary phase (later on  $\phi = a$  for steam and  $\phi = b$  for water),  $\alpha_\phi$  is the phase fraction,  $\rho_\phi$  is the density, and  $\mathbf{U}_\phi$  represents the velocity of the  $\phi$  phase.  $\Gamma_\phi$  expresses the mass source/sink per unit volume. This source term can be defined by using a phase change model (see the details in Section 3.2 below).

#### 3.1.2. Momentum transfer equation

In the case of two-phase flow, the momentum equations are solved for each phase independently depending upon the phase volume fraction. The momentum equation for phase  $\phi$  is expressed as

$$\begin{aligned} \frac{\partial \alpha_\phi \rho_\phi \mathbf{U}_\phi}{\partial t} + \nabla \cdot (\alpha_\phi \rho_\phi \mathbf{U}_\phi \mathbf{U}_\phi) + \alpha_\phi \nabla \cdot \boldsymbol{\tau}_\phi + \nabla \cdot (\alpha_\phi \rho_\phi \mathbf{R}_\phi) \\ = -\alpha_\phi \nabla \bar{p} + \alpha_\phi \rho_\phi \mathbf{g} + \mathbf{M}_\phi, \end{aligned} \quad (2)$$

where  $\boldsymbol{\tau}_\phi$  and  $\mathbf{R}_\phi$  describe the viscous stress tensor and the turbulent stress tensor, respectively. The terms on the right hand side of Eq. (2) represent the forces acting on the  $\phi$  phase in the control volume, where  $\nabla \bar{p}$ ,  $\mathbf{g}$  and  $\mathbf{M}$  denote the overall pressure gradient, the gravitational force, and the interphase momentum forces, respectively. In general, the interphase momentum transfer term consists of all the interfacial forces, e.g., drag, lift, virtual mass, wall lubrication force, etc. In the present study, only the effect of drag force was considered while the other interfacial forces were omitted. Thus, the interphase momentum exchange coefficient  $M_{ab}$  can be written as

$$M_{ab} = \alpha_a \alpha_b \frac{3}{4} C_{D,a} \rho_b \frac{1}{d_B} |U_a - U_b| (U_a - U_b). \quad (3)$$

Here  $d_b$  is the bubble diameter which is considered as a constant value (i.e., 1 mm) during the simulations with both the codes and  $C_D$  is the drag coefficient, which is determined by Schiller and Naumann (1933).

#### 3.1.3. Energy conservation

The energy conservation equation is given by

$$\begin{aligned} \frac{\partial}{\partial t} (\alpha_\phi \rho_\phi H_\phi) + \nabla \cdot (\alpha_\phi \rho_\phi \mathbf{U}_\phi H_\phi) \\ = \nabla \cdot (\alpha_\phi \rho_\phi D_{T,eff,\phi} \nabla H_\phi) + \Gamma_\phi H_{i,\phi} + Q_\phi, \end{aligned} \quad (4)$$

where  $H_\phi$  and  $H_{i,\phi}$  are the specific enthalpy and the interfacial enthalpy of the  $\phi$  phase, respectively. The term  $D_{T,eff,\phi}$  indicates the phase effective thermal diffusivity ( $m^2/s$ ).  $Q_\phi$  denotes the volumetric interfacial heat transfer rate ( $kg/m^3s$ ).

### 3.2. Phase change models

In this work, the phase change model has been used to simulate the DCC phenomenon, which describes the phase change induced by interphase heat transfer of adjacent convective flows. The approach is only appropriate for the change of phase in pure substances and deals with the heat transfer processes on each side of the phase interface. The interfacial heat transfer modelling is based on the two-resistance approach, in which the heat transfer is calculated between each phase and the interface between the phases (Peltola, 2012). The sensible heat fluxes from the interface to steam and from the interface to water are defined as follows,

$$q_a = a_{ia} h_{i,a} (T_s - T_a), \quad (5)$$

$$q_b = a_{ib} h_{i,b} (T_s - T_b). \quad (6)$$

Here  $a_{ia}$  and  $a_{ib}$  are the interfacial area densities ( $m^{-1}$ ) for steam and water, respectively. The interfacial area density was calculated from the gradient of void fraction (i.e.,  $a_{i\phi} = |\nabla \alpha_{i\phi}|$ ). The interfacial temperature,  $T_s$ , is set to the saturation temperature. The terms  $h_{i,a}$  and  $h_{i,b}$  represent the heat transfer coefficients of steam and water.

The interface mass transfer is determined from the total heat balance. The total heat flux balance is yielded from equations

$$Q_a = q_a - \Gamma_{i,b} H_{i,a} \quad (7)$$

$$Q_b = q_b + \Gamma_{i,b} H_{i,b}. \quad (8)$$

Here  $\Gamma_{i,b}$  denotes the mass flux due to the phase change from steam to water. By enforcing the overall heat balance,  $Q_a + Q_b = 0$ , the mass transfer due to the phase change can be calculated from

$$\Gamma_{i,b} = \frac{q_a + q_b}{H_{i,a} - H_{i,b}}. \quad (9)$$

### 3.3. Heat transfer models

The heat transfer coefficient for the water phase is defined as

$$h_{i,b} = \frac{Nu_b \lambda_b}{L_t}, \quad (10)$$

where  $\lambda_b$  determines the thermal conductivity and  $L_t$  is the characteristic length.  $Nu_b$  is the Nusselt number, which is dependent on the turbulent Reynolds number and the Prandtl number. The Nusselt number calculation was based on the HD and the LH models used previously in the NEPTUNE\_CFD simulations of Tanskanen et al. (2008) and Tanskanen (2012). The steam side heat transfer has been omitted in this study because the steam side is in saturated conditions and the heat transfer efficiency of steam is much smaller than that of liquid water.

#### 3.3.1. The HD model (Hughes and Duffey, 1991)

The HD model is based on the surface renewal model of Hughes and Duffey (1991). This model has been tested for a concurrent horizontal stratified flow of steam–water in a rectangular channel (Hughes and Duffey, 1991). The Nusselt number formulation is defined as

$$Nu_b = \frac{2}{\sqrt{\pi}} Re_t Pr^{1/2}, \quad (11)$$

where  $Re_t$  is calculated as

$$\text{Re}_t = \frac{u_t L_t}{\nu_b} \quad (12)$$

The turbulent length scale is defined as

$$L_t = C_\mu \frac{k_b^{3/2}}{\epsilon_b} \quad (13)$$

and the turbulent velocity scale,  $u_t$ , has the form

$$u_t = \min \left( |U_b|, C_\mu^{1/4} k_b^{1/2} \right) \quad \text{or} \quad u_t = (\nu_b \epsilon_b)^{1/4} \quad (14)$$

where  $k_b$  and  $\epsilon_b$  are the turbulence kinetic energy and its dissipation rate, respectively, and  $C_\mu$  is the turbulent viscosity constant of the  $k$ - $\epsilon$  turbulence model. The first definition of  $u_t$  in Eq. (14) is the modified version, which is implemented in the standard NEPTUNE\_CFD code, and the latter is the original version of the HD model. Both produced similar results with the standard  $k$ - $\epsilon$  turbulence model. Therefore, the latter one is used in this study.

### 3.3.2. The LH model (Lakehal et al., 2008)

The LH model is based on the surface divergence theory of Banerjee (1990). The applicability of this model has typically been tested for mildly sheared concurrent and countercurrent horizontal two-phase flows (Lakehal et al., 2008). The Nusselt number is defined as

$$\text{Nu}_b = Bf[\text{Re}_t^m] \text{Re}_t \text{Pr}^{1/2} \quad (15)$$

Here  $B$  is the model constant (i.e.,  $B = 0.35$  for  $\text{Pr} \approx 1$  and  $B = 0.45$  for  $\text{Pr} \gg 1$ ) and  $f(\text{Re}_t^m)$  is given as

$$f[\text{Re}_t^m] = \left[ 0.3 \left( 2.83 \text{Re}_t^{3/4} - 2.14 \text{Re}_t^{2/3} \right) \right]^{1/4} \text{Re}_t^{-1/2} \quad (16)$$

where  $\text{Re}_t$ , is determined from  $k_b$ ,  $\epsilon_b$ , and  $\nu_b$  as

$$\text{Re}_t = \frac{k_b^2}{\nu_b \epsilon_b} \quad (17)$$

The same form of the heat transfer equation is used by the LH model as given in Eq. (10), but it uses a different form of the  $L_t$ , i.e.,

$$L_t = \frac{\nu_b}{u_t} \text{Re}_t \quad (18)$$

where  $u_t$  is derived from the later definition of Eq. (14).

### 3.4. Turbulence models

The standard  $k$ - $\epsilon$  model equations of the turbulent kinetic energy and its dissipation rate in OpenFOAM are solved for the continuous phase, which can be written as follows,

$$\frac{\partial k_\phi}{\partial t} + U_\phi \nabla k_\phi - \nabla \cdot \left( \left( \nu_\phi + \frac{\nu_{t,\phi}}{\sigma_k} \right) \nabla k_\phi \right) + R_{k,\phi} \nabla k_\phi = G_\phi - \epsilon_\phi \quad (19)$$

$$\begin{aligned} \frac{\partial \epsilon_\phi}{\partial t} + U_\phi \nabla \epsilon_\phi - \nabla \cdot \left( \left( \nu_\phi + \frac{\nu_{t,\phi}}{\sigma_\epsilon} \right) \nabla \epsilon_\phi \right) + R_{\epsilon,\phi} \nabla \epsilon_\phi \\ = C_1 G_\phi \frac{\epsilon_\phi}{k_\phi} - C_2 \frac{\epsilon_\phi^2}{k_\phi} \end{aligned} \quad (20)$$

In Eqs. (19) and (20),  $R_{k,\phi}$  and  $R_{\epsilon,\phi}$  are the volume fraction gradient fluxes. The term  $G$  is the production term of the turbulent kinetic energy. The turbulent viscosity is calculated as

$$\nu_{t,\phi} = C_\mu \frac{k_\phi^2}{\epsilon_\phi} \quad (21)$$

The values of model constants such as  $C_\mu$ ,  $C_1$ ,  $C_2$ ,  $\sigma_k$ ,  $\sigma_\epsilon$  are 0.09, 1.44, 1.92, 1.0, 1.3, respectively (Launder and Sharma, 1974). In the turbulence model transport equations, the mass transfer terms

between the phases were neglected. This means that it was assumed that steam coming into the water has the same local turbulence kinetic energy and dissipation as water (Peltola, 2012). In the OpenFOAM simulations, the transport equations Eqs. (19) and (20) can be solved for one continuous phase only (here liquid phase), while the dispersed phase (here vapour phase) turbulent viscosity and turbulent kinetic energy are the continuous phase values scaled with the turbulence response coefficient. In the NEPTUNE\_CFD simulations, the liquid phase turbulence was solved by the standard  $k$ - $\epsilon$  model while the vapour phase was treated as a laminar flow but it was possible to solve vapour phase with turbulence models. However, in this study only the liquid phase turbulence was important.

## 4. Simulation set-up

### 4.1. Geometrical details and grid generation

In order to solve the case as 2D-axisymmetric one with a 3D solver, a  $1^\circ$  sector of the POOLEX pool was modelled. Thus, the grid of hexahedral cells was generated by rotating a quadrilateral grid to contain a single cell thickness in respect to  $z$ -axis (Fig. 3). The total radius of the domain was set to 1.2 m, which was the mean radius from the centre of the blowdown pipe to the wall of the condensation pool. The height of the computational domain was set to 2.63 m. By using this height, the initial surface of water could be set on the upper edge of the domain. Moreover, the lower conical part of the test vessel was truncated off at 0.8 m from the mouth of the blowdown pipe. In the STB-31 experiment, the location of the steam-water interface was almost stationary at the blowdown pipe mouth. Therefore, the grid was refined near the pipe mouth. In order to check the influence of computational grid density on the CFD results, a grid independence study was performed. Three different grid sizes were used, in which the number of the grid elements was increased from Grid A (4295 cells) over Grid B (8200 cells) to Grid C (14,485 cells). Due to the weak inlet mass flow rate, the velocities within calculation domain remained low. Thus the wall function approach of  $k$ - $\epsilon$  turbulence model ( $y^+ > 30$  preferred) would lead to a notably coarse calculation grid. Thus the solution was extended up to the wall. To resolve the viscous sublayer near the wall boundary, the  $y^+$  value should be close to unity. Therefore, the grid density close to the pipe wall was refined to achieve smaller  $y^+$  value for all selected grids (i.e.,  $y_{\text{Grid A}}^+ = 2.5$ ,  $y_{\text{Grid B}}^+ = 0.8$ , and  $y_{\text{Grid C}}^+ = 0.5$ ). Estimation of interfacial  $y^+$  values was not included in this study, because  $y^+$  independent interface models (e.g., I13C) were not applied. The intermediate Grid B was selected for this study. In the refined region of Grid B, the minimum cell dimensions were approximately 4 mm and 2.5 mm in horizontal and vertical directions, respectively. The selection of the grid size has been discussed in Section 5.3.

### 4.2. Set up of simulation

The 2D-axisymmetric unsteady CFD simulations of this work were performed with the finite volume formulation. In both the CFD codes, the initial volume fraction of steam was set to unity in the blowdown pipe, and the volume fraction of water was set to unity outside the pipe setting the interface location exactly to the tip of the blowdown pipe. The pressure in the water volume was initialised by using the hydrostatic pressure. The pressure and the temperature fields of the steam were initialised according to the STB-31 test conditions (Table 2). The water surface as the upper boundary of the computational domain was fixed to the atmospheric pressure of 0.10287 MPa. Additionally, the steam was assumed to be approximately at the saturated state

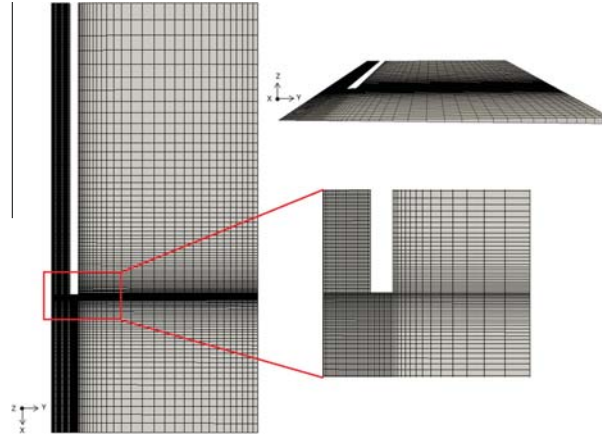


Fig. 3. Schematic views of the 2D-axisymmetric grid of the STB-31 calculations.

( $T_a = T_{sat}$ ). The pool walls were considered to be adiabatic and no-slip boundary conditions were imposed on all the wall surfaces. It is worth of noticing that the turbulence kinetic energy would be miscalculated at the near wall region despite of grid resolution due to the standard  $k-\epsilon$  (i.e., high Reynolds number) formulation. However, the effect of near wall miscalculation was not crucial in these simulations, because the free interface region dominated the total condensation rate. Reliable modelling of non-condensable gases fraction and its effects would be a notable additional challenge in the CFD simulations. Thus, the effect of non-condensable gases was omitted in the CFD simulations. The effect of non-condensable gases should be minor according to the analysis of experimental data, but the uncertainty of the analysis leaves the question partially open.

#### 4.2.1. OpenFOAM solver settings

All the calculations with OpenFOAM were performed with the version 1.7.1. The solution methodology was based on incompressible formulation. The solution procedure used the PIMPLE algorithm for the pressure-velocity coupling, which is a combination of PISO (Pressure Implicit with Splitting of Operators) and SIMPLE (Semi-Implicit Method for Pressure-Linked Equations) algorithms (Peltola, 2012). At the blowdown pipe inlet, a velocity boundary condition was used for steam. Based on a quasi-steady period in the experiment, the inlet velocity of  $0.043 \text{ ms}^{-1}$  was selected for steam corresponding to the mass flow rate of  $1.0594 \text{ gs}^{-1}$ . An upwind discretization scheme was employed for the phase volume fraction, the phase velocities, and the turbulent kinetic energy and its dissipation rate. Simulations were performed with the fixed time step size of  $0.0001 \text{ s}$  for the total time span of  $10 \text{ s}$ . More details about OpenFOAM CFD simulations setting are listed in Table 3.

#### 4.2.2. NEPTUNE\_CFD solver settings

The NEPTUNE\_CFD simulation cases of the STB-31 experiment were conducted with the constant pressure boundary conditions in order to keep the steam-water interface just at the pipe outlet (i.e.,  $0.119435 \text{ MPa}$ ). In the NEPTUNE\_CFD simulations, steam phase was solved with compressible formulation and water phase was solved with incompressible formulation. The steam tables of CATHARE code built in NEPTUNE\_CFD were enabled, and the

Table 3  
OpenFOAM solver settings for the STB-31 case.

<i>General settings</i>	
Compressible	Phase a: No, Phase b: No
Turbulence	Phase b: $k-\epsilon$ , Phase a: None
Drag model	"Schiller and Naumann (1933)"
Gravity	On
<i>Heat transfer settings</i>	
Steam tables	No
<i>Numerical scheme settings</i>	
Time stepping	Fixed
Max $ 1 - \alpha_a + \alpha_b $	$1 \times 10^{-5}$
Pressure-velocity coupling	"PIMPLE"

Table 4  
NEPTUNE\_CFD solver settings for the STB-31 case (Tanskanen, 2012).

<i>General settings</i>	
Compressible	Phase a: Yes, Phase b: No
Turbulence	Phase b: $k-\epsilon$ , Phase a: None
Turb. couplings to Phase b	Yes, "Separated phase"
Drag model	"SIMMER"
Interfacial $\nabla P_{\text{hyd}}$ correction	Yes, "Refined gradient method"
Gravity	On
<i>Heat transfer settings</i>	
Steam tables	Yes, CATHARE Water Std rev6 ext.
Steam table limits	H-P clipping, physical values
<i>Numerical scheme settings</i>	
Time stepping	Adaptive
Max $ 1 - \alpha_1 + \alpha_2 $	$1 \times 10^{-6}$
Pressure solver	"gradco", multigrid
$\alpha$ - $P$ coupling	"Recal"

enthalpy scalars were initialized by using the initial temperature and pressure. An adaptive time marching was used. The details about the NEPTUNE\_CFD solver settings are presented in Table 4.

## 5. Results and discussion

### 5.1. Qualitative analysis

A 300 s period (from 2014 s to 2340 s) from the STB-31 experiment was selected as reference for the CFD simulations. Fig. 4 pre-

sents instantaneous volume fraction fields of steam in the blowdown pipe predicted by the HD model. The results show that the steam–water interface begins to move upwards inside the pipe as the simulation progress. This is due to the relatively high condensation rate prediction by the HD model as shown in Fig. 5.

Figs. 6 and 7 display the corresponding fields of the steam volume fraction and the condensation mass flux near the blowdown pipe mouth calculated by the LH model. The presented numerical results for both the CFD codes were obtained by using the Grid B. It can be seen that weak oscillatory motion of the steam–water interface occurred in the simulation with the LH model (Fig. 6). However, it is clear that a 2D model depicts axisymmetric waves which are quite different from the ones occurs in real and 3D conditions. Therefore, it is apparent that the predicted values of wavelengths, frequencies of oscillations and interfacial deformations would be physically different from the experimentally observed ones. Due to this fact they were not compared further in this study. As there were not mechanical vibrations present in the CFD simulation, this oscillatory interfacial motion was due to an instability in the total DCC rate. The instability in total DCC rate occurs probably because the DCC rate in the smooth free surface area could be lower than the amount of injected steam, which forces the steam to spread onto the wall of the pipe lip. The temporarily increased

interfacial area increases the total DCC rate as well (Fig. 6). The cycle starts again after the excess steam is condensed near the pipe lip. The NEPTUNE\_CFD simulation predicted relatively lower oscillatory motion of the steam–water interface compared to the OpenFOAM simulation as shown in Fig. 8(a). The contours of turbulent kinetic energy times phase fraction of water, and the velocity times volume fraction of the steam of OpenFOAM and NEPTUNE\_CFD are presented in Fig. 8(b) and (c), respectively. In the OpenFOAM simulation, the turbulence kinetic energy and therefore the DCC rate at the outer surface and the lip area of the pipe seem to be higher than in the NEPTUNE\_CFD case. This is probably due to the bit higher residual bubble escape around the pipe mouth in the OpenFOAM case. However, the higher interfacial turbulence kinetic energy in the NEPTUNE\_CFD case indicates that there are differences in the modelling of interfacial turbulence between the codes as well. In both the codes, the standard  $k-\epsilon$  formulation and standard no-slip boundary conditions may yield local mispredictions in the near wall turbulence values as well.

### 5.2. Quantitative analysis

The rate of DCC cannot be measured easily in the blowdown experiments. However, in the STB-31 test, the steam–water inter-

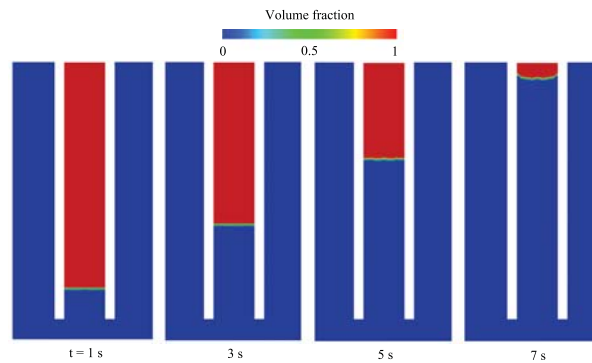


Fig. 4. Instantaneous fields of the steam volume fraction in a 2D-axisymmetric OpenFOAM simulation of the STB-31 experiment by using the HD model.

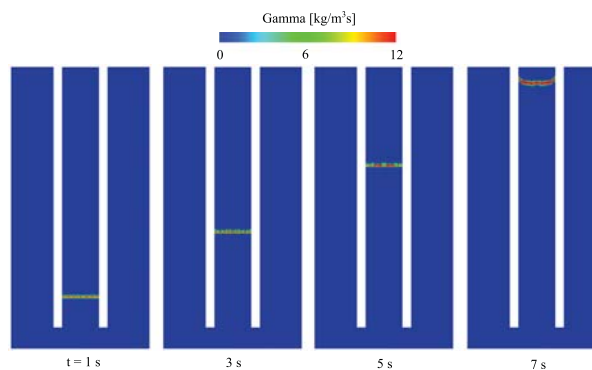


Fig. 5. Instantaneous fields of the condensation mass flux in a 2D-axisymmetric OpenFOAM simulation of the STB-31 experiment by using the HD model.

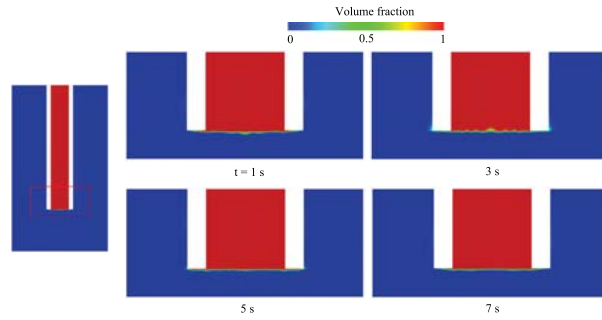


Fig. 6. Instantaneous fields of the steam volume fraction near blowdown pipe mouth in a 2D-axisymmetric OpenFOAM simulation of the STB-31 experiment by using the LH model.

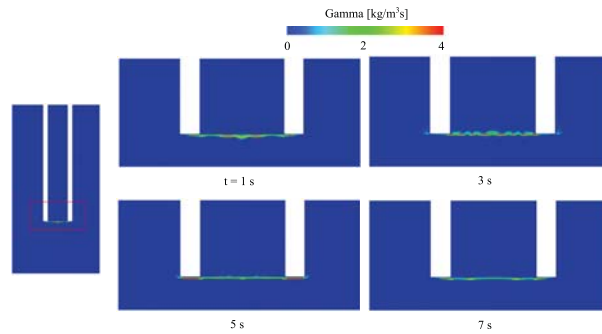


Fig. 7. Instantaneous fields of the condensation mass flux near blowdown pipe mouth in a 2D-axisymmetric OpenFOAM simulation of the STB-31 experiment by using the LH model.

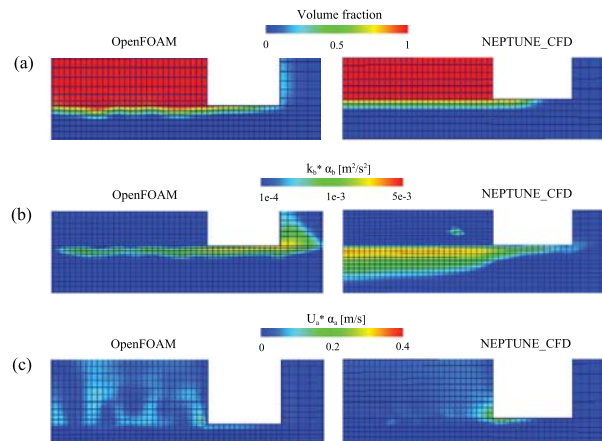


Fig. 8. Contours of (a) the steam volume fraction, (b) the water phase turbulent kinetic energy times water phase fraction, and (c) the steam phase velocity times steam volume fraction near blowdown pipe mouth in 2D-axisymmetric simulations of the STB-31 experiment by using the LH model with OpenFOAM and NEPTUNE\_CFD.

face was very stable and stationary at the blowdown pipe mouth (Fig. 2(a)). Therefore, it could be assumed that the injected steam mass flow rate was almost equal to the condensation mass flow rate itself. With the help of this assumption, it was possible to compare the test and simulation results of the DCC rates.

Averaged condensation mass flow rates predicted by the HD and LH DCC models with both the CFD codes are presented in Fig. 9. The measured steam mass flow rate and its measurement error range is presented in Fig. 9 as well. The effect of non-condensable gases was not included in the measurement results here for the sake of simplicity. As mentioned in Section 2, the estimated effect of non-condensable gases was small but it contained high uncertainties. Thus it was excluded from this study and the results presented. The results show that the HD model overestimates the condensation mass flow rate significantly with both the CFD codes while the LH model predicts the condensation mass flow rate almost to the measured values. The NEPTUNE\_CFD simulations were conducted by using pressure boundary conditions and steam tables, whereas the OpenFOAM simulations were carried out by using velocity inlet boundary condition and fixed steam properties. These differences result in slightly different interfacial behaviour which is a probable reason for the 50% overestimation in the LH DCC mass flow rate results by NEPTUNE\_CFD compared to the OpenFOAM and measurements. The condensation mass flow rate includes the effect of interface area fluctuations during the simulations. Because the interfacial area changes due to the fluctuation, it may have an effect on the total condensation rate. Therefore, it was essential to calculate also the interfacial mass fluxes by dividing the total DCC rates by the total interfacial areas.

Fig. 10 shows the averaged condensation mass flux results predicted by both of the DCC models. The HD model overpredicts the condensation mass flux with 100–200% and 600% with NEPTUNE\_CFD and OpenFOAM, respectively. In the case of OpenFOAM simulation with the HD model, the steam–water interface retreated into the blowdown pipe. The LH model predicted the condensation mass flux very close to the assumed values of the STB-31 test with both of the CFD codes.

The averaged total interfacial areas are shown in Fig. 11, in which the solid black line indicates the cross-sectional area of the blowdown pipe outlet in the STB-31 test thus excluding the

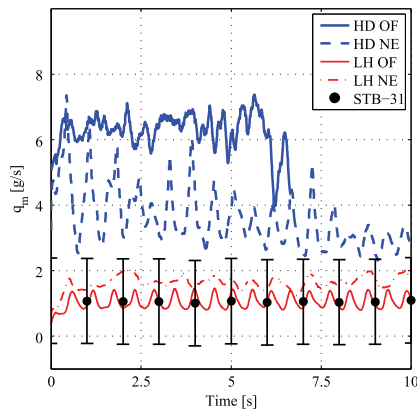


Fig. 9. Averaged condensation mass flow rate predictions of the HD and the LH models using OpenFOAM (OF) and NEPTUNE\_CFD (NE) versus the STB-31 experimental data (STB-31). Data is averaged applying moving average of 0.25 s by using Savitzky–Golay filtering in MATLAB (Orfanidis, 1996).

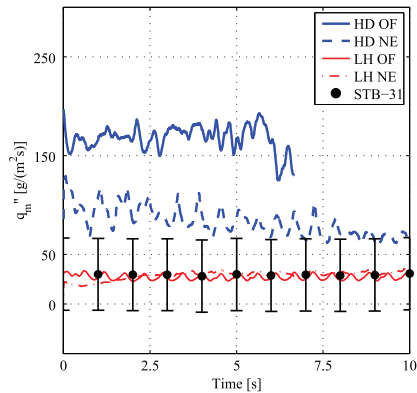


Fig. 10. Averaged condensation mass flux predictions of the HD and the LH models using OpenFOAM (OF) and NEPTUNE\_CFD (NE) versus the STB-31 experimental data (STB-31). Data is averaged applying moving average of 0.25 s by using Savitzky–Golay filtering in MATLAB (Orfanidis, 1996).

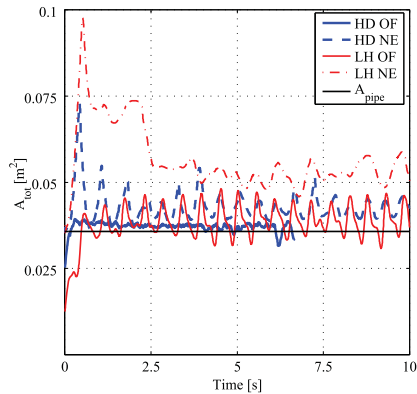
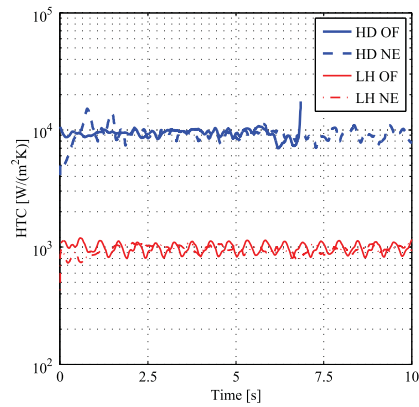
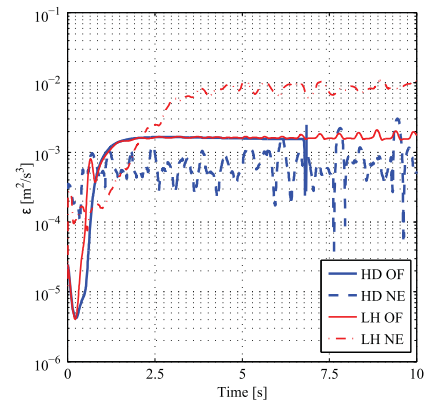


Fig. 11. Total interfacial area predictions of the HD and the LH models using OpenFOAM (OF) and NEPTUNE\_CFD (NE).  $A_{pipe}$  indicates the cross-sectional area of the blowdown pipe outlet in the STB-31 test thus excluding the thick wall area of the pipe lip. Data is averaged applying moving average of 0.25 s by using Savitzky–Golay filtering in MATLAB (Orfanidis, 1996).

thick wall area of the pipe lip. It can be seen that in the HD case with NEPTUNE\_CFD and in the LH case with OpenFOAM, the total interfacial area is very near the blowdown pipe cross-sectional area, i.e., the interface is very stable and oscillates only slightly. In the NEPTUNE\_CFD case, this is due to the hydrostatically well suited pressure inlet boundary condition which stabilizes the interface to the pipe mouth regardless of the unsuited DCC rate. In the OpenFOAM case, the velocity boundary condition matches well to the DCC rate prediction by LH. The situation is opposite with the LH model case of NEPTUNE\_CFD and HD model case of OpenFOAM. Smaller DCC rate by the LH model in NEPTUNE\_CFD leads to interface expansion and small bubble formation regardless of the pressure boundary condition. High condensation rate in the HD case of OpenFOAM collapses the steam volume within the pipe



**Fig. 12.** Interface volume average of heat transfer coefficients of the HD and the LH models using OpenFOAM (OF) and NEPTUNE\_CFD (NE). Data is time averaged applying moving average of 0.25 s by using Savitzky–Golay filtering in MATLAB (Orfanidis, 1996).



**Fig. 14.** Volume averaged dissipation rate of turbulence kinetic energy of liquid in the HD and the LH models using OpenFOAM (OF) and NEPTUNE\_CFD (NE). Data is time averaged applying moving average of 0.25 s by using Savitzky–Golay filtering in MATLAB (Orfanidis, 1996).

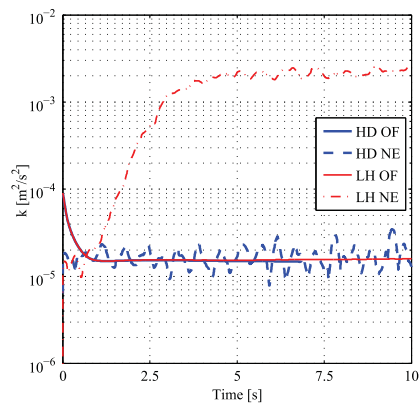


**Fig. 13.** Volume averaged turbulence kinetic energy of liquid in the HD and the LH models using OpenFOAM (OF) and NEPTUNE\_CFD (NE). Data is time averaged applying moving average of 0.25 s by using Savitzky–Golay filtering in MATLAB (Orfanidis, 1996).

because the velocity boundary condition does not maintain the pressure. Therefore, the total interfacial area in the HD case of OpenFOAM is almost constant and near about the blowdown pipe cross-sectional area.

In the CFD simulations, heat transfer coefficients may have different values in each computational cell. However, some generalized information of them can be obtained by calculating the average heat transfer coefficient from all the interfacial cells. Fig. 12 presents the average heat transfer coefficients predicted by both of the DCC models. It can be seen that both of the CFD codes yielded almost same values for the heat transfer coefficients. The HD model predicted the heat transfer coefficient about 10 times higher than the LH model.

The turbulent properties (e.g., turbulent kinetic energy and its dissipation rate) have an important role in both of the DCC models.

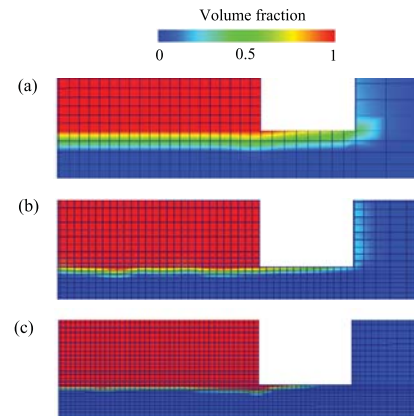


**Fig. 15.** Volume fraction fields predicted by (a) Grid A (b) Grid B and (c) Grid C near blowdown pipe mouth in a 2D-axisymmetric OpenFOAM simulation of the STB-31 experiment by using the LH model.

Fig. 13 shows the averaged turbulent kinetic energy of liquid over the whole domain. Only the liquid phase turbulent kinetic energy was recorded in this study. The turbulence kinetic energy of the liquid phase was very small everywhere except at the blowdown pipe mouth i.e., interface, lip region and the outer wall of pipe. The turbulence kinetic energy was uniform and moderate beneath the interface, but it was higher at the lip region and near the outer wall, because the minor escaping steam amount increased turbulence there. The volume averages of turbulence values were used because the local values would be subjected more to the differences in interface motion and residual bubble escape between the simulations. Averages of the turbulence quantities only at the vicinity of interface would be the most suitable ones, but due to the lacking of such data averaging of turbulence kinetic energy and dissipation rate of turbulence kinetic energy in the OpenFOAM

simulations, only the available domain averages could be compared between the codes in this study. The averaged turbulent kinetic energy had similarly constant values in the other cases, but the magnitude of turbulent kinetic energy was clearly higher in the NEPTUNE\_CFD LH case. This was likely due to the fact that steam escaped from the blowdown pipe mouth, which increased the total interfacial area and the interfacial shear. Thus, the average turbulent kinetic energy was increased.

The dissipation rate of turbulent kinetic energy of liquid was also affected by the higher turbulent kinetic energy in the LH case of the NEPTUNE\_CFD as shown in Fig. 14. The HD model leads to oscillating turbulence kinetic energy and dissipation rate values in the NEPTUNE\_CFD simulation, whereas these values are almost constant in the OpenFOAM cases. This difference is likely due to the differences in the interfacial behaviour i.e., its oscillation.

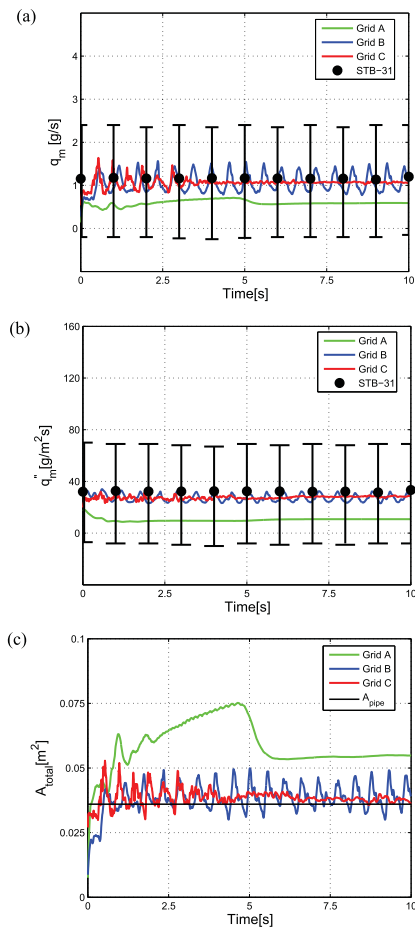


**Fig. 16.** Predicted (a) condensation mass flow rate, (b) condensation mass flux, and (c) total interfacial area by the LH model using OpenFOAM (OF) versus the STB-31 experimental data (STB-31).  $A_{pipe}$  indicates the cross-sectional area of the blowdown pipe outlet in the STB-31 test thus excluding the thick wall area of the pipe lip.

### 5.3. Grid independence study

Fig. 15(a)–(c) presents the steam volume fraction field near the blowdown pipe mouth predicted by the LH model with the Grid A, Grid B and Grid C. It can be seen that the Grid A predicted visibly more smeared interface profile than the Grid B and Grid C. Relatively sharp interface was captured by the Grid C. Therefore, it was essential to investigate the influence of grid density to the convergence of the DCC phenomena.

Fig. 16 displays the condensation mass flow rate, the condensation mass flux, and the total interfacial area predicted by the LH model with three different grids. The results are compared to the measured data of the STB-31 test as well. It can be seen that the coarser grid (i.e., Grid A) underestimated the condensation rate while the Grid B and Grid C yielded good match to the measured data (Fig. 16(a)). Also, the condensation mass flux prediction was affected by the grid density. Fig. 16(b) shows that the Grid B and Grid C resulted good correspondence with the condensation mass flux in the STB-31 test while the Grid A led to lower condensation mass flux. The discrepancy in the predicted condensation mass flux by the Grid A can be a reason for the higher interfacial area (Fig. 16(c)). The finer grid (i.e., Grid C) produced almost accurate interfacial area. Presented results show that Grid B and Grid C were able to predict the low DCC rate phenomena of this study. The Grid B was selected for the further calculations, because the results of it were near to the results with Grid C and its resolution corresponded to the grid in the NEPTUNE\_CFD simulations. Because the OpenFOAM simulations were most stable with a notably short and constant time-stepping, the Grid B was also more efficient computationally than the Grid C.

The NEPTUNE\_CFD simulations of Tanskanen (2012) were carried out by using two different grids. The coarser grid corresponded to the OpenFOAM Grid B, and the denser one was circa 50% denser than Grid C. As with OpenFOAM, the condensation rate in the NEPTUNE\_CFD cases was not notably sensitive to the grid resolution. However, the different inlet boundary condition types caused a small difference to the location of the steam–water interface near the pipe lip between the OpenFOAM and NEPTUNE\_CFD simulations. Thus it was not possible to compare the grid sensitivity further between the codes in this study.

## 6. Conclusions

In this work, a special case of low-Reynolds number DCC mode possible in suppression pools of BWRs was studied by using the Eulerian two-fluid approach with the OpenFOAM CFD code. The steam blowdown test ‘STB-31’ of the POOLEX test facility and earlier NEPTUNE\_CFD simulations were used as the reference. In the experiment, the steam–water interface was almost flat and positioned quasi-steadily at the outlet of the blowdown pipe.

The CFD simulations of the STB-31 case were performed with the DCC models of Hughes and Duffey (1991) (HD) and Lakehal et al. (2008) (LH). Qualitatively, the HD model in OpenFOAM simulations predicted high condensation rate. In the corresponding HD simulation with NEPTUNE\_CFD, the steam–water interface was forced to the pipe mouth by the pressure inlet boundary condition. The qualitative behaviour of the steam–water interface corresponded well to the test results in the LH simulations with both of the solvers. A mildly oscillatory interface was observed in the LH simulations with openFOAM and occasionally in the test. As the DCC rate is dependent on the turbulence kinetic energy in the models tested, the oscillation in the simulations can be explained by the difference in the turbulence kinetic energy between the pipe lip, outer surface and free interface regions. The escaping steam around the pipe lip has considerable velocity,

which probably increases local interfacial shear and therefore turbulence kinetic energy as well.

Although the direct measurement of the DCC rate was not possible in the test, the DCC rate in the STB-31 test could be assumed equal to the measured inlet steam flow rate due to the very stable steam–water interface. As seen qualitatively, also the values of condensation mass flow rate and condensation mass flux obtained by the LH model were in a good agreement with the STB-31 test. The HD model overestimated the DCC rate strongly. Taking into account the interface oscillations, most of the simulations indicated that the total interfacial area was near the cross-sectional area of pipe. The averaged heat transfer coefficients were almost equal between the solvers. The HD model predicted one order of magnitude higher heat transfer coefficient than the LH model, which explains the DCC rate results. Generally, the average turbulence kinetic energy and dissipation rate values were also consistent between the solvers. The NEPTUNE\_CFD LH simulation was an exception with notably higher values. This difference can be explained by stronger interface motion in that NEPTUNE\_CFD case. The grid independence study was carried out as well, and the results indicated that certain grid density was required to converge to correct DCC rate even in the low-Reynolds number DCC case.

It can be concluded that the OpenFOAM and NEPTUNE\_CFD CFD solvers produce similar results in the simulations of this special low-Reynolds number steam blowdown test, and the surface divergence model of Lakehal et al. (2008) produces promising results in this case.

Corresponding comparative simulations are encouraged concerning the more vigorous and challenging condensation modes possible in the BWR suppression pools.

#### Acknowledgements

The research leading to these results was partly funded by the European Atomic Energy Community's (Euratom) Seventh Framework Programme FP7/2007–2011 under grant agreement No. 323263. This research work was also funded by the Finnish Nuclear Waste Management Fund (VYR) via The Finnish Research Programme on Nuclear Power Plant Safety SAFIR2014 and the Academy of Finland via the Doctoral Programme for Nuclear Engineering and Radiochemistry (YTERA). The authors gratefully acknowledge this support.

#### References

- Aust, E., Seeliger, D., 1982. Pool dynamics and dynamic loads in pressure suppression containment systems. *Transactions of the American Nuclear Society* 41, 696–699.
- Banerjee, S., 1990. Turbulence structure and transport mechanisms at interfaces. In: 9th International Heat Transfer Conference, Keynote Lectures.
- Bestion, D., 2012. Applicability of two-phase CFD to nuclear reactor thermalhydraulics and elaboration of best practice guidelines. *Nucl. Eng. Des.* 253, 311–321.
- Chan, C., Lee, C., 1982. A regime map for direct contact condensation. *Int. J. Multiphase Flow* 8, 11–20.
- Chen, C.L., Dhir, V.K., 1982. Hydrodynamics of a bubble formed at vent pipe exit. *Int. J. Multiphase Flow* 8/2, 147–163.
- Coste, P., Laviéville, J., Pourreau, J., Baudry, C., Guingo, M., 2012. Validation of the large interface method of NEPTUNE\_CFD 1.0.8 for pressurized thermal shock (PTS) applications. *Nucl. Eng. Des.* 253, 296–310.
- Coste, P., Pourreau, J., Laviéville, J., Boucker, M., 2008. Status of a two-phase CFD approach to the pts issue. In: XCFD4NRS, Grenoble, France.
- Ghiaasiaan, S., 2008. *Two-Phase Flow, Boiling and Condensation in Conventional and Miniature Systems*, 1 ed. Cambridge University Press, New York, ISBN 978-0-521-88276-7.
- Grafton, W.A., McIntyre, T.R., Ross, M.A., 1977. Mark II Pressure Suppression Test Program, Phase II and III tests. Technical Report. General Electric Co., San Jose, CA (USA). Boiling Water Reactor Projects Dept.
- Gulawani, S.S., Dahikar, S.K., Mathpati, C.S., Joshi, J.B., Shah, M.S., RamaPrasad, C.S., Shukla, D.S., 2009. Analysis of flow pattern and heat transfer in direct contact condensation. *Chem. Eng. Sci.* 64, 1719–1738.
- Hart, J., Slegers, W.J.M., de Boer, S.L., Huggenberger, M., Jimenez, J.L., Gonzalez, J.L.M.C., Puigjaner, F.R., 2001. TEPS-technology enhancement for passive safety systems. *Nucl. Eng. Design* 209 (1–3), 243–252.
- Hughes, E.D., Duffey, R.B., 1991. Direct contact condensation and momentum transfer in turbulent separated flows. *Int. J. Multiphase Flow* 17, 599–619.
- Kang, H.S., Song, C.H., 2008. CFD analysis for thermal mixing in a subcooled water tank under a high steam mass flux discharge condition. *Nucl. Eng. Des.* 238, 492–501.
- Kennedy, W., McGovern, D., Maraschin, R., Wolfe, K., 1978. Rigid and flexible vent header testing in the quarter scale test facility. Mark I Containment Program, Task 5. 3. 3. Technical Report. Acurex Corp., Mountain View, CA (USA). Alternate Energy Div.
- Lahey, R., Moody, F., 1993. *The Thermal-Hydraulics of a Boiling Water Reactor*, 2 ed. American Nuclear Society.
- Laine, J., Puustinen, M., 2006. Condensation Pool Experiments with Steam using Insulated DN200 Blowdown Pipe. Research Report POOLEX 3/2005. Lappeenranta University of Technology.
- Lakehal, D., Fulgosi, M., Yadigaroglu, G., 2008. DNS of condensing stratified steam water flow. *ASME J. Heat Transfer* 130, 021501–021510.
- Lauder, B.E., Sharma, B.I., 1974. Application of the energy dissipation model of turbulence to the calculation of flow near a spinning disc. *Lett. Heat Mass Transfer* 1, 131–138.
- Laviéville, J., Quémerais, E., Mimouni, S., Boucker, M., Méchitoua, N., 2006. NEPTUNE\_CFD V1.0 theory manual. Technical Report. EDF.
- McIntyre, T.R., Ross, M.A., Myers, L.L., 1976. Mark II pressure suppression test program: Phase I tests. [BWR]. Technical Report. General Electric Co., San Jose, CA (USA). Boiling Water Reactor Systems Dept.
- Meier, M., 1999. Numerical and experimental study of large steam–air bubbles injected in a water pool. Ph.D. thesis. ETH, Swiss Federal Institute of Technology, Zurich. DISS. ETH No. 13091.
- Meier, M., Andreani, M., Yadigaroglu, G., 1998. Experimental study of large steam–air bubbles condensing in a suppression pool. In: IMECA'98, ASME, Anaheim.
- Meier, M., Yadigaroglu, G., Andreani, M., 2000. Numerical and experimental study of large steam–air bubbles injected in a water pool. *Nucl. Sci. Eng.* 136, 363–375.
- Orfanidis, S.J., 1996. *Introduction to Signal Processing*, 1st ed. Prentice-Hall, ISBN 9780132091725.
- Pättikangas, T., Niemi, J., Laine, J., Puustinen, M., Purhonen, H., 2010. CFD modelling of condensation of vapour in the pressurized PPOOLEX facility. In: CFD for Nuclear Reactor Safety Applications (CFD4NRS-3) Workshop, Bethesda, MD, USA, 14–16 September 2010, p. 12.
- Peltola, J., 2012. twoPhaseNuFoam v0.3. Technical Report. VTT.
- Puustinen, M., Kyrki-Rajamäki, R., Tanskanen, V., Räsänen, A., Purhonen, H., Riikonen, V., Laine, J., Hujala, E., 2013. BWR suppression pool studies with POOLEX and PPOOLEX test facilities at LUT. In: The 15th International Topical Meeting on Nuclear Thermal Hydraulics (NURETH-15), Pisa, Italy, 12–17 May 2013.
- Schiller, L., Naumann, A., 1933. Über die grundlegenden Berechnungen bei der Schwerkraftbereitung. *Z. Verein Deutscher Ing.* 77, 318–320.
- Smith, B.L., 2007. A numerical investigation of three-dimensional flows in large volumes in the context of passive containment cooling in BWRs. *Nucl. Eng. Design* 237 (11), 1175–1184.
- Song, C.H., Cho, S., Kang, H.S., 2012. Steam jet condensation in a pool: from fundamental understanding to engineering scale analysis. *J. Heat Transfer* 134 (3). <http://dx.doi.org/10.1115/1.4005144>, 031004–031004–15.
- Tanskanen, V., 2012. CFD modelling of direct contact condensation in suppression pools by applying condensation models of separated flow. *Acta Universitatis Lappeenrantaensis* 472. Lappeenranta University of Technology, ISBN 978-952-265-221-8, ISBN 978-952-265-222-5 (PDF), ISSN 1456-4491.
- Tanskanen, V., Lakehal, D., Puustinen, M., 2008. Validation of Direct Contact Condensation CFD Models Against Condensation Pool Experiments, in: XCFD4NRS, Grenoble, France.
- Thiele, R., 2010. Modeling of direct contact condensation with OpenFOAM. Master thesis. KTH, Royal Institute of Technology, Division of Nuclear Reactor Technology, Royal Institute of Technology, Stockholm, Sweden. ISSN 0280-316X.
- Tuunanen, J., Kouhia, J., Purhonen, H., Riikonen, V., Puustinen, M., Semken, R.S., Partanen, H., Saure, I., Pylkkö, H., 1998. General description of the PACTEL test facility. VTT Research Notes 1929. VTT. ISBN 951-38-5338-1.
- Wikdahl, C.E., 2007. Marvikenreaktor – ett industripolitiskt utvecklingsprojekt i otakt med tiden. Technical Report SKI Rapport 2007:18. SKI.
- Yadigaroglu, G., 2004. Computational Fluid Dynamics for nuclear applications: from CFD to multi-scale CMFD. *Nucl. Eng. Des.* 235, 153–164.

## **Publication II**

Patel, G., Tanskanen, V., Rintala, V., and Hyvärinen, J. (2015).  
**Numerical study of direct contact condensation of steam on stable interface in  
a BWR suppression pool test facility**

The 16th International Topical Meeting on Nuclear Reactor  
Thermal Hydraulics (NURETH-16), Chicago, IL, August 30–September 4,  
pp. 3176-3189.

© NURETH-16, 2015

Reprinted with permission from the publisher



# NUMERICAL STUDY OF DIRECT CONTACT CONDENSATION OF STEAM ON STABLE INTERFACE IN A BWR SUPPRESSION POOL TEST FACILITY

G. Patel\*, V. Tanskanen, V. Rintala and J. Hyvärinen

LUT School of Energy Systems / Nuclear Engineering

Lappeenranta University of Technology (LUT)

PO Box 20, FIN-53851 Lappeenranta, Finland

giteshkumar.patel@lut.fi; vesa.tanskanen@lut.fi; ville.rintala@lut.fi; juhani.hyvarinen@lut.fi

## ABSTRACT

The analysis of direct contact condensation (DCC) phenomena occurring in a suppression pool of BWR during steam discharge into sub-cooled water is interesting both from the numerical phase change modelling and the nuclear reactor safety points of view. This paper presents the computational fluid dynamics (CFD) simulations of a special case of low-Reynolds number DCC mode possible in suppression pools, in which the low-Reynolds number DCC corresponds to the steam. The presented CFD calculations were conducted by employing the Eulerian two-fluid approach of the OpenFOAM CFD solver. The interfacial heat transfer in these simulations was modelled by using the DCC model based on the surface divergence theory. The test STB-31 of the POOLEX facility of Lappeenranta University of Technology was used as a reference. In this test, the condensation was limited to only occur on a stable steam-water interface by applying very low steam mass flux and thermal insulation of the blowdown pipe. The results of OpenFOAM CFD solver were compared with the previously simulated results of the NEPTUNE\_CFD code and with some preliminary results of the TransAT code. The influence of grid refinement on the DCC phenomena was assessed based on a grid convergence index. Moreover, the significance of reference bubble diameter in large interface drag modelling was studied considering various diameters. The sensitivity of sub-cooling rate on the DCC phenomenon was studied with different pool temperatures as well. The simulation results indicate that the implemented surface divergence model predicts the condensation rate quite accurately in this special case.

## KEYWORDS

CFD, direct contact condensation, two-phase flow, suppression pool, interfacial area

## 1. INTRODUCTION

In a BWR, the suppression pool is one of the key safety systems during a loss of coolant accident (LOCA) or safety valve actuation. It provides a large pressure and heat sink by condensing vapor into liquid and absorbing the energy discharged from a reactor vessel [1]. The sub-cooling of the pool liquid and the mass flux of injected vapor determine the character of occurring direct contact condensation (DCC). By increasing mass flux, different condensation modes can be observed, varying from the DCC onto stable interfaces, through oscillatory interfaces and chugging bubbles, to condensation within quasi-steady jet interfaces. In a LOCA case, several modes will be experienced. The steam discharge into sub-cooled water is connected with hydrodynamic and thermodynamic issues like bubble dynamics, thermal stratification, mixing, steam condensation within ducts and at wall surfaces, etc. Injected steam interacts with pool water

---

\* Corresponding author

by heat transfer, rapid condensation and momentum exchange, inducing hydrodynamic loads to the pool structures. Therefore, the proper analysis concerning steam blowdown phenomena either by experiments or with numerical simulations is of great importance from the nuclear reactor safety point of view.

Many comprehensive experimental studies with suppression pools have been reported in the literature by various injection systems both with horizontal and vertical blowdown pipes. A small review about experimental studies of suppression pool can be found from [2]. In the field of nuclear safety analysis, Computational Fluid Dynamics (CFD) has become an increasingly applicable tool for thermal-hydraulic investigations [3]. Nevertheless, the published work on the numerical simulations of the DCC phenomena in the pressure suppression pool with vertical air/steam blowdown is rather sparse. As earlier examples, the works of [4], [5] and [6] can be mentioned; they utilized the volume of fluid method for the simulations of vapor injection in water pool. The Eulerian two-fluid approach was used for the CFD modelling of chugging condensation regime by [2] and [7]. In the works of [2] and [8], the preliminary results were presented of the performance of DCC models based on the surface renewal and the surface divergence theories considering the special case corresponding the 'oscillatory interface condensation' mode [9] and the 'condensation within the blowdown pipe' mode [1].

In this paper, further analysis of that stable steam-water interface case is presented employing the Eulerian two-fluid approach of the OpenFOAM CFD solver. The standard k- $\epsilon$  turbulence model was used to model the flow turbulence. The heat transfer correlation of [10] based on the surface divergence theory was employed to model interfacial heat transfer. The steam blowdown test 'STB-31' of the POOLEX test facility of Lappeenranta University of Technology (LUT) and earlier NEPTUNE\_CFD simulations of [2] were used as the references. In the experiment, the steam-water interface was almost flat and positioned quasi-steadily at the outlet of the blowdown pipe by virtue of very low steam mass flux applied and thermal insulation of the blowdown pipe. The paper discusses the influence of grid density on the DCC phenomena and the influence of reference bubble diameter in interface drag modelling. Furthermore, the DCC phenomena sensitivity to the sub-cooling rate is demonstrated in this paper.

## 2. POOLEX STB-31 EXPERIMENT

The POOLEX test facility was constructed at LUT for BWR containment studies [11]. The POOLEX test program was aimed to study and to enhance the understanding of various phenomena occurring in a BWR containment during steam discharge into sub-cooled liquid. The schematic of the POOLEX facility is shown in Fig. 1. The POOLEX facility was a cylinder shaped stainless steel pool with an open top and a conical bottom. The inner diameter of the pool was 2.4 m and the height was 5.0 m. The test facility consisted of the steam generator, the steam lines assembly, the blowdown pipe, and the water-pool. The steam generators of the Parallel Channel Test Loop (PACTEL) facility [12] were used as a steam source during the test. The steam lines from PACTEL to POOLEX facility were thermally insulated to prevent steam from condensing before being conveyed to the blowdown pipe. During test, the steam flow rate was measured with a rotameter (Krohne Model H250). There were 5 circular windows installed in the pool wall for visual observation of the interior. The details about measurement instrumentation and data acquisition can be found from [13].

A DN200 stainless steel pipe was used as a blowdown pipe which was insulated to prevent condensation on the wall, and its lower end was submerged in the water pool. The inner diameter of DN200 pipe was 0.2141 m. During the STB-31 test, the pool was filled with isothermal water and the total volume of water in this pool was approximately 12m<sup>3</sup>. The steam mass flow rate was controlled by using a manual throttle valve throughout the test to prevent steam bubble formation and to keep the steam-water interface as close as possible to the pipe outlet. Although the steam-water interface was almost smooth during the quasi-steady periods in the test, some very low amplitude oscillations were observed in the video samples. The oscillation could have originated from possible minor mechanical vibrations of the facility or from the

condensation phenomena itself. During the experiment, there were several quasi-steady state intervals suitable for the CFD validation. The experimental conditions of the STB-31 test are specified in Table I.

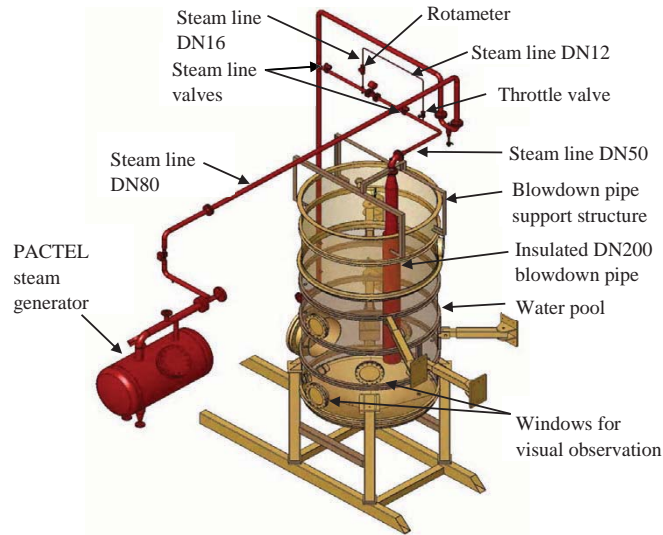


Figure 1. POOLEX test facility [13].

Table I. The test parameters of the STB-31 experiment [13].

Initial pool water level	2.95 m
Blowdown pipe submergence depth	1.81 m
Initial pool water temperature	32 °C
Steam temperature in blowdown pipe	104.35 °C
Steam pressure in blowdown pipe	0.119435 MPa
Steam flow rate	0.5...1.5 gs <sup>-1</sup>
Total duration of test	6000 s

### 3. MODELING AND SIMULATION STRATEGIES

#### 3.1. Physical Models

All results presented in this paper were obtained by using the OpenFOAM CFD solver version 1.7.1. The steam-water system was simulated with the Eulerian two-fluid approach. In this approach, the interface between the phases is not tracked, because the existence of separate conservation equations for each phase does not require that. However, separate closure laws (e.g., drag, lift and added mass forces) are needed to close the equations and make the behavior of smeared interface physical. In the case of a large interface

under phase change i.e. stratified flow, the interfacial drag force and the heat/mass transfer rate are the most relevant additions needed. The transport equations of mass, momentum, and energy for two-phase flow are expressed as

$$\frac{\partial}{\partial t}(\alpha_\phi \rho_\phi) + \nabla \cdot (\alpha_\phi \rho_\phi \mathbf{U}_\phi) = \Gamma_\phi, \quad (1)$$

$$\frac{\partial}{\partial t}(\alpha_\phi \rho_\phi \mathbf{U}_\phi) + \nabla \cdot (\alpha_\phi \rho_\phi \mathbf{U}_\phi \mathbf{U}_\phi) + \alpha_\phi \nabla \cdot \boldsymbol{\tau}_\phi + \nabla \cdot (\alpha_\phi \rho_\phi \mathbf{R}_\phi) = -\alpha_\phi \nabla \bar{p} + \alpha_\phi \rho_\phi \mathbf{g} + \mathbf{M}_\phi, \quad (2)$$

$$\frac{\partial}{\partial t}(\alpha_\phi \rho_\phi H_\phi) + \nabla \cdot (\alpha_\phi \rho_\phi \mathbf{U}_\phi H_\phi) = \nabla \cdot (\alpha_\phi \rho_\phi D_{T, \text{eff}, \phi} \nabla H_\phi) + \Gamma_\phi H_{i, \phi} + Q_\phi, \quad (3)$$

where  $\phi$  indicates an arbitrary phase (afterwards  $\phi=a$  for steam and  $\phi=b$  for water),  $\alpha_\phi$  is the phase fraction,  $\rho_\phi$  is the density and  $\mathbf{U}_\phi$  is the velocity of the  $\phi$  phase.  $\Gamma_\phi$  is the mass transfer rate. In Eq. (2),  $\boldsymbol{\tau}_\phi$ ,  $\mathbf{R}_\phi$ ,  $\nabla \bar{p}$ ,  $\mathbf{g}$ , and  $\mathbf{M}_\phi$  denote the viscous stress tensor, the turbulent stress tensor, the overall pressure gradient, the gravity acceleration and the interfacial momentum transfer between phases, respectively. The effect of drag force was taken into account only, while the other interfacial forces were omitted in this work. The interfacial momentum exchange coefficient  $\mathbf{M}_{ab}$  can be expressed as

$$\mathbf{M}_{ab} = \alpha_a \alpha_b \frac{3}{4} C_D \rho_b \frac{1}{d_B} |U_a - U_b| (U_a - U_b), \quad (4)$$

where  $C_D$  is the drag coefficient which was obtained using the drag correlation of Schiller and Naumann [14], which can be written as  $C_D = \frac{24}{\text{Re}_B} (1 + 0.15 \text{Re}_B^{0.687})$ , and  $d_B$  is the bubble diameter. In Eq. (3),  $H_\phi$  and  $H_{i, \phi}$  indicate the specific enthalpy and the interfacial enthalpy of the  $\phi$  phase. The terms  $D_{T, \text{eff}, \phi}$  and  $Q_\phi$  are the phase effective thermal diffusivity and the volumetric interfacial heat transfer rate, respectively. The interfacial mass transfer was calculated from the total heat balance (i.e.  $Q_a + Q_b = 0$ ) as

$$\Gamma_{i, b} = \frac{q_a + q_b}{H_{i, a} - H_{i, b}}, \quad (5)$$

where,  $q_a$  and  $q_b$  are the sensible heat fluxes from the interface to steam and from interface to water, respectively, which can be defined as

$$q_a = a_{ia} h_{i, a} (T_{sat} - T_a), \quad (6)$$

$$q_b = a_{ib} h_{i, b} (T_{sat} - T_b). \quad (7)$$

Here  $a_{ia}$  and  $a_{ib}$  are the interfacial area densities ( $\text{m}^{-1}$ ) for steam and water, respectively. The interfacial area density was calculated from the gradient of void fraction (i.e.,  $a_{i\phi} = |\nabla \alpha_{i\phi}|$ ). The interfacial temperature,  $T_{sat}$ , was set to the saturation temperature. The terms  $h_{i, a}$  and  $h_{i, b}$  represent the heat transfer coefficients of steam and water. The heat transfer coefficient for the water phase can be defined as

$$h_{i, b} = \frac{\text{Nu}_b \lambda_b}{L_{i, b}}, \quad (8)$$

where  $\text{Nu}_b$ ,  $\lambda_b$  and  $L_{i, b}$  indicate the Nusselt number, the thermal conductivity and the characteristic length, respectively. In the present work, the surface divergence based DCC model of Lakehal et al. 2008 (LH) [10] was used as the water side heat transfer model. The applicability of this model has been discussed before by [2] and [8]. In the DCC model,  $\text{Nu}_b$  is defined as

$$Nu_b = Bf [Re_t^m] Re_t Pr^{1/2}. \quad (9)$$

B is the model constant (i. e., B = 0.35 for Pr ≈ 1 and B = 0.45 for Pr ≫ 1; here, B=0.35 was used) and f [Re<sub>t</sub><sup>m</sup>] can be written as

$$f [Re_t^m] = \left[ 0.3 \left( 2.83 Re_t^{3/4} - 2.14 Re_t^{2/3} \right) \right]^{1/4} Re_t^{-1/2}. \quad (10)$$

Here,  $Re_t = \frac{k_b^2}{v_b \epsilon_b}$ , where,  $k_b$ ,  $\epsilon_b$ , and  $v_b$  are the turbulence kinetic energy (TKE), the dissipation rate of TKE, and the kinematic viscosity of water. In Eq. (8),  $L_{t,b} = \frac{v_b}{u_t} Re_t$ , where, the velocity parameter,  $u_t$ , was defined as  $u_t = (v_b \epsilon_b)^{1/4}$ . Flow turbulence was solved by employing the standard k-ε turbulence model of [15]. In the present work, the transport equations of turbulence model were solved for one continuous phase only (i.e., water), while the ‘dispersed’ phase (i.e., steam) turbulent viscosity and turbulent kinetic energy were the continuous phase values scaled with the turbulence response coefficient. In NEPTUNE\_CFD simulations, the liquid phase turbulence was solved by the standard k-ε model while the vapor phase was treated as a laminar flow. TransAT was applied as a single fluid solver i.e. using Level-Set method for two phase flow and turbulence was modeled by the standard k-ε turbulence. Therefore these codes solve the interfacial turbulence differently at least to some extent. However, in this stable interface case, the differences in drag modelling and interfacial area modelling influenced more than the differences in the turbulence modelling.

### 3.2. Numerical Details

#### 3.2.1. Geometrical details and simulation set up

In order to solve the case as 2D-axisymmetric one with a 3D solver, all of the presented numerical results of this study were simulated using a 1° sector of the POOLEX pool. Therefore, a 2D-axisymmetric grid of hexahedral cells was generated by rotating a quadrilateral grid to contain a single cell thickness in respect to z-axis. The total radius and the height of the computational domain was set to 1.2 m and to 2.63 m, respectively. By using this height, the initial surface of water could be set on the upper edge of the domain. Moreover, the lower conical part of the test vessel was truncated off at 0.8 m from the mouth of the blowdown pipe. The computational grid for the simulation is presented in Fig. 2.

In the case of STB-31 test, the location of the steam-water interface was almost stationary at the blowdown pipe mouth. Therefore, the grid was more refined near the pipe mouth. A grid independence study was performed considering four different grid, i.e., Grid A (2500 cells), Grid B (6270), Grid C (14014), and Grid D (20940). The minimum cell sizes in the refined region of Grid A, B, C and D were circa 0.1 × 6 mm, 0.03 × 3 mm, 0.006 × 0.6 mm and 0.001 × 0.2 mm, respectively. In the STB-31 test, the inlet steam mass flow rate was very small. Therefore, the velocities within the calculation domain remained low. However, the wall function approach of k – ε turbulence model ( $y^+ > 30$  preferred) would lead to a notably coarse calculation grid relative to the interface and condensation modelling. Therefore, the grid densities near to the blowdown pipe wall were high i.e.  $y_{Grid A}^+ \approx 5.3$ ,  $y_{Grid B}^+ \approx 1.9$ ,  $y_{Grid C}^+ \approx 0.6$ , and  $y_{Grid D}^+ \approx 0.1$ . The discretization error, the main source of computational errors, can be defined as the difference between the exact solution of the governing equations and the discretized system. These errors can arise from numerical algorithms, the grid structure and/or quantity, boundary conditions, etc. In the present work, the errors resulting from the number of grid points are discussed. The study of the grid refinement influence on the CFD results was performed by using the grid convergence index (GCI) method. The GCI method proposed by Celik et al. [16] was used. This method is based on the Richardson extrapolation technique [17], in which

multiple solutions of the numerical calculation are calculated by adjusting a parameter (grid size) and are used then to extrapolate a more accurate solution. The grid convergence was evaluated by using a relative error measure of different parameters between the grids as  $e_a^{nm} = \left| \frac{\Phi_n - \Phi_m}{\Phi_n} \right|$ . Here  $\Phi_n$  and  $\Phi_m$  denote the corresponding solutions of  $n^{th}$  and  $m^{th}$  grid, respectively. An extrapolated relative error was calculated as  $e_{\text{ext}}^{nm} = \left| \frac{\Phi_{\text{ext}}^{nm} - \Phi_n}{\Phi_{\text{ext}}^{nm}} \right|$ , where,  $\Phi_{\text{ext}}^{nm}$  is the extrapolated value which can be defined as  $\Phi_{\text{ext}}^{nm} = \frac{r_{nm}^p \Phi_m - \Phi_n}{r_{nm}^p - 1}$ . Here,  $r_{nm}$  represents the grid refinement factor which can be evaluated from the ratio of corresponding grid sizes of  $n$  and  $m$  grids, and  $p$  indicates the order of the discretization method. More details of the procedure to estimate the discretization error can be found from [16].

The GCI provides a uniform measure of convergence for grid refinement tests. The GCI can be estimated as

$$GCI^{nm} = F_s \frac{e_a^{nm}}{r_{nm}^p - 1} \quad (11)$$

Here,  $F_s$  is the safety factor, which was 1.25. This value is based on the experience obtained by applying GCI to many situations [18]. Furthermore, the theory of Richardson extrapolation and therefore of the proposed GCI depends on the assumption that the Taylor series expansion is valid asymptotically and the two grids are within the asymptotic range. The asymptotic range of convergence between grids can be achieved as

$$GCI^{23} = r_{nm}^p GCI^{12} \quad (12)$$

Here, superscripts 12 and 23 indicate from fine to intermediate and from intermediate to coarse grid refinements, respectively. The influence of grid density and the grid discretization error is discussed in Section 4.

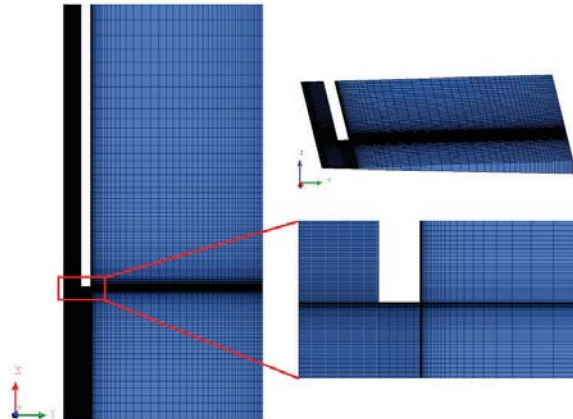


**Figure 2. The 2D-axisymmetric grid of the POOLEX pool.**

The CFD simulations of this work were performed with the finite volume formulation. The pressure in the water volume was initialized by using the hydrostatic pressure. The pressure and the temperature fields of

the steam were initialized according to the STB-31 test conditions (Table I). The water surface as the upper boundary of the computational domain was fixed to the atmospheric pressure of 0.10287 MPa. Moreover, the steam was assumed to be approximately at the saturated state. Initially, the turbulent kinetic energy and its dissipation rate fields in the pool-water were initialized with generic  $10^{-4}$  and  $10^{-3}$ , respectively. The pool walls were considered to be adiabatic and no-slip boundary conditions were imposed on all the wall surfaces. Reliable modelling of non-condensable gases fraction and its effects would be a notable additional challenge in the CFD simulations. Thus, the effect of non-condensable was omitted in the CFD simulations. The uncertainties due to the non-condensable gases in the STB-31 test are discussed in [2], in which he applied the Couette flow film model of [19] to produce an estimation of the non-condensables effect on the condensation rate during the selected period of the experiment. His analysis was based on the air and steam partial pressures derived from the measured temperatures and the total pressure at the outlet of the pipe. The analysis indicated that 3–50 % higher condensation rates would occur without the presence of non-condensable gases. The solution methodology was based on incompressible formulation of OpenFOAM. The pressure-velocity coupling was done using the PIMPLE algorithm which is a combination of PISO and SIMPLE algorithms. A velocity boundary condition was set to the blowdown pipe inlet for the steam phase. Based on the selected quasi-steady period in the STB-31 experiment, the inlet velocity of  $0.043 \text{ ms}^{-1}$  was used corresponding to the mass flow rate of  $1.0594 \text{ gs}^{-1}$ . A 2<sup>nd</sup> order upwind discretization scheme was employed for the phase volume fraction, the phase velocities, and the turbulent kinetic energy and its dissipation rate. The normalized RMS residuals of the order of  $10^{-4}$  or lower were used as convergence criteria. Simulations were performed with the fixed time step size of 0.1 ms for the total time span of 15 s.

#### 4. RESULTS AND DISCUSSION

The total duration of the STB-31 experiment was about 6000 s containing several quasi-steady state intervals in which the steam-water interface was almost stable at the blowdown pipe mouth. A 300 s period (from 2014 s to 2340 s) from the STB-31 experiment was selected as reference for the CFD simulations. Firstly, the influence of computational grid density on DCC phenomena was studied based on four different grid sizes. Fig. 3 shows the steam volume fraction field near the blowdown pipe mouth predicted with different grids. It is observed that the coarser grid (Grid A) resulted in visibly more smeared steam-water interface compared to the other grids. As the grid density increases, the interface profile becomes sharper. The sharpest interface was captured by the finest grid (Grid D). Based on these qualitative results, it was essential to investigate the influence of grid density to the convergence of the DCC phenomena.

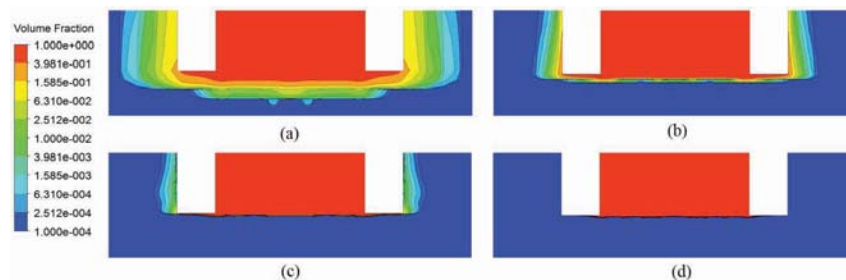
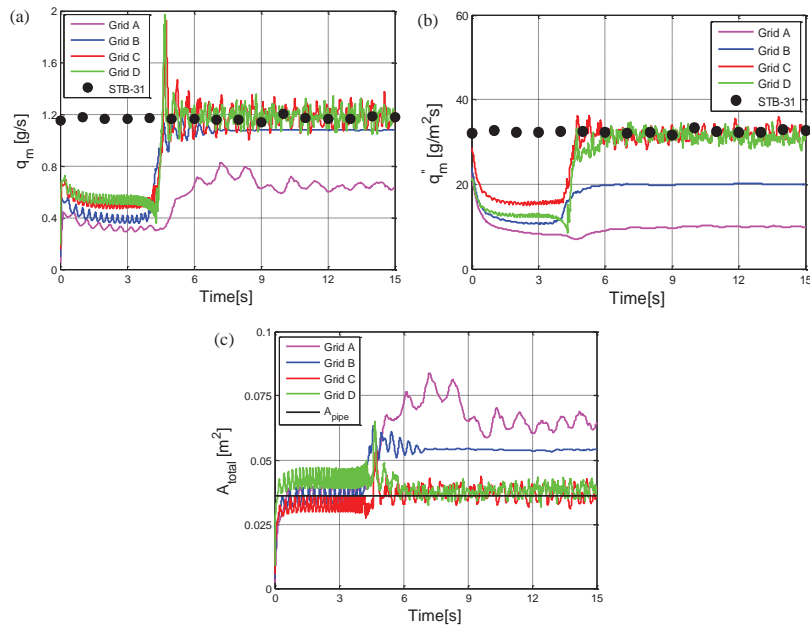


Figure 3. Volume fraction fields predicted by (a) Grid A, (b) Grid B, (c) Grid C, and (d) Grid D near blowdown pipe mouth in a 2D-axisymmetric OpenFOAM simulation of the STB-31 test.

The DCC rate cannot be measured easily in the blowdown experiments. In the STB-31 test, the steam mass flow rate was controlled through the experiment to prevent steam bubble formation and to keep the steam-water interface as close as possible to the blowdown pipe outlet. Therefore, it could be assumed that the injected steam mass flow rate was almost equal to the condensation mass flow rate itself. Based on this assumption, it was possible to compare the test and simulation results of the DCC rates. Fig. 4 presents the predicted condensation mass flow rate, the condensation mass flux, and the total interfacial area with different grids. The CFD results are compared to the measured data of the STB-31 test. The relatively high measurement error in the condensation mass flow rate is not displayed in the figure. The range of measurement error was  $\pm 1.3 \text{ gs}^{-1}$ . In the grid independence test simulations, the steam-water interface was initialized 5 cm inside from the blowdown pipe outlet at  $t = 0$ . The steam-water interface starts to approach to the blowdown pipe mouth as simulation time elapsed. It took about 5 s of simulation time to reach to the blowdown pipe mouth. Therefore, for all the cases, the condensation mass flow rate was lower than the STB-31 inlet flow rate at the beginning of the simulations as shown in Fig. 4(a). The Grid A produced clearly weaker condensation rate than the others. As the grid density increased, the predicted condensation mass flow rate reached to the measured value. Grid C and Grid D yielded to relatively similar and accurate results of the DCC rate. The condensation mass flow rate includes the effect of interface area fluctuations during the simulations. Because the interfacial area changes due to the interface fluctuation, that have an effect on the total condensation rate. For this reason, it was essential to present also the interfacial mass fluxes (Fig. 4(b)) by dividing the total DCC rates by the total interfacial areas (Fig. 4(c)).



**Figure 4. Predicted (a) condensation mass flow rate, (b) condensation mass flux, and (c) total interfacial area by the LH model using OpenFOAM versus the STB-31 test data.  $A_{\text{pipe}}$  indicates the cross-sectional area of the blowdown pipe outlet in the STB-31 test.**

As presented in Fig. 4(b), the Grid A and Grid B strongly underpredicted the condensation mass flux, while the Grid C and Grid D predicted the condensation mass flux very close to the measurements. The interfacial area should be close to the cross-sectional area of pipe outlet. Grid A and Grid B over predicted the total interfacial area by 140-150 % and 170-200 % of the cross-sectional area of the outlet, respectively. The Grid C and Grid D produced better results. However, in both the Grid C and Grid D case, slight wavy-motions of the steam-water interface occurred. Possible mechanical vibrations were not modeled in the CFD simulation. Therefore, the oscillating wavy interfacial motion appears likely due to an instability in the total DCC rate. The instability in total DCC rate occurs probably because the DCC rate in the smooth free surface area could be lower than the amount of injected steam, which forces the steam to spread onto the wall of the pipe lip where the condensation rate increases. The 2D-axisymmetric geometry enhances this effect.

The GCI method was used to calculate the discretization error for the CFD simulations with selected grid refinements. Table II summarizes the discretization errors for the condensation mass flow rate and the total interfacial area. The Cases AB, BC and CD indicate the grid refinements from Grid A to B, Grid B to C, and Grid C to D, respectively. It can be seen that the calculated relative error (i.e.,  $e_a$ ) decreased as the grid density increased. Moreover, the successive grid refinements resulted in a reduction for an extrapolated relative error (i.e.,  $e_{ext}$ ) as well. The GCI value for the successive grid refinements reduced well for both the quantities. The GCI values indicate that the grid refinement from Grid C to Grid D yielded a negligible discretization numerical error which was less than 0.1 %. Furthermore, the asymptotic range of convergence has been calculated. For the grid group of A, B and C, the asymptotic range of convergence for condensation mass flow rate and total interfacial area are 1.04448 and 1.09235, respectively and for the grid group of B, C and D, the asymptotic range of convergence for condensation mass flow rate and total interfacial area are 1.00569 and 1.00238, respectively. This analysis shows that the asymptotic range of convergence for the grid groups are approximately unity, which indicates that the solution is well within the asymptotic range of convergence. Based on this analysis, the finest grid, Grid D was selected for the further calculations.

**Table II. Details of the grid discretization error.**

Quantity	Error (%)	Case AB	Case BC	Case CD
Condensation mass flow rate	$e_a$	60.82	12.00	0.52
	$e_{ext}$	19.04	1.48	0.07
	GCI	47.27	2.10	0.09
Total interfacial area	$e_a$	15.30	26.89	0.84
	$e_{ext}$	29.25	2.30	0.05
	GCI	23.95	2.05	0.06

Also, the results of Grid D of OpenFOAM code were compared with the previously simulated results of the NEPTUNE\_CFD of [2]. During the STB-31 test, it was noticed that there were non-condensing bubbles (air bubbles) escaping around the pipe lip. Therefore, it was assumed that dissolved air was released from the pool water, and it slowly accumulated as a layer between steam and water inside the blowdown pipe. In order to mitigate the non-condensable gases effect on the condensation rate, it was essential to remove the layer of air from the blowdown pipe. That was done by increasing the steam flow rate at certain time intervals. Therefore, during STB-31 test, the steam mass flow rate at inlet was increased at regular time periods (e.g., during 1185...1525 s, 2455...2830 s, and 3800...3950 s). After such a strong blowdown, steam mass flow rate was decreased to attain stable interface conditions again. Fig. 5(a) displays video frames of stable interface (left) and strong blowdown (right) during the STB-31 POOLEX test. Fig. 5(b) and (c) compare the contours of steam volume fraction and turbulent kinetic energy weighted by volume fraction of water of OpenFOAM and NEPTUNE\_CFD, respectively. It can be seen that both the CFD solvers predicted well the profile of the steam-water interface. The turbulence kinetic energy and therefore

the DCC rate at the outer surface and at the lip area of the pipe seem to be higher in the OpenFOAM simulation than in the NEPTUNE\_CFD case. This may occur due to the bit higher residual bubble escape around the pipe mouth in the OpenFOAM case. However, the higher interfacial turbulence kinetic energy in the NEPTUNE\_CFD case indicates that there are differences in the modelling of interfacial turbulence between the codes as well. In both the codes, the standard k- $\epsilon$  formulation and standard no-slip boundary conditions may yield local mispredictions in the near wall turbulence values as well. Higher interfacial turbulence in the NEPTUNE\_CFD case may reduce the amount of escaping steam around the pipe lip reducing therefore the turbulence on the lip wall region as well.

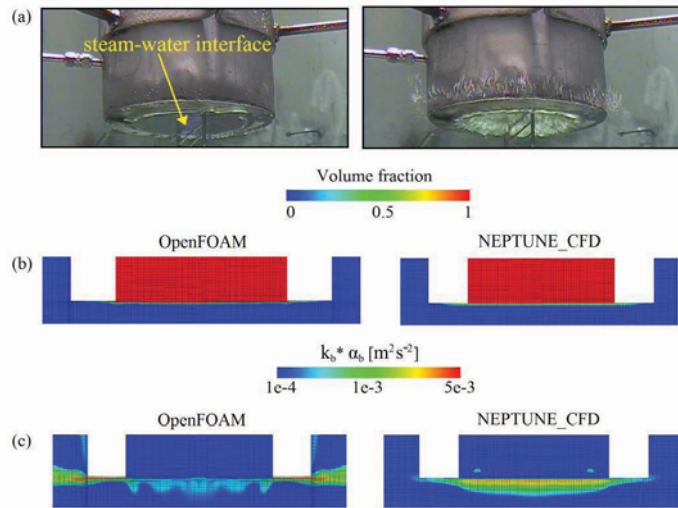


**Figure 5. (a) Instantaneous images of stable steam-water interface (left) and strong blowdown of steam (right) during STB-31 POOLEX test, (b) contours of the steam volume fraction, and (c) the water phase turbulence kinetic energy times phase fraction of water near blowdown pipe mouth in 2D-axisymmetric simulations of STB-31 test with the OpenFOAM and NEPTUNE\_CFD.**

Furthermore, the predicted condensation mass flow rate of OpenFOAM was compared with the NEPTUNE\_CFD and also the preliminary TransAT results of [2] in Fig. 6. Concerning reliable comparison, the available TransAT transient is too short compared to OpenFOAM and NEPTUNE\_CFD simulations. The solid black lines indicate the measurement error range of the measured steam flow rate during STB-31 test. In this case, the steam-water interface was initialized exactly at the blowdown pipe outlet. The OpenFOAM simulation predicted the condensation mass flow rate almost to the measured values. The NEPTUNE\_CFD simulations were conducted by using a pressure boundary condition at inlet and steam tables, whereas the OpenFOAM simulations were carried out by using the velocity inlet boundary condition and constant steam properties. These differences resulted in slightly different interfacial behavior which was a probable reason for the 50 % overestimation in the condensation mass flow rate results by NEPTUNE\_CFD compared to the OpenFOAM and measurements. Although the condensation rate in the TransAT case is higher than in the other cases, the order of magnitude is same, which is not obvious in DCC simulations with different methods and computational grids. The TransAT grid was almost two times

denser than the OpenFOAM and NEPTUNE\_CFD ones. Moreover, the TransAT code version was an interface tracking method code (Level-Set) using constant material properties. Regardless of the differences in the DCC rates of the codes, all the results fall quite well between the measurement error bounds.

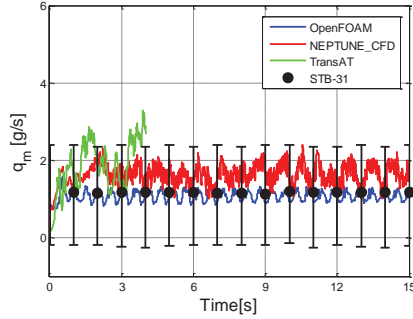


Figure 6. Predicted condensation mass flow rate by the LH model using OpenFOAM, NEPTUNE\_CFD and TransAT versus the STB-31 experimental data.

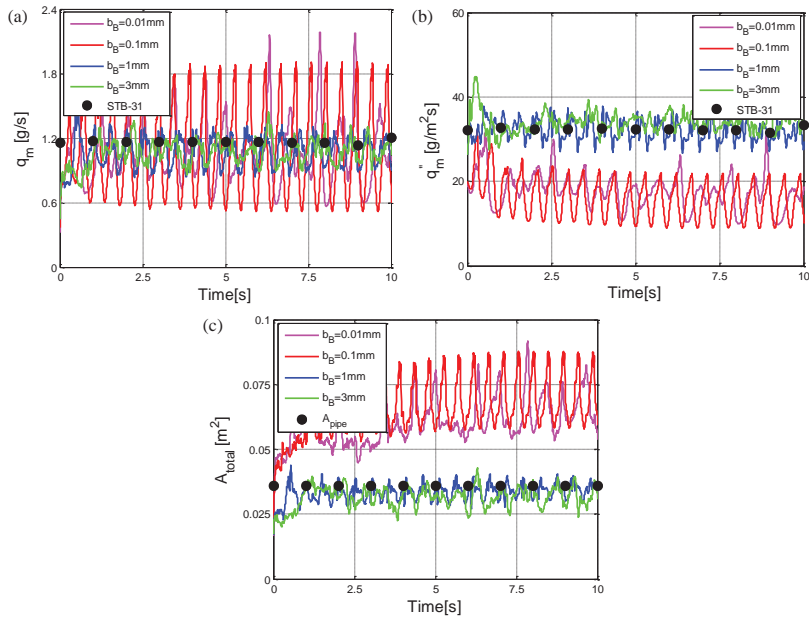


Figure 7. Predicted (a) condensation mass flow rate, (b) condensation mass flux, and (c) total interfacial area with different bubble sizes using OpenFOAM versus the STB-31 test data.

The influence of reference bubble diameter of the steam phase on the DCC rate in large interface drag modelling by the Schiller-Naumann drag coefficient was studied by testing various diameters. Four reference bubble diameters were considered, i.e., 0.01 mm, 0.1 mm, 1 mm and 3 mm. The corresponding results are presented in Fig. 7. The smaller bubble diameter cases (i.e.,  $d_b = 0.01$  mm and 0.1 mm) yielded higher interfacial area than the bigger bubble diameter cases (Fig. 7(c)). Therefore, the enlarged interfacial area increases the total DCC rate locally (Fig. 7(a)). However, in the case of  $d_b = 0.01$  mm and 0.1 mm, the condensation mass flux is decreased more than 50 % in turn (Fig. 7(b)). It can be seen that the profiles of condensation mass flow rate, condensation mass flux and total interfacial area with  $d_b = 1$  mm and 3 mm are quite near to the measured values. As the modeled case operates in clearly separated flow regime, the reference diameter in the bubbly flow drag coefficient in the interfacial momentum transfer model turns out as a fitting parameter.

The influence of sub-cooling rate on the DCC phenomena was studied with different pool temperatures (i.e.,  $T_b = 288.15$  K, 308.15 K and 328.15 K). Fig. 8(a) demonstrates that the condensation mass flow rate was decreased as the pool temperature increased. The cold temperature in the interface region increases the condensation rate and, therefore, the total interfacial area decreases due to rapid phase change (Fig. 8(c)). Due to lower DCC rate (i.e., condensation mass flux) in the case of  $T_b = 328.15$  K, the interfacial area increases. Although the effect of pool sub-cooling on the DCC rate is quite obvious, it is essential to see of how easily it changes the behavior of the interface in certain geometries such as the blowdown pipe outlet.

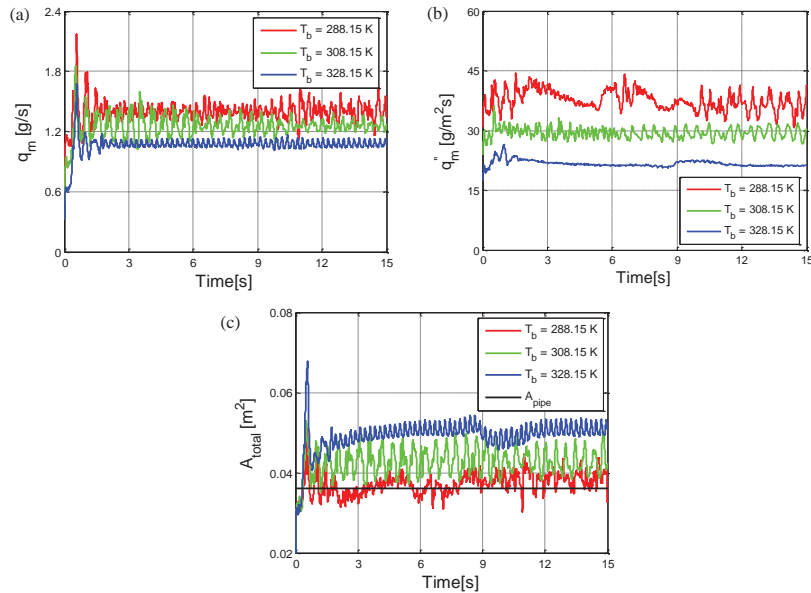


Figure 8. Predicted (a) condensation mass flow rate, (b) condensation mass flux, and (c) total interfacial area with different pool water temperatures by the LH model using OpenFOAM.

## 5. CONCLUSIONS

In this study, a CFD analysis of DCC of steam was conducted by using the Eulerian two-fluid approach of the OpenFOAM CFD solver. A special case of relatively low-Reynolds number (i.e., about 500 corresponding to the steam injection blowdown pipe diameter) DCC mode possible in suppression pools of BWRs was modelled, in which the steam-water interface was flat and positioned quasi-steadily at the outlet of the blowdown pipe. The surface divergence theory based DCC model of [10] was employed to estimate the interfacial heat transfer in the simulations. As the reference, the steam blowdown test 'STB-31' of the POOLEX test facility of Lappeenranta University of Technology was used. The simulated results of the OpenFOAM CFD solver were discussed together with previously simulated results of NEPTUNE\_CFD of [2] and a short sample of results obtained with TransAT of [2]. In the STB-31 test, the steam mass flow rate was controlled to prevent steam bubble formation and to maintain the steam-water interface position stationary as close as possible to the blowdown pipe outlet. Therefore, it was assumed that the injected steam mass flow rate was almost equal to the condensation mass flow rate itself.

Firstly, the influence of computational grid refinement on the DCC phenomena was investigated via grid convergence index analysis. The predictions of the condensation mass flow rate and the total interfacial area were sensitive to the grid refinements. However, it can be concluded that adequate grid density (i.e., the grid which contained the minimum cell dimensions approximately 0.001 mm and 0.2 mm in horizontal and vertical directions, respectively) was achieved to obtain correct rate of DCC in this low-Reynolds number DCC case. The qualitative and quantitative behavior of the steam-water interface agreed well to the test results in the simulations with the OpenFOAM and NEPTUNE\_CFD CFD solvers. However, mild oscillatory and wavy behavior of interface was recognized in the OpenFOAM simulations. In the DCC model used, the DCC rate is dependent on the turbulence kinetic energy. Therefore, the observed oscillations in the OpenFOAM simulations can be described by the difference in the turbulence kinetic energy between the pipe lip, outer surface and free interface regions. In the OpenFOAM simulations, a small amount of steam escaped occasionally nearby the pipe lip, which raised local interfacial shear and consequently turbulence kinetic energy as well. Also, the influence of reference bubble diameter of steam in interfacial drag modelling on the DCC phenomena was studied. The interfacial drag coefficient suitable for bubbly flow was used for separated flow by adjusting the reference bubble diameter. Results indicated that by trying a very small bubble diameter also the condensation mass flux can be affected i.e. become underestimated significantly. The sensitivity of sub-cooling rate on the DCC phenomena was studied with different pool temperatures as well. The effect of pool sub-cooling on the DCC rate was notable even in the mild condensation case of almost flat steam-water interface.

The presented CFD results provide motivation for further condensation model validation and development work particularly for more vigorous and challenging condensation modes of steam blowdown appear in suppression pools of BWRs.

## ACKNOWLEDGMENTS

The research leading to these results was funded by the Finnish Nuclear Waste Management Fund (VYR) via The Finnish Research Programme on Nuclear Power Plant Safety SAFIR2014 and the Academy of Finland via the Doctoral Programme for Nuclear Engineering and Radiochemistry (YTERA). The research leading to NEPTUNE\_CFD and TransAT results is partly funded by the European Atomic Energy Community's (Euratom) Seventh Framework Programme FP7/2007-2011 under grant agreements No. 232124 and No. 323263. The authors gratefully acknowledge this support.

## REFERENCES

1. R. Lahey and F. Moody, "Thermal-Hydraulics of a Boiling Water Reactor," 2<sup>nd</sup> edition, Chapter 11, American Nuclear Society, USA (1993).
2. V. Tanskanen, "CFD modelling of direct contact condensation in suppression pools by applying condensation models of separated flow," *Acta Universitatis Lappeenrantaensis 472. Lappeenranta University of Technology*. ISBN 978-952-265-221-8, ISBN 978-952-265-222-5, Ph.D. thesis, ISSN 1456-4491 (2012).
3. D. Bestion, "Applicability of two-phase CFD to nuclear reactor thermalhydraulics and elaboration of best practice guidelines," *Nucl. Eng. Des.*, **253**, pp. 311-321 (2013).
4. M. Meier, G. Yadigaroglu and M. Andreani, "Numerical and experimental study of large steam-air bubbles injected in a water pool," *Nucl. Sci. Eng.*, **136**, pp. 363-375 (2000).
5. G. Yadigaroglu, "Computational Fluid Dynamics for nuclear applications: from CFD to multi-scale CMFD," *Nucl. Eng. Des.*, **235**, pp. 153-164 (2004).
6. R. Thiele, "Modeling of direct contact condensation with OpenFOAM," *Division of Nuclear Reactor Technology, Royal Institute of Technology, KTH*, Stockholm, Sweden. Master thesis, ISSN 0280-316X (2010).
7. V. Tanskanen, A. Jordan, M. Puustinen, and R. Kyrki-Rajamäki, "CFD simulation and pattern recognition analysis of the chugging condensation regime," *Annals of Nuclear Energy*, **66**, pp. 133-143 (2014).
8. G. Patel, V. Tanskanen and R. Kyrki-Rajamäki, "Numerical modelling of low-Reynolds number direct contact condensation in a suppression pool test facility," *Annals of Nuclear Energy*, **71**, pp. 376-387 (2014).
9. C. Chan and C. Lee, "A regime map for direct contact condensation," *Int. J. Multiphase Flow*, **8**, pp. 11-20 (1982).
10. D. Lakehal, M. Fulgosi and G. Yadigaroglu, "DNS of Condensing Stratified Steam Water Flow," *ASME J. Heat Transfer* **130**, 021501-10 (2008).
11. M. Puustinen, R. Kyrki-Rajamäki, V. Tanskanen, A. Räsänen, H. Purhonen, V. Riikonen, J. Laine and E. Hujala, "BWR suppression pool studies with POOLEX and PPOOLEX test facilities at LUT," in: The 15th International Topical Meeting on Nuclear Thermal Hydraulics (NURETH-15), Pisa, Italy, May 12-17 2013, pp. 1-12 (2013).
12. J. Tuunanen, J. Kouhia, H. Purhonen, V. Riikonen, M. Puustinen, R. S. Semken, H. Partanen, I. Saure and H. Pylkkö, "General description of the PACTEL test facility," *VTT Research Notes 1929*, VTT, Finland, ISBN 951-38-5338-1 (1998).
13. J. Laine and M. Puustinen, "Condensation Pool Experiments with Steam using Insulated DN200 Blowdown Pipe," *Research Report POOLEX 3/2005*. Lappeenranta University of Technology, Lappeenranta, Finland (2006).
14. L. Schiller and A. Naumann, "Über die grundlegenden Berechnungen bei der Schwerkraftbereitung," *Z. Verein Deutscher Ing.* **77**, pp. 318-320 (1933).
15. B. E. Launder and B. I. Sharma, "Application of the energy dissipation model of turbulence to the calculation of flow near a spinning disc," *Letters in Heat Mass Transfer*, **1**, pp. 131-138 (1974).
16. I. B. Celik, U. Ghia, P. J. Roache, C. J. Freitas, H. Coleman, and P. E. Raad, "Procedure for estimation and reporting of discretization error in cfd applications," *J. Fluids Eng.*, **130** (7), 1-4 (2008).
17. L. F. Richardson and J. A. Gaunt, "The deferred approach to the limit," *Philos. Trans. Roy. Soc. London. Ser. A*, **226**, pp. 299-361 (1927).
18. P. J. Roache, "Perspective: A method for uniform reporting of grid refinement studies," *J. Fluids Eng.*, **116**, pp. 405-413 (1994).
19. S. Ghiaasiaan, "Two-Phase Flow, Boiling and Condensation in Conventional and Miniature Systems," 1<sup>st</sup> edition, Cambridge University Press, New York, ISBN 978-0-521-88276-7 (2008).

## **Publication III**

Patel, G., Tanskanen, V., Hujala, E., and Hyvärinen, J. (2016).  
**Direct contact condensation modeling in pressure suppression pool  
system (in press)**

Nuclear Engineering and Design

Vol. xxx, pp. xxx-xxx.

© Elsevier, 2016

Reprinted with permission from the publisher





Contents lists available at ScienceDirect

Nuclear Engineering and Design

journal homepage: [www.elsevier.com/locate/nucengdes](http://www.elsevier.com/locate/nucengdes)

## Direct contact condensation modeling in pressure suppression pool system

G. Patel, V. Tanskanen\*, E. Hujala, J. Hyvärinen

LUT School of Energy Systems/Nuclear Engineering, Lappeenranta University of Technology (LUT), PO Box 20, FIN-53851 Lappeenranta, Finland

### HIGHLIGHTS

- Chugging condensation mode in drywell–wetwell suppression pool system was simulated.
- Bubble volumes and frequencies were obtained from video data by pattern recognition.
- Eulerian two-fluid approach of the compressible flow solvers was applied.
- Good results were obtained if Rayleigh–Taylor instability was taken into account.

### ARTICLE INFO

#### Article history:

Received 31 May 2016  
 Received in revised form 12 August 2016  
 Accepted 19 August 2016  
 Available online xxxx

### ABSTRACT

The pressure suppression pool of boiling water reactor as a safety system has vital importance from the nuclear reactor safety point of view and it is an interesting challenge for numerical simulations of flow with rapid phase change. This paper presents the recent analysis of computational fluid dynamics (CFD) simulations of chugging direct contact condensation (DCC) mode observed in the drywell–wetwell suppression pool (PPOOLEX) experiments of Lappeenranta University of Technology. A pattern recognition algorithm was employed to determine the bubble volume and the chugging frequency during the test. The numerical simulations were performed by using Eulerian–Eulerian two-fluid approach of the compressible flow NEPTUNE\_CFD software and the OpenFOAM CFD code. The interfacial heat transfer between steam and water was modeled by using three DCC models. Flow turbulence was solved by employing two  $k-\epsilon$  turbulence models. The significance of interfacial area modeling on the chugging DCC was tested by implementing Rayleigh–Taylor Interfacial area model. The performance of different DCC models, the effects of turbulence modeling and interfacial area modeling are presented. The sensitivity of chugging DCC to the initial conditions and to the modeled domain, and the effect of interfacial momentum transfer closure modeling on the chugging are briefly discussed. The choice of DCC model, accuracy of interfacial area modeling and the magnitude of liquid turbulence near the interface are all needed to replicate chugging in a drywell–wetwell suppression pool system. In coarse grid case, the DCC model of Coste 2004 with the Rayleigh–Taylor interface instability model of Pellegrini et al. (2015) provided best results.

© 2016 Elsevier B.V. All rights reserved.

### 1. Introduction

The boiling water reactor (BWR) cooling system can be more compact than the pressurized water reactor (PWR) one, due to the absence of secondary circuit. The proper functioning of pressure suppression pool (PSP) is very essential in BWRs containment because the pressure build-up and the released energy in the containment during a loss of coolant accident (LOCA) or safety relief valve actuation are mitigated in the PSP (Lahey and Moody, 1993).

In the fundamental engineering literature, the mostly studied vapor condensation issues include either dropwise condensation or filmwise condensation along a wall which separates the vapor and the coolant. However, the condensation heat transfer mode appearing particularly in a PSP system during transient and accidents conditions can be categorised as direct contact condensation (DCC) in which the continuous vapor and liquid phases share a large interface where the phase change takes place.

During a LOCA or safety relief valve actuation, a large amount of steam and non-condensable gases are blown via the upper drywell of the PSP system to the wetwell compartment through the blow-down pipes. Steam condenses in the water pool and the non-condensables rise up to the gas space of wetwell. The nature and

\* Corresponding author.  
 E-mail address: [vesa.tanskanen@lut.fi](mailto:vesa.tanskanen@lut.fi) (V. Tanskanen).

<http://dx.doi.org/10.1016/j.nucengdes.2016.08.026>  
 0029-5493/© 2016 Elsevier B.V. All rights reserved.

**Nomenclature***Latin alphabet*

<i>d</i>	diameter scale (m)
<i>g</i>	acceleration ( $\text{m s}^{-2}$ )
<i>h</i>	heat transfer coefficient ( $\text{W m}^{-2} \text{K}^{-1}$ )
<i>H</i>	total enthalpy ( $\text{J kg}^{-1}$ )
<i>k</i>	turbulent kinetic energy ( $\text{m}^2 \text{s}^{-2}$ )
<i>L</i>	length scale (m)
<i>Nu</i>	Nusselt number (–)
<i>P</i>	pressure (Pa)
<i>Pr</i>	Prandtl number (–)
<i>q''</i>	heat flux ( $\text{W m}^{-2}$ )
<i>Re</i>	Reynolds number (–)
<i>t</i>	time (s)
<i>u</i>	velocity component ( $\text{m s}^{-1}$ )
<b>U</b>	velocity ( $\text{m s}^{-1}$ )
<i>V</i>	velocity scale ( $\text{m s}^{-1}$ )

*Greek alphabet*

$\alpha$	phase fraction (–)
----------	--------------------

$\Gamma$	mass transfer rate ( $\text{kg s}^{-1}$ )
$\varepsilon$	turbulence dissipation rate ( $\text{m}^2 \text{s}^{-3}$ )
$\lambda$	thermal conductivity ( $\text{W m}^{-1} \text{K}^{-1}$ )
$\mu$	dynamic viscosity (Pa s)
$\nu$	kinematic viscosity ( $\text{m}^2 \text{s}^{-1}$ )
$\Pi$	bulk interfacial heat transfer rate ( $\text{W m}^{-3}$ )
$\rho$	density ( $\text{kg m}^{-3}$ )
$\sigma$	surface tension ( $\text{N m}^{-1}$ )
$\tau$	stress tensor (Pa)

*Subscripts*

1,2	liquid phase, vapor phase
<i>i,j</i>	cartesian tensor notation
<i>k</i>	arbitrary phase
<i>K</i>	Kolmogorov scale
sat	saturation
<i>T</i>	turbulent

efficiency of steam DCC phenomena in condensation pool depends on the sub-cooling of the pool liquid, the mass flux of injected vapor, drywell and wetwell volumes, the geometry of the vents and its corresponding exit shapes, and the fraction of non-condensables within the vapor.

As a whole, the discharge of steam into condensation pool is a quite intricate event which is associated with hydrodynamics and thermodynamics including bubble dynamics, thermal stratification, turbulent mixing, natural circulation, steam condensation within water pool, ducts, and at wall surfaces. The DCC of steam in water pool contains both the slow and very rapid time scale phenomena, which makes the analysis of condensation challenging either with experiments or numerical simulations (Tanskanen et al., 2014). Moreover, the rapid pressure oscillations resulting from steam condensation are generally unfavorable for the delicate measurement instrumentation and for the time-stepping of simulations. However, the steam blowdown experiments are important in order to enhance the understanding of physics involved in it.

Since the early '70s, several experimental studies of DCC of steam have been conducted. Some major experimental studies have been performed with vertical steam injection into condensation pool including various aspects, e.g., experiments done in the Marviken facility during 1972 to 1981 Wikdahl (2007), works of McIntyre et al. (1976), Grafton et al. (1977), Kennedy et al. (1978), Chan and Lee (1982), Aust and Seeliger, 1982, Nariai and Aya (1986), Walsche and Cachard (1996), Meier et al. (2000), the suppression pool experiments conducted with the PANDA (Smith, 2007) and LINX (Hart et al., 2001) experimental facilities, and Laine and Puustinen (2005) with the POOLEX. More details could be found in Tanskanen (2012) where he summarized the brief review of the experimental efforts conducted by other researchers on condensation pool experiments. More recently, experimental work has been performed by Puustinen et al. (2013) with the PPOOLEX facility aiming different issues of BWR containment. The POOLEX facility of Lappeenranta University of Technology (LUT) was an open wetwell facility with a long and straight blowdown pipe, and the PPOOLEX facility of LUT is a closed pressure vessel including drywell and wetwell.

Some extensive works were performed to classify the condensation modes in as regime maps e.g., Aya and Nariai (1987, 1991), Chan and Lee (1982), Liang and Griffith (1994) and de With et al.

(2007). A few works exist e.g., Aya and Nariai (1986) and Ali et al. (2007) in which analytical study of the oscillatory condensation modes is presented, including chugging.

Large scale computational fluid dynamics (CFD) simulations are now more affordable due to advancements in computational power. In the field of nuclear safety analysis, CFD has become an increasingly applicable tool for thermalhydraulic investigations (Bestion, 2012). Since 2000, gradual improvement in CFD simulations of chugging DCC in vertical vent pipes can be seen. For example, Meier et al. (2000, 2004) presented numerical study of large steam–air bubbles in a water pool without mass transfer by utilizing Volume of Fluid method. Further, Thiele (2010) tried VOF simulations with mass transfer based on temperature difference. Pättikangas et al. (2010) employed two-fluid Eulerian approach for PSP simulations with heat and mass transfer. Tanskanen (2012) and Tanskanen et al. (2014) simulated the STB-28 test done at POOLEX facility. Their results demonstrated the improved capability of Eulerian two-phase CFD codes to rather successfully predict chugging DCC in a blowdown pipe–wetwell system. In their work, a pattern recognition algorithm has been employed to extract the information of bubble size and bubble appearance frequency during the rapid chugging condensation mode. Pellegriani et al. (2015) conducted CFD simulations of chugging DCC of the same experiment of POOLEX facility. They proposed a method to treat the surface with growing instabilities based on the Rayleigh–Taylor theory. Tanskanen et al. (2015) presented a summary of their initial less successful simulations of the PPOOLEX DCC-05-4 test.

This paper presents the recent analysis of CFD simulations of the drywell–wetwell suppression pool system PPOOLEX. A set of numerical simulations have been performed with the CFD codes, NEPTUNE\_CFD and OpenFOAM, in which a chugging DCC test case (DCC-05-4) is modeled by using the Eulerian two-fluid approach. In this work, the performance of different condensation models, the effects of turbulence modeling, interfacial area modeling, interfacial momentum transfer, geometry and interface initialization are analyzed. The significance of interfacial area modeling on the chugging DCC is tested by implementing Rayleigh–Taylor Interfacial (RTI) area model proposed by Pellegriani et al. (2015) to the NEPTUNE\_CFD code. The pattern recognition data of a PPOOLEX test has been used here as a reference measurement of the bubble oscillations in the chugging condensation mode.

## 2. PPOOLEX DCC-05 experiment

The PPOOLEX test facility at LUT is a scaled down experimental facility for BWR containment safety related research. A schematic view of the PPOOLEX test facility is shown in Fig. 1. The PPOOLEX test facility consists both the drywell and wetwell (condensation pool) compartments of the containment.

The total height is 7.45 m and the inner diameter is 2.4 m. The main component of the facility is the approximately 31 m<sup>3</sup> cylindrical test vessel. The drywell compartment is thermally insulated to prevent wall condensation. The test facility is able to resist overpressure up to 4 bar and underpressure of 0.5 bar. A DN100 blowdown pipe was used in the DCC-05 test. The blowdown pipe was positioned inside the wetwell compartment at a non-axisymmetric location (i.e. 420 mm apart from the center of pool). During the tests, the visual observation of the interior is possible via the windows on the side walls and in the bottom segment of the wetwell compartment.

Steam flow rate during the tests is measured with a vortex flow meter. The test facility is equipped with several thermocouples for measuring steam, pool water and structural temperatures and with pressure transducers for observing pressures in the drywell, inside the blowdown pipe(s), at the suppression pool bottom and in the gas phase of the wetwell. Standard instrumentation includes also strain gauges, vertical acceleration and movement transducers and valve position sensors. The drywell is equipped with a steam fraction measurement for estimating non-condensable gas presence.

The DCC-05 experiment was aimed to acquire test data for the validation of DCC models used in CFD codes and to obtain the multi-camera high speed video data of blowdown event to be used in the development work of pattern recognition algorithms. Therefore, the test facility included the system of three high speed cameras in order to capture the blowdown event of steam in water pool. Also, the temperatures were measured in various elevations within the blowdown pipe in order to achieve the frequency and the amplitude of steam/water interface oscillations.

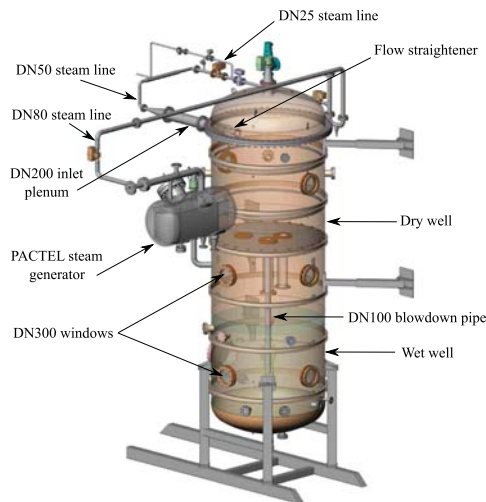


Fig. 1. PPOOLEX test facility (Puustinen et al., 2013).

The DCC-05 experiment was started in isothermal wetwell water (25°C) conditions so that the blowdown pipe outlet was submerged by ~1 m. During the clearing blow phase, practically all air was displaced from the drywell into the gas space of the wetwell after 500 s of the steam blowdown initiation. After that, the idea was to keep the pool water temperature rise as low as possible (rise of 10 K realized) but use a large range of different steam flow rates. Steam flow rates between 75 and 200 g s<sup>-1</sup> were used in the chugging blows of DCC-05 (Fig. 2).

The information about formation and break up of bubbles can be extracted by visual observation using a suitable pattern recognition algorithm. Tanskanen (2012) introduced a pattern recognition approach with which condensation rate in chugging DCC was analyzed indirectly from the video material of the suppression pool tests. However, the algorithm was based on a single camera output. For the DCC-05 PPOOLEX experiments, the introductory version of the pattern recognition algorithm was upgraded by Hujala (2013) to use three almost perpendicularly located high speed cameras. Volume of the bubbles were calculated by using bubble boundary data and numerical integration. From the data of the bottom camera an approximation, that the cross-sectional area of the bubbles is circular, can be estimated. The volume of the bubble can be measured by using cylindrical shaped plate elements of the height of single pixel. Each pixel row had its own diameter. Volume of a single row with the height of 1 pixel is easy to calculate. By collecting all the rows containing bubble pixels it was possible to estimate the volume of the bubble. The largest diameter seen in the side camera images should be the same as the diameter in the bottom camera image. Fig. 3 shows the recognized bubble volume in the DCC-05-4 experiment which was calculated by using pattern recognition.

In this work, Fast Fourier Transform (FFT) has been used to estimate the frequency of chugging motion from the recognized bubble volume obtained with pattern recognition. The FFT works best for purely periodic signals, therefore power spectrum of the volume data with peaks occurring at uneven time intervals tends to give multiple spikes with nearly equal frequencies. Fig. 4 shows the FFT from the recognized bubble volume in the DCC-05-4 experiment. It can be seen that the chugging frequencies are around 2 Hz, however, there are more energetic (larger) bubbles collapsing less frequently. A less distinguishable rapid interface oscillation of 50 Hz can be observed. This was result of the fluctuation or flickering of the interface at the natural frequency of oscillation before a bubble collapses (Brennen, 2014; Leighton, 1994).

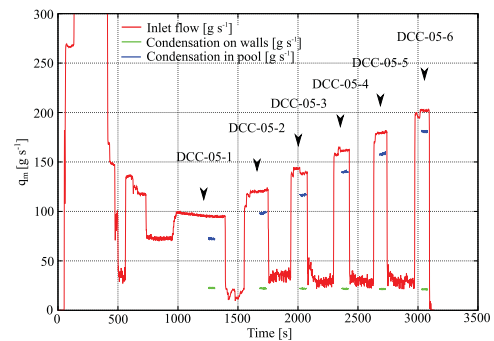


Fig. 2. Six chugging blows of the DCC-05 experiment (Tanskanen et al., 2015).

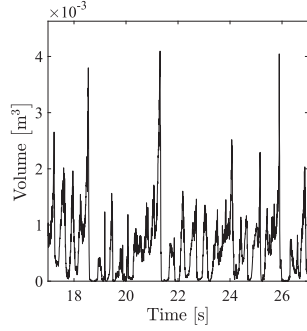


Fig. 3. The recognized bubble volume in the DCC-05-4 experiment.

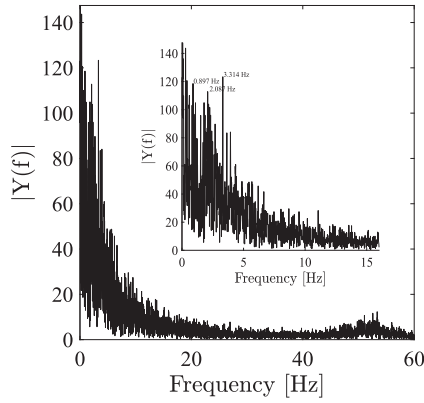


Fig. 4. FFT from the recognized bubble volume in the DCC-05-4 experiment.

### 3. Numerical models

#### 3.1. Governing equations

The chugging phenomenon in vertical blowdown pipes is associated with strong pressure oscillations due to the extensive and rapid phase change. Also, most of the incompressible flow solvers of the computational fluid dynamics (CFD) software for two-phase system are inadequate in order to handle rapid and strong pressure oscillations of chugging phenomenon. Therefore, compressible flow formulation is favorable in such conditions (Tanskanen et al., 2015). In this study, the compressible flow Eulerian Finite Volume multi-field solver NEPTUNE\_CFD (Bestion and Guelfi, 2005; Guelfi et al., 2007; Laviéville et al., 2006) version 2.0.1 utilizing CATHARE steam tables was used for chugging simulations. The OpenFOAM simulations were based on compressible two-flow solver of OpenFOAM 2.3.1. The equations for conservation of mass, momentum and energy in both CFD codes can be expressed as below, respectively:

$$\frac{\partial}{\partial t}(\alpha_k \rho_k) + \nabla \cdot (\alpha_k \rho_k \mathbf{U}_k) = \Gamma_k, \quad (1)$$

$$\frac{\partial}{\partial t}(\alpha_k \rho_k \mathbf{U}_k) + \nabla \cdot (\alpha_k \rho_k \mathbf{U}_k \mathbf{U}_k) = \alpha_k \nabla \cdot (\tau_{k,ij} + \tau_{k,ij}^t) - \alpha_k \nabla P + \alpha_k \rho_k \mathbf{g} + \mathbf{M}_k + \alpha_k \mathbf{S}_k, \quad (2)$$

$$\frac{\partial}{\partial t}(\alpha_k \rho_k H_k) + \nabla \cdot (\alpha_k \rho_k \mathbf{U}_k H_k) = \alpha_k \frac{\partial P}{\partial t} + \alpha_k \rho_k \mathbf{U}_k \mathbf{g} - \nabla \cdot (\alpha_k \mathbf{Q}_k) + \Gamma_k H_k + \Pi_k + q_{wall,k}^{\prime\prime}, \quad (3)$$

Here,  $k$  indicates an arbitrary phase (later on  $k = 1$  for liquid phase and  $k = 2$  for vapor phase). In the momentum equation,  $\tau_{k,ij}$  and  $\tau_{k,ij}^t$  describe the molecular and turbulent stress tensors, respectively,  $\mathbf{M}_k$  indicates the interfacial momentum transfer between the phases, and  $\mathbf{S}_k$  denotes the external momentum source term. In this study, the  $\mathbf{M}_k$  term contains only the momentum transfer by a drag model i.e. the Large Interface Model 'Coste LIM' of Coste (2013) or the 'separated phase drag model' (Laviéville et al., 2006) in NEPTUNE\_CFD simulations. The 'SN drag model' of Schiller and Naumann (1933) was used in OpenFOAM simulations, because it was the most suitable option of the already implemented models for gas–liquid flow. Despite of its limited applicability for fully separated phases, it produces reasonable drag if the reference bubble diameter value is adjusted to a suitable value. In this study, 1 mm bubble size was used as the reference based on the results of stable interface simulations of Patel et al. (2015). In the energy equation,  $\mathbf{Q}_k$  is the conductive heat flux.

#### 3.2. Phase change and heat transfer modeling

By imposing the overall heat balance, the mass transfer due to the phase change at the steam–liquid interface can be calculated as

$$\Gamma_k = \frac{\Pi_1 + \Pi_2}{H_2 - H_1}, \quad (4)$$

In this work, the steam is in saturated state, therefore the vapor phase heat transfer contribution  $\Pi_2$  is negligible. The interfacial heat transfer for liquid phase is defined as

$$\Pi_1 = a_i h_1 (T_{sat} - T_1). \quad (5)$$

Here,  $a_i$  is the interfacial area density which was calculated from the gradient of void fraction as

$$a_i = |\nabla \alpha_1|, \quad (6)$$

and  $h_1$  is the heat transfer coefficient for the liquid phase which is calculated as

$$h_1 = \frac{Nu_1 \lambda_1}{L_1}. \quad (7)$$

For the Nusselt number in chugging simulations, the correlations predicting high condensation rates in separated flow cases have been promising (Tanskanen, 2012; Tanskanen et al., 2014). In this work, three Nusselt number correlations have been tested and their performance have been discussed. The details about Nusselt number correlations are listed below.

##### 3.2.1. Hughes and Duffey model based on small eddies

The Hughes and Duffey model on small eddies (hereafter 'HD 1 model') is based on the surface renewal model of Hughes and Duffey (1991). The Nusselt number formulation is defined as

$$Nu_1 = \frac{2}{\sqrt{\pi}} Re_{K,1} Pr_1^{1/2}, \quad (8)$$

where  $Re_{K,1}$  is the Reynolds number based on Kolmogorov length and velocity scales,  $L_K$  and  $V_K$ :

$$V_K = (v\varepsilon)^{1/4} \text{ and } L_K = \left(\frac{v^3}{\varepsilon}\right)^{1/4}. \quad (9)$$

##### 3.2.2. Hughes and Duffey model based on large eddies

The 'HD 2 model' is the correlation of Hughes and Duffey (1991) based on the surface renewal theory of Banerjee (1978) which

includes the large eddies. The Nusselt number correlation for the HD 2 model can be presented as

$$\text{Nu}_1 = \frac{2}{\sqrt{\pi}} \text{Re}_{\tau,1}^{1/2} \text{Pr}_1^{1/2}, \quad (10)$$

where  $\text{Re}_{\tau,1}$  is the turbulent Reynolds number which can be calculated as

$$\text{Re}_{\tau,1} = \frac{V_{\tau,1} L_{\tau,1}}{\nu_1}. \quad (11)$$

The turbulent velocity and length scales:  $V_{\tau}$  and  $L_{\tau}$  can be defined as

$$V_{\tau} = C_{\mu}^{1/4} k^{1/2} \quad \text{and} \quad L_{\tau} = \frac{C_{\mu}^{3/4} k^3}{\varepsilon}, \quad (12)$$

where the  $C_{\mu}$  is the turbulence viscosity constant of the  $k-\varepsilon$  model.

### 3.2.3. The Coste 2004 model

The Nusselt number formulation of the Coste continuous 'Coste C' model of Coste (2004) can be written as

$$\text{Nu}_1 = \text{Re}_{\tau,1}^{7/8} \text{Pr}_1^{1/2}, \quad (13)$$

where the turbulent velocity and length scales:  $V_{\tau}$  and  $L_{\tau}$  in the  $\text{Re}_{\tau,1}$  are

$$V_{\tau} = \left(\frac{2}{3}k\right)^{1/2} \quad \text{and} \quad L_{\tau} = L_k = \left(\frac{\nu^3}{\varepsilon}\right)^{1/4}. \quad (14)$$

In the Coste C model, the  $V_{\tau}$  is limited with  $V_{\tau} = \min(|\mathbf{U}_1|, (\frac{2}{3}k)^{1/2})$ .

### 3.2.4. Turbulence modeling

In the NEPTUNE-CFD simulations, flow turbulence was solved by employing the standard  $k-\varepsilon$  turbulence model of Launder and Spalding (1974) for both phases. The equations of the turbulent kinetic energy and its dissipation can be written as follows,

$$\frac{\partial}{\partial t}(\rho_k k_k) + \nabla \cdot [\rho_k \mathbf{U}_k k_k - \left(\mu + \frac{\mu_t}{\sigma_k}\right) \nabla k] = \mathbb{P}_k + \mathbb{G}_k - \varepsilon_k + \Pi_{qk} \quad (15)$$

$$\begin{aligned} \frac{\partial}{\partial t}(\rho_k \varepsilon_k) + \nabla \cdot [\rho_k \mathbf{U}_k \varepsilon_k - \left(\mu + \frac{\mu_t}{\sigma_\varepsilon}\right) \nabla \varepsilon] \\ = C_{\varepsilon 1} \frac{\varepsilon_k}{k_k} [\mathbb{P}_k + (1 - C_{\varepsilon 3}) \mathbb{G}_k] - \rho_k C_{\varepsilon 2} \frac{\varepsilon_k^2}{k_k} + C_{\varepsilon 4} \frac{\varepsilon_k}{k_k} \Pi_{qk}. \end{aligned} \quad (16)$$

Here,  $\mu_t$  is the turbulent viscosity,  $\sigma_k$  and  $\sigma_\varepsilon$  are the turbulent Prandtl numbers for  $k$  and  $\varepsilon$ ,  $\mathbb{P}$  is the production of  $k$ ,  $\mathbb{G}$  is the stratification attenuation term, and  $\Pi_q$  is the production or destruction of  $k$  due to the influence of other phases. The model constants are  $\sigma_k = 1.0$ ,  $\sigma_\varepsilon = 1.3$ ,  $C_{\varepsilon 1} = 1.44$ ,  $C_{\varepsilon 2} = 1.92$ ,  $C_{\varepsilon 4} = 1.2$ ,  $C_{\varepsilon 3} = 0$  if  $\mathbb{G} \geq 0$  and  $C_{\varepsilon 3} = 1$  if  $\mathbb{G} < 0$ . The turbulent viscosity  $\mu_t$  is defined in the standard  $k-\varepsilon$  model as

$$\mu_{t,k} = \rho_k C_{\mu} \frac{k_k^2}{\varepsilon_k}, \quad (17)$$

where  $C_{\mu} = 0.09$ .

In the OpenFOAM simulations, the  $k-\varepsilon$  model is the one proposed by Lahey (2005). This ' $Lk-\varepsilon$ ' model was used for the continuous liquid phase turbulence. This model includes dispersed phase induced turbulence terms in the  $k$  and  $\varepsilon$  transport equations. In addition, the  $Lk-\varepsilon$  model uses modified turbulent viscosity term written as

$$\mu_{t,1} = \rho C_{\mu} \frac{k_1^2}{\varepsilon_1} + C_{\mu} \alpha_2 d_2 |\mathbf{U}_1|, \quad (18)$$

where  $\mathbf{U}_1$  indicates the relative velocity. Moreover, the  $Lk-\varepsilon$  turbulence model contains the additional dispersed phase induced production terms  $S_{k,1}$  and  $S_{\varepsilon,1}$ , respectively:

$$S_{k,1} = C_{p1} \frac{\alpha_1 \rho_1 \alpha_2}{d_2} \left[ |\mathbf{U}_1 - \mathbf{U}_2|^3 + \left(\frac{C_d \text{Re}_d \nu_1}{d_2}\right)^{3/4} |\mathbf{U}_1 - \mathbf{U}_2|^3 \right] + C_{12} k_2, \quad (19)$$

$$S_{\varepsilon,1} = C_3 S_{k,1} \frac{\varepsilon_1}{k_1} + c_{12} \varepsilon_2. \quad (20)$$

In Eq. (19),  $C_{p1}$  is the model constant and  $C_{12}$  is the transfer coefficient between the turbulence models of both the phases which is calculated from local phase fraction, gas phase turbulent time scale and simulation time step. More details about utilized turbulence models in OpenFOAM simulations can be found in Lahey (2005) and in Peltola (2015).

### 3.2.5. Rayleigh–Taylor instability (RTI) model

Generally, the interfacial area density is obtained from the gradient of volume fraction. However, the accuracy of this value depends on the grid resolution related to the interfacial details. The high accelerations cause interfacial instabilities e.g. Rayleigh–Taylor instability, which increase the interfacial roughness significantly. Pellegrini et al. (2015) proposed a simple model to treat the surface with growing instabilities based on the Rayleigh–Taylor theory. In the work of Pellegrini et al. (2015), the interfacial wave amplitude  $\eta$  was expressed as

$$\frac{d\eta}{dt} = n\eta, \quad (21)$$

where  $n$  is a function as  $n = f(g, \kappa, A)$ . Here,  $g$  is the acceleration (e.g. gravitational, but can be general as well),  $\kappa$  is the wave number and  $A$  is the Atwood number ( $A = \frac{\rho_1 - \rho_2}{\rho_1 + \rho_2}$ ).

Pellegrini et al. (2015) derived  $n$  from Duff et al. (1962) and Livescu (2004) as

$$n = \Re \left( \sqrt{\left( Ag - \frac{\sigma \kappa^2}{\rho_1 - \rho_2} \right) \kappa + \nu^2 \kappa^4 - \nu \kappa^2} \right), \quad (22)$$

where  $\nu = \frac{\mu_1 + \mu_2}{\rho_1 + \rho_2}$ . In two-fluid modeling, the interfacial area density is usually calculated as in Eq. 6. Using that, Pellegrini et al. (2015) simplified the area with approximation to square waves, therefore, the amplified length is expressed as

$$L = \sqrt{a_1 \Delta v}, \quad (23)$$

where  $\Delta v$  indicates the cell volume. The amplified length is then obtained by adding the portion of wave as

$$L_{\text{amplified}} = L + \frac{kL\eta}{\pi}. \quad (24)$$

The interfacial area can be written as

$$a_{i,\text{amplified}} = \left( \frac{\kappa\eta + 1}{\pi} \right)^2 a_i. \quad (25)$$

Here, the wave number should be maximizing the wave growth. In order to simplify the calculation, Pellegrini et al. (2015) estimated it as

$$\kappa_{\text{max}} = \sqrt{\frac{Ag(\rho_1 + \rho_2)}{3\sigma}}. \quad (26)$$

The value of acceleration is calculated from the pressure gradient normal to the interface as

$$\mathbf{g} = \frac{\nabla P \cdot \frac{\nabla \alpha_1}{|\nabla \alpha_1|}}{\rho}. \quad (27)$$

where,  $\rho$  refers to the average density of fluid in the interfacial cell. The amplitude of the wave is expressed as

$$\eta_t = \eta_{t-\Delta t} e^{n\Delta t}. \quad (28)$$

As an initial perturbation, Pellegrini et al. (2015) used a small value i.e.  $\eta_{t=0} = 10^{-5}$  m. In the current CFD implementation, the value of  $\eta$  is also limited by the cell size by using

$$\eta_t = \min(\eta_t, L). \quad (29)$$

#### 4. Computational model and simulation set-up

A relatively long sample of transient had to be simulated in order to obtain enough data. As that was computationally time consuming in 3D simulations (Tanskanen et al., 2015), a 2D-axisymmetric representation of the PPOOLEX geometry was developed in the present study to make a greater case matrix possible.

##### 4.1. Geometrical details and grid generation

A 2D-axisymmetric geometry containing a  $1^\circ$  sector of the PPOOLEX pool was modeled. Therefore, the grid of hexahedral cells was generated by rotating a quadrilateral grid to contain a single cell thickness in respect to z-axis. The main idea in the axisymmetric grid was to transfer the blowdown pipe to the center axis of the facility and the inlet plenum as well, but keep the other dimensions i.e. volumes of different parts of the pool unchanged. Due to the large size of the wetwell and relatively low inlet velocity, the inlet plenum re-location towards the blowdown pipe did not have significant effect on the phenomena in the wetwell (Tanskanen et al., 2016). Concerning the blowdown pipe relocation, the 2D simplification lost the likely asymmetric field of pool liquid circulation and asymmetric bubble shapes as well. However, the effect of these simplifications was assumed small due to the short samples simulated i.e. pool mixing remained weak, and due to the mainly symmetric bubbles which were observed when the DN100 blowdown pipe was used in the experiment.

In rapid condensation simulations, the interface area increase can be significant due to the acceleration by pressure decrease and chugging motion of the interface. This problem can be approached by two ways. First of these is a denser grid with which the interface details can be captured better. The second and more practical from the engineering point of view is an interface model that modifies the interfacial area density (Eq. (6)) to include the effect of increased interfacial area in the cases of coarse grids. The denser grid option was tested by making a grid able to capture at least the initial interfacial perturbation wave length of Rayleigh–Taylor instability in the DCC-05-4 case. The critical wave length can be calculated with (Ishii and Hibiki, 2011)

$$\lambda_c = 2\pi \sqrt{\frac{\sigma}{g(\rho_1 - \rho_2)}}. \quad (30)$$

According to axial interface location data from the pattern recognition study of DCC-05-4 test, acceleration can be as high as  $g = 500$  or even  $1000 \text{ ms}^{-2}$ . Then  $\lambda_c = 2.2$  or  $1.5 \text{ mm}$  would be the corresponding critical wave lengths. Therefore, a grid with minimum  $1 \text{ mm}$  cell size was considered. The grid was refined inside the blowdown pipe and in the mouth region of the grid up to  $1 \text{ mm}$ . In order to analyze the other modeling issues on the chugging phenomenon, a similar but coarser grid with  $5 \text{ mm}$  cell size was used. Fig. 5 presents the 2D-axisymmetric geometry with the  $5 \text{ mm}$  grid. The grid with  $1 \text{ mm}$  cell size contained 273,200 computational cells, while the  $5 \text{ mm}$  cell size grid had 72,000 computational cells. These grids were suitable for standard wall functions as in the denser grid,  $y^+ = 60$  inside the blowdown pipe. In

order to study the damping effect of the suppression pool drywell, a truncated geometry and grid without the drywell were made as well.

The sub-test DCC-05-4 was selected as the CFD validation case of this study. The initial and boundary parameters for the simulation of the case are listed in Table 1.

For the sake of simplicity, the wall condensation was not simulated in this study. The amount of wall condensation was estimated analytically using the correlation of Chen et al. (1987). The calculated value of wall condensate was deduced from the inlet mass flow rate to compensate its effect on the available steam mass flux in the blowdown pipe. Fig. 6 summarizes the initial temperature and pressure fields of the DCC-05-4 simulation.

In most of the simulations, the initial location of the steam–water interface at  $t = 0 \text{ s}$  was set at elevation  $1.8 \text{ m}$  corresponding water level in pool inside the blowdown pipe. Therefore, the volume fraction of the vapor phase was set to unity inside the blow-

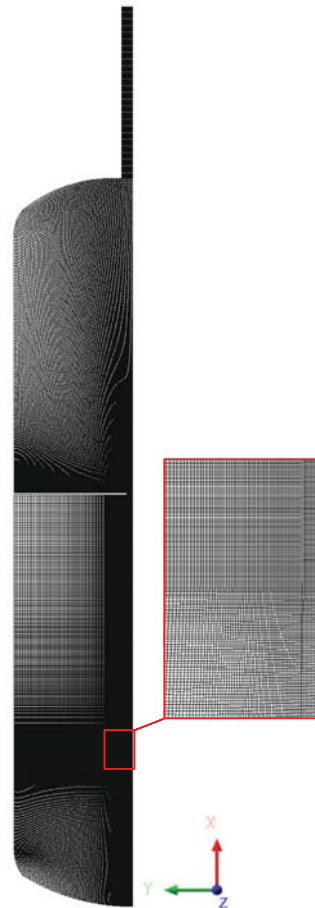


Fig. 5. 2D-axisymmetric representation of the PPOOLEX facility with  $5 \text{ mm}$  grid resolution.

**Table 1**  
Initial and boundary conditions of DCC-05-4 simulation.

Maximum simulation duration	51 s (test sample)
Initial interface level in pipe	0.042 m or 1.03 m (above pipe outlet)
Water level in pool	1.03 m (above pipe outlet)
Initial drywell pressure	301310 Pa
Initial wetwell gas space pressure	293370 Pa
$T_{sat}$ in drywell	406.8 K
T in drywell gas space	313.7–330 K
T in wetwell liquid	300.7–315.6 K (stratified)
T in water plug in pipe	374.3–405.6 K
Actual inlet mass flow rate	+0.1616 kg s <sup>-1</sup> (mean)
Wall condensation estimation	-0.0217 kg s <sup>-1</sup> (Chen et al., 1987)
Reduced inlet mass flow rate	+0.1399 kg s <sup>-1</sup> (inlet BC.)
Inlet temperature	429.2 K
NC gas mass fraction in drywell gas space	0.984–0.964 (calculated)

down pipe up to 1.8 m. Some cases were also conducted with different steam-water interface initialization near blowdown pipe outlet in order to study the influence of interface initialization on chugging DCC. In all the simulations, the pool walls were considered to be adiabatic and a no-slip boundary condition was imposed at all the wall surfaces. In both the CFD codes, the 2D-axisymmetric unsteady CFD simulations were performed with the finite volume formulation. The code specific settings for the NEPTUNE\_CFD 2.0.1 and OpenFOAM 2.3.1 are presented in Table 2.

The simulation case matrix and the varied parameters are presented in Table 3.

## 5. Results and discussion

The instantaneous condensation rate can not be measured reliably, but the characteristic phenomena like bubble size, bubble collapse rate and chugging frequency can be compared between experimental and simulation data qualitatively at least. The DCC rate depends on the chosen DCC model or correlation, interfacial

**Table 2**  
CFD solver specific settings for the DCC-05-4 case.

NEPTUNE_CFD solver settings	
Predefined flow	Free-surface flow
Compressible	Phase 1: Yes, Phase 2: Yes
Energy resolution	Phase 1: Yes, Phase 2: Yes
Non-condensable gases	Off
Thermodynamics (tables)	Phase 1: Cathare Water L, Phase 2: Cathare Water V
Conjugate heat transfer	Off
Turbulence	Phase 1: $k-\epsilon$ , Phase 2: $k-\epsilon$
Continuous phases coupling	Sep.phases with condensation
Interfacial momentum transfer	See Table 3
DCC model	See Table 3
Gravity	-9.81 ms <sup>-2</sup>
Inlet thermal condition	Phase 1: $H_{sat}(P)$ , Phase 2: $T_{mp} = 429.25$ k
Inlet $D_0$	0.2141 m
Navsto sub-cycles; Max. Alpha-P cycles	1; 50
Max.  1 - sum( $\alpha$ )	1e-8
Time step option	adaptive
Initial time step size	1e-5 s
CFI; FOU	1; 10
OpenFOAM solver settings	
Pressure-velocity coupling	PIMPLE
Compressible	Phase 1: Yes, Phase 2: Yes
Energy resolution	Phase 1: Yes, Phase 2: No
Non-condensable gases	No
Thermodynamics (tables)	No
Turbulence	Phase 1: $k-\epsilon$ , Phase 2: $k-\epsilon$
Interfacial momentum transfer	See Table 3
DCC model	See Table 3
Gravity	-9.81 ms <sup>-2</sup>
Max.  1 - sum( $\alpha$ )	1e-5
Time step option	adaptive
Initial time step size	1e-4 s
Courant number	< 1

area density modeling and subcooling rate. Of these, only the subcooling rate is assumed well initialized and modeled in the simulations. In this chapter, the effects of the DCC heat transfer model

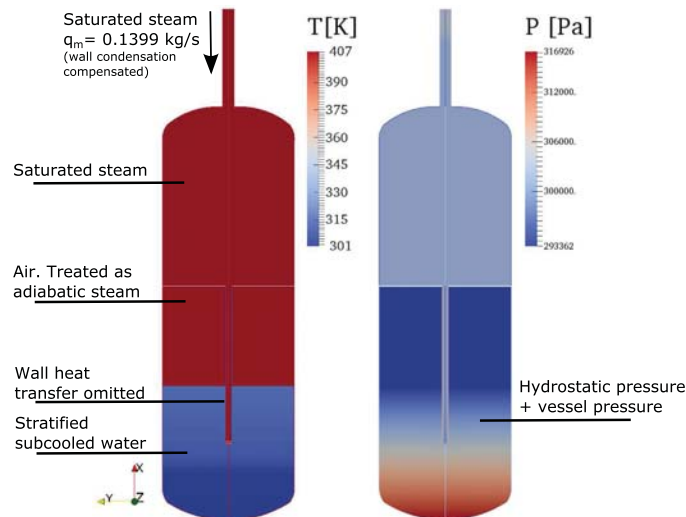


**Fig. 6.** Initial temperature and pressure fields in the simulations of the DCC-05-4 case.

Please cite this article in press as: Patel, G., et al. Direct contact condensation modeling in pressure suppression pool system. Nucl. Eng. Des. (2016), <http://dx.doi.org/10.1016/j.nucengdes.2016.08.026>

**Table 3**  
Simulation cases and varied parameters.

Case ID	Code	DCC model	Interfacial area density	Interfacial momentum transfer	Turbu. model	$\sigma$ model	Initial interface location	Grid
CASE1	NE	Coste C	$ \nabla \alpha_1 $	Coste LIM	$sk - \epsilon$	none	w. level	5 mm
CASE2	NE	HD 1	$ \nabla \alpha_1 $	Coste LIM	$sk - \epsilon$	none	w. level	5 mm
CASE3	NE	HD 2	$ \nabla \alpha_1 $	Coste LIM	$sk - \epsilon$	none	w. level	5 mm
CASE4	NE	Coste C	$ \nabla \alpha_1 $	Sep.Phases	$sk - \epsilon$	none	w. level	5 mm
CASE5	OF	Coste C	$ \nabla \alpha_1 $	SN	$Lk - \epsilon$	none	w. level	5 mm
CASE6	NE	Coste C	$ \nabla \alpha_1 $	Coste LIM	$sk - \epsilon$	none	w. level	1 mm
CASE7	NE	Coste C	$ \nabla \alpha_1  + RTI$	Coste LIM	$sk - \epsilon$	none	w. level	5 mm
CASE8	NE	Coste C	$ \nabla \alpha_1 $	Coste LIM	$sk - \epsilon$	none	near outlet	5 mm
CASE9	NE	Coste C	$ \nabla \alpha_1 $	Coste LIM	$sk - \epsilon$	none	near outlet	5 mm trunc.
CASE10	OF	Coste C	$ \nabla \alpha_1 $	SN	$Lk - \epsilon$	none	near outlet	5 mm
CASE11	OF	Coste C	$ \nabla \alpha_1 $	SN	$Lk - \epsilon$	none	w. level	5 mm trunc.
CASE12	NE	Coste C	$ \nabla \alpha_1  + RTI$	Sep.Phases	$sk - \epsilon$	devel.	w. level	5 mm
CASE13	NE	Coste C	$ \nabla \alpha_1  + RTI$	Coste LIM	$sk - \epsilon$	devel.	w. level	5 mm
CASE14	NE	HD 1	$ \nabla \alpha_1  + RTI$	Coste LIM	$sk - \epsilon$	devel.	w. level	5 mm

NE = NEPTUNE\_CFD; OF = OpenFOAM; Coste C = Coste (2004) continuous model; HD 1 = Hughes and Duffey (1991) model; HD 2 = Hughes and Duffey (1991) model based on large eddies; RTI = Rayleigh-Taylor instability model (Pellegrini et al., 2015).

Coste LIM = Large Interface Model of Coste (2013); Sep.Phases = separated phase drag model (Laviéville et al., 2006); SN = Schiller and Naumann (1933) drag model.  $sk - \epsilon$  = standard  $k - \epsilon$  turbulence model of Launder and Spalding (1974);  $Lk - \epsilon = k - \epsilon$  turbulence model of Lahey (2005); w. level = water level of the wetwell. devel. = under development/not validated; trunc. = truncated PPOOLEX geometry.

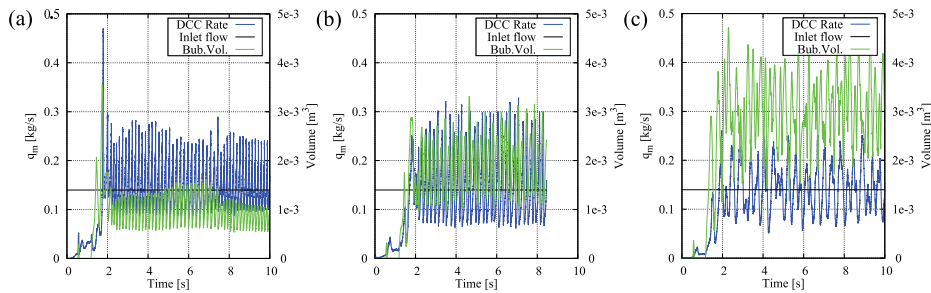


Fig. 7. DCC rates and bubble volumes in (a) CASE1, (b) CASE2, and (c) CASE3.

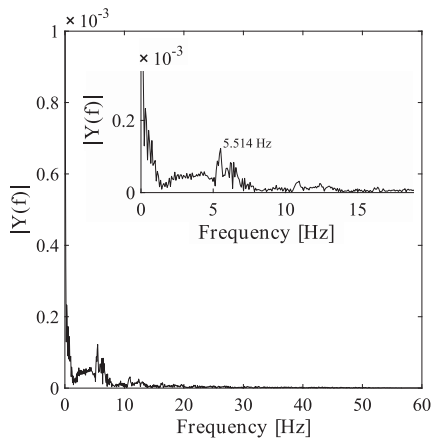


Fig. 8. FFT from the recognized bubble volume in the simulation of CASE1.

in general, turbulence kinetic energy within the DCC models and the interfacial area density modeling on the DCC rate is demonstrated. Furthermore, the sensitivity of chugging DCC to the initial

conditions and to the modeled domain is briefly tested. At the end of the chapter, the effect of interfacial momentum transfer closure modeling on the chugging is demonstrated.

### 5.1. Effect of DCC model

The DCC model of Coste (2004) and the NEPTUNE\_CFD modification of Hughes and Duffey (1991) were proven promising in the chugging simulations of PPOOLEX blowdown pipe and wetwell system (Tanskanen, 2012). As to the results in the drywell-wetwell system of PPOOLEX, Fig. 7 summarizes the DCC rate and bubble size results of the basic cases.

Comparing the bubble volume data of Figs. 3 and 7, it can be seen that chugging did not occur in these simulations. Although the DCC rate was occasionally much higher than the inlet rate, it was due to the increase in the size of inflating bubble and not due to the interface ripping induced by rapid condensation. That is, even though the DCC rate was higher than the inlet rate, it was not still high enough to change the characteristic oscillating motion of non-condensing bubble towards actual chugging motion. After the CASE1, 2 and 3, the Rayleigh-Taylor instability model tests CASE7 and CASE14 were carried out. Based on the results, the highest DCC yielding model i.e. Coste (2004) was chosen as the default model for most of the simulation cases in this study. Fig. 8 shows the FFT of the bubble volume in the CASE1.

Power spectrum of bubble size in CASE1 is an example of the non-chugging cases. Compared this to the experimental data of

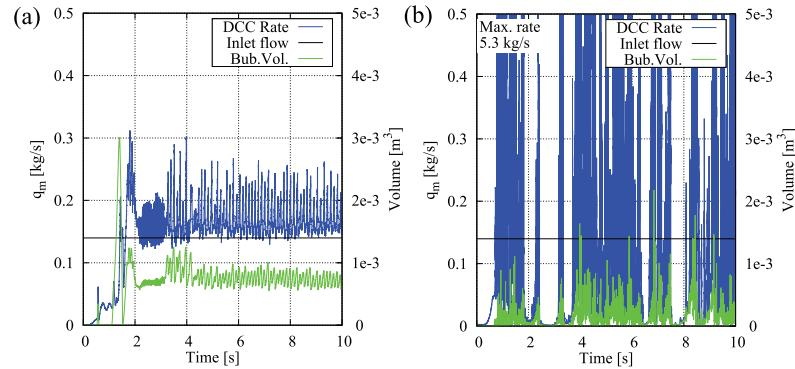


Fig. 9. DCC rates and bubble volumes in (a) CASE4 and (b) CASE5.

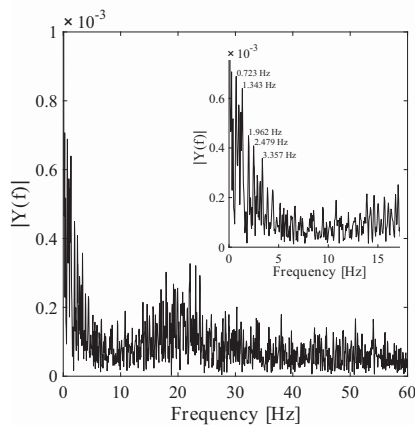


Fig. 10. FFT from the recognized bubble volume in the simulation of CASE5.

Fig. 4, the 0.5–3.3 Hz peak bunch is missing as well as the rapid interface oscillation of 50 Hz. Instead, a clear 5.5 Hz oscillation of permanently present bubble interface could be seen, demonstrating the absence of chugging.

### 5.2. Effect of turbulence modeling

The results of the DCC models used here are proportional to the velocity scale relative to the near interface turbulence kinetic energy or dissipation rate. The CASE4 in Fig. 9 was a NEPTUNE\_CFD case with the standard  $k-\varepsilon$  model, and the CASE5 was an OpenFOAM simulation with the  $k-\varepsilon$  model of Lahey (2005), which should produce more turbulence kinetic energy. The momentum (drag) transfer models in these two cases were the basic separated phases models of the codes in order to make the case set-ups comparable between the codes.

As it should, the CASE4 result of NEPTUNE\_CFD was very similar to the CASE1 result. Although bubble size was in CASE4 slightly smaller, the bubble stayed at the pipe outlet without chugging initiated. In the OpenFOAM CASE5, condensation rates were much

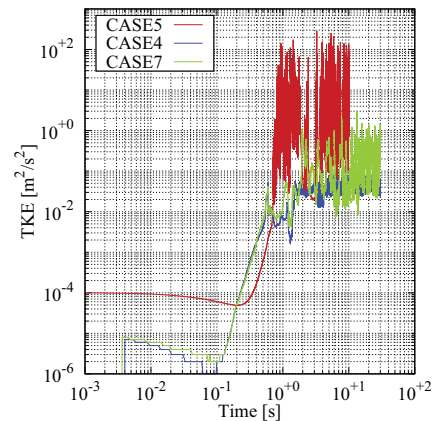


Fig. 11. Interfacial liquid turbulence kinetic energy level in CASE4, CASE5, and CASE7.

higher than in the cases with the standard  $k-\varepsilon$  model. Bubbles collapsed and chugging occurred, but the frequency seemed too high and bubble sizes too small compared to the experiment. Fig. 10 shows the power spectrum of bubble size in the CASE5.

Some indications of 0.5–3.3 Hz frequencies of experiment could be seen in the CASE5, but the 20 Hz oscillation did not correspond to the test at all. Fig. 11 shows the interfacial turbulence kinetic energy history of the CASE4, CASE5 and CASE7.

The CASE4 could be considered as a case without chugging, the CASE5 as a case with too high chugging frequency and the CASE7 as a case with relatively correct chugging frequency. Turbulence kinetic energy near the interface was dramatically different between these cases, having the average orders of magnitude  $10^{-2} \text{ m}^2 \text{ s}^{-2}$  in the CASE4,  $10^{-1} \text{ m}^2 \text{ s}^{-2}$  in the CASE7 and  $10^{-1} - 10^1 \text{ m}^2 \text{ s}^{-2}$  in the CASE5.

### 5.3. Effect of interfacial area modeling

In ideal CFD simulations, interfacial instabilities can be captured increasingly better by increasing the grid resolution to cover the

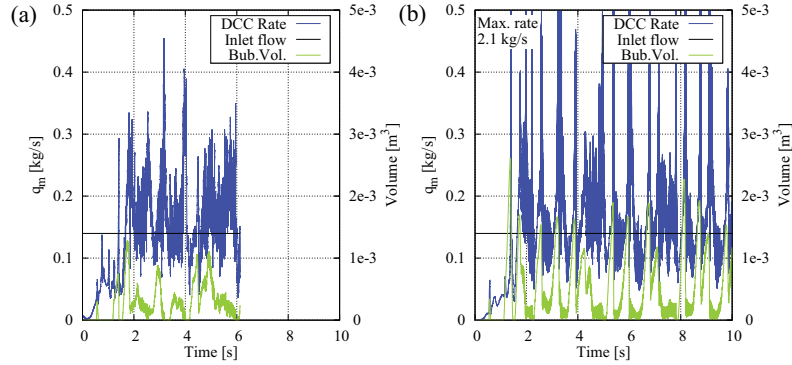


Fig. 12. DCC rates and bubble volumes in (a) CASE6 and (b) CASE7.

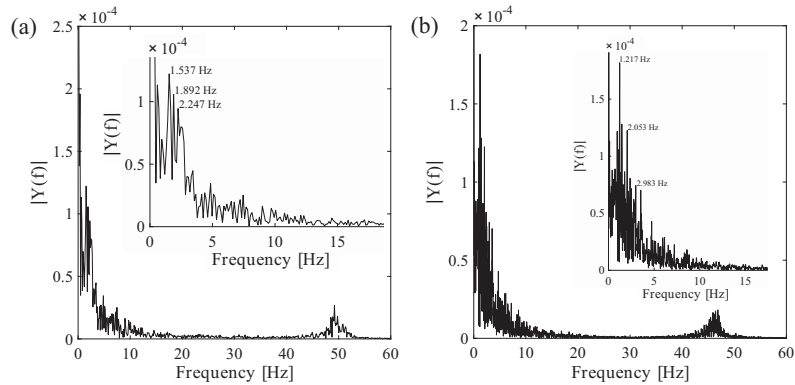


Fig. 13. FFT from the recognized bubble volume in the simulation of (a) CASE6 and (b) CASE7.

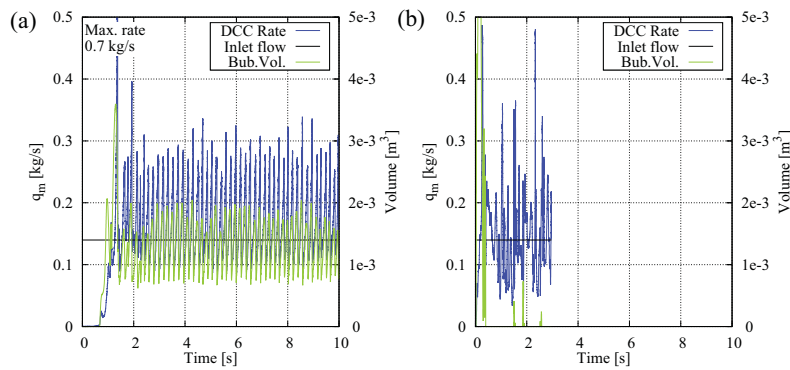


Fig. 14. DCC rates and bubble volumes in (a) CASE8 and (b) CASE9.

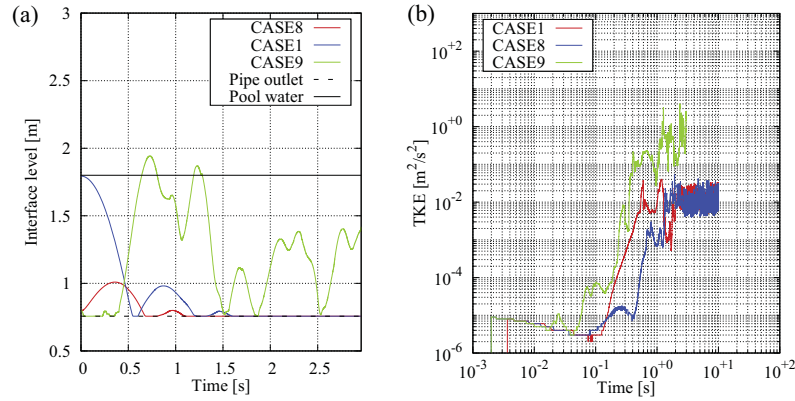


Fig. 15. (a) Interface level inside the blowdown pipe (left), and interfacial liquid turbulence kinetic energy level in CASE1, CASE8, and CASE9.

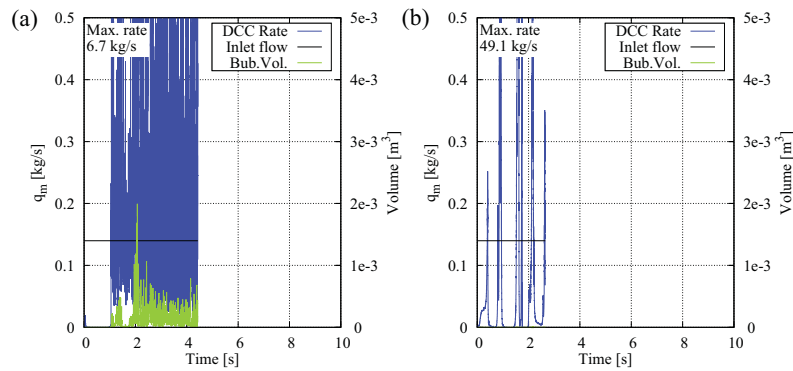


Fig. 16. DCC rates and bubble volumes in (a) CASE10 and (b) CASE11.

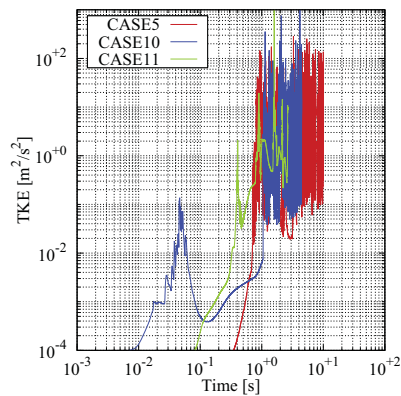


Fig. 17. Interfacial liquid turbulence kinetic energy level in CASE5, CASE10, and CASE11.

critical wave lengths of invoking instabilities, e.g. the Rayleigh–Taylor instability at first, then the Kelvin–Helmholtz instability on the waves generated by the Rayleigh–Taylor one etc. The grid resolution in the CASE6 (Fig. 12) was good enough to capture the critical wave length of the Rayleigh–Taylor instability calculated from the recognized interface acceleration in the experiment. As it was not ideal in engineering sense to use such or even denser grids in the simulations, thus the Rayleigh–Taylor instability was modeled in the CASE7 (Fig. 12) by using the Pellegrini et al. (2015) model in the same coarse grid set-up as in the other cases in this paper.

Chugging occurred in both the cases CASE6 and CASE7, as the resolved or modeled increasing interfacial area increased the condensation rate, which in turn led to interface collapse and thus to cyclic process. The power spectra of bubble volumes in these two cases are shown in Fig. 13.

It was quite trivial to calculate volumes and interfacial areas during the CFD simulations, while the corresponding operation for the video material from the experiment tended to lose details of interface and structures beyond the visible interface. Taking this in the account, the FFT result of bubble volumes in the CASE6 and

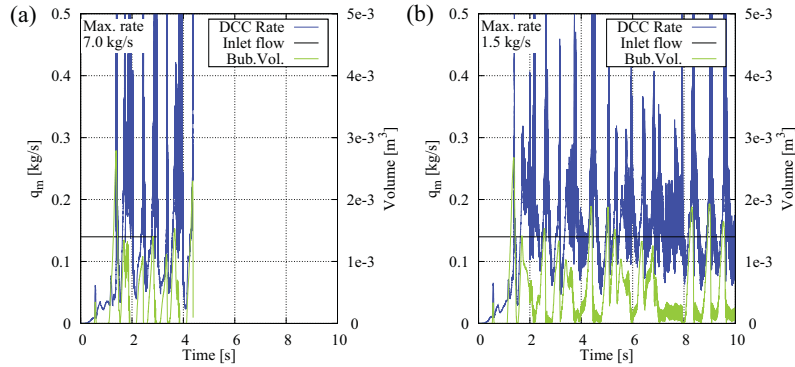


Fig. 18. DCC rates and bubble volumes in (a) CASE12 and (b) CASE13.

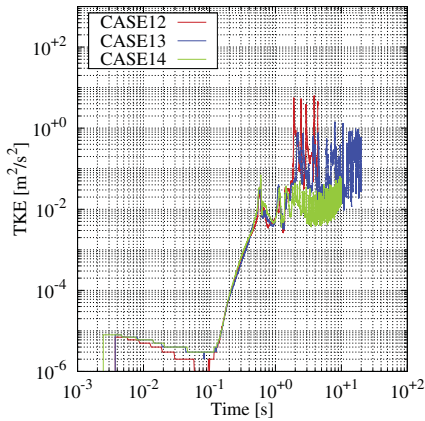


Fig. 19. Interfacial liquid turbulence kinetic energy level in CASE12, CASE13, and CASE14.

CASE7 were outstandingly near the experimental result of Fig. 4. In both the cases a group of maxima could be seen at 1–3 Hz and also the rapid oscillation of 50 Hz, indicating chugging.

5.4. Effect of geometry and interface initialization

One may ask why the chugging occurred in the simulations of a straight tube POOLEX experiment (Tanskanen, 2012; Tanskanen et al., 2014), although the grid was coarse and not any special interfacial instability modeling was applied. Tanskanen (2012) mentioned that the level of initial interface inside the blowdown pipe matters as a long traverse of interface and water plug before the first bubble generates lot of turbulence near the blowdown pipe exit, which initiates chugging more easily. The CASE8 in Fig. 14 demonstrated the effect of initial interface set near to the blowdown pipe outlet, which is in fact the correct location based on the starting point of experimental data of the DCC-05-4 subtest. The CASE9 in Fig. 14 was a test without the drywell taken into account i.e. drywell was removed from the geometry and massflow boundary condition was brought from the inlet plenum to the inlet of blowdown pipe.

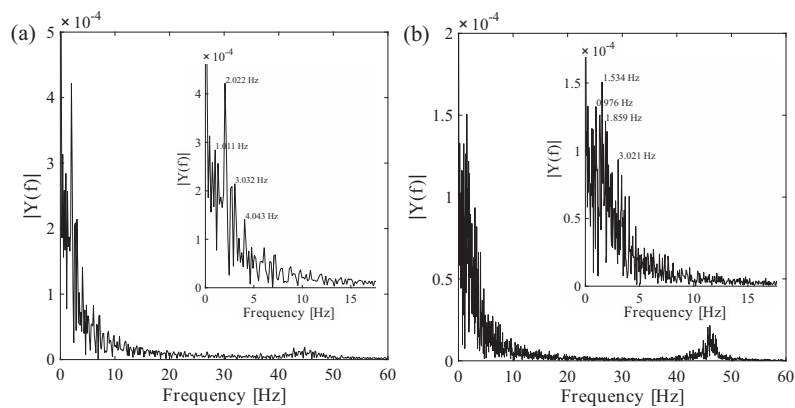


Fig. 20. FFT from the recognized bubble volume in the simulation of (a) CASE12 and (b) CASE13.

Please cite this article in press as: Patel, G., et al. Direct contact condensation modeling in pressure suppression pool system. Nucl. Eng. Des. (2016), <http://dx.doi.org/10.1016/j.nucengdes.2016.08.026>

The CASE8 could be compared to the one of CASE1, as the initial interface location was the only difference. Results were almost identical apart from the first 2s of simulations. With the higher initial level (CASE1), there was one chug before the stabilization, while the CASE8 was stabilized immediately. The CASE9 set-up without drywell led to vigorous chugging with interface mostly churning inside the blowdown pipe. Fig. 15 (a) shows the interface location inside the blowdown pipe in the CASE1, CASE8 and CASE9.

The CASE8 started with a small upward motion of interface before the downward motion, bubble eruption, and stabilization. The CASE1 started with the downward motion, bubble eruption, collapse and then with similar stabilizing cycle as in the CASE8. At the end, the interfacial turbulence kinetic energy was same in both the cases as seen in Fig. 15(b). In the CASE9, a large bubble erupted immediately, after which interface collapsed deeply up to the blowdown pipe causing internal churning and low-frequency external chugging. Probably the internal motion increased the interfacial turbulence kinetic energy to the range of  $10^{-1} \text{ m}^2 \text{ s}^{-2}$  in the CASE9. Although there was chugging in the CASE9, it was qualitatively different than in the experiment. The corresponding OpenFOAM results with the  $k-\varepsilon$  model of Lahey (2005) are presented in Figs. 16 and 17.

Lower initial interface level did not help in the CASE10 as the maximum condensation rate was even higher than in the high initialization of CASE5. That is, chugging occurred, but the frequency was much higher than in the experiment. The drywell was removed in the OpenFOAM CASE11, which led to results without externally visible chugging as the steam condensed tremendously inside the blowdown pipe.

While the turbulence in the standard  $k-\varepsilon$  cases was strongly affected by the truncation of geometry, the turbulence was quite equally high in the  $Lk-\varepsilon$  cases. However, the geometry change itself was more interesting issue as the turbulence level was likely just a mere consequence of that. That is, there was not any more damping effect of such a large gas space without drywell. In practice this meant that soft 'pressure boundary condition' at blowdown pipe inlet changed to a rigid velocity boundary condition, which did not respond to the changes in the condensation rate. This led to rapid loss of steam inside the pipe leading to internal chugging which was further maintained by the strong turbulence generation by the wall shear stress within the blowdown pipe.

##### 5.5. Effect of interfacial momentum transfer model

The CASE12, CASE13 and CASE14 were included to this study in order to test the effect of interfacial momentum transfer modeling assuming that the interfacial instability modeling would be in any case crucial for good results. Fig. 18 shows the DCC rate and bubble volume results for the CASE12 and CASE13.

The only difference between the CASE13 and CASE7 set-up was that the surface tension modeling was attempted in the CASE13. Effect of surface tension should not be very remarkable in the set-up studied, and the results were very similar. The chugging rate in the CASE13 (Fig. 20) was near to the one of CASE7. The result of CASE12 with the basic separated phase drag model (with surface tension) differed from the Coste LIM CASE7 and CASE13 in some extent. The simpler separated phases drag model took into account only the normal interfacial component of the drag, while the Coste LIM model would be able to calculate tangential friction as well. However, the turbulence kinetic energy rose occasionally higher with the basic separated phase drag model as seen in Fig. 19. Chugging occurred in the CASE12, but the rapid fluctuation phase of 50 Hz was less evident (Fig. 20).

A typical chugging cycle from a large bubble to rapid collapse and to a new eruption is presented in Fig. 21 for the CASE13. The

corresponding DCC rate and bubble size in the CASE13 are presented as well. It can be seen that a large steam bubble was formed at the blowdown pipe outlet in Fig. 21(a), and it rapidly condensed due to preferably high enough condensation rates (Fig. 21(b)). Following the collapse of steam bubble, the steam/water interface was retreated inside the blowdown pipe in Fig. 21(c), but a toroidal bubble formed in Fig. 21(d). The most of small amplitude high

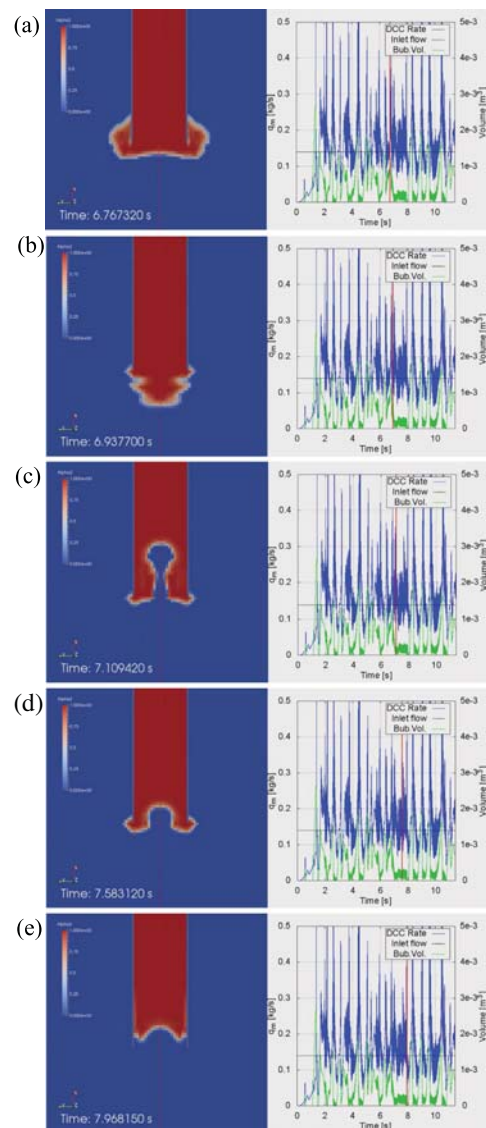


Fig. 21. Instantaneous steam volume fraction, corresponding DCC rates and bubble volumes in CASE13.

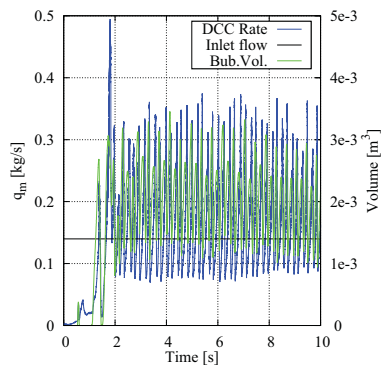


Fig. 22. DCC rates and bubble volumes in CASE14.

frequency oscillations seemed to occur in this phase, after which the toroidal bubble collapsed also as seen in Fig. 21(e) prior to the initial large bubble of a new cycle.

The results presented in this study suggest that the interfacial instability computation is the most crucial part of the DCC modeling of chugging condensation mode. Thus it was necessary to present the result of the second best DCC model (HD 1) with the Rayleigh–Taylor instability model applied (Fig. 22).

The HD 1 DCC model did not provide enough condensation in the CASE14, and the result was as poor as in the CASE2 even though the Rayleigh–Taylor instability modeling had been applied.

## 6. Conclusions

Modeling of chugging in a BWR suppression pool is numerically challenging due to the rapid condensation which leads to high velocities and pressure oscillations. In CFD, these lead to short time-stepping and high grid resolution requirements. In the reasonable engineering scales, these requirements could be met only partially which gives room for the other incompleteness in the required closure models.

Earlier work on the open-top suppression pool cases has shown that direct contact condensation mass transfer modeling requires an interface heat transfer model that provides high enough heat transfer rates. It was shown later that even relatively low heat transfer rates could be enough in these cases if the interface instability modeling is sufficient.

This work shows that physically justified yet simple modeling of interfacial waves (instabilities) necessarily improves the prediction of chugging in most cases but it is not the most dominant factor in the simulations including the drywell system as well.

Pattern recognition analysis of the PPOOLEX data was used to obtain chugging bubble frequencies. Numerical simulation with the Coste (2004) DCC model and Rayleigh–Taylor instability model yielded bubble frequencies in excellent agreement with the data. The performance of the Rayleigh–Taylor instability model was comparable to the corresponding dense grid simulations without the need of instability modeling. However, certain high enough DCC heat transfer rate was required in order to invoke chugging regardless of interfacial instability modeling. The standard  $k-\epsilon$  model was applied in the most successful simulations, because e.g. the Lahey (2005) modification of  $k-\epsilon$  model led to too high turbulence and thus too high chugging rate. The interfacial momentum transfer models (drag, surface tension...) and the ini-

tial state of the simulations have visible effects on the results, but these modeling issues as not as dominant factor in successful simulations as the DCC model, the interfacial area modeling and the turbulence modeling.

In addition to the FFT results shown here, more information can still be gathered from the pattern recognition and measurement data of the DCC-05 test. With that data, the analysis presented here could be sharpened. Otherwise, the next step in improving chugging modeling is to validate the best model combinations in 3D simulations and with other pipe geometries, even with spargers.

## Acknowledgements

The research leading to these results is partly funded by the European Atomic Energy Community's (Euratom) Seventh Framework Programme FP7/2007–2011 under grant agreements No. 232124 and No. 323263. The research is also funded partly by the Finnish Nuclear Waste Management Fund (VYR) via The Finnish Research Programmes on Nuclear Power Plant Safety SAFIR2010, SAFIR2014 and SAFIR2018, and the Academy of Finland via the Doctoral Programme for Nuclear Engineering and Radiochemistry (YTERA). The authors gratefully acknowledge all this support. The authors would like to acknowledge the CSC-IT Center for Science, Finland for providing the scientific computing platform.

## References

- Ali, S.M., Verma, V., Ghosh, A.K., 2007. Analytical thermal hydraulic model for oscillatory condensation of steam in presence of air. *Nucl. Eng. Des.* 237, 2025–2039.
- Aust, E., Seeliger, D., 1982. Pool dynamics and dynamic loads in pressure suppression containment systems. *Trans. Am. Nucl. Soc.* 41, 696–699.
- Aya, I., Nariai, H., 1986. Occurrence threshold of pressure oscillations induced by steam condensation in pool water. *Bull. JSME* 29 (235), 2131–2137.
- Aya, I., Nariai, H., 1987. Boundaries between regimes of pressure oscillation induced by steam condensation in pressure suppression containment. *Nucl. Eng. Des.* 99, 31–40.
- Aya, I., Nariai, H., 1991. Evaluation of heat-transfer coefficient at direct contact condensation of cold water and steam. *Nucl. Eng. Des.* 131, 17–24.
- Banerjee, S., 1978. A surface renewal model for interfacial heat and mass transfer in transient two-phase flow. *Int. J. Multiph. Flow* 4, 571–573.
- Bestion, D., 2012. Applicability of two-phase CFD to nuclear reactor thermalhydraulics and elaboration of best practice guidelines. *Nucl. Eng. Des.* 253, 311–321.
- Bestion, D., Gueffi, A., 2005. Status and perspective of two phase flow modelling in the NEPTUNE multiscale thermalhydraulic platform for nuclear reactor simulation. *Nucl. Eng. Technol.* 37 (6), 511–524.
- Brennen, C., 2014. *Cavitation and Bubble Dynamics*. Cambridge University Press, ISBN 978-1-107-64476-2.
- Chan, C.K., Lee, C.K.B., 1982. A regime map for direct contact condensation. *Int. J. Multiph. Flow* 8, 11–20.
- Chen, S., Gerner, F., Tien, C., 1987. General film condensation correlations. *Exp. Heat Transfer* 1, 93–107.
- Coste, P., 2004. Computational simulation of multi-d liquid–vapor thermal shock with condensation. In: *Proceedings of ICMF04*, Yokohama, Japan, May 30–June 4.
- Coste, P., 2013. A large interface model for two-phase CFD. *Nucl. Eng. Des.* 255, 38–50.
- de With, A.P., Calay, R.K., de With, G., 2007. Three-dimensional condensation regime diagram for direct contact condensation of steam injected into water. *Int. J. Heat Mass Transfer* 50, 1762–1770.
- Duff, R., Harlow, F., Hirt, C., 1962. Effects of diffusion on interface instability between gases. *Phys. Fluids* 5 (4), 417–425.
- Grafton, W.A., McIntyre, T.R., Ross, M.A., 1977. Mark II Pressure Suppression Test Program, Phase II and III tests: Technical Report. Boiling Water Reactor Projects Dept, General Electric Co., San Jose, CA, USA.
- Gueffi, A., Bestion, D., Boucker, M., Boudier, P., Fillion, P., Grandotto, M., Hérard, J.M., Hervieu, E., Pétraud, P., 2007. NEPTUNE: A new software platform for advanced nuclear thermal hydraulics. *Nucl. Sci. Eng.* 156, 281–324.
- Hart, J., Slegers, W.J.M., de Boer, S.L., Huggenberger, M., Jimenez, J.L., Gonzalez, J.L.M., Puigjaner, F.R., 2001. TEPS—technology enhancement for passive safety systems. *Nucl. Eng. Des.* 209 (1–3), 243–252.
- Hughes, E.D., Duffey, R.B., 1991. Direct contact condensation and momentum transfer in turbulent separated flows. *Int. J. Multiph. Flow* 17, 599–619.
- Hujala, E., 2013. Evaluation of Bubble Formation and Break Up in Suppression Pools by Using Pattern Recognition Methods (Master thesis). Lappeenranta University of Technology, LUT Energy, Lappeenranta, Finland.

- Ishii, M., Hibiki, T., 2011. *Thermo-Fluid Dynamics of Two-Phase Flow*. Springer Science+Business Media, ISBN 978-1-4419-7984-1, e-ISBN 978-1-4419-7985-8.
- Kennedy, W., McGovern, D., Maraschin, R., Wolfe, K., 1978. Rigid and flexible vent header testing in the quarter scale test facility, Mark I Containment Program, Task 5. 3. 3. Technical Report. Acurex Corp., Alternate Energy Div, Mountain View, CA, USA.
- Lahey, R., 2005. The simulation of multidimensional multiphase flows. *Nucl. Eng. Des.* 235, 1043–1060.
- Lahey, R., Moody, F., 1993. *The Thermal-Hydraulics of a Boiling Water Reactor*. American Nuclear Society.
- Laine, J., Puustinen, M., 2005. Condensation Pool Experiments with Steam using DN200 Blowdown Pipe. NKS-111 ISBN 87-7893-171-1. Lappeenranta University of Technology.
- Lauder, B., Spalding, D., 1974. The numerical computation of turbulent flows. *Comput. Methods Appl. Mech. Eng.* 3 (2), 269–289.
- Laviéville, J., Quémérais, E., Mimouni, S., Boucker, M., Méchitoua, N., 2006. NEPTUNE CFD V1.0 theory manual: Technical Report. EDF.
- Leighton, T., 1994. *The Acoustic Bubble*. Academic Press, ISBN 978-0-12-441920-9.
- Liang, K., Griffith, P., 1994. Experimental and analytical study of direct contact condensation of steam in water. *Nucl. Eng. Des.* 147, 425–435.
- Livescu, D., 2004. Compressibility effects on the Rayleigh-Taylor instability growth between immiscible fluids. *Phys. Fluids* 16 (1), 118–127.
- McIntyre, T.R., Ross, M.A., Myers, L.L., 1976. Mark II pressure suppression test program: Phase I tests. [BWR]. Technical Report. Boiling Water Reactor Systems Dept., General Electric Co., San Jose, CA, USA.
- Meier, M., Yadigaroglu, G., Andreani, M., 2000. Numerical and experimental study of large steam-air bubbles injected in a water pool. *Nucl. Sci. Eng.* 136, 363–375.
- Nariai, H., Aya, I., 1986. Fluid and pressure oscillations occurring at direct contact condensation of steam flow with cold water. *Nucl. Eng. Des.* 95, 35–45.
- Patel, G., Tanskanen, V., Rintala, V., Hyvärinen, J., 2015. Numerical study of direct contact condensation of steam on stable interface in a BWR suppression pool test facility. In: The 16th International Topical Meeting on Nuclear Reactor Thermal Hydraulics (NURETH-16), Chicago, IL, August 30–September 4, 14.
- Pätrikangas, T., Niemi, J., Laine, J., Puustinen, M., Purhonen, H., 2010. CFD modelling of condensation of vapor in the pressurized PPOOLEX facility. In: CFD for Nuclear Reactor Safety Applications (CFD4NRS-3) Workshop, Bethesda, MD, USA, 14–16 September 2010, 12.
- Pellegrini, M., Naitoh, M., Josey, C., Baglietto, E., 2015. Modeling of Rayleigh-Taylor instability for steam direct contact condensation. In: The 16th International Topical Meeting on Nuclear Reactor Thermal Hydraulics (NURETH-16), Chicago, IL, August 30–September 4, 15.
- Peltola, J., 2015. OpenFOAM 2.3.1 twoPhaseEulerFoam and twoPhaseNuFoam v0.6 extension to simulation of subcooled nucleate boiling: Technical Report. VTT.
- Puustinen, M., Kyrki-Rajamäki, R., Tanskanen, V., Räsänen, A., Purhonen, H., Riikonen, V., Laine, J., Hujala, E., 2013. BWR suppression pool studies with POOLEX and PPOOLEX test facilities at LUT. In: The 15th International Topical Meeting on Nuclear Thermal Hydraulics (NURETH-15), Pisa, Italy, 12–17 May 2013.
- Schiller, L., Naumann, A., 1933. Über die grundlegenden berechnungen bei der schwerkraftbereitung. *Z. Vereins deutscher Ing.* 77, 318–320.
- Smith, B.L., 2007. A numerical investigation of three-dimensional flows in large volumes in the context of passive containment cooling in BWRs. *Nucl. Eng. Des.* 237 (11), 1175–1184.
- Tanskanen, V., 2012. CFD modelling of direct contact condensation in suppression pools by applying condensation models of separated flow. *Acta Universitatis Lappeenrantaensis* 472. Lappeenranta University of Technology. ISBN 978-952-265-221-8, ISBN 978-952-265-222-5 (PDF), ISSN 1456-4491.
- Tanskanen, V., Jorden, A., Puustinen, M., Kyrki-Rajamäki, R., 2014. CFD simulation and pattern recognition analysis of the chugging condensation regime. *Ann. Nucl. Energy* 66, 133–143.
- Tanskanen, V., Patel, G., Puustinen, M., Hujala, E., Kyrki-Rajamäki, R., Hyvärinen, J., 2015. CFD modelling of chugging condensation regime of BWR suppression pool experiments. In: The 16th International Topical Meeting on Nuclear Thermal Hydraulics (NURETH-16), Chicago, IL, August 30–September 4, 14.
- Tanskanen, V., Hujala, E., Puustinen, M., 2016. Numerical simulation of a PPOOLEX chugging case with a Rayleigh-Taylor instability model for interfacial area: Research Report INSTAB 4/2015. LUT.
- Thiele, R., 2010. Modeling of direct contact condensation with OpenFOAM (Master thesis). KTH, Royal Institute of Technology, Division of Nuclear Reactor Technology, Royal Institute of Technology, Stockholm, Sweden. ISBN 0280-316X.
- Walsche, C.D., Cachard, F.D., 1996. Experimental investigation of condensation and mixing during venting of a steam/non-condensable gas mixture into a pressuresuppression pool. Technical Report. IAEA Report, 53–61.
- Wikdahl, C.E., 2007. Marvikenreaktor – ett industripolitiskt utvecklingsprojekt i ottakt med tiden. Technical Report SKI Rapport 2007:18. SKI.
- Yadigaroglu, G., 2004. Computational Fluid Dynamics for nuclear applications: from CFD to multi-scale CMFD. *Nucl. Eng. Des.* 235, 153–164.



## **Publication IV**

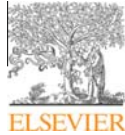
Patel, Y., Patel, G., and Turunen-Saaresti, T. (2015).  
**Influence of turbulence modelling on non-equilibrium condensing  
flows in nozzle and turbine cascade.**

International Journal of Heat and Mass Transfer.  
Vol. 88, pp. 165-180.

© Elsevier, 2015

Reprinted with permission from the publisher





Contents lists available at ScienceDirect

## International Journal of Heat and Mass Transfer

journal homepage: [www.elsevier.com/locate/ijhmt](http://www.elsevier.com/locate/ijhmt)

## Influence of turbulence modelling on non-equilibrium condensing flows in nozzle and turbine cascade



Yogini Patel\*, Giteshkumar Patel, Teemu Turunen-Saaresti

Fluid Dynamics Laboratory, LUT Energy, School of Technology, Lappeenranta University of Technology, PO Box 20, FIN-53851 Lappeenranta, Finland

## ARTICLE INFO

## Article history:

Received 17 December 2014  
 Received in revised form 23 April 2015  
 Accepted 23 April 2015  
 Available online 14 May 2015

## Keywords:

CFD  
 Condensation  
 Steam  
 Turbulence modelling  
 Loss coefficient

## ABSTRACT

The accurate analysis of a condensing flow plays an important role in the development of high-efficiency steam turbines. This paper presents an investigation of turbulence modelling influence on non-equilibrium condensing steam flows in a Laval nozzle and in a stationary cascade of turbine blades using a commercial computational fluid dynamics (CFD) code. The calculations were conducted by employing 2D compressible Reynolds-averaged Navier–Stokes (RANS) equations coupled with a two equation turbulence model. The condensation phenomena were modelled on the basis of the classical nucleation theory. The standard  $k-\epsilon$  turbulence model was modified, and the modifications were implemented in the CFD code. The influence of inlet flow turbulence on condensing process was discussed. The impact of turbulence modelling on wet-steam flow was examined based on the experimental data available in the literature. The cascade loss coefficients were calculated numerically as well. The presented study of losses that occur due to the irreversible heat and mass transfer during the condensation process emphasised the importance of turbulence modelling for wet-steam flows in turbines. The paper demonstrates that the accurate computational prediction of condensing steam flow requires the turbulence to be modelled accurately.

© 2015 Elsevier Ltd. All rights reserved.

### 1. Introduction

Two-phase wet-steam flows consisting of tiny liquid droplets have a fundamental importance in both scientific contexts and in industrial applications, such as the combustion of liquid droplets, meteorological processes, the formations of contrails from aircraft exhausts, chemical engineering applications, and condensation of steam in turbines. Particular attention has been given to wet-steam flow research in turbines to take into account the thermodynamical and mechanical losses, blade erosion, and the influence of the condensation process on blade aerodynamics. With a large role played by steam turbines in the area of power generation, any progress in understanding the condensation and loss mechanisms might lead to improved designs of steam turbines, and, as a result, yield handsome economic dividends. Therefore, detailed analysis of condensing steam flow, either by experiments or with numerical simulations, has great importance.

The condensing steam flow in nozzles and in turbines has been widely studied experimentally, theoretically, and numerically since the work of Stodola [1] in order to enhance knowledge about

the complicated physics involved. Comprehensive experimental works have been organised for condensing flow in the nozzle by numerous researchers, that is, Barschdorff [2], Moore et al. [3], Bakhtar et al. [4], Moses and Stein [5], Skillings et al. [6], Bakhtar and Zidi [7,8], Gyarmathy [9]. The experimental work for condensing steam flows in turbine cascades has been performed as well. For example, Bakhtar et al. [10,11] and White et al. [12] conducted experiments of non-equilibrium condensing steam flow in turbine cascades, in which they provided a large set of measurement data for various parameters.

Many numerical studies over the past several decades have been directed toward modelling condensing steam flow utilising various approaches, where the vapour phase is always treated by the Eulerian method and the liquid phase is solved by the Lagrangian/Eulerian method. Much of the modelling work was initially performed on convergent–divergent (CD) nozzles with simplified one-dimensional flow, considering both the inviscid and turbulence conditions. Later on, studies were dedicated to two-dimensional flows in turbine cascades, with more sophisticated numerical models utilised to handle the additional dimension. For example, in the studies of Bakhtar and Tochai [13], Young [14,15], White and Young [16], Bakhtar et al. [17], White et al. [12], the most often used numerical approach was the

\* Corresponding author. Tel.: +358 40 765 2489.

E-mail addresses: [yogini.patel@lut.fi](mailto:yogini.patel@lut.fi) (Y. Patel), [giteshkumar.patel@lut.fi](mailto:giteshkumar.patel@lut.fi) (G. Patel), [teemu.turunen-saaresti@lut.fi](mailto:teemu.turunen-saaresti@lut.fi) (T. Turunen-Saaresti).

Nomenclature	
<i>Latin alphabet</i>	
$C_p$	specific heat at constant pressure $\text{J kg}^{-1} \text{K}^{-1}$
$C_v$	specific heat at constant volume $\text{J kg}^{-1} \text{K}^{-1}$
$h$	specific enthalpy $\text{J kg}^{-1}$
$H$	total enthalpy $\text{J kg}^{-1}$
$I$	nucleation rate $\text{m}^{-3} \text{s}^{-1}$
$k$	turbulent kinetic energy $\text{m}^2 \text{s}^{-2}$
$K_t$	thermal conductivity $\text{W m}^{-1} \text{K}^{-1}$
$M$	liquid mass $\text{kg}$
$M_m$	molecular mass $\text{kg mol}^{-1}$
$P$	pressure $\text{Pa}$
$r$	radius $\text{m}$
$\bar{r}$	average radius $\text{m}$
$r_c$	critical radius $\text{m}$
$R$	gas constant $\text{J kg}^{-1} \text{K}^{-1}$
$Re_i$	Reynolds number
$s$	entropy $\text{J kg}^{-1} \text{K}^{-1}$
$S_1$	mass source term $\text{kg m}^{-2} \text{s}^{-1}$
$S_2$	momentum source term $\text{kg m}^{-2} \text{s}^{-2}$
$S_3$	energy source term $\text{W m}^{-3} \text{K}^{-1}$
$t$	time $\text{s}$
$T$	temperature $\text{K}$
$u$	velocity component $\text{m s}^{-1}$
<i>Greek alphabet</i>	
$\beta$	liquid phase mass fraction
$\gamma$	specific heat ratio
$\Gamma$	mass generation rate $\text{kg m}^{-3} \text{s}^{-1}$
$\Gamma_E$	thermal diffusion coefficient $\text{W m}^{-1} \text{K}^{-1}$
$\varepsilon$	turbulence dissipation rate $\text{m}^2 \text{s}^{-3}$
$\eta$	number of liquid droplets per unit volume $\text{m}^{-3}$
$\mu$	dynamic viscosity $\text{Pa s}$
$\mu_t$	turbulent viscosity $\text{kg m}^{-1} \text{s}^{-1}$
$\rho$	density $\text{kg m}^{-3}$
$\sigma$	liquid surface tension $\text{N m}^{-1}$
$\tau$	viscous stress tensor $\text{Pa}$
$\tau_p$	droplet response time $\text{s}$
$\chi$	turbulence intensity
<i>Subscripts</i>	
$d$	droplet
$m, l, v$	mixture, liquid phase, vapour phase
$i, j$	cartesian tensor notation
$x$	cartesian coordinate
0, 1, 2	total, inlet, outlet condition of cascade

inviscid time-marching scheme of Denton [18] for turbomachinery flows.

An Eulerian–Lagrangian approach for two-phase steam flow was adopted by Gerber [19] to conduct numerical simulations of low-pressure (LP) CD nozzle and turbine cascade. He utilised the  $k$ – $\varepsilon$  turbulence model by assuming oneway coupling between the gas phase turbulence and dispersed droplets. Later on, Gerber and Kermani [20] presented an Eulerian–Eulerian multi-phase method for non-equilibrium condensation in nozzles. Moreover, Senoo and White [21,22] utilised a coupled numerical approach, considering the two-phase flow as a mixture, to simulate inviscid wet-steam flow in LP steam turbine stator cascade and in Laval nozzle. Wróblewski et al. [23], Dykas and Wróblewski [24,25] have developed in-house CFD codes for modelling non-equilibrium wet-steam flow. They validated their code using the single-fluid and two-fluid approaches coupled with both one-equation and two-equation turbulence models as well. Moreover, numerical work concerning wet-steam flows through multistage stator rotor cascade channels in a low-pressure steam turbine were performed by Yamamoto et al. [26–28], Starzmann et al. [29], Miyake et al. [30], who solved flow turbulence using the SST  $k$ – $\omega$  turbulence model.

Turbine flows include a variety of complex flow phenomena, including laminar-to-turbulent transition, flow separation, secondary flow mixing, rotor–stator interaction, and heat transfer. A common thread among all of these phenomena is turbulence. The turbulence plays an important role in the processes of mass, momentum, and heat transfer in boundary layers on the surface walls, especially on the possible deposition of condensed liquid droplets. Turbulence may have some direct/indirect influence on shock wave generation under the conditions of subcooled steam flow [31]. Additionally, the accurate prediction of absolute losses requires the turbulence to be modelled accurately [32,33].

However, published work on the influence of turbulence on the condensing steam flow is rather sparse. White [34] presented a numerical method based on a simple stream function technique for the prediction of condensing steam flow in a CD nozzle to analyse the influence of the viscous effect on condensation within

compressible boundary layers. Moreover, Simpson and White [35] conducted a numerical study performing viscous calculations for a steady flow condition with CD nozzle using the standard  $k$ – $\varepsilon$  turbulence model, and they concluded that the growth of the boundary layer has a significant impact on the predicted pressure distributions and droplet sizes. Additionally, Avetissian et al. [36] investigated the influence of the turbulence level and inlet wetness on the process of spontaneous condensation in Laval nozzles, utilising the moment method and the Delta-approximation method to determine the droplet size spectrum. They concluded that the effect of both high-level turbulence and inlet wetness causes the shock of spontaneous condensation to disappear. Later on, the effect of turbulence was investigated by Avetissian et al. [31]. Their study emphasised the steady and unsteady spontaneously condensing transonic turbulent flows in 2D flat nozzles and round shape nozzle dealing with and without initial moisture at the nozzle inlet. Additionally, the influence of turbulence parameters and real gas models in condensing steam flow in a CD nozzle has been studied by Patel et al. [37]. The performance of various turbulence models for the wet-steam flow has been studied by Patel et al. [38]. In the work of Patel et al. [38], the SST  $k$ – $\omega$  model was modified to predict steam condensing flow and losses in turbine cascade. It was concluded that the prediction of steam condensing flow in turbine cascade is influenced by turbulence.

The aim of this work is to investigate the influence of turbulence modelling on the process of spontaneously condensing flow in a nozzle and turbine blade cascade using the Eulerian–Eulerian approach. The significance of turbulence modelling on the loss mechanism is discussed, as well. The achieved numerical results are analysed with the available experimental data.

## 2. Governing equations

### 2.1. Conservation equations

All results presented in this paper were obtained by means of ANSYS Fluent 14.0 CFD code. The mixture of vapour and liquid phases was governed by Reynolds-averaged Navier–Stokes

(RANS) equations, which were coupled with the two-equation turbulence model. The conservation of mass, momentum, and energy equations for a compressible flow are expressed as follows,

$$\frac{\partial \rho}{\partial t} + \frac{\partial}{\partial x_i}(\rho u_i) = S_1, \quad (1)$$

$$\frac{\partial}{\partial t}(\rho u_i) + \frac{\partial}{\partial x_j}(\rho u_i u_j) = -\frac{\partial P}{\partial x_i} + \frac{\partial \tau_{ij}}{\partial x_j} + S_2, \quad (2)$$

$$\frac{\partial}{\partial t}(\rho H) + \frac{\partial}{\partial x_j}(\rho u_j H) = \frac{\partial P}{\partial t} + \frac{\partial}{\partial x_j} \left( \Gamma_f \frac{\partial T}{\partial x_j} \right) + \frac{\partial}{\partial x_j}(u_j \tau_{ij}) + S_3, \quad (3)$$

In Eq. (1), the source term  $S_1$  represents the mass transfer due to the condensation process or evaporation on the already existing droplet. The term  $S_2$  in Eq. (2) is the momentum source term, which includes the momentum exchange between the liquid droplets and the surrounding vapour, and the smaller terms from the gradient of the Reynolds stress tensor. In Eq. (3), the source term  $S_3$  includes the interphase heat transfer.

The formulation of conservation equations was based on the mixture properties of the vapour and liquid phases, which can be calculated from the following mixing law

$$\phi_m = \phi_l \beta + (1 - \beta) \phi_v. \quad (4)$$

Here,  $\phi$  represents  $h, s, C_p, C_v, \mu$ , and  $K_t$ . Additionally, two transport equations for the liquid-phase mass-fraction,  $\beta$ , and the number of liquid droplets per unit volume,  $\eta$ , were calculated and can be expressed as

$$\frac{\partial \rho \beta}{\partial t} + \frac{\partial}{\partial x_i}(\rho u_i \beta) = \Gamma, \quad (5)$$

$$\frac{\partial \rho \eta}{\partial t} + \frac{\partial}{\partial x_i}(\rho u_i \eta) = I, \quad (6)$$

respectively, where  $\Gamma$  is the mass generation rate per unit volume due to condensation and evaporation, and  $I$  is the nucleation rate. Some assumptions have been made concerning solving the vapour-liquid mixture flow. The condensed liquid phase consists of droplets whose radii are on the order of 1  $\mu\text{m}$  or less. Therefore, it was assumed that the volume of the condensed liquid phase was negligible. Moreover, the interactions between droplets were omitted, and the slip velocity between the liquid droplets and the vapour surrounding them was negligible.

## 2.2. Nucleation and droplet growth model

The phase change phenomenon regarding the condensing steam flow involves two main processes: nucleation and droplet growth. The rate of formation of liquid droplet embryos due to the homogeneous condensation per unit mass of the mixture was obtained from the classical theory of non-isothermal homogeneous condensation given by Frenkel [39] as

$$I = \frac{q_c}{(1 + \theta)} \left( \frac{\rho_v^2}{\rho_l} \right) \sqrt{\frac{2\sigma}{M_m^3 \pi}} e^{-\left( \frac{4\pi r^2 \sigma}{3k_B T} \right)}. \quad (7)$$

In Eq. (7),  $q_c$  denotes the condensation coefficient, which was assumed to be unity;  $K_b$  is Boltzmann's constant; and  $\theta$  is non-isothermal correction coefficient. In the classical homogeneous nucleation theory, the mass generation rate per unit volume,  $\Gamma$  was estimated by the addition of mass increase owing to nucleation and due to the growth/demise of liquid droplets. The mass generation rate per unit volume  $\Gamma$  was obtained from Ishizaka et al. [40], and can be expressed as

$$\Gamma = \frac{4}{3} \pi \rho_l r^3 + 4 \pi \rho_l \eta r^2 \frac{\partial \bar{r}}{\partial t}, \quad (8)$$

There are two mechanisms involved in the steam condensation process. The first one is related to the mass transfer from the vapour phase to the droplets, and the other is the transfer of heat from the created droplets to the vapour phase in the form of latent heat [40]. The droplets growth rate can be derived on the basis of heat transfer conditions surrounding the droplet [41]. The droplets growth can be defined as

$$\frac{\partial \bar{r}}{\partial t} = \frac{P}{h_{lv} \rho_l \sqrt{2\pi R T}} \frac{\gamma + 1}{2\gamma} C_p (T_d - T), \quad (9)$$

More details pertaining to the droplet temperature calculation have been presented by Young [42].

## 2.3. Equation of state

In the modelling of non-equilibrium flows, subcooled thermodynamic properties are crucial because nucleation and droplet growth rate are quite sensitive to such properties. In the present work, the vapour properties were estimated by the formulations of Young [43]. The equation of state for the vapour phase utilised a virial form with temperature and density as the independent variables, which can be written as

$$P = \rho_v RT (1 + B \rho_v + C \rho_v^2), \quad (10)$$

where  $B$ , and  $C$  are the second and the third virial coefficients. Along with the vapour properties, it is essential to calculate the liquid properties under the conditions close to the saturation line accurately. The properties, such as,  $\rho_l, \sigma, C_{pl}, \mu_l$ , and  $K_{tl}$ , were obtained from Young [42], Reynolds [44], Eckert and Drake [45].

## 2.4. Turbulence modelling

In an LP turbine, more than 90% of the total mass concentration of the liquid phase consists of a very large number of very fine droplets having sub-micron size [46]. Therefore, it could be assumed that there is no direct influence of the droplets on the flow turbulence, and in this study, direct influence was not investigated. However, there is an indirect influence through the velocity field introduced to the turbulence models. The turbulence in the vapour phase does have an influence on the dispersion of the liquid droplets. In the work of Patel et al. [38], various turbulence models, performance was discussed to predict the wet-steam flow in the turbine cascade. In the present work, the standard  $k-\varepsilon$  ( $SK-\varepsilon$ ) turbulence model was employed for modelling the flow turbulence. Due to the relatively small mass concentrations and sizes of droplets, the turbulence equations were solved for the mixture of the vapour and liquid phases. The equations of  $k$  and  $\varepsilon$  can be written as

$$\frac{\partial}{\partial t}(\rho k) + \frac{\partial}{\partial x_i}(\rho u_i k) = \frac{\partial}{\partial x_j} \left( \left( \mu + \frac{\mu_t}{\sigma_k} \right) \frac{\partial k}{\partial x_j} \right) + G_k + G_b - \rho \varepsilon - Y_M + S_k, \quad (11)$$

$$\frac{\partial}{\partial t}(\rho \varepsilon) + \frac{\partial}{\partial x_i}(\rho u_i \varepsilon) = \frac{\partial}{\partial x_j} \left( \left( \mu + \frac{\mu_t}{\sigma_\varepsilon} \right) \frac{\partial \varepsilon}{\partial x_j} \right) + \frac{\varepsilon}{k} (C_{1\varepsilon} G_k - C_{2\varepsilon} \rho \varepsilon) + C_{1\varepsilon} C_{3\varepsilon} G_b + S_\varepsilon, \quad (12)$$

respectively, where  $S_k$  and  $S_\varepsilon$  are the source terms,  $G_k$  and  $G_b$  represent the production of turbulence kinetic energy due to the mean velocity gradients and buoyancy, respectively, and  $Y_M$  is the contribution of the fluctuating dilatation in compressible turbulence to the overall dissipation rate. The original form of  $\mu_t$ , is given by

$$\mu_t = \rho C_\mu \frac{k^2}{\varepsilon}. \quad (13)$$

The applicability of the Sk- $\varepsilon$  turbulence model has been proven in various flow phenomena. However, there are still some limitations to its relevance: for example, flows with large velocity gradients, strong contraction or expansion, surface curvature, rotational effects such as swirl or separated flows, and transition. Therefore, the proper modelling of non-equilibrium homogeneous condensing steam flows in nozzles and turbine blade channels requires some modification to the Sk- $\varepsilon$  model. In the present work, the Sk- $\varepsilon$  turbulence model has been modified (based on Avetissian et al. [36,31]) by adding the modulation of turbulence kinetic energy due to liquid droplets via source terms. The effect of liquid droplets in the flow introduces an extra turbulent kinetic energy and its dissipation to the flow via the acceleration/deceleration of the droplets. Additionally, the turbulent viscosity was modified by means of an expansion procedure for resolving implicit algebraic equations for the Reynolds stress tensor in terms of mean velocity gradients [47,48]. The modified term of turbulent viscosity, including the turbulence production to dissipation ratio, is expressed as

$$\mu_t = \frac{\rho C_\mu}{1 + (G_k/\varepsilon - 1)/C_1} \frac{k^2}{\varepsilon}, \quad (14)$$

where  $C_1$  is the Rotta return-to-isentropy approximation of the pressure-strain correlation [49]. The source term of the turbulence kinetic energy equation represents the addition of turbulent kinetic energy which includes the effect of mass generation rate and droplet response time. The source term,  $S_k$ , in Eq. (11) is defined as

$$S_k = \frac{4M}{\tau_p} (1 - f_u) k, \quad (15)$$

The response time of droplet to changes in the flow velocity or flow temperature are important in establishing non-dimensional parameters to characterise the flow, which relates to the time required for a liquid droplet to respond to a change in velocity. The droplet response time,  $\tau_p$  was calculated as

$$\tau_p = \frac{2r^2 \rho_l}{9\mu}. \quad (16)$$

In Eq. (15),  $f_u$  is the coefficient of droplet response to the fluid velocity fluctuations, which can be written as [50]

$$f_u = \frac{2\left(\frac{\tau_p}{T_L}\right) + \left(\frac{\tau_p}{T_L}\right)^2}{2\left(\frac{\tau_p}{T_L}\right) + 2\left(\frac{\tau_p}{T_L}\right)^2 + \left(\frac{\tau_p}{T_L}\right)^2}, \quad (17)$$

where  $T_L$  and  $\tau_T$  are the Lagrangian integral timescale and the Taylor time microscale, respectively, which are defined as

$$T_L = C_\mu^{\frac{1}{2}} \frac{k}{\varepsilon}, \quad (18)$$

$$\tau_T = \left(\frac{2Re_\lambda}{15^{\frac{1}{2}} a_0}\right)^{\frac{1}{2}} \left(\frac{\mu}{\rho \varepsilon}\right)^{\frac{1}{2}}, \quad (19)$$

where  $Re_\lambda$  is determined as

$$Re_\lambda = \left(\frac{20k^2 \rho}{3\varepsilon \mu}\right)^{\frac{1}{2}}. \quad (20)$$

The source term of the dissipation equation represents the modulation of turbulent dissipation via liquid droplets. The source term,  $S_\varepsilon$ , in Eq. (12) is presented as

$$S_\varepsilon = C_{2\varepsilon} \frac{\varepsilon}{k} S_k. \quad (21)$$

The model constants were considered as:  $\sigma_k = 1.0$ ,  $\sigma_\varepsilon = 1.3$ ,  $C_{1\varepsilon} = 1.44$ ,  $C_{2\varepsilon} = 1.92$ , and  $C_\mu = 0.09$  [51]. The abovementioned

equations (from Eqs. (14)–(21)) have been implemented by the authors within the commercial CFD code using user defined subroutines. Furthermore, the enhanced wall treatment was utilised to improve the near-wall flow details. The enhanced wall treatment blends the linear and logarithmic laws of the wall and provides the smooth transition between the log-law and viscous sub-layer. To resolve the viscous sublayer near the wall boundaries, the  $y^+$  value should be sufficiently smaller. Therefore, the grid density close to the wall surfaces was refined to achieve the  $y^+$  value close to unity value for all cases.

### 3. Numerical details

All of the presented numerical results of nozzle and turbine stator cascade were performed with steady state RANS equations. The conservation equations of the mixture of the vapour and liquid phases were discretized applying conservative finite-volume integration over a control volume with multi-grid method. The solution methodology of flow solving algorithm was based on explicit density based couple solver. The Roe scheme of Roe [52] was used to calculating the convective fluxes. An upwind scheme was employed for the spatial discretization. The structured meshes were utilised to generate the computational grid. The results presented in this work were converged to normalised RMS residuals of the order of  $10^{-4}$  or lower.

#### 3.1. Grid independence study

In order to check the influence of computational grid density on the CFD results, a grid independence study was performed in nozzle and turbine cascade. Furthermore, the influence of grid refinements was conducted using the grid convergence index (GCI) method. The GCI method proposed by Celik et al. [53] was used in this work. This method is based on the Richardson extrapolation technique, in which multiple solutions to the numerical calculation are found by adjusting a parameter (grid size) and are used to extrapolate a more accurate solution [54,55]. The grid convergence was evaluated using a relative error measure of different parameters between the grids as,

$$e_a^{ij} = \left| \frac{\phi_i - \phi_j}{\phi_j} \right|, \quad (22)$$

where  $\phi_i$  and  $\phi_j$  are the selected parameter of  $i$ th and  $j$ th grids, respectively. An extrapolated relative error was calculated as,

$$e_{ext}^{ij} = \left| \frac{\phi_{ext}^{ij} - \phi_i}{\phi_{ext}^{ij}} \right|, \quad (23)$$

where  $\phi_{ext}^{ij}$  is the extrapolated value, which can be calculated as,

$$\phi_{ext}^{ij} = \frac{r_{ij}^p \phi_j - \phi_i}{r_{ij}^p - 1}. \quad (24)$$

Here,  $r$  represents the grid refinement factor and  $p$  is the order of the discretization method. Further details pertaining to the GCI method can be found from Celik et al. [53]. The GCI provides a uniform measure of convergence for grid refinement studies [56]. The GCI value can be achieved as,

$$GCI^{ij} = F_s \frac{e_a^{ij}}{r_{ij}^p - 1}, \quad (25)$$

where  $F_s$  is the safety factor, which is 1.25. The influence of the grid density was discussed in Section 4.2.

4. Results and discussions

4.1. Results of the Barschdorff nozzle

Firstly, the influence of turbulence modelling on condensation phenomenon was examined with the Barschdorff [2] nozzle. The presented CFD results of the nozzle were carried out considering a sufficiently refined grid to obtain a grid independent solution. The grid generation in the region of condensation was fine enough to resolve the droplet formation and the droplet growth accurately. The boundary conditions corresponding to the experiments of Barschdorff [2] have been applied at the inlet:  $P_0 = 78,390$  Pa,  $T_0 = 380.55$  K. The nozzle outlet was fixed with the supersonic condition. First, the effect of the freestream turbulence intensity on the condensing steam flow was investigated. The turbulence intensity of the flow is one of the most important parameters that influence directly the flow field and flow transition, as well. Therefore, it could also be possible that the flow turbulence intensity has some impact on the condensation process. The calculations were performed with various freestream inlet turbulence intensities (i.e.,

$\chi = 0.02, 0.05, 0.1,$  and  $0.2$ ) with the Sk- $\epsilon$  turbulence model. In the case of condensing steam flow, the flow is initially dry, but after reaching the Wilson point, liquid droplets are formed and a two-phase flow is generated. The liquid droplet is growing rapidly by exchanging latent heat with the surrounding subcooled vapour. Therefore, the heat addition increases the flow temperature and pressure. The flow pressure rise is called the ‘condensation disturbance’ [57]. Fig. 1 shows the predicted results with various freestream inlet turbulence intensities along the nozzle centreline.

It is obvious that the flow intensity is proportional to the flow turbulent kinetic energy and its dissipation rate. The higher value of turbulence intensity increases the viscous dissipation in the flow, which influences the flow expansion. It is apparent that the flow expansion has been increased in the case of lower freestream inlet turbulence intensity as presented in Fig. 1(a). Moreover, the flow turbulence intensity influenced the subcooling level, the nucleation rate, and the wetness fraction as well (Figs. 1(b)–(d)). The nucleation region was slightly expanded in the downstream, while the wetness fraction was decreased with the higher freestream inlet turbulence intensity. Furthermore, the droplet

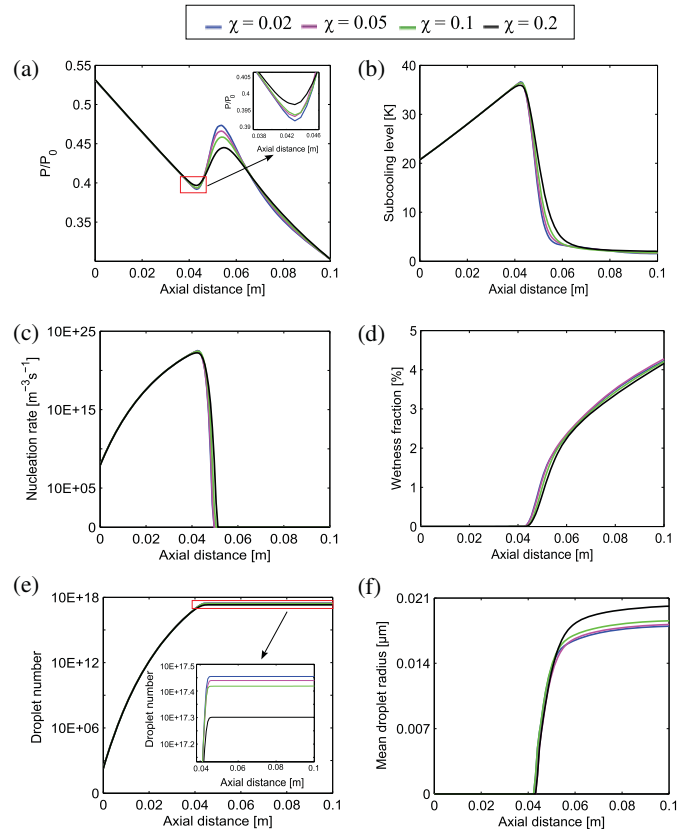
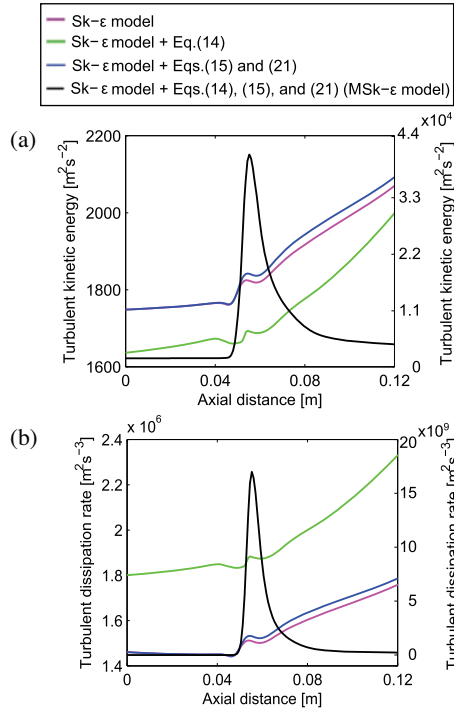


Fig. 1. Predicted results of (a) pressure, (b) subcooling level, (c) nucleation rate, (D) wetness fraction, (E) droplet number, and (F) mean droplet radius along the nozzle centreline. 0 axial distance indicates the nozzle throat.



**Fig. 2.** Distribution of (a) the turbulent kinetic energy, and (b) the turbulent dissipation rate at nozzle centreline predicted by the  $Sk-\epsilon$  model and other subsequent modifications with it. The right side scales of  $y$ -axis present the  $MSK-\epsilon$  model.

number was increased, and the mean droplet radius was decreased with the lower turbulence intensity (Fig. 1(e) and (f)). Additionally, it is important to notice that the magnitude of the condensation disturbance was also influenced by the freestream turbulence intensity as presented in Fig. 1(a). As discussed above, the flow temperature and pressure increases due to the latent heat releases from the rapidly growing droplets. If the droplet number will be higher, it releases higher latent heat, which increases the peak of condensation disturbance. Therefore, the predicted peak of condensation disturbance was highest in the case of lower inlet freestream turbulence intensity.

Furthermore, the influence of turbulence modelling was analysed by a modified the  $Sk-\epsilon$  model. Fig. 2(a) and (b) present the predicted distribution of the turbulent kinetic energy and the turbulent dissipation rate with various modification to the  $Sk-\epsilon$  model, respectively. Fig. 2(a) shows that the steep rise for the turbulent kinetic energy was started around 0.046 m axial distance for all the models, which indicates the peak location of the nucleation rate. Moreover, the gradual increment in the turbulent kinetic energy appeared from 0.057 m axial distance for pink, green, and blue lines. This location demonstrates the condensation peak. Subsequent addition of the source terms (i.e., Eqs. (15) and (21)) to the  $Sk-\epsilon$  model increased the turbulent kinetic and its dissipation rate. Particularly, this increment resulted after the second phase generation. However, the reduction in the turbulent kinetic energy for the  $Sk-\epsilon$  model including the modified viscosity term

(i.e. Eq. (14)) can be explained by the considerably higher dissipation rate as shown in Fig. 2(b). Moreover, it would be interesting to examine the influence of the model modification by including both: the modified viscosity term (i.e., Eq. (14)) and the source terms (i.e., Eqs. (15) and (21)) to the  $Sk-\epsilon$  ( $MSK-\epsilon$ ) turbulence model. The black solid line indicates the predicted trends of the turbulent kinetic energy and its dissipation rate with the  $MSK-\epsilon$  turbulence model in Fig. 2(a) and (b), respectively. It can be seen that the  $MSK-\epsilon$  model predicted a notably higher value of the turbulent kinetic energy and its dissipation rate compared to the  $Sk-\epsilon$  model, particularly after the throat at the downstream of the nozzle. The right side  $y$ -axis scales in Fig. 2(a) and (b) are indicated for the  $MSK-\epsilon$  model. The trends of turbulent kinetic energy and its dissipation rate profiles predicted by the  $MSK-\epsilon$  model and the  $Sk-\epsilon$  model including modified viscosity term are similar before second phase generation due to modified viscosity effect. The variation observed before the droplet formation (approx. 0.046 m) in Fig. 2 is resulted only due to scale differences in  $y$ -axis. The addition of source terms to the turbulence models increased liquid mass generation rate. Therefore, the  $Sk-\epsilon$  model including source terms and the  $MSK-\epsilon$  model yielded higher liquid mass generation rate than the models without the source terms. However, the combined effect of source terms addition and the viscosity modification (i.e.,  $MSK-\epsilon$  model) increased turbulent kinetic energy and

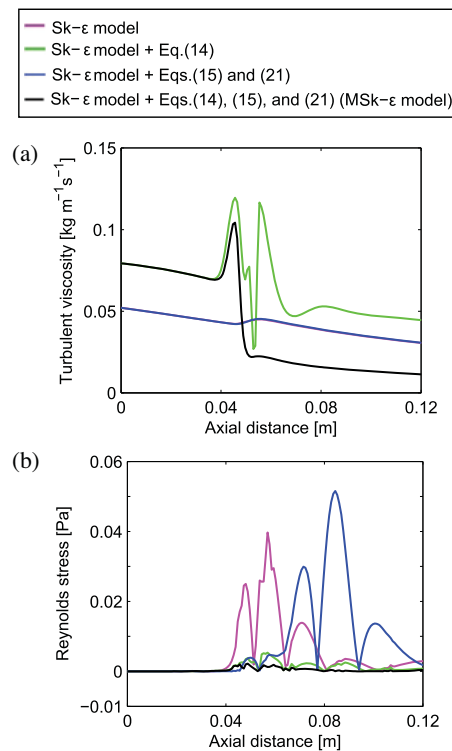


**Fig. 3.** Distribution of (a) the turbulent viscosity, and (b) the Reynolds stress along the nozzle centreline predicted by the  $Sk-\epsilon$  model and other subsequent modifications with it.

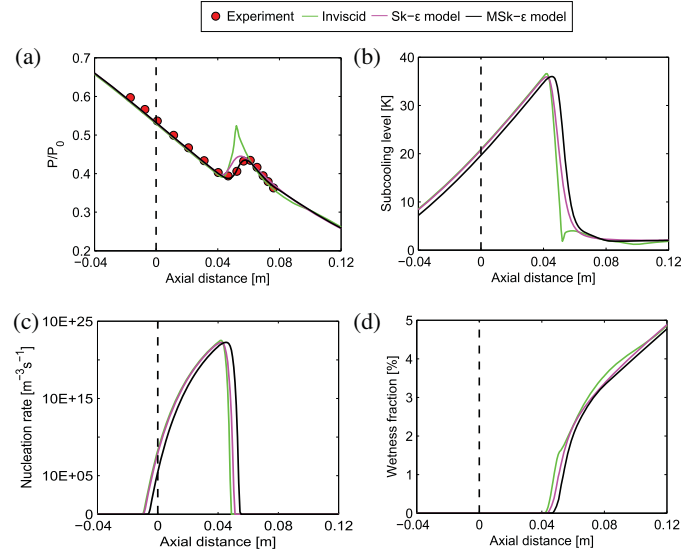


Fig. 4. Predicted profiles of (a) the pressure ratio, (b) subcooling level, (c) nucleation rate, and (d) wetness fraction along the nozzle centreline. The black vertical dashed line at  $x = 0$  axial distance indicates the nozzle throat.

Table 1  
Experimental conditions for the turbine cascade cases of White et al. [12].

Test No.	Upstream stagnation conditions			Downstream conditions	
	$P_{01}$ [kPa]	$T_{01}$ [K]	$\Delta T_{01}$ [kPa]	$P_2$ [kPa]	$M_{2s}$
L1	40.3	354.0	4.5	16.3	1.24
L2	40.9	354.0	4.0	19.4	1.11
L3	41.7	357.5	7.5	20.6	1.08
W1	41.9	350.0	wet (~1.6%)	17.8	1.20
H3	41.4	376.0	26.0	19.4	1.10

its dissipation rate notably. The significant increment is noted from axial distance of 0.046–0.066 m in both the turbulent properties. In this region, the droplet growth rate is higher and due to that the liquid mass generation rate is increased. Consequently, both the turbulent properties are significantly higher in the case of MSk- $\epsilon$  model. The mass generation rate remains stable/constant due to lower droplet growth rate after the axial distance of 0.08 m. Therefore, the profiles of turbulent kinetic energy and its dissipation rate in the case of MSk- $\epsilon$  model are almost constant towards the downstream of nozzle.

The predicted profiles of turbulent viscosity and the Reynolds stress along the nozzle centreline with various modification to the turbulence model are presented in Fig. 3.

It can be seen that the turbulent viscosity is relatively higher for the Sk- $\epsilon$  model including the modified viscosity term and the MSk- $\epsilon$  model. This is likely due to the modified viscosity terms which contain the production to dissipation ratio. However, the Sk- $\epsilon$  model and the Sk- $\epsilon$  model with source terms were estimated to have an almost identical distribution of the turbulent viscosity. The jump was located around 0.046 m axial distance for the Sk- $\epsilon$  model with modified viscosity term, and the MSk- $\epsilon$  model indicates the location of the highest rate of the nucleation. Additionally, the increment in the turbulent viscosity

demonstrates the region where the droplet growth is mainly occurring. It is clear that the droplet growth is increasing the turbulent viscosity (causing turbulence) and then bigger droplets (which are not much growing) are decreasing the turbulent viscosity (stabilizing the flow). After the nozzle throat in the downstream, the MSk- $\epsilon$  model yielded a comparatively lower value of the turbulent viscosity than the other models, due to higher viscous dissipation. Fig. 3(b) shows that the Sk- $\epsilon$  model and the Sk- $\epsilon$  model with source terms yielded a notably higher value of the Reynolds stress along the nozzle centreline. The Reynolds stress is calculated based on the Boussinesq approximation, in which the Reynolds stress is proportional to the turbulent viscosity and the velocity gradients. The oscillations in Reynolds stress in the cases of Sk- $\epsilon$  model and Sk- $\epsilon$  model with the source terms resulted due to relatively stronger velocity gradients compared to the MSk- $\epsilon$  model and the Sk- $\epsilon$  model with modified viscosity after the second phase generation. Furthermore, the jumps in the Reynolds stress profiles noted at 0.046 m and 0.057 m axial distances for the Sk- $\epsilon$  model indicate the nucleation and the condensation peak regions, respectively. However, these jumps were shifted more downstream for the Sk- $\epsilon$  model including source terms. In contrast, the Sk- $\epsilon$  model with modified viscosity term and the MSk- $\epsilon$  model estimated comparatively the lower value of the Reynolds stress. Furthermore, the predicted pressure distribution of the inviscid calculation, and the Sk- $\epsilon$  and the MSk- $\epsilon$  turbulence models along the nozzle centreline are compared with the experiments of [2] in Fig. 4(a). Both turbulence models yielded good agreement of pressure distribution with the experiments. However, the Sk- $\epsilon$  model failed to capture the right location of condensation disturbance. In the case of MSk- $\epsilon$  model, the increased viscous dissipation influenced on the temperature distribution via energy source, which affected the heat transfer rates. Therefore, the condensation process is extended to the downstream for the MSk- $\epsilon$  model. The MSk- $\epsilon$  model yielded an accurate profile of the pressure rise. The intensity of the condensation disturbance for the

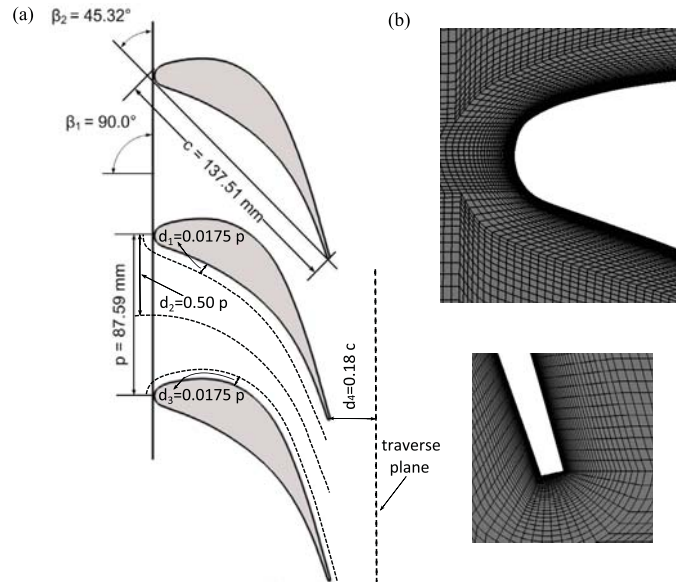


Fig. 5. (a) LP turbine stator blade geometry used for the experiments of White et al. [12], where the dotted black lines indicate the locations in which the CFD data are obtained, and (b) the computational mesh around the leading and trailing edge of the stator blade (Grid B).

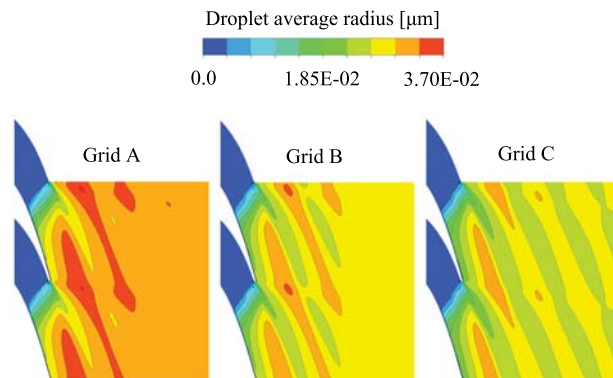


Fig. 6. Contours of the droplet average radius predicted by the  $Sk-\epsilon$  turbulence model with various grid densities.

Table 2  
Details about the grid discretization error.

Case	Parameter	$e_a$ (%)	$e_{ext}$ (%)	GCI (%)
Case A	Static pressure	0.14	0.25	0.32
	Velocity	0.09	0.05	0.06
	Wetness fraction	0.18	1.12	1.38
Case B	Static pressure	0.05	0.09	0.11
	Velocity	0.01	0.01	0.01
	Wetness fraction	0.17	1.03	1.30

inviscid case was almost double than other cases, in which the increment in the pressure rise was resulted due to the higher rate of latent heat released via droplets. Fig. 4(b) and (c) show that the model modification influenced on the sub-cooling level and the nucleation rate as well. The expansion process is extended to the downstream due to the turbulent viscosity modification and the source terms addition (Fig. 4(a)). Therefore, the nucleation region for the  $MSK-\epsilon$  model has been shifted little bit towards the downstream of the nozzle. It can also be seen that the  $MSK-\epsilon$  model predicted marginally lower wetness fraction than the inviscid calculation and the  $Sk-\epsilon$  model.

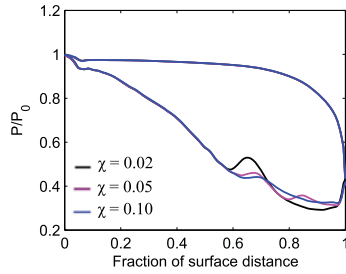


Fig. 7. Blade surface pressure distribution predicted by the MSK- $\epsilon$  turbulence model with various freestream turbulence intensities.

4.2. Results of stationary turbine stator cascade

The influence of turbulence modelling was investigated with the steam turbine cascade of White et al. [12]. White et al. [12] performed experiments with the turbine blade profile, which is the planar stator cascade of the fifth stage stator blade from the six-stage LP cylinder of a 660 MW steam turbine. The test cases of White et al. [12] were more associated with the flow in the steam turbine where there is an interaction between the aerodynamic effects and the condensation process itself.

In the present work, five experimental cases named with L1, L2, L3, W1, and H3 of the test series of White et al. [12] were modelled. The selected tests were varied by different exit isentropic Mach numbers and accordingly different total pressure ratios  $P_{01}/P_2$ . Cases L1, L2, and L3 were the low inlet superheat tests and Case H3 was the high inlet superheat test, while Case W1 was per-

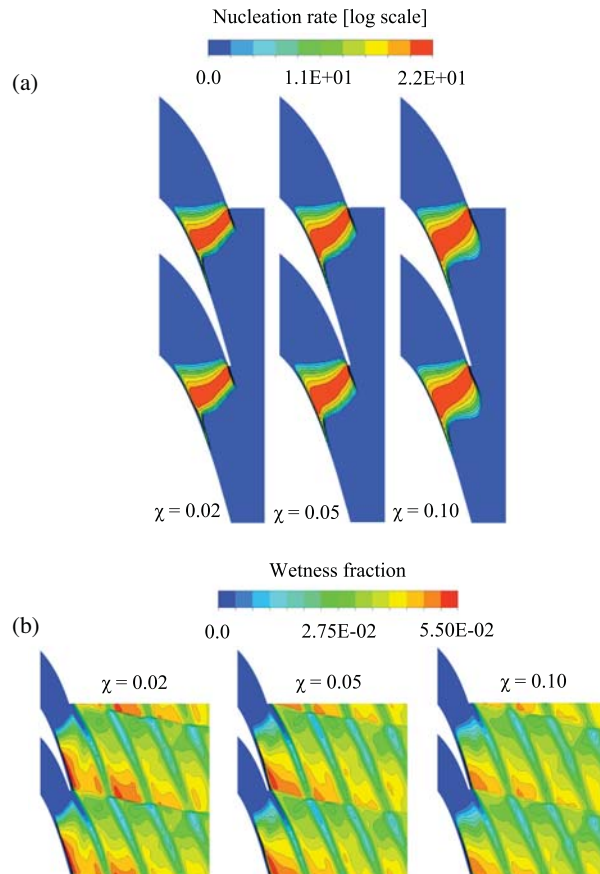


Fig. 8. Contours of (a) the nucleation rate, and (b) the wetness fraction predicted by the MSK- $\epsilon$  turbulence model with various freestream turbulence intensities.

formed with the inlet wetness. Details of the experimental conditions of the selected cases are listed in Table 1.

There were four stator vanes in the experiments of White et al. [12]. In this work, only two passages of the experimental facility were modelled employing a periodic boundary condition in the  $y$ -direction. The outlet of the computational domain was considered downstream of the traverse plane. A schematic view of the LP turbine stator blade geometry of the White et al. [12] experiments is shown in Fig. 5(a). The structured and non-uniform grid was generated for the computational domain. The O-grid around the blade surfaces was generated. A sufficiently fine grid was constructed around the leading and trailing edges of the stator to resolve the boundary layers as presented in Fig. 5(b).

For the grid independence study, three different grid sizes were used, where the number of the grid elements was increased from Grid A (40,970 cells) over Grid B (76,554 cells) to Grid C (103,582 cells). Fig. 6 presents the predicted average droplet radius with the selected grids, showing that the estimation of the droplet size is sensitive to the grid refinement from coarser to finer. Grid A predicted comparatively bigger droplet sizes than Grid B and C.

The GCI method was used to estimate the discretization error measurement. Table 2 summarises the discretization error measurement for an averaged value of the static pressure, velocity, and wetness fraction at the pitchwise traverse position which was at 50 mm downstream of the trailing edge. In Table 2, Cases A and B represent the grid refinements from Grid A to B and Grid B to C, respectively. The calculated relative error was very small for all parameters. It can be seen that the wetness fraction was more sensitive to the grid refinement than the others. Moreover, the successive grid refinements resulted in a reduction for an extrapolated relative error as well. Table 2 shows that the GCI value for the successive grid refinements (i.e., Case A to Case B) has been reduced for all three variables. The GCI values indicate that the grid refinement from Grid B to C yielded a minimal numerical error. Therefore, an intermediate grid (i.e., Grid B) was chosen for the rest of the study.

The influence of the freestream turbulence intensity on turbine cascade flow was studied with three different values of  $\chi = 0.02$ , 0.05, and 0.1. Fig. 7 shows the effect of the freestream turbulence intensity on the pressure distribution along the blade surfaces. It is noted that the increment in the turbulence intensity reduces the flow expansion. The reduction in the flow expansion leads to a decrease in the heat release from the droplets. Therefore, the higher freestream turbulence intensity weakens the condensation disturbance strength, and its location is extended to the downstream. The predicted contours of the nucleation rate and wetness fraction with various freestream turbulence intensities are presented in Fig. 8. It was observed that when the freestream turbulence intensity increases from  $\chi = 0.02$  to 0.1, the nucleation rate occurred in a larger area. As the flow expansion rate increases, the superheated steam crosses the saturation line and becomes saturated steam. It can be seen that the lower freestream turbulence intensity predicted a relatively higher wetness fraction due to the higher expansion rate on the suction side of the blades (Fig. 8(b)).

In fluid flow problems, near wall surfaces, fluid viscosity plays a dominant role in momentum and heat transfer. Moreover, the rapid variation of flow variables occurs within the boundary layer region. The turbulent flow consists of a spectrum of different scales (eddy sizes) in which the largest eddies are of the order of the flow geometry. These structures are deformed and stretched by the fluid dynamics until they break into smaller eddies, and the process is repeated so that energy is transported to smaller and smaller structures. Finally, at small scales the kinetic energy is dissipated by the viscosity of the fluid. The whole process of transport of energy from the large scale of injection to the small dissipative

scale, through the hierarchy of eddies is known as the turbulent cascade. It would be worthwhile to identify the influence of turbulence modelling near wall surfaces and in the main flow stream (at the middle of the passage). Therefore, the various flow properties were calculated near the blade surfaces and at the mid-passage. The information about these locations was displayed in Fig. 5(a). Fig. 9 shows the predicted results of turbulent kinetic energy,

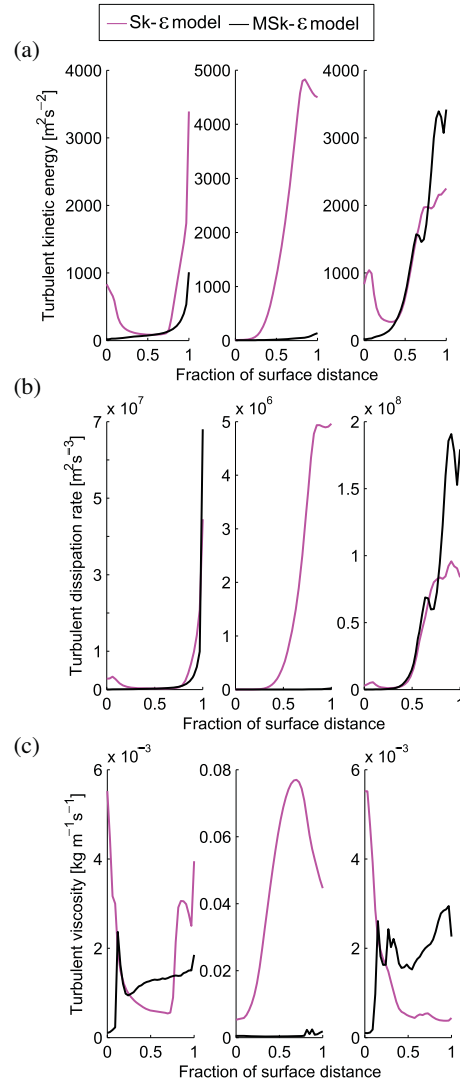
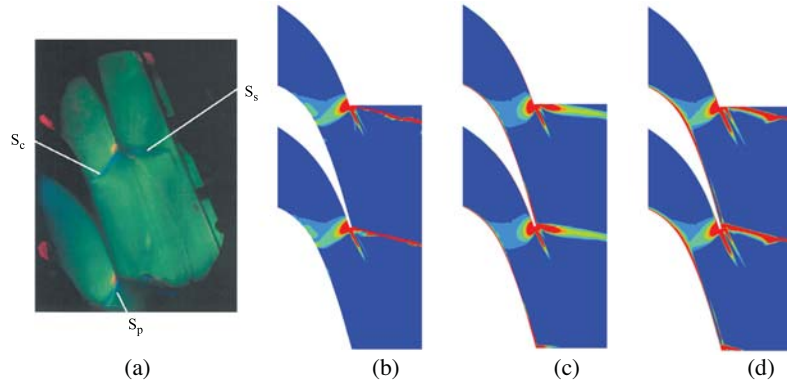
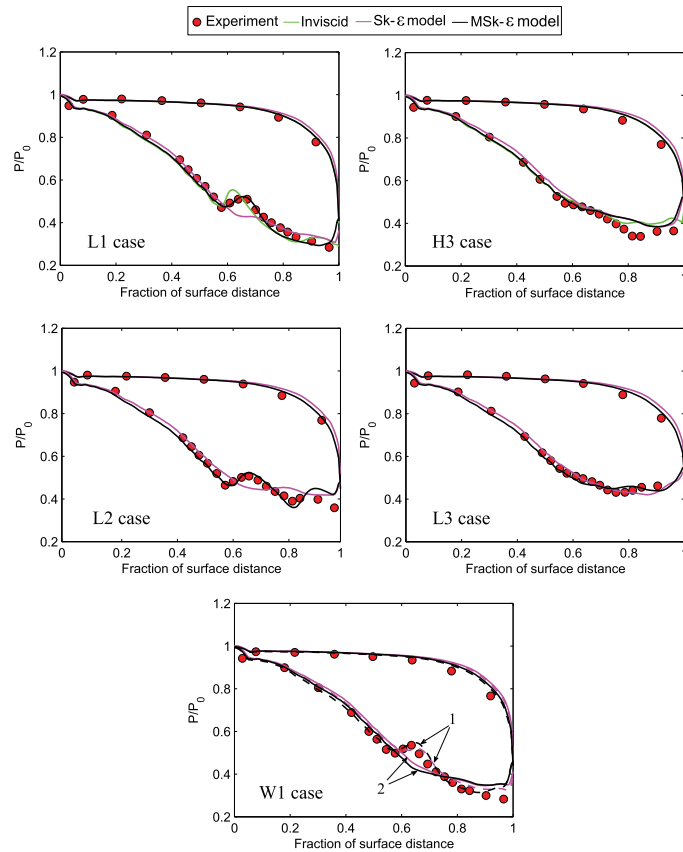


Fig. 9. Predicted results of (a) turbulent kinetic energy, (b) turbulent dissipation rate, and (c) turbulent viscosity at near pressure side (left side), mid-passage (middle), and near suction side (right side) for Case L1. Here 0 and 1 at the  $x$ -axis indicate the locations near the leading and trailing edges of the blade, respectively.



**Fig. 10.** (a) Reproduced image of the original experimental Schlieren graph of Case L1 of [12] compared with predicted density gradients of, (b) the inviscid, (c) the Sk- $\epsilon$  model, and (d) the MSk- $\epsilon$  model.



**Fig. 11.** Predicted results of blade surface pressure distribution and compared with the experimental data of [12]. In Case W1, the indication 1 and 2 represent the saturated inflow and the wet inflow, respectively.

turbulent dissipation rate, and turbulent viscosity near the blade surfaces and in the mid-passage. The large differences have been observed in the predicted values of turbulent kinetic energy, turbulent dissipation rate, and turbulent viscosity at the mid-passage by the  $Sk-\epsilon$  model and the  $MSk-\epsilon$  model. Near the pressure side, the  $MSk-\epsilon$  model predicted lower value of turbulent kinetic energy than the  $Sk-\epsilon$  model, likely due to the higher dissipation rate for the  $MSk-\epsilon$  model near the pressure side. The jump locating around 0.8 fraction of the surface distance near the pressure side indicates the location of the highest rate of the nucleation. The  $MSk-\epsilon$  model estimated a considerably higher turbulent kinetic energy and its dissipation rate compared to the  $Sk-\epsilon$  model near the suction side, particularly after the second phase generation. This notable increment in the turbulent kinetic energy, turbulent dissipation rate, and turbulent viscosity can be explained by the viscosity modification and the added source terms effects, which increase the viscous dissipation near the suction surface.

Fig. 10 presents the Schlieren photograph and the calculated density gradient of Case L1. The experimental Schlieren photograph is the reproduced image of the original experimental photograph of White et al. [12], in which the expansion is indicated by red, orange, and yellow colours, while light blue and green colours express the small values of the compression. Moreover, the condensation shock, pressure side shock, and suction side shock are labelled with  $S_c$ ,  $S_p$ , and  $S_s$ , respectively. It can be seen that the oblique shock profile is little bit curved across the central blade passage, and it is not reflected from the suction surface. Additionally, the pressure side shock interacts and merges with the condensation shock across the central blade. Figs. 10(b)–(d) show the density gradient contour for the selected models. The inviscid calculation yielded a relatively thinner profile of the  $S_s$  shock due to the absence of viscous dissipation. It is observed that the  $MSk-\epsilon$  model predicted the  $S_s$  shock with a higher intensity

than the others, likely due to the higher entropy generation resulting from the viscous dissipation at the trailing edge. The  $Sk-\epsilon$  model failed to predict the  $S_s$  shock. In general, the shockwave patterns yielded by the  $MSk-\epsilon$  model and the inviscid calculation match well with the experiment photograph.

Moreover, the quantitative analysis of the calculated results was performed based on the experimental data of White et al. [12]. The calculated pressure distribution on the blade surfaces with the  $Sk-\epsilon$  model and the  $MSk-\epsilon$  model is compared with the measured data in Fig. 11 for the selected test cases. The results of inviscid calculation are displayed only for the L1 and H3 cases. Fig. 11 shows that the yielded trends of pressure side pressure distribution by the inviscid and the turbulence models are similar. However, some variation was observed in the suction side pressure distribution. In Case L1, the  $MSk-\epsilon$  model estimated the correct location and the intensity of the condensation disturbance on the suction side, while the inviscid calculation yielded the correct intensity of the pressure rise, but the location was moved little to the flow upstream. The predicted subcooling level in the case of  $Sk-\epsilon$  model is lower due to lower expansion rate than the  $MSk-\epsilon$  model. The  $Sk-\epsilon$  model estimated less number of droplets which directly influenced on the latent heat released by droplets. Therefore, the  $Sk-\epsilon$  model failed to capture the condensation disturbance. However, some discrepancy was observed between the calculated and the measured pressure distribution after the condensation shock on the surface side. The inlet superheat is 26 K for Case H3. Therefore, the effects of condensation were absent on the surface pressure distributions. Moreover, the measured data displays a second pressure rise close to the blade trailing edge. However, this is not observed in the calculated results. This pressure rise is not caused by the condensation phenomena; it happens due to the reflections from the upper tailboard during measurement [12]. Relatively good correspondence has been observed

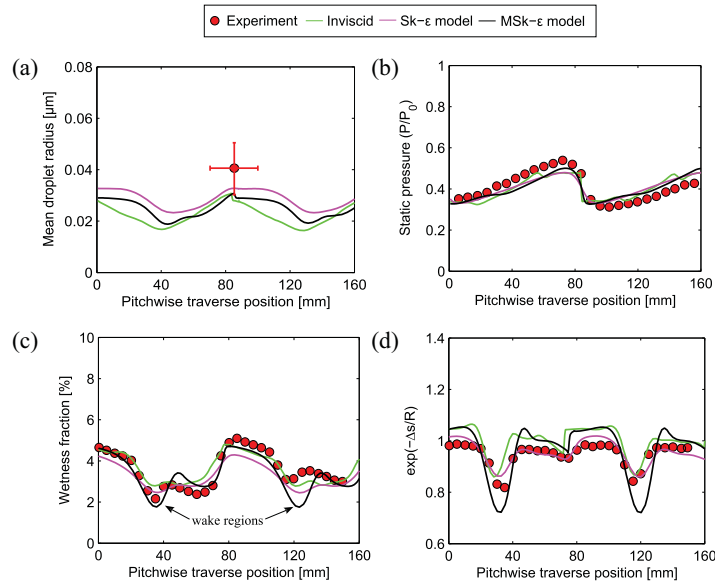


Fig. 12. Predicted results of Case L1: (a) mean droplet radius, (b) static pressure, (c) wetness fraction, and (d) non-dimensional entropy compared with the experiments of White et al. [12].

between the predicted and the measured results except near the suction surface trailing edge. Particularly, the  $Sk-\epsilon$  and the  $MSk-\epsilon$  models yielded similar trends near the suction surface trailing edge. Furthermore, both the turbulence models validated with the other low inlet superheat cases i.e. L2 and L3. It can be seen that the  $MSk-\epsilon$  model yielded good results of blade surfaces' pressure distribution for both cases. In Case L2, the  $Sk-\epsilon$  model failed to obtain the condensation disturbance. Moreover, the comparison between the predicted blade pressure profile of the  $Sk-\epsilon$  model and the  $MSk-\epsilon$  model including the wet inflow and the saturated inflow, and the measured data is given in Fig. 11 for Case W1. For Case W1, the inlet droplet radius ( $\approx 0.5 \mu\text{m}$ ) and liquid mass fraction ( $\approx 1.6\%$ ) was assumed corresponding to the experimental values. It can be seen that the calculation with wet inflow with both the turbulence models was failed to predict the pressure rise resulted because the condensation on the primary liquid droplet was high enough preventing excessive departures from the equilibrium. Therefore, the secondary nucleation was relatively weak and remained up for a longer period [12]. It might be possible that the utilised values of inlet wetness fraction and liquid droplet size in the experiments have differed marginally from the assumed values [12]. However, the saturated inflow with the  $MSk-\epsilon$  model is in good correspondence with the measurements. The  $Sk-\epsilon$  model predicted the condensation disturbance with lower intensity.

In addition, White et al. [12] provided experimental data for the mean droplet size, static pressure distribution, wetness fraction, and normalised entropy at a specific location at downstream for Case L1. Therefore, it was also possible to compare the predicted and the experimental results at traverse plane. The position of traverse plane is indicated in Fig. 5(a). The predicted pitchwise distribution of the mean droplet radius, static pressure, wetness fraction, and normalised entropy at the traverse position are compared with the experimental data in Fig. 12. The variation of the droplet radius distribution across the passage is mostly dependent on the total number of droplets created during nucleation process, which is influenced by the distinct expansion rates along the blade passage and also due to the interaction between trailing edge shock waves and the nucleation zone. It can be seen that the mean droplet radius is relatively larger particularly in the downstream of mid-pitch region due to lower expansion rate. Additionally, near the suction surface, nucleation occurs in the very rapid expansion region resulting in an enormous number of tiny droplets. Therefore, in these regions (i.e., 35–45 mm and 115–125 mm), the mean droplet radius is decreased compared to the mid-pitch region. Fig. 12(a) shows that the mean droplet radius predicted by the  $Sk-\epsilon$  model is slightly bigger, while after the model modification the mean droplet radius is reduced due to the higher droplet number. Relatively similar trends of the static pressure have been observed between the predicted and the experimental results. The wetness fraction is relatively lower between 35–45 mm and 115–125 mm at the traverse position because in these regions the trailing edge wake flows pass the traverse plane. Moreover, the flow mixing is higher in these regions, in which the temperature is comparatively higher. Therefore, the wetness fraction is relatively low in these regions. Furthermore, the cascade experiments were conducted for three passages, and therefore, it could be difficult to achieve periodicity in the downstream of the flow field. However, the CFD results yielded periodic profiles due to periodic boundary conditions. This could be the reason for some discrepancy observed between the predicted and the measured results in the second passage. Fig. 12(c) shows that the  $MSk-\epsilon$  model yielded better correspondence with the measured wetness fraction profile than others. Fig. 12(d) shows the comparison between the calculated and the measured data of pitchwise variations in non-dimensional entropy,  $\exp(-\Delta s/R)$ , in which  $\Delta s$  is the increment in a specific entropy above the cascade inlet value. Fig. 12

shows that the  $Sk-\epsilon$  model estimated good trends for the result of the non-dimensional entropy distribution, except in the wake region. The  $MSk-\epsilon$  model predicted relatively higher entropy compared to the inviscid calculation and the  $Sk-\epsilon$  model, particularly, in the wake region of the blade, likely due to the higher turbulent dissipation in that region, which increases the entropy generation.

#### 4.3. Loss analysis

The primary goal of turbomachinery designers is to increase the performance of turbomachinery by increasing the efficiency. The reduction in the efficiency of turbomachinery is entitled as loss. The only rational measure of loss in an adiabatic machine is entropy generation [58]. The entropy generation happens due to three main processes: (i) viscous friction (either in boundary layers or in free shear layers), (ii) heat transfer, and (iii) non-equilibrium processes (occur in very rapid expansions or in shock waves) [58].

The local entropy generation rates are considerably high in the blade wakes, at the edges of separated regions and in vortices, in which, the shearing rates are relatively high. Moreover, in these regions, the flow turbulence is the leading phenomenon, which governs the heat, mass, and momentum transfer processes. Consequently, the accurate prediction of entropy generation needs accurate turbulence modelling. The predicted contours of entropy generation by the inviscid calculation, and the  $Sk-\epsilon$  and  $MSk-\epsilon$  models are presented in Fig. 13 for Case L1.

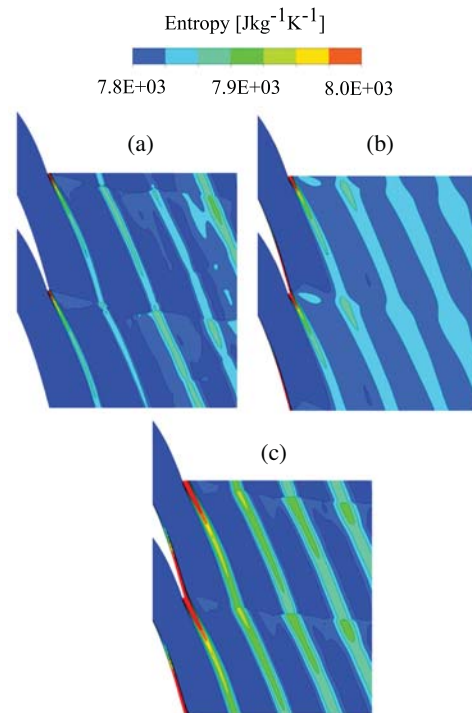


Fig. 13. Contours of entropy predicted by (a) the inviscid, (b) the  $Sk-\epsilon$  model, and (c) the  $MSk-\epsilon$  model.

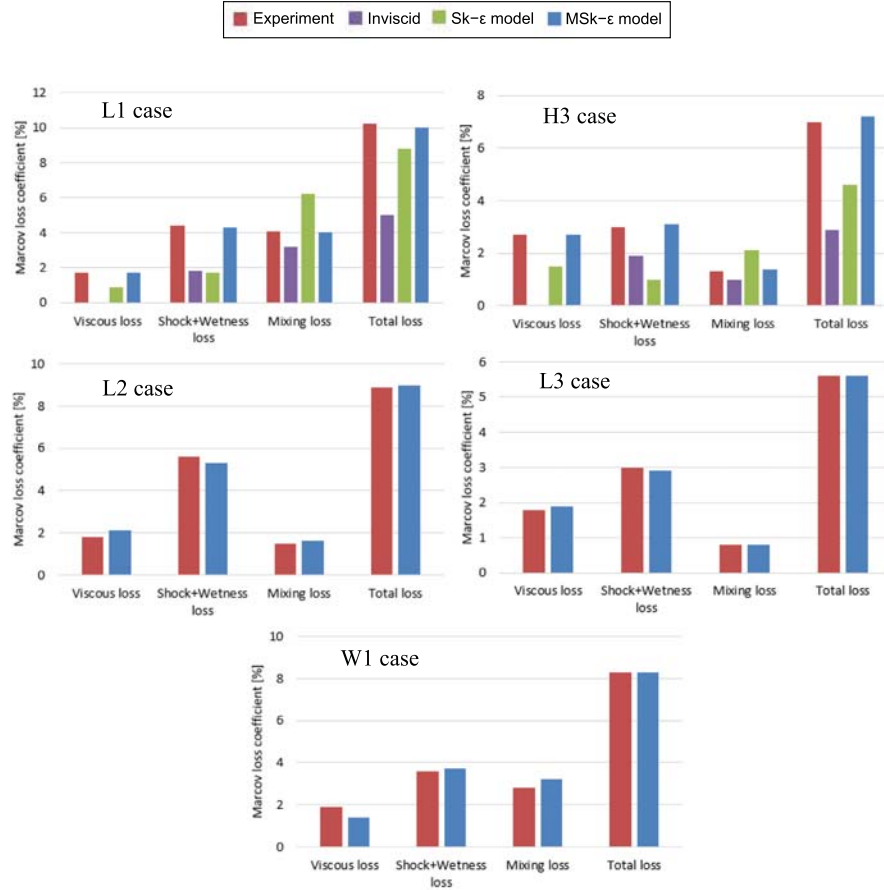


Fig. 14. Predicted Markov loss coefficients compared with the experiments of White et al. [12].

It appears that the inviscid calculation yielded relatively weak entropy generation compared to the Sk- $\epsilon$  and the MSK- $\epsilon$  models owing to the lack of the boundary layer effect in the inviscid calculation. The MSK- $\epsilon$  model predicted the highest entropy generation among all the cases particularly in the blade wake region. Furthermore, White et al. [12] presented information about the losses that occur due to the irreversible heat and mass transfer during the condensation process. Accordingly, it was possible to analyse the influence of turbulence modelling on the loss mechanism occurring in the condensing steam flow. In the present work, the Markov energy loss coefficient based on the entropy increase was calculated. The Markov energy loss coefficient is defined as,

$$\zeta = \frac{T_2 \cdot \Delta s}{0.5u_2^2}. \quad (26)$$

For the loss coefficient calculation, it was assumed that all of the parameters were 'mixed-out' values to a plane far downstream of the cascade. The Markov energy loss coefficients were divided into three components [12]:

- (i) Shockwave plus wetness loss was calculated from the mass-averaged values across a section of the traverse plane, excluding the wake regions.
- (ii) Viscous loss was calculated by subtracting the shock wave and wetness loss from the mass-averaged loss across the entire pitch at the traverse plane.
- (iii) Mixing loss was calculated by subtracting the total mass-averaged loss at the traverse plane from the fully mixed-out loss.

Fig. 14 presents the comparison between the predicted and the measured losses for all the selected cases.

It can be seen that the Sk- $\epsilon$  model underpredicts the viscous loss, while the MSK- $\epsilon$  model estimates an accurate value of the viscous loss for Cases L1 and H3. The intensity of the  $S_p$  shock wave for the MSK- $\epsilon$  model is comparatively higher than that of the Sk- $\epsilon$  model (Fig. 10). Moreover, it can be observed that the  $S_p$  shock merges with the  $S_c$  shock, thickening the suction side boundary layer onto the suction side of the adjacent blade, which increases

the viscous loss. Therefore, the MSk- $\epsilon$  model yields higher viscous loss than the Sk- $\epsilon$  model.

For Cases L1 and H3, the predicted magnitude of the shock plus wetness loss for the MSk- $\epsilon$  model corresponds well with the experimental values. In contrast, the inviscid calculation and the Sk- $\epsilon$  model calculated a notably smaller value of the shock plus wetness loss. The magnitude of mixing loss increases with the high Mach numbers. Among the selected test cases, Case L1 was performed with the highest exit Mach number. Therefore, the mixing loss for the L1 case is higher than for the other test cases. Furthermore, it is known that the combined action of shock waves, expansion waves, and viscous forces causes a gradual transition from nonuniform flow condition in the trailing edge plane to uniform conditions far downstream, which induce mixing loss. The boundary layer effect was absent in the inviscid calculations, reducing the viscous forces. Therefore, the inviscid calculation estimated lower mixing loss compared to both turbulence models. As shown in Fig. 9(c), the Sk- $\epsilon$  model estimated fairly larger value of the turbulent viscosity than the MSk- $\epsilon$  model. Therefore, this could be the reason for the higher entropy generation in the mid-passage at downstream for the Sk- $\epsilon$  model (Fig. 13), which indicated the higher value of mixing loss. The presented values of the total loss in Fig. 14 indicate the sum of viscous loss, shock plus wetness loss, and mixing loss. It can be seen that the inviscid calculation failed to predict the total loss for both cases. Also, the Sk- $\epsilon$  models yielded some variation with the measured losses. The MSk- $\epsilon$  model estimated accurate trends of the losses occurring in the condensing flow of turbine cascade. Additionally, losses were calculated for Cases L2, L3 and W1 by the MSk- $\epsilon$  model. Good agreement was observed between the predicted and the measured losses.

## 5. Conclusions

In this work, the influence of turbulence modelling on non-equilibrium homogeneously condensing steam flow was presented, adopting the Eulerian–Eulerian approach based on compressible Reynolds-averaged Navier–Stokes equations. The standard  $k$ - $\epsilon$  (Sk- $\epsilon$ ) turbulence model was modified by introducing the modulation of turbulence kinetic energy and its dissipation due to liquid droplets via source terms. Additionally, the definition of turbulent viscosity was modified by production to dissipation ratio.

In the case of laval nozzle, the presented results illustrated that the freestream turbulence intensity of the flow and the condensation disturbance magnitude were inversely proportional. Moreover, the flow turbulence intensity influenced the growth rate and droplet size. It can be concluded that the inviscid calculation and the Sk- $\epsilon$  turbulence model were inadequate in predicting the two-phase flow phenomena in a nozzle. After the addition of the source terms and modified turbulent viscosity into the Sk- $\epsilon$  turbulence model, the modified Sk- $\epsilon$  (MSk- $\epsilon$ ) turbulence model predicted relatively higher viscous dissipation. The viscous dissipation changes the temperature distribution via energy source, which affects the heat transfer rates. Therefore, the nucleation process and droplet growth rate were influenced by the turbulence model modification. It can be concluded that the MSk- $\epsilon$  model corresponds well with the experimental results and mimics crucial trends of the condensation process of a nozzle.

The influence of turbulence modelling was further studied with the condensing steam flow in a stationary cascade of turbine blades operating under transonic conditions. Five test cases were modelled and discussed. The calculations of turbine cascade flow were conducted with different inlet freestream turbulence intensities. The predicted results demonstrated that the high freestream turbulence intensity expanded the nucleation region, and consequently the condensation disturbance disappeared. As seen

qualitatively, also the wetness fraction was reduced with a higher freestream turbulence intensity.

The results of blade surface pressure distribution, liquid droplet size, variation of static pressure, wetness and normalised entropy along the traverse plane at downstream, and Schlieren photograph predicted by the inviscid calculation, the Sk- $\epsilon$  and the MSk- $\epsilon$  turbulence models were compared with the experimental data. It is demonstrated that the Sk- $\epsilon$  model failed to predict condensation disturbance in the turbine cascade. In the case of the MSk- $\epsilon$  model, the subcooling level was increased due to the higher flow expansion. As the subcooling level increases, the rate of nucleation of liquid droplets increases, affecting the droplets growth rates. The MSk- $\epsilon$  model yielded a higher number of droplets, which released more latent heat to the vapour phase, thus increasing the pressure rise. The presented results indicated that the MSk- $\epsilon$  model predicted the condensation disturbance more accurately than the inviscid calculation and the Sk- $\epsilon$  model. Generally, the MSk- $\epsilon$  model produced more promising trends for the results at the traverse plane of the downstream than the inviscid calculation and the Sk- $\epsilon$  model.

The cascade loss coefficients were calculated from the numerical simulations. The presented loss analysis indicated that the MSk- $\epsilon$  estimated an accurate value of the viscous loss, shock plus wetness loss, mixing loss, and total loss for the selected cases. Both the inviscid calculation and the Sk- $\epsilon$  model failed to predict shock plus wetness loss and mixing loss. The study demonstrated that the ignorance of turbulence modelling to condensing steam flow calculation may induce an incorrect estimation of the key phenomena.

The presented study shows that the prediction of condensing steam flows is influenced by turbulence modelling. Therefore, the accurate computational prediction of condensing steam flow requires the turbulence to be accurately modelled. This work will be continued in the future with the aim to investigate the influence of turbulence in 3D turbine cascade condensing flow with steady and unsteady conditions.

## Acknowledgements

The authors would like to acknowledge the Finnish Graduate School in Computational Fluid Dynamics and the Academy of Finland for the financial support.

## References

- [1] A. Stodola, *Die Dampfturbinen*, 4. Edition., Springer verlag, Berlin, 1910.
- [2] D. Barschdorff, *Verlauf der zustandsgrossen und gasdynamische zusammenhaenge der spontanen kondensation reinen wasserdampfes in lavalduesen*, *Forsch. Ingenieurwes.* 37 (1971) 146–157.
- [3] M.J. Moore, P.T. Walters, R.I. Crane, B.J. Davidson, Predicting the fog drop size in wet steam turbines, in: *Wet Steam 4 Conference*, Institute of Mechanical Engineers (UK), University of Warwick, Paper C37/73, 1973.
- [4] F. Bakhtar, D. Ryley, K. Tubman, J. Young, *Nucleation studies in flowing high pressure steam*, *Inst. Mech. Eng.* 189 (1975) 427–436.
- [5] C.A. Moses, G.D. Stein, *On the growth of steam droplets formed in a Laval nozzle using both static pressure and light scattering measurements*, *J. Fluids Eng.* 100 (1978) 311–322.
- [6] S. Skillings, P. Walters, M. Moore, *A study of supercritical heat addition as potential loss mechanism in condensing steam turbines*, in: *Int. Mech. Engrs., Intl. Conf. on Turbomachinery*, Cambridge, C259/87, 1987, pp. 125–134.
- [7] F. Bakhtar, K. Zidi, *Nucleation phenomena in flowing high-pressure steam: experimental results*, *Proc. Inst. Mech. Eng.* 203 (1989) 195–200.
- [8] F. Bakhtar, K. Zidi, *Nucleation phenomena in flowing high-pressure steam, part 2: theoretical analysis*, *Proc. Inst. Mech. Eng.* 204 (1990) 233–242.
- [9] G. Gyarmathy, *Nucleation of steam in high-pressure nozzle experiments*, in: *Proc. of 6th European Conference on Turbomachinery*, Lille, France, March 7–11, 2005, pp. 458–469.
- [10] F. Bakhtar, M. Ebrahimi, B. Bamkole, *On the performance of a cascade of turbine rotor tip section blading in nucleating steam, part 2: wake traverses*, *Proc. Inst. Mech. Eng. Part C: J. Mech. Eng. Sci.* 209 (1995) 169–177.
- [11] F. Bakhtar, M. Ebrahimi, R. Webb, *On the performance of a cascade of turbine rotor tip section blading in nucleating steam, part 1: surface pressure*

- distributions, *Proc. Inst. Mech. Eng. Part C: J. Mech. Eng. Sci.* 209 (1995) 115–124.
- [12] A.J. White, J.B. Young, P.T. Walters, Experimental validation of condensing flow theory for a stationary cascade of steam turbine blade, *Philos. Trans. R. Soc. London A* 354 (1996) 59–88.
- [13] F. Bakhtar, M.T.M. Tochai, An investigation of two-dimensional flows of nucleating and wet steam by the time-marching method, *Int. J. Heat Fluid Flow* 2 (1980) 5–18.
- [14] J.B. Young, Critical conditions and the choking mass flow rate in non-equilibrium wet steam flows, *ASME J. Fluids Eng.* 106 (1984) 452–458.
- [15] J.B. Young, Two-Dimensional nonequilibrium wet steam calculations for nozzles and turbine cascades, *ASME J. Turbomach.* 114 (1992) 569–579.
- [16] A.J. White, J.B. Young, Time-marching method for the prediction of two-dimensional unsteady flows of condensing steam, *AIAA J. Propul. Power* 9 (4) (1993) 579–587.
- [17] F. Bakhtar, M.R. Mahpeykar, K.K. Abbas, An investigation of nucleating flows of steam in a cascade of turbine blading-theoretical treatment, *ASME J. Fluids Eng.* 117 (1995) 138–144.
- [18] J.D. Denton, An improved time-marching method for turbomachinery flow calculation, *J. Eng. Power* 105 (3) (1983) 514–521.
- [19] A. Gerber, Two-phase Eulerian/lagrangian model for nucleating steam flow, *ASME J. Fluids Eng.* 124 (2002) 465–475.
- [20] A.G. Gerber, M.J. Kermani, A pressure based Eulerian-Eulerian multi-phase model for non-equilibrium condensation in transonic steam flow, *Int. J. Heat Mass Transfer* 44 (2004) 2217–2231.
- [21] S. Senoo, A.J. White, Numerical simulations of unsteady wet steam flows with non-equilibrium condensation in the nozzle and the steam turbine, in: *Proc. ASME-FEDSM2006, FEDSM-2006-98202*, Maimi, Florida, USA, July 17–20, 2006, pp. 757–767.
- [22] S. Senoo, A.J. White, Non-equilibrium unsteady wet-steam condensation modelling: computations in a steam turbine cascade and a nozzle, in: *Baumann Centenary Conference, BCC-2012-07*, University of Cambridge, UK, September 10–11, 2012.
- [23] W. Wróblewski, S. Dykas, A. Gepert, Steam condensing flow in turbine channels, *Int. J. Multiphase Flow* 35 (6) (2009) 498–506.
- [24] S. Dykas, W. Wróblewski, Single- and two-fluid models for steam condensing flow modeling, *Int. J. Multiphase Flow* 37 (9) (2011) 1245–1253.
- [25] S. Dykas, W. Wróblewski, Two-fluid model for prediction of wet steam transonic flow, *Int. J. Heat Mass Transfer* 60 (2013) 88–94.
- [26] S. Yamamoto, Y. Sasao, K. Sano, H. Satsuki, K. Ishizaka, H. Ooyama, Parallel computation of condensate flows through 2-d and 3-d multistage turbine cascades, in: *Proc. International Gas Turbine Congress, Tokyo, 2007*.
- [27] S. Yamamoto, Y. Sasao, S. Sato, K. Sano, Parallel-implicit computation of three-dimensional multistage stator-rotor cascade flows with condensation, in: *Proc. 18th AIAA Computational Fluid Dynamics Conference, AIAA 2007-4460*, Miami, Florida, USA, June 2007.
- [28] S. Yamamoto, Y. Sasao, H. Kato, H. Satsuki, H. Ooyama, K. Ishizaka, Numerical and experimental investigation of unsteady 3-d wet-steam flows through two-stage stator-rotor cascade channels, in: *Proc. ASME Turbo Expo, GT2010-22796*, Glasgow, UK, June 14–18, 2010, pp. 1–9.
- [29] J. Starzmann, M. Schatz, M.V. Casey, J.F. Mayer, F. Sieverding, Modelling and validation of wet steam flow in a low pressure steam turbine, in: *Proc. ASME Turbo Expo, GT2011-45*, Vancouver, Canada, June 6–10, 2011, pp. 1–12.
- [30] S. Miyake, Y. Sasao, S. Yamamoto, S. Tabata, T. Miyawaki, H. Ohyama, Simulation of unsteady 3D wet-steam flows through three-stage stator-rotor blade rows with equilibrium and non-equilibrium condensations, in: *Proc. of ASME Turbo Expo, GT2012-68828*, Copenhagen, Denmark, June 11–15, 2012, pp. 1–9.
- [31] A.R. Avetissian, G.A. Philippov, L.I. Zaichik, Effects of turbulence and inlet moisture on two-phase spontaneously condensing flows in transonic nozzles, *Int. J. Heat Mass Transfer* 51 (2008) 4195–4203.
- [32] D.G. Gregory-Smith, J.A. Walsh, C.P. Graves, K.P. Fulton, Turbulence measurements and secondary flows in a turbine rotor cascade, *ASME J. Turbomach.* 110 (4) (1988) 479–485.
- [33] G.D. MacIsaac, T.J. Praisner, S.A. Sjolander, Measurements of losses and reynolds stresses in the secondary flow downstream of a low-speed linear turbine cascade, *ASME J. Turbomach.* 134 (6) (2012) 1–12. 061015.
- [34] A. White, Numerical investigation of condensing steam flow in boundary layers, *Int. J. Heat Fluid Flow* 21 (2000) 727–734.
- [35] D.A. Simpson, A.J. White, Viscous and unsteadyflow calculations of condensing steam in nozzles, *Int. J. Heat Fluid Flow* 26 (1) (2005) 71–79.
- [36] A.R. Avetissian, G.A. Philippov, L.I. Zaichik, The effect of turbulence on spontaneously condensing wet-steam flow, *Nucl. Eng. Des.* 235 (2005) 1215–1223.
- [37] Y. Patel, G. Patel, T. Turunen-Saaresti, The effect of turbulence and real gas models on the two phase spontaneously condensing flows in nozzle, in: *Proc. of ASME Turbo Expo, GT2013-94778*, San Antonio, USA, June 3–7, 2013, pp. 1–7.
- [38] Y. Patel, T. Turunen-Saaresti, G. Patel, A. Grönman, Numerical investigation of turbulence modelling on condensing steam flows in turbine cascade, in: *Proc. of ASME Turbo Expo, GT2014-26307*, Düsseldorf, Germany, June 16–20, 2014, pp. 1–14.
- [39] J. Frenkel, *Kinetic Theory of Liquids*, Oxford University Press, New York, 1946.
- [40] K. Ishizaka, T. Ikhagi, D. Daigui, A high-resolution numerical method for transonic nonequilibrium condensation flows through a steam turbine cascade, in: *Proc. of 6th International Symposium on Computational Fluid Dynamics, 1995*, pp. 479–484.
- [41] P.G. Hill, Condensation of water vapour during supersonic expansion in nozzles, *J. Fluid Mech.* 25 (3) (1966) 593–620.
- [42] J.B. Young, The spontaneous condensation of steam in supersonic nozzles, *Phys. Chem. Hydrodyn.* 3 (1982) 57–82.
- [43] J.B. Young, An equation of state for steam for turbomachinery and other flow calculations, *J. Eng. Gas Turbines Power* 110 (1988) 1–7.
- [44] W.C. Reynolds, Thermodynamic properties, in: *SI: Graphs, Tables, and Computational Equations for 40 Substances*, Department of mechanical Engineering, Stanford University, 1979.
- [45] E.R.G. Eckert, R.M. Drake, *Analysis of Heat and Mass Transfer*, McGraw-Hill Co., 1972.
- [46] A. Guha, Two-phase flows with phase transition, in: *VKI Lecture Series 1995-06*, von Karman Institute for Fluid Dynamics, Belgium, 1995, pp. 1–110.
- [47] C.G. Speziale, On nonlinear k-l and k-e models of turbulence, *J. Fluid Mech.* 178 (1987) 459–475.
- [48] T.B. Gatski, C.G. Speziale, On explicit algebraic stress models for complex turbulent flows, *J. Fluid Mech.* 254 (1993) 59–78.
- [49] J.L. Lumley, The second-order models of turbulent flows, in: *Prediction Methods for Turbulent Flows, Hemisphere, New York, 1980*.
- [50] L. Zaichik, O. Simonin, V. Alipchenkov, Two statistical models for predicting collision rates of inertial particles in homogeneous isotropic turbulence, *Phys. Fluids* 15 (2003) 2995–3005.
- [51] B.E. Launder, D.B. Spalding, The numerical computation of turbulent flows, *Comput. Methods Appl. Mech. Eng.* 3 (1974) 269–289.
- [52] P.L. Roe, Characteristic based schemes for the Euler equations, *Annu. Rev. Fluid Mech.* 18 (1986) 337–365.
- [53] I.B. Celik, U. Ghia, P.J. Roache, C.J. Freitas, H. Coleman, P.E. Raad, Procedure for estimation and reporting of discretization error in cfd applications, *J. Fluids Eng.* 130 (7) (2008) 1–4. 078001.
- [54] L.F. Richardson, The approximate arithmetical solution by finite differences of physical problems involving differential equations, with an application to the stresses in a masonry dam, *Philos. Trans. R. Soc. London. Ser. A* 210 (1910) 307–357.
- [55] L.F. Richardson, J.A. Gaunt, The deferred approach to the limit, *Philos. Trans. R. Soc. London. Ser. A* 226 (1927) 299–361.
- [56] P.J. Roache, Perspective: a method for uniform reporting of grid refinement studies, *J. Fluids Eng.* 116 (1994) 405–413.
- [57] P.P. Wegener, Non-equilibrium flow with condensation, *Acta Mech.* 21 (1–2) (1975) 65–91.
- [58] J.D. Denton, The 1993 igit scholar lecture: loss mechanisms in turbomachines, *ASME J. Turbomach.* 115 (4) (1993) 621–656.

## **Publication V**

Patel, G., Patel, Y., and Turunen-Saaresti, T. (2015).  
**Influence of trailing edge geometry on the condensing steam flow  
in low-pressure steam turbine.**

Proceedings of ASME Turbo Expo 2015:  
Turbine Technical Conference and Exposition.  
Vol. 8, pp. 1-11.

© ASME, 2015

Reprinted with permission from the publisher



GT2015-43189

INFLUENCE OF TRAILING EDGE GEOMETRY ON THE CONDENSING STEAM  
FLOW IN LOW-PRESSURE STEAM TURBINE

Giteshkumar Patel\*

Fluid Dynamics Laboratory  
School of Technology  
Lappeenranta University of Technology  
Lappeenranta, Finland  
Email: giteshkumar.patel@lut.fi

Yogini Patel

Fluid Dynamics Laboratory  
School of Technology  
Lappeenranta University of Technology  
Lappeenranta, Finland  
Email: yogini.patel@lut.fi

Teemu Turunen-Saaresti

Fluid Dynamics Laboratory  
School of Technology  
Lappeenranta University of Technology  
Lappeenranta, Finland  
Email: teemu.turunen-saaresti@lut.fi

ABSTRACT

The paper describes the influence of trailing edge geometries on the non-equilibrium homogeneously condensing steam flow in the stationary cascade of turbine blades. The computational fluid dynamics (CFD) simulations were performed with the ANSYS Fluent CFD code using the Eulerian-Eulerian approach. The condensation phenomena were simulated on the basis of the classical nucleation theory, and the steam properties were calculated with the real gas model. Flow turbulence was solved by employing the modified version of the shear-stress transport (SST)  $k-\omega$  turbulence model. For this study, three trailing edge profiles; that is, conic, semicircular and square were considered. The influence of the trailing edge shapes were discussed together with experimental data available in the literature. The presented results show that the trailing edge geometries influence on the nucleation process, the droplet size, wetness fraction, the shock waves structure generated at trailing edge and its angles, the flow angle, the entropy generation and flow mixing in the wake. The cascade loss coefficients were calculated for the low inlet superheat case and for the high inlet superheat case. The presented results demonstrated that the losses that occur due to the irreversible heat and mass transfer during the condensation process were also influenced due to the trailing edge shapes.

\*Corresponding author

Nomenclature

$C_p$	specific heat at constant pressure ( $\text{J kg}^{-1} \text{K}^{-1}$ )
$h_{fg}$	specific enthalpy ( $\text{J kg}^{-1}$ )
$H$	total enthalpy ( $\text{J kg}^{-1}$ )
$I$	nucleation rate ( $\text{m}^{-3} \text{s}^{-1}$ )
$k$	turbulent kinetic energy ( $\text{m}^2 \text{s}^{-2}$ )
$M$	liquid mass (kg)
$P$	pressure (Pa)
$r$	radius (m)
$r_*$	critical radius (m)
$R$	gas constant ( $\text{J kg}^{-1} \text{K}^{-1}$ )
$s$	entropy ( $\text{J kg}^{-1} \text{K}^{-1}$ )
$S_1$	mass source term ( $\text{kg m}^{-2} \text{s}^{-1}$ )
$S_2$	momentum source term ( $\text{kg m}^{-2} \text{s}^{-2}$ )
$S_3$	energy source term ( $\text{W m}^{-3} \text{K}^{-1}$ )
$t$	time (s)
$T$	temperature (K)
$u$	velocity component ( $\text{m s}^{-1}$ )
$v$	flow velocity ( $\text{m s}^{-1}$ )

Greek Letters

$\rho$	density ( $\text{kg m}^{-3}$ )
$\beta$	liquid phase mass fraction
$\omega$	specific dissipation rate ( $\text{s}^{-1}$ )
$\eta$	number of liquid droplets per unit volume ( $\text{m}^{-3}$ )
$\sigma$	liquid surface tension ( $\text{N m}^{-1}$ )
$\Gamma_E$	thermal diffusion coefficient ( $\text{W m}^{-1} \text{K}^{-1}$ )

## Subscript

$d$	droplet
$l$	liquid phase
$v$	vapour phase
$i, j$	cartesian tensor notation
$x$	cartesian coordinate
0, 1, 2	total, inlet, outlet condition of cascade

## 1 INTRODUCTION

The efficiency of the entire power plant is largely dependent on the efficiency of the energy conversion in the turbine. Nowadays, the research on low pressure (LP) turbine stages is of special importance due to their relatively low efficiency. A marginal improvement in the LP turbine performance would produce significant economic benefits. It is essential to understand and to analyze the condensation process that occurs in the LP turbine because condensation in the LP turbine introduces thermodynamic and aerodynamic losses, as well as erosion in rotating and stationary parts. Therefore, the condensing steam flows in turbines have been widely studied for more than a century.

Comprehensive studies have been done by many researchers experimentally and theoretically to enhance the knowledge about the complicated physics of condensing steam flows. However, experimental facilities for condensing steam flows are in short supply throughout the world. Additionally, the measurements of some key parameters of these flows are very challenging, for example the droplet sizing measurements. Therefore, numerical study of condensing steam flows is necessary and feasible. Along with the experimental and theoretical studies, extensive numerical studies on condensing steam flow have also been done by numerous researchers on various aspects of it.

In the condensing steam flow, the flow is initially dry, but after reaching the Wilson point, liquid droplets are formed, and a two-phase flow is generated. The rapidly growing liquid droplets release latent heat to the surrounding vapour phase, which increases the flow temperature and pressure. The flow pressure rise is called the 'condensation disturbance' [1]. Some flow phenomena would affect the nucleation process such as viscous boundary layer and shock wave [2–5]. The condensing process is sensitive to the variation of local flow field as well as to the boundary conditions. Moreover, the blade profiles including the shape and thickness may have some influence on the condensing phenomena occurring in the LP turbine.

Many work have been done to analyze the aerodynamics of the LP turbine blades, for example Stein et al. [6] studied the impact of key geometrical features on the aerodynamic performance of transonic tip sections using CFD solvers. The geometrical features were subsonic overlap, supersonic overlap, trailing edge thickness, trailing edge wedge angle and camber distribution. Torre et al. [7] investigated the effect of airfoil thickness

on the efficiency of LP turbines experimentally in a multistage turbine high-speed rig. Zhou et al. [8] presented the effects of the blade trailing edge thickness on the profile loss of ultrahigh-lift low-pressure turbine blades using experimental, numerical and analytical methods. However, the published work on the effects of the trailing edge geometry in condensing steam flows and its corresponding influence on the loss mechanism is rather sparse. For example Singh [9] investigated numerically the effects of geometrical changes on the wetness generation in the blade profile of a LP turbine rotor blade cascade of Bakhtar et al. [10]. This work concluded that the geometrical changes including blade chord length have large effects on the amount of wetness generated. Also, An et al. [11] studied the effect of blade profile modification on the nucleation zone distribution and the degree of boundary layer separation in primary nucleation stage in the wet steam flows adopting Eulerian method. They altered the blade profiles by changing the blade curvature distribution of the profile. They concluded that the nucleation rate and the flow outlet angle were influenced by the blade modification.

The shapes and the size of the trailing edge of the turbine blades have strong effects on the pressure fields within the blade passage. Additionally, since the liquid phase generation is influenced by the local rate of change of the pressure fields, it can be expected that the trailing edge shapes would have significant effects on the droplet growths and other parameters. Therefore, the aim of this work is to investigate the influence of trailing edge geometries on the non-equilibrium homogeneously condensing steam flow in the stationary cascade of turbine blades using the Eulerian-Eulerian approach. For this purpose, three different trailing edge shapes are considered. The numerical results are compared and discussed with the experimental data of White et al. [12]. Moreover, the cascade loss coefficients are calculated for all the selected cases.

## 2 NUMERICAL METHODOLOGY

All the results presented in this paper have been obtained by means of the ANSYS Fluent 14.5 CFD code. The CFD simulations of two-phase vapour-liquid mixture were conducted by employing 2D steady state compressible Reynolds-averaged Navier-Stokes (RANS) equations based on the Eulerian-Eulerian approach. When modeling non-equilibrium flows, the prediction of nucleation and droplet growth rate are quite sensitive to the thermodynamic properties calculations. In the present work, the estimation of real gas properties was based on Young [13] formulations, in which the equation of state for the vapour phase utilizes a virial form with temperature and density as the independent variables. More details about the virial coefficients formulation and the constants values can be found from Young [13].

## 2.1 Governing equations

The governing equations of mass, momentum, and energy conservation for the mixture of vapour and liquid phases can be written as

$$\frac{\partial \rho}{\partial t} + \frac{\partial}{\partial x_i}(\rho u_i) = S_1, \quad (1)$$

$$\frac{\partial}{\partial t}(\rho u_i) + \frac{\partial}{\partial x_j}(\rho u_i u_j) = -\frac{\partial P}{\partial x_i} + \frac{\partial \tau_{ij}}{\partial x_j} + S_2, \quad (2)$$

$$\begin{aligned} \frac{\partial}{\partial t}(\rho H) + \frac{\partial}{\partial x_j}(\rho u_j H) = & \frac{\partial P}{\partial t} + \frac{\partial}{\partial x_j} \left( \Gamma_E \frac{\partial T}{\partial x_j} \right) \\ & + \frac{\partial}{\partial x_j}(u_i \tau_{ij}) + S_3, \end{aligned} \quad (3)$$

where  $i$  and  $j$  are the Cartesian tensor notations.  $\tau_{ij}$  represents the stress tensor components. In eq. (1), the source term  $S_1$  represents the mass transfer due to the condensation process or evaporation on the already existing droplet. The  $S_2$  term in eq. (2) is the momentum source term which includes the momentum exchange between the liquid droplets and the surrounding vapour, and the smaller terms from the gradient of the Reynolds stress tensor. In eq. (3), the source term  $S_3$  includes the interphase heat transfer. Moreover, two additional transport equations were solved for the liquid phase mass fraction, and the number of liquid droplets per unit volume, which can be written as following, respectively,

$$\frac{\partial \rho \beta}{\partial t} + \frac{\partial}{\partial x_i}(\rho u_i \beta) = \Gamma, \quad (4)$$

$$\frac{\partial \rho \eta}{\partial t} + \frac{\partial}{\partial x_i}(\rho u_i \eta) = \rho I, \quad (5)$$

where  $\Gamma$  is the mass generation rate per unit volume due to condensation and evaporation, and  $I$  is the nucleation rate. However, the following assumptions have been considered in the CFD code concerning the vapour-liquid mixture flow modeling; (i) the slip velocity between the liquid droplets and the vapour surrounding them was negligible, (ii) the condensed liquid phase consisted of droplets whose radii were on the order of  $1 \mu\text{m}$  or less, and therefore, it was assumed that the volume of the condensed liquid phase was negligible; and (iii) the interactions between droplets were omitted.

## 2.2 Nucleation and droplet growth model

The classical nucleation theory given by Frenkel [14] was adopted to model the homogeneous condensation phenomenon. The rate of the formation of liquid droplet embryos due to the homogeneous condensation per unit mass of the mixture was calculated as

$$I = \frac{q_c}{(1+\theta)} \left( \frac{\rho_v}{\rho_l} \right) \sqrt{\frac{2\sigma}{M^3 \pi}} e^{-\left( \frac{4\pi r_*^2 \sigma}{3k_b T} \right)}, \quad (6)$$

where  $q_c$  denotes the condensation coefficient that was assumed to be unity,  $M$  is the mass of a molecule,  $\sigma$  is the surface tension of the liquid phase,  $r_*$  is the Kelvin-Helmholtz critical droplet radius,  $k_b$  is Boltzmann's constant, and  $\theta$  is the non-isothermal correction coefficient.

The mass generation rate was obtained from Ishizaka et al. [15], and it can be written as

$$\Gamma = \frac{4}{3} \pi \rho_l I r_*^3 + 4\pi \rho_l \eta \bar{r}^2 \frac{\partial \bar{r}}{\partial t}. \quad (7)$$

The mass generation rate,  $\Gamma$ , was based on the sum of mass increase due to nucleation (the formation of critically sized droplets) and also due to the growth/demise of these droplets. In eq. (7),  $\bar{r}$  denotes the average radius of the liquid droplet, which was calculated based on the critical droplet size and the droplets growth. If the droplet radius is larger than  $r_*$ , it will grow; otherwise the droplet evaporates [16]. The critical droplet radius was calculated as

$$r_* = \frac{2\sigma}{\rho_l R T \ln S}, \quad (8)$$

where  $S$  is the super saturation ratio defined by the ratio of vapour pressure to the equilibrium saturation pressure. The droplet growth rate was estimated from the proposed formula of Hill [17], which can be defined as

$$\frac{\partial \bar{r}}{\partial t} = \frac{P}{h_{fg} \rho_l \sqrt{2\pi R T}} \frac{\gamma+1}{2\gamma} C_p (T_d - T), \quad (9)$$

where  $T_d$  is the droplet temperature. The details about droplet temperature calculation have been presented in Young [18].

## 2.3 Turbulence models

Previously, Patel et al. [19] presented the modified version of the shear-stress transport (SST)  $k$ - $\omega$  turbulence model of Menter [20] in which they modified the turbulent viscosity term of the

SST  $k$ - $\omega$  turbulence model, and also the source terms were included in both of the turbulence equations. The performance of modified SST  $k$ - $\omega$  model has been validated by Patel et al. [19] with three experimental cases of the turbine cascade of White et al. [12]. Therefore, in this study, the modified version of the SST  $k$ - $\omega$  turbulence model of Patel et al. [19] is used for modeling the flow turbulence. The equations of the turbulence kinetic energy  $k$ , and its specific dissipation rate  $\omega$  for the mixture of vapour and liquid phases can be written in the following form, respectively,

$$\frac{\partial}{\partial t}(\rho k) + \frac{\partial}{\partial x_i}(\rho k u_i) = \frac{\partial}{\partial x_j} \left[ \Gamma_k \frac{\partial k}{\partial x_j} \right] + \tilde{G}_k - Y_k + S_k \quad (10)$$

$$\frac{\partial}{\partial t}(\rho \omega) + \frac{\partial}{\partial x_i}(\rho \omega u_i) = \frac{\partial}{\partial x_j} \left[ \Gamma_\omega \frac{\partial \omega}{\partial x_j} \right] + \tilde{G}_\omega - Y_\omega + D_\omega + S_\omega, \quad (11)$$

where  $\Gamma_k$  and  $\Gamma_\omega$  are the effective diffusivities of  $k$  and  $\omega$ , respectively. In eqs. (10) and (11),  $\tilde{G}_k$  and  $\tilde{G}_\omega$  represent the generation of turbulence kinetic energy and its specific dissipation rate due to the mean velocity gradients, respectively. The terms  $Y_k$  and  $Y_\omega$  represent the dissipations of  $k$  and  $\omega$  due to turbulence, respectively.  $D_\omega$  is the cross-diffusion term.  $S_k$  and  $S_\omega$  are the source terms of the equations of turbulence kinetic energy, and its specific dissipation rate, respectively. Additional details pertaining to the model modifications can be found from Patel et al. [19].

### 3 NUMERICAL DETAILS

In this work, the steam turbine cascade of White et al. [12] has been selected as a reference case, which is the planar stator cascade of the fifth stage stator blade from the six-stage LP cylinder of a 660 MW steam turbine. The experiments of White et al. [12] are related to the flow in steam turbines in which there is an interaction between aerodynamics effects and the condensation process itself. These phenomena are absent in steady nozzle flows. White et al. [12] have provided experimental data for various test conditions.

There were four stator vanes in the experiments of White et al. [12]. In this work, only a single passage of the experimental facility has been modeled. Originally, the sharp trailing edge profile was used in the experiments. In the present work, three trailing edge geometries were considered: (i) conic trailing edge (CTE), (ii) semicircular trailing edge (RTE), and (iii) square trailing edge (STE), in order to check the influence of the trailing-edge shapes on the condensing steam flow field (Figure 1(a)). The RTE profile has at its end a circle of radius 0.8045

mm. The STE profile was approximated from the RTE profile. To generate the STE profile, the circle of RTE profile was cut at its centre in the axial direction with a  $15^\circ$  angle. The CTE profile has about an  $8^\circ$  angle between the suction surface and pressure surface. This angle has been generated by tapering the suction surface. If the total blade suction surface distance is defined between 0 and 1, in which 0 indicates the leading edge and 1 indicates the trailing edge. Based on this, the suction surface of the blade in the case of CTE was only tapered from 0.716 to 1. Therefore, the original throat area of the passage was unchanged for the CTE profile.

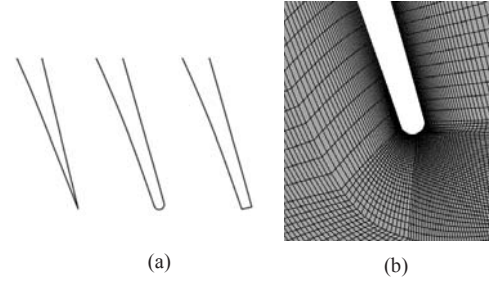


Figure 1. (a) Blade trailing edge geometries: conic trailing-edge (left), semicircular trailing-edge (middle) and square trailing-edge (right) (b) grid generation around semicircular trailing-edge case.

The 2D-structured grid has been generated in the computational domain for all the cases. Moreover, the O-grid around the blade surfaces were generated as shown in Figure 1(b). Sufficiently fine grid was constructed around the leading and trailing edges of the stator to resolve the boundary layers. Moreover, the grid density close to the wall boundaries was refined to achieve smaller  $y^+$  value. The computational grids of CTE case, RTE case, and STE case were contained around 39260, 40016, and 39875 cells. The sufficient grid density is essential to resolve the flow details [19]. In the present study, sufficiently finer grid is considered for all the cases. All the numerical calculations were performed with the steady state assumption. The conservation equations of the mixture of vapour and liquid phases were discretized applying the conservative finite-volume integration over a control volume with the multi-grid method. A second order upwind scheme was employed for the spatial discretization. The simulations presented in this work were converged to normalized RMS residuals of the order of  $10^{-4}$  or lower.

#### 4 RESULTS AND DISCUSSIONS

In the present work, the low inlet superheat experimental case named with L1 of White et al. [12] has been modeled. On the basis of the measurement data, L1 case with the inlet conditions  $P_{01} = 40.3$  kPa,  $T_{01} = 354$  K and outlet static pressure  $P_2 = 16.3$  kPa were selected. The inflow angle was  $0^\circ$ .

Figure 2 presents the comparison of the predicted pressure distribution around the blade surfaces with the experimental data of White et al. [12]. It shows that the static pressure distribution of the pressure side of the blade is not influenced with the trailing edge shapes. Moreover, all the cases modeled the correct location of the condensation. However, small discrepancy has been captured in the predicted pressure gradient on the suction side near the trailing edge between the selected trailing edge shapes. Particularly, the STE profile shows a slightly lower diffusion in the rear part of the blade. The predicted contours of static pres-

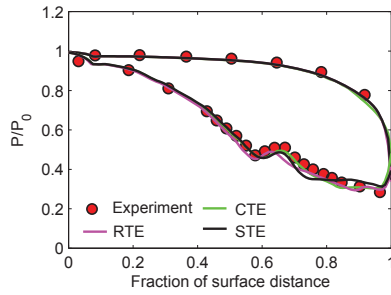


Figure 2. Blade surface pressure distribution comparison between predicted and measurements of White et al. [12].

sure by the CTE, the RTE, and the STE profiles are presented in Figure 3. It can be seen that the pressure distribution along the channel and in the downstream of passage is influenced with the trailing edge shapes. In the case of CTE profile the pressure distribution is influenced near the rear part of suction surface due to tapering. However, the highest expansion is observed in the cases of RTE particularly at the end of the pressure side (which is displayed with tiny region of blue colour). Therefore, the subcooling level is highest for the RTE profile which increases the nucleation rate. It has been known fact that the nucleating and growth processes are sensitive to the local pressure distribution and expansion rate [12]. The expansion rate varies in the blade passage, in which, it is relatively very low at the entrance and extremely high in the vicinity of the throat. As a consequence, the zone of rapid condensation occurs downstream of the throat, where the

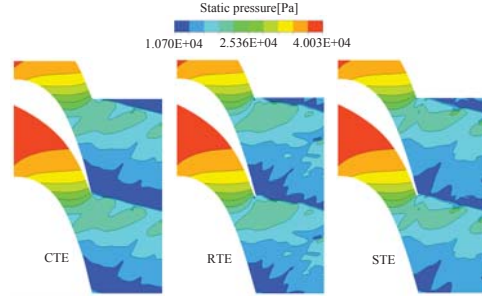


Figure 3. Predicted contours of the static pressure.

flow is bounded by solid surface. In condensing steam flows, the nucleation rate is especially large near the suction surface and at the trailing edge of the pressure surface. This happens due to the rapid acceleration and consequent high subcooling. Figure 4 shows the contours of the nucleation rate predicted by the CTE, the RTE, and the STE profiles. It can be seen that the nucleation

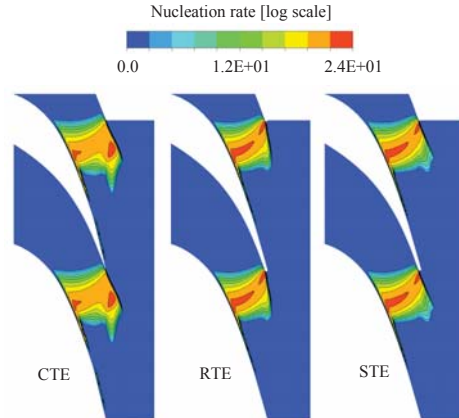


Figure 4. Predicted contours of the nucleation rate.

rate is smaller and the nucleation region is longer in the mid-pitch region for all the cases. Moreover, in the case of CTE, the nucleation zone is extended more to the wake region of the blade. This

is resulted due to the suction surface tapering because the flow area near the rear part of trailing edge for the CTE profile is enlarged. The highest nucleation rate is observed in the case of RTE and the lowest nucleation rate is noted in the case of CTE. The variation in the pressure and velocity distribution near the trailing edge would induce a different droplet number distribution. The droplet number in the blade wake is higher than that in the mainstream. This happens due to the rapid deflection of steam on the pressure surface near the trailing edge where nucleation rate reaches its peak value as shown in Figure 4. Therefore, the droplet number carried into the blade wake region is greater than that in the mainstream. The distinct nucleation rates influence on the total number of droplets via distinct droplet growth rates. Therefore, the droplets number per unit volume is calculated and presented in Figure 5 for all the cases. The droplets number per

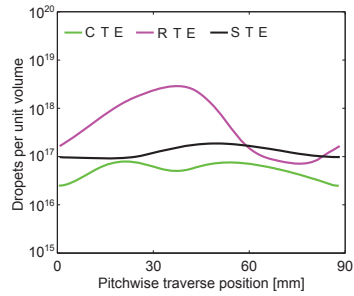


Figure 5. Predicted results of droplets per unit volume.

unit volume is estimated at the traverse plane which is situated at the position of one fourth axial chord length away from the trailing edge in axial flow direction. It can be seen that the RTE profile predicted higher number of droplets than the other profiles due to lower growth rates. It is a fact that the droplet radius distribution across the passage is mostly dependent on the total number of droplets created during the nucleation process, which is influenced by the distinct expansion rates along the blade passage and also due to the interaction between the trailing edge shock waves and the nucleation zone. The predicted contours of the average droplet radius for all cases are presented in Figure 6. A higher nucleation rate can be related to a lower growth rate, i.e. if a large number of tiny liquid droplets nucleate, their growth will be lower. On the other side, when a lower nucleation occurs, the growth rate is predominant and larger droplets are present. Therefore, the CTE predicted higher droplet radius compared to the RTE and the STE cases. The RTE profile estimated relatively

smaller droplet radius due to higher number of droplets per unit volume. Moreover, for all the cases, the droplet average radius is lower in the blade wakes. This appears because the temperature is relatively higher in the blade wakes, which prevents the droplet growth. This phenomenon yielded the cyclic patterns of the droplet sizes in the downstream of the flow.

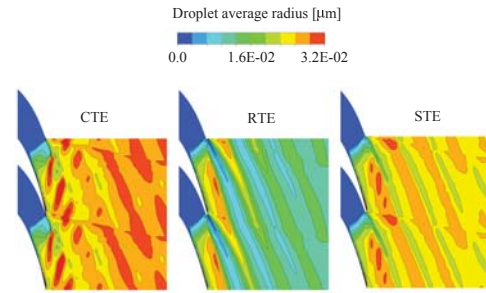


Figure 6. Predicted contours of droplet average radius.

Furthermore, the average droplet radius along the pitchwise traverse position at four different distances from the trailing edge of the blade has been compared (Figure 7). It is clear that the RTE profile has smaller sizes of droplets and the CTE profile has much larger droplet radii (nearly twice the value of the RTE profile). It is a fact that, the liquid phase generation is influenced by the local rate of change of the pressure fields. Perhaps it is worthwhile to check the influence of the trailing edge shapes on the wetness prediction. Therefore, the average wetness fractions predicted by the CTE, the RTE, and the STE profiles at downstream of the cascade were calculated and wetness trends are presented in Figure 8. It can be seen that the average wetness is decreased gradually as move to the downstream of the cascade for all cases. The average wetness fractions estimated by the CTE and the RTE are very similar. The STE profile predicted relatively higher wetness than the other profiles from the blade wake to the far downstream. However, at the outlet, marginal variation has been captured between all profiles. The explanation for the variation in the droplet sizes and the wetness fraction is associated with the rate of pressure change (expansion) in the flow field.

Figure 9(a) shows the Schlieren image of the L1 case, which is the reproduced image of the original experimental photograph of White et al. [12]. It has been adopted from Senoo and White [21]. In Figure 9(a), the condensation shock, pressure side shock, and suction side shock are marked with  $S_c$ ,  $S_p$ , and  $S_s$ , respectively. The red, orange, and yellow colours indicate the expansion

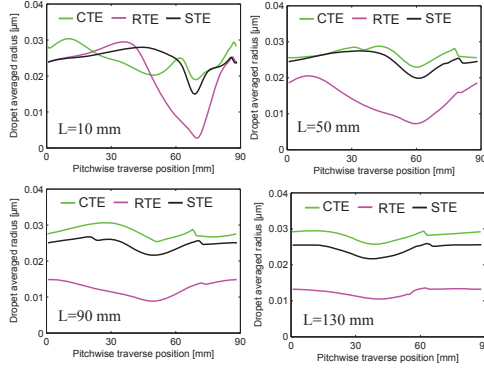


Figure 7. Predicted results of the droplet average radius at downstream of the cascade.  $L$  represents the distance from the trailing edge of the blade.

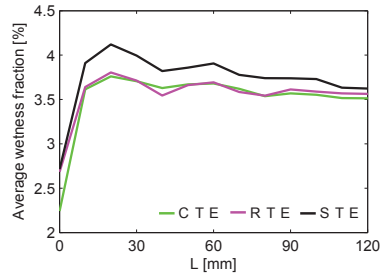


Figure 8. Predicted results of the average wetness fraction at downstream of the cascade.  $L$  is the distance from the trailing edge of the blade.

sion phenomenon, while light blue and green colours represent small values of the compression. It can be seen that the oblique shock profile is little bit curved across the central blade passage. The  $S_p$  interacts and merges with the  $S_c$  across the central blade passage. Moreover, the low base pressure is generated immediately behind the trailing edge, and the flow is expanded around the trailing edge, and then decompressed by a strong shock wave at the point where the suction and pressure side flows meet. This phenomenon is observed in all the cases of the predicted density gradient contours as well (Figure 9(b), (c), and (d)). However,

the intensity of  $S_p$  predicted by the CTE profile was marginally lower than those of the RTE and the STE profiles. In the case of RTE profile, the intensity of  $S_p$  is highest than other profiles which contributes to the suction side boundary layer generation. Moreover, in the cases of CTE and RTE, some reflections have been observed that interact with the  $S_s$ . However, these reflections were not generated from the outlet boundary but they were generated somewhere from the downstream. It seems that the wake is hitting to the reflected shockwave and which causing this disturbance. It may also be possible that the trailing shapes influence the shock waves structure generated at the trailing edge and its angles. It is slightly difficult to find exact information about the angles between them. However, in this work, the angle of  $S_s$  w.r.to blade wake has been calculated for all profiles, which are  $\theta_{CTE} \approx 48^\circ$ ,  $\theta_{RTE} \approx 52^\circ$ , and  $\theta_{STE} \approx 58^\circ$ . Here, the indicated subscripts CTE, RTE, and STE represents the corresponding profiles that are the CTE, the RTE, and the STE, respectively.

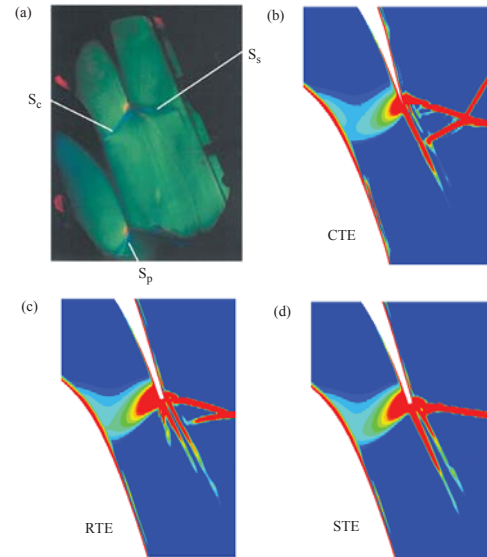


Figure 9. (a) Reproduced image of the original experimental photograph of Schlieren graph of the L1 case of White et al. [12] compared with predicted density gradients of the (b) CTE (c) RTE, and (d) STE cases.

In supersonic flow, there are some known influential phenomena for example shock waves, mixing, etc., which would

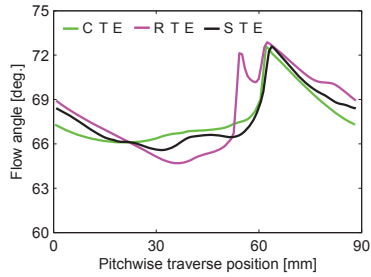


Figure 10. Predicted results of flow angle at the outlet of cascade.

have some impact on the flow angle. Therefore, the flow angle at the outlet of the cascade has been calculated and presented in Figure 10. It can be seen that the RTE profile predicted lower flow angle particularly in the wake region (i.e. between 25 mm to 40 mm at pitchwise traverse position in Figure 10), while the CTE profile yielded a higher value there. The maximum value of the flow angle in all the cases has been captured at about 70 mm at pitchwise traverse position due to shockwave interaction.

In addition, White et al. [12] provided test data of the static pressure, wetness fraction, and normalized entropy at a specific location at downstream. Therefore, it is possible to compare the predicted and the experimental results at traverse plane. The traverse plane is situated at the position of one fourth axial chord length away from the trailing edge in axial flow direction (see Figure 11 (upper most)). The predicted pitchwise distribution of the static pressure, wetness fraction, and normalized entropy at the traverse position are compared with the experimental data in Figure 11. The predicted trends are in good agreement with the experiments. However, for all profiles, the steep location has been changed in the static pressure and wetness fraction between 75 mm to 85 mm due to the interaction of the shock wave  $S_3$  at the traverse plane. Also, the variation in the steep location in each cases resulted due to dissimilarity in the shock wave angle as discussed above. The wetness fraction is relatively lower between 35 mm to 45 mm at the traverse position because in this region the trailing edge wake flow passes the traverse plane. This is the region of higher mixing. Therefore, temperature is comparatively higher, which causes a lower wetness fraction. Generally good trends of non-dimensional entropy have been captured by all trailing edge profiles with the experiments of White et al. [12]. However, some discrepancy has been observed between the predicted results, particularly in the wake region. The CTE profile has a lower value of non-dimensional entropy than the RTE and STE profiles.

The entropy generation occurs due to three main processes:

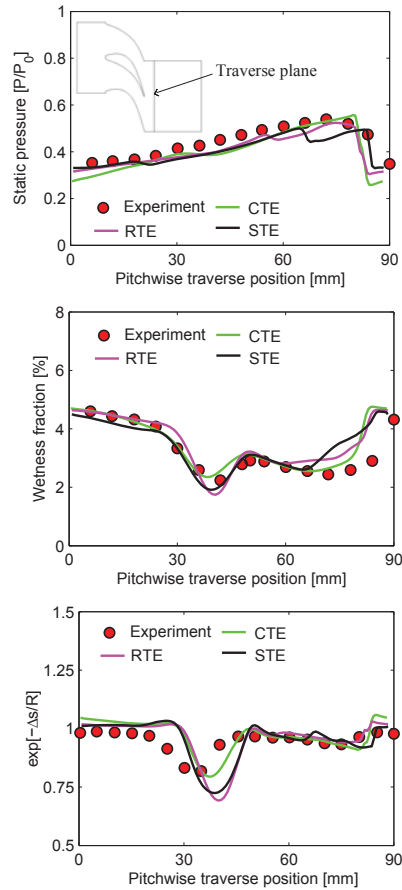


Figure 11. Predicted results of static pressure (upper), wetness fraction (middle), non-dimensional entropy (lower) compared with the experiments of White et al. [12].

(i) viscous friction (either in boundary layers or in free shear layers), (ii) heat transfer, and (iii) non-equilibrium processes (occur in very rapid expansions or in shock waves) [22]. Regarding to the entropy generation and flow mixing in the wake, the trailing edge shape is one of the main parameters. Figure 12 shows the

contours of the turbulent kinetic energy predicted by the CTE, the RTE, and the STE profiles. It is a fact that the STE profile has relatively higher turbulent kinetic energy due to strong wake than the RTE profile, while the CTE profile predicted very low turbulent kinetic energy. The turbulent kinetic energy in the wake region will subsequently dissipate by viscous effects. Moreover, the flow mixing contributes to the entropy generation. Therefore, the local entropy generation rates are considerably high in the wakes, at the edges of separated regions, and in vortices, in which the shearing rates are relatively high. Figure 13 shows the predicted contours of entropy for all cases. It appears that the CTE profile predicted the lowest entropy generation compared to other cases.

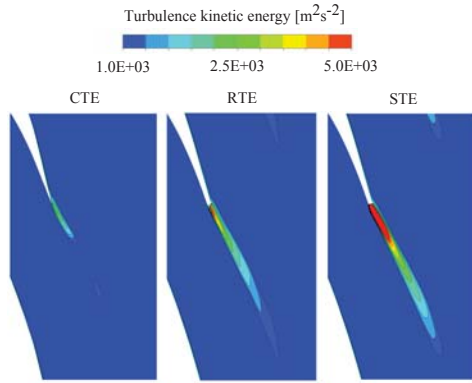


Figure 12. Predicted contours of turbulence kinetic energy.

The prime objective of turbomachinery designers is to improve the performance by increasing the efficiency. Any cutback in the efficiency of turbomachinery caused by the flow is termed loss. One objective of this paper was to analyze the influence of trailing edge shapes on the loss mechanism of condensing steam flow. Moreover, White et al. [12] presented information about the losses that occur due to the irreversible heat and mass transfer during the condensation process. Therefore, in the present work, the Markov energy loss coefficient based on the entropy increase has been calculated. The Markov energy loss coefficient is defined as  $\zeta = \frac{T_2 \Delta s}{0.5 v_2^2}$ . White et al. [12] divided the loss coefficients into three components: (i) viscous loss, (ii) shockwave plus wetness loss, and (iii) mixing loss. Detailed information pertaining to the losses evaluation can be found from White et al. [12]. Figure 14 presents the comparison between the com-

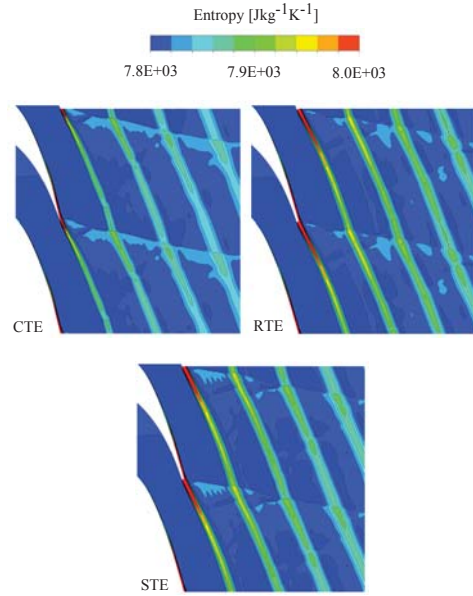


Figure 13. Predicted contours of entropy.

puted and measured Markov loss coefficients for L1 case and H3 case. The H3 case is the high inlet superheat case that has  $\Delta T_{01} = 26.0$  K. The inlet conditions of H3 case were  $P_{01} = 41.4$  kPa and  $T_{01} = 376$  K, while the outlet static pressure,  $P_2$ , was 19.4 kPa. The main purpose for H3 case selection was to check the influence of the trailing edge profiles on the losses.

The magnitude of mixing loss increases with high Mach numbers. Therefore, the mixing loss of the L1 case is relatively higher than the H3 case. As presented before that the  $S_p$  merges with the  $S_c$ , and it thickens the suction side boundary layer onto the suction side of the adjacent blade. Therefore, it increases the viscous losses. The intensity of  $S_p$  shock wave for the RTE profile is relatively higher than other cases. This could be the explanation of higher viscous loss prediction in the case of RTE profile. It can be seen that the CTE profile predicted low value of shock plus wetness loss than the RTE and STE profiles both for L1 and H3 cases. It is interesting to note that the magnitude of shock plus wetness losses predicted by the RTE and STE profiles for L1 and H3 cases are almost in the same range. Moreover, it is observed that the value of the mixing loss for the STE profile was higher due to stronger wake than those of the other profiles. The

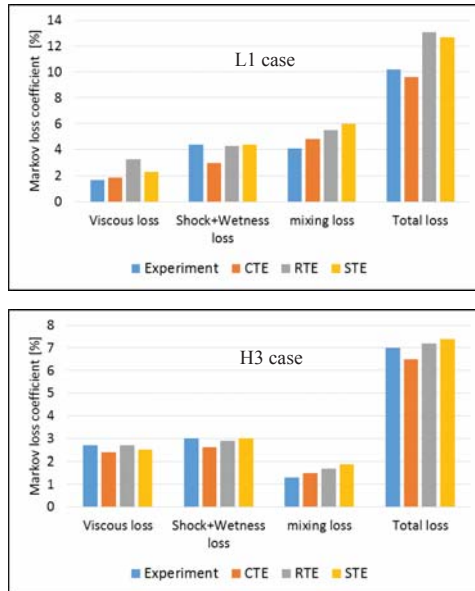


Figure 14. Predicted Markov loss coefficients compared with the experiments of White et al. [12].

explanation for the higher value of mixing loss in the STE profile is associated with the higher entropy generation in the wake region as shown in Figure 13. The CTE profile predicted relatively smaller total loss than the RTE and STE profiles for L1 and H3 cases.

## 5 CONCLUSIONS

This study emphasized the influence of the trailing edge geometry on the non-equilibrium homogeneously condensing steam flow in the stationary cascade of turbine blades. The experimental test cases of White et al. [12] were used as the reference. In this study, the two-phase vapour-liquid mixture was modeled adopting the Eulerian-Eulerian approach by means of ANSYS Fluent 14.5 CFD code. The condensation phenomena were simulated on the basis of the classical nucleation theory, and the steam properties were calculated by the real gas model.

Three trailing edge geometries were considered. The conic trailing edge was generated with  $8^\circ$  degree wedge angle by tapering the suction surface. The presented analysis exhibits that

the conic trailing edge has a very different pressure gradient particularly at the suction surface near trailing edge which makes the biggest contribution to the nucleation rate. Based on the presented results, it can be concluded that the nucleation region and nucleation rate have been influenced due to the variation in trailing edge geometries. Moreover, the droplet sizes are much sensitive to the trailing edge shapes. The conic trailing edge estimated bigger droplet radius than the other cases, while semi-circular trailing edge predicted the smallest droplet sizes. The trailing shapes influenced also on the wetness fraction, on the shock waves structure generated at the trailing edge and its angles, and on the flow angle. Additionally the entropy generation and flow mixing in the wake were influenced due to the trailing edge shapes.

Based on the presented information of the losses by White et al. [12], the Markov energy loss coefficients were calculated for the low inlet superheat case and for the high inlet superheat case. It can be concluded that the cascade loss coefficients are sensitive to the trailing edge shapes. The conic trailing edge predicted lower value of total loss than other selected shapes.

Further work will concentrate on the influence of the pressure surface tapering in the case of turbine cascade flow. Also the influence of the trailing edge thickness, its size and shape in the case of stator-rotor turbine cascade flows will be studied.

## ACKNOWLEDGEMENTS

The authors would like to acknowledge the Finnish Cultural Foundation and Academy of Finland for the financial support.

## REFERENCES

- [1] Wegener, P. P., 1975. *Non-equilibrium Flow with Condensation*. Acta Mech. 21 (1-2), pp. 65-91.
- [2] Simpson, D. A., and White, A. J., 2005. "Viscous and unsteady-flow calculations of condensing steam in nozzles". *Int. J. Heat and Fluid Flow*, Vol. 26 (1), pp. 71-79.
- [3] White, A., 2000. "Numerical investigation of condensing steam flow in boundary layers". *Int. J. Heat and Fluid Flow*, Vol. 21, pp. 727-734.
- [4] Winkler, G., and Schnerr, G., 2001. "Nucleating unsteady flows in low-pressure steam turbine stages". *Proc. Instn. Mech. Eng.*, Vol. 215 (A), pp. 773-781.
- [5] Kermani, M., and Gerber, A., 2003. "A general formula for the evaluation of thermodynamic and aerodynamic losses in nucleating steam flow". *Int. J. Heat Mass Transfer*, Vol. 46 (17), pp. 3265-3278.
- [6] Stein, A., Hofer, D. C., Filippenko, V., and Slepski, J., 2010. "Aerodynamic design of transonic tip sections". In Proc. ASME Turbo Expo, GT2010-22165, Glasgow, UK, June 14-18, pp. 1-10.

- [7] D.Torre, Vázquez, R., Armañanzas, L., Partida, F., and García-Valdecasas, G., 2012. “The effect of airfoil thickness on the efficiency of lp turbines”. In Proc. of ASME Turbo Expo, GT2012-68556, Copenhagen, Denmark, June 11-15, pp. 1-10.
- [8] Zhou, C., Hodson, H., and Himmel, C., 2014. “The effects of trailing edge thickness on the losses of ultrahigh lift low pressure turbine blades”. *J. Turbomach.*, **Vol. 136** (8), pp. 081011–1–9.
- [9] Singh, U., 2001. “A study of the effects of geometrical changes on wetness in low pressure steam turbine”. In The 4th European Conference on Turbomachinery, Firenze, Italy, pp. 823-841.
- [10] Bakhtar, F., Ebrahimi, M., and Webb, R., 1995. “On the performance of a cascade of turbine rotor tip section blading in nucleating steam, part 1: surface pressure distributions”. *Proc. Inst. Mech. Eng. Part C: J. Mech. Eng. Sci.*, **Vol. 209**, pp. 115–124.
- [11] An, L., Wang, Z., and Han, Z., 2009. “Numerical study and control method of interaction of nucleation and boundary layer separation in condensing flow”. *Front. Energy Power Eng. China*, **Vol. 3** (3), pp. 254–261.
- [12] White, A. J., Young, J. B., and Walters, P. T., 1996. “Experimental validation of condensing flow theory for a stationary cascade of steam turbine blade”. *Philos. Trans. Roy. Soc. Lond.*, **Vol. A 354**, pp. 59–88.
- [13] Young, J. B., 1988. “An equation of state for steam for turbomachinery and other flow calculations”. *J. Eng. Gas Turbines Power*, **Vol. 110**, pp. 1–7.
- [14] Frenkel, J., 1946. *Kinetic Theory of Liquids*. Oxford University Press, New York.
- [15] Ishizaka, K., Ikohagi, T., and Daiguji, D., 1995. “A high-resolution numerical method for transonic nonequilibrium condensation flows through a steam turbine cascade”. In Proc. of 6th International Symposium on Computational Fluid Dynamics, pp. 479-484.
- [16] Young, J. B., 1992. “Two-Dimensional nonequilibrium wet steam calculations for nozzles and turbine cascades”. *ASME J. Turbomachinery*, **Vol. 114**, pp. 569–579.
- [17] Hill, P. G., 1966. “Condensation of water vapour during supersonic expansion in nozzles”. *J. Fluid Mech.*, **Vol. 25**, pp. 593–620.
- [18] Young, J. B., 1982. “The spontaneous condensation of steam in supersonic nozzles”. *Physico Chemical Hydrodynamics*, **Vol. 3**, pp. 57–82.
- [19] Patel, Y., Turunen-Saaresti, T., Patel, G., and Grönman, A., 2014. “Numerical investigation of turbulence modelling on condensing steam flows in turbine cascade”. In Proc. of ASME Turbo Expo, GT2014-26307, Düsseldorf, Germany, June 16-20, pp. 1-14.
- [20] Menter, F. R., 1994. “Two-equation eddy-viscosity turbulence models for engineering applications”. *AIAA Journal*, **Vol. 32** (8), pp. 1598–1605.
- [21] Senoo, S., and White, A. J., 2012. “Non-equilibrium unsteady wet-steam condensation modelling: computations in a steam turbine cascade and a nozzle”. In Proc. The Cambridge Baumann Centenary Conference on Wet Steam Flows, BCC-2012-07, University of Cambridge, CD-ROM.
- [22] Denton, J. B., 1993. “Loss mechanisms in turbomachines”. *ASME J. Turbomachinery*, **Vol. 115**, pp. 621–650.



## **Publication VI**

Patel, Y., Patel, G., and Turunen-Saaresti, T. (2016).  
**Influence of turbulence modelling to condensing steam flow in the  
3D low-pressure steam turbine stage.**

Proceedings of ASME Turbo Expo 2016:  
Turbomachinery Technical Conference and Exposition.  
pp. 1-11.

© ASME, 2016

Reprinted with permission from the publisher



GT2016-57590

INFLUENCE OF TURBULENCE MODELLING TO CONDENSING STEAM FLOW IN  
THE 3D LOW-PRESSURE STEAM TURBINE STAGE

<b>Yogini Patel*</b> Laboratory of Fluid Dynamics School of Energy Systems Lappeenranta University of Technology Lappeenranta, Finland Email: yogini.patel@lut.fi	<b>Giteshkumar Patel</b> Laboratory of Fluid Dynamics School of Energy Systems Lappeenranta University of Technology Lappeenranta, Finland Email: giteshkumar.patel@lut.fi	<b>Teemu Turunen-Saaresti</b> Laboratory of Fluid Dynamics School of Energy Systems Lappeenranta University of Technology Lappeenranta, Finland Email: teemu.turunen-saaresti@lut.fi
--	---	---

ABSTRACT

*With the tremendous role played by steam turbines in power generation cycle, it is essential to understand the flow field of condensing steam flow in a steam turbine to design an energy efficient turbine because condensation at low pressure (LP) turbine introduces extra losses, and erosion in turbine blades. The turbulence has a leading role in condensing phenomena which involve a rapid change of mass, momentum and heat transfer. The paper presents the influence of turbulence modelling on non-equilibrium condensing steam flows in a LP steam turbine stage adopting CFD code. The simulations were conducted using the Eulerian-Eulerian approach, based on Reynolds-averaged Navier-Stokes equations coupled with a two equation turbulence model, which is included with nucleation and droplet growth model for the liquid phase. The SST  $k-\omega$  model was modified, and the modifications were implemented in the CFD code. First, the performance of the modified model is validated with nozzles and turbine cascade cases. The effect of turbulence modelling on the wet-steam properties and the loss mechanism for the 3D stator-rotor stage is discussed. The presented results show that an accurate computational prediction of condensing steam flow requires the turbulence to be modelled accurately.*

\*Corresponding author

Nomenclature

$h_{lv}$	specific enthalpy ( $\text{J kg}^{-1}$ )
$H$	total enthalpy ( $\text{J kg}^{-1}$ )
$I$	nucleation rate ( $\text{m}^{-3} \text{s}^{-1}$ )
$M$	mass generation rate ( $\text{kg m}^{-3} \text{s}^{-1}$ )
$M_m$	droplet mass (kg)
$P$	pressure (Pa)
$r$	radius (m)
$r_*$	critical radius (m)
$R$	gas constant ( $\text{J kg}^{-1} \text{K}^{-1}$ )
$S_d$	mass source term ( $\text{kg m}^{-2} \text{s}^{-1}$ )
$S_E$	energy source term ( $\text{W m}^{-3}$ )
$S_{F,m}$	momentum source term ( $\text{kg m}^{-2} \text{s}^{-2}$ )
$t$	time (s)
$T$	temperature (K)
$u$	velocity component ( $\text{m s}^{-1}$ )

Greek Letters

$\alpha$	phase volume fraction
$\Gamma_E$	thermal diffusion coefficient ( $\text{W m}^{-1} \text{K}^{-1}$ )
$\eta$	number of liquid droplets per unit volume ( $\text{m}^{-3}$ )
$\mu$	dynamic viscosity ( $\text{kg/m}\cdot\text{s}$ )
$\rho$	density ( $\text{kg m}^{-3}$ )
$\sigma$	liquid surface tension ( $\text{N m}^{-1}$ )
$\tau$	viscous stress tensor (Pa)
$\tau_p$	droplet response time (s)

## Subscript

$d$	droplet index
$i, j$	cartesian tensor notation
$l$	liquid phase
$v$	vapour phase
$x$	cartesian coordinate
$0, 1, 2$	total, inlet, outlet conditions

## 1 INTRODUCTION

Today, steam turbines play an important role in the global power production. Thus, the advancement and understanding of technologies relevant to enhancing the general performance of steam turbines is important in order to meet the global electricity demand. However, due to the comparatively low efficiency of low pressure (LP) turbine stages, the research concerning LP stages is of special importance for the scientific community, steam turbine vendors and power plant owners. Particularly, in penultimate stages of LP turbine, the temperature of superheated vapour decreases due to rapid expansion and a condensation process takes place shortly after the state path crosses the vapour-saturation line. The expansion process causes the superheated dry steam to first subcool and then nucleate to form a two-phase mixture of saturated vapour and fine liquid droplets which is generally known as wet-steam. The presence of the liquid phase within the turbine causes irreversible thermodynamic losses, aerodynamic losses and mechanical losses or erosion. For more than a century, extensive studies of condensing steam flows have been executed by numerous researchers experimentally, theoretically and numerically. However, the experimental facilities for wet-steam flows are in short supply throughout the world. Additionally, the precise measuring of essential parameters (e.g., droplet size and its distribution, wetness fraction, etc) of these flows is very challenging and, therefore, the numerical simulations of the condensing steam flows are the most feasible option.

Turbine flows involve very intricate flow phenomena including flow transition, flow separation and mixing due to stator-rotor interaction, and turbulence is involved in all these phenomena. Moreover, the role of turbulence in wet-steam flows is significant in the processes of phase change, momentum and heat transport either at main flow regions or in boundary layers on the solid walls, particularly on the possible deposition of condensed liquid droplets. Consequently, it is essential to simulate turbulence in wet-steam flow precisely, as the ignorance of turbulence modelling to condensing steam flow calculation may cause an erroneous appraisal of key phenomena and eventually result in the modelling of erroneous losses.

In recent years, 3D numerical modelling of wet-steam flow across LP turbine including multistage blade rows has become feasible because of immense improvement in computational power for computational fluid dynamics (CFD) cal-

culations. Nevertheless, in literature the work regarding 3D steady/unsteady CFD simulations is rather sparse. A few works e.g., [1] and [2], exists, in which CFD simulations on condensing steam flows through multistage stator-rotor cascade channels of a LP steam turbine with non-equilibrium and equilibrium condensations are presented. [3] presented numerical results of wet-steam flow with a three stage LP steam turbine test rig, in which the effect of different theoretical models for nucleation and droplet growth were examined. Further, the effect of droplet size on the deposition characteristics of the last stage stator blade and also the effect of inter-phase friction on flow field were studied by [4]. However, reported work concerning the influence of turbulence on the condensing steam flow at 3D turbine stage/stages is not available. Only few publications are available e.g., [5] and [6] in which authors conducted an analysis of turbulence modelling influence to wet-steam flow considering 2D nozzles and stator turbine cascade.

This work is the continuation of the previous works. In previous studies of [7], the influence of turbulence modelling to 2D nozzle and stator cascade flows was analyzed. Also, its corresponding influence on loss mechanism was presented. In the present work, the numerical investigation of turbulence modelling effect on condensation phenomena is extended to 3D stator-rotor stage. For this purpose, only steady state simulations were performed using a mixing plane as interface between stator and rotor domain by neglecting the interaction between the stator wakes and the rotor blade. The Eulerian-Eulerian approach has been used to model two-phase flow. In this work, the performance of modified shear-stress transport (SST)  $k-\omega$  turbulence model is demonstrated with the SST  $k-\omega$  turbulence model. The significance of turbulence modelling on the loss mechanism in 3D stator-rotor stage is discussed as well.

## 2 NUMERICAL METHODOLOGY

In this paper, all the presented results were obtained by means of the ANSYS CFX. The real gas properties were evaluated from the IAPWS-IF97 formulation in which the thermodynamic properties of steam in the subcooled region were calculated by means of extrapolations from the superheated region.

### 2.1 Governing equations

The mass conservation equations for vapour and liquid phases are written as follows, respectively,

$$\frac{\partial}{\partial t}(\rho_v \alpha_v) + \frac{\partial}{\partial x_j}(\rho_v \alpha_v u_{jv}) = - \sum_{d=1}^D S_d - \sum_{d=1}^D m^* \alpha_v I_d, \quad (1)$$

$$\frac{\partial}{\partial t}(\rho_l \alpha_l) + \frac{\partial}{\partial x_j}(\rho_l \alpha_l u_{jl}) = \sum_{d=1}^D S_d + \sum_{d=1}^D m^* \alpha_v I_d. \quad (2)$$

Here,  $m^*$  is the mass of stable nucleus. To estimate liquid phase, a separate equation was used to calculate droplet numbers which can be written as

$$\frac{\partial}{\partial t}(\rho_l \eta) + \frac{\partial}{\partial x_j}(\rho_l \eta u_{jl}) = \rho_l \alpha_v I_l. \quad (3)$$

In an LP turbine, more than 90% of the total mass concentration of the liquid phase consists of a very large number of very fine droplets having sub-micron size [8]. However, due to the negligible drag effect of liquid droplets on vapour phase it could be considered that all the phases flow at the identical velocity field. Therefore, in this work, only one momentum equation was used. The momentum equation of vapour phase was based on the Reynolds-averaged Navier-Stokes (RANS) equations which can be written as

$$\frac{\partial}{\partial t}(\rho_v \alpha_v u_{iv}) + \frac{\partial}{\partial x_j}(\rho_v \alpha_v u_{iv} u_{jv}) = -\alpha_v \frac{\partial P}{\partial x_i} + \frac{\partial}{\partial x_j}(\alpha_v \tau_{ijv}) + S_{F,m}. \quad (4)$$

The energy conservation equation for the vapour phase was written as

$$\frac{\partial}{\partial t}(\rho_v \alpha_v H_v) + \frac{\partial}{\partial x_j}(\rho_v \alpha_v u_{jv} H_v) = -\alpha_v \frac{\partial P}{\partial t} + \frac{\partial}{\partial x_j}(\alpha_v \Gamma_E \frac{\partial T_v}{\partial x_j}) + \frac{\partial}{\partial x_j}(\alpha_v u_{iv} \tau_{ijv}) + S_E. \quad (5)$$

More details pertaining to the governing equations and their source terms can be found in [9].

## 2.2 Nucleation and droplet growth model

The phase change phenomenon in condensing steam flow involves two main processes viz., nucleation and droplet growth. In this work, the nucleation rate was obtained from the classical theory of non-isothermal homogeneous condensation given by [10] which can be written as,

$$I = \frac{q_c}{(1+\theta)} \left( \frac{\rho_v^2}{\rho_l} \right) \sqrt{\frac{2\sigma}{M_m^3 \pi}} e^{-\left( \frac{4\pi r_0^2 \sigma}{3k_b T} \right)}. \quad (6)$$

Here,  $q_c$  is a condensation coefficient,  $K_b$  is the Boltzmann's constant and  $\theta$  is the non-isothermal correction factor which has been

adopted from [11]. The droplet growth rate equation of [12] was utilised and can be expressed as,

$$\frac{dr}{dt} = \frac{k_v}{r(1+cK_n)} \cdot \frac{(T_l - T_v)}{(h_v - h_l)\rho_l}, \quad (7)$$

where,  $K_n$  is the Knudsen number,  $c$  is the empirical factor, which is 3.18, and  $k_v$  is the thermal conductivity. More details on droplet growth rate can be found in [9].

## 2.3 Turbulence models

In the present work, the SST  $k$ - $\omega$  turbulence model was employed for modelling the flow turbulence. Due to the very small sizes of droplets in the vapour phase, the direct effect of liquid droplets on the flow turbulence was not considered. However, an indirect influence exists though the velocity field introduced to the turbulence models. Particularly, the vapour phase turbulence could influence the dispersion of the liquid droplets. Due to the relatively small mass concentrations and sizes of droplets, the turbulence equations were calculated for the mixture of the vapour and liquid phases. The transport equations for the turbulent kinetic energy,  $k$ , and its specific rate of dissipation,  $\omega$ , can be written as [13],

$$\frac{\partial}{\partial t}(\rho k) + \frac{\partial}{\partial x_j}(\rho u_j k) = \frac{\partial}{\partial x_j} \left[ \left( \mu + \frac{\mu_t}{\sigma_k} \right) \frac{\partial k}{\partial x_j} \right] + P_k - \beta \rho k \omega + P_{kb} + S_k, \quad (8)$$

$$\frac{\partial}{\partial t}(\rho \omega) + \frac{\partial}{\partial x_j}(\rho u_j \omega) = \frac{\partial}{\partial x_j} \left[ \left( \mu + \frac{\mu_t}{\sigma_\omega} \right) \frac{\partial \omega}{\partial x_j} \right] + \alpha \frac{\omega}{k} P_k - \beta \rho \omega^2 + P_{\omega b} + S_\omega. \quad (9)$$

Here,  $P_k$  indicates the production rate of turbulence due to viscous forces,  $P_{kb}$  and  $P_{k\omega}$  represent the buoyancy turbulence terms for  $k$  and  $\omega$  equations, respectively. The model constants were considered as:  $\alpha = \frac{5}{9}$ ,  $\beta = 0.075$ ,  $\beta = 0.09$ ,  $\sigma_k = 2$ , and  $\sigma_\omega = 2$ . The turbulent viscosity,  $\mu_t$ , is defined in the SST  $k$ - $\omega$  turbulence model as

$$\mu_t = \frac{a_1 \rho k}{\max(a_1 \omega, S F_2)}, \quad (10)$$

where  $a_1$  is the model constant,  $S$  is the strain rate magnitude and  $F_2$  is the blending functions. In this work, the SST  $k$ - $\omega$  turbulence model was modified in the manner described in the previous work of [7]. The SST  $k$ - $\omega$  turbulence model was modified

to include the modulation of turbulence kinetic energy due to liquid droplets via source terms (i.e.,  $S_k$  and  $S_\omega$  in Eqs. (8) and (9), respectively). Therefore, the added source terms introduce an extra turbulent kinetic energy and its dissipation to the flow via the acceleration/deceleration of the droplets. These modifications directly influence on turbulent viscosity and Reynolds stresses. In such a way momentum and energy transport equations will be affected. Furthermore, the definition of  $\mu_t$  was modified by means of an expansion procedure for resolving implicit algebraic equations for the Reynolds stress tensor in terms of mean velocity gradients. The modified turbulent viscosity term including turbulence production to dissipation ratio can be written as

$$\mu_t = \frac{a_1 \rho k}{\max(a_1 \omega, SF_2)} \frac{C_1}{C_1 + \left[ \frac{P_k}{\omega \beta^* k} - 1 \right]}, \quad (11)$$

where  $C_1$  defines the Rotta return-to-isotropy approximation of the pressure-strain correlation. Here  $S_k$  represents the addition of turbulent kinetic energy including the effect of liquid mass generation and droplet response time which can be expressed as  $S_k = \frac{4M}{\tau_p} (1 - f_u) k$ , where  $f_u$  indicates the coefficient of droplet response to the fluid velocity fluctuations. The term  $S_\omega$  can be written as  $S_\omega = C_2 \omega \beta^* S_k$ , where  $C_2$  and  $\beta^*$  are the model constants. More details about model constants and corresponding closer relations of these modification are discussed in [7]. The abovementioned modifications were implemented by the authors within the CFD code using user defined subroutines.

### 3 COMPUTATIONAL GRID AND NUMERICAL DETAILS

To study the influence of turbulence modelling on condensing steam flow in a LP turbine, a 3D stator-rotor stage was used. The used stator vane is the stator cascade of White [14]. However, the utilised rotor blade is not that of a real turbine geometry. It was intended to be representative of 25% of reaction for rotor at mid span. The stator blade row consisted of 30 blades while the rotor blade row included 31 blades. The blade height of stator and rotor outlet was 76 mm and 126.5 mm, respectively. However, for the sake of simplicity, both blade profiles had constant radial thickness without twisting. Moreover, the domain was modelled without rotor tip clearance in order to exclude the influence of tip swirls on the flow. The flow inlet condition was set as:  $P_0 = 40300$  Pa,  $T_0 = 354$  K which are the similar inlet flow conditions as of [14]. Only single passage of stator and rotor was modelled employing a periodic boundary condition in the circumferential direction. An adiabatic no-slip wall boundary was defined at the blade surfaces and at the domain walls. The computational grid is displayed in Figure 1. The grid quality/density near solid boundaries is very important to precisely resolve boundary layers. Therefore, the grid distribution near the solid surfaces was fine enough to achieve sufficiently smaller  $y^+$

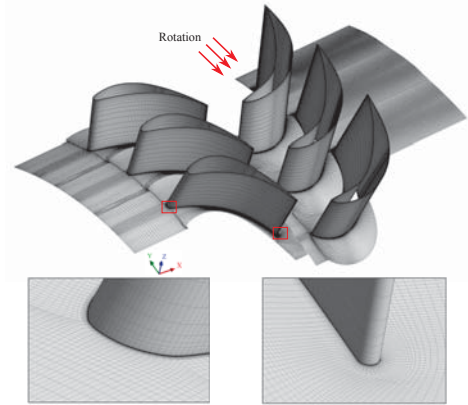


Figure 1. The computational grid.

value i.e.  $y_{stator}^+ = 3.5$  and  $y_{rotor}^+ = 2.5$ . An O-grid was generated near to the blade surfaces with boundary layers meshing. Moreover, the grid was more refined around the leading and trailing edges of the stator and rotor blades. Based on the previous experiences of the conducted grid independence study for 2D stator cascade case, an adequate grid refinement was assumed for this case. The computational grid included about 2.87 million hexahedral cells. All the simulations were based on finite-volume discretization and the solution of the RANS equations was done with a coupled solver. The advection was treated with high resolution scheme. Furthermore, flow turbulence models, volume fraction and energy equations were calculated using high resolution methodology. An automatic wall treatment was utilised, which provides an automatic switching from a low-Reynolds number formulation to a wall function treatment based on grid spacing near to the wall surfaces.

### 4 RESULTS AND DISCUSSIONS

Firstly, the performance of SST  $k-\omega$  and modified SST  $k-\omega$  (MSST  $k-\omega$ ) turbulence models were examined with the nozzle cases of [15] and [16], and also with the steam turbine stator cascade case of [14]. In Figure 2, it can be seen that both models predicted accurate pressure distributions, and the location and magnitude of the condensation shock, and yielded good correspondence with the experiments for both nozzles. Furthermore, the agreement between the predicted and the measured mean droplet radius size at the specified exit location is reasonably good for the Nozzle A of [15] for both models. However, some variation has been observed for the [16] nozzle case.

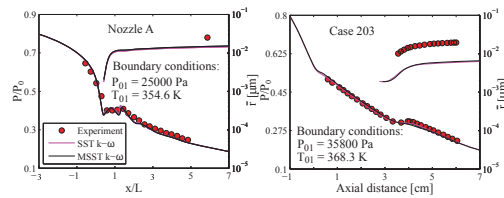


Figure 2. Comparison between the predicted and the measured data of [15] (left) and [16] (right).

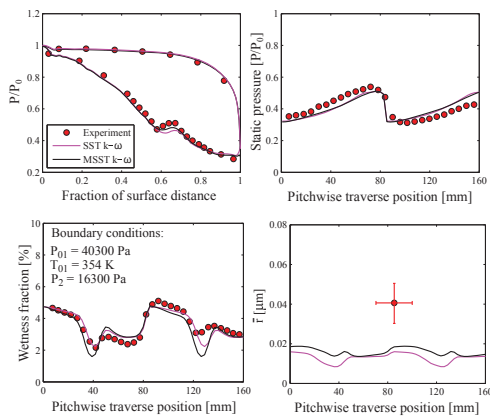


Figure 3. Comparison between the predicted and the measured data of [14] for the L1 case.

Further, the low inlet superheat experimental case named L1 of [14] has been modelled. The comparison between the predicted results of the SST  $k-\omega$  model, the MSST  $k-\omega$  model and the measured data is shown in Figure 3. The traverse plane is situated at the position of one fourth axial chord length from the trailing edge in axial flow direction. It can be seen that both models yielded correct trends of pressure distribution on blade surfaces. However, the MSST  $k-\omega$  model estimated the correct location and intensity of the condensation disturbance on the suction side compared to the SST  $k-\omega$  model. The predicted trends of static pressure and wetness fraction at traverse plane by both models are in good agreement with the experiments. Nevertheless, some discrepancy has been noted for mean droplet radius prediction.

It is fact that the flow in LP turbine has a strong three-dimensional nature due to the arrangements of stator and rotor

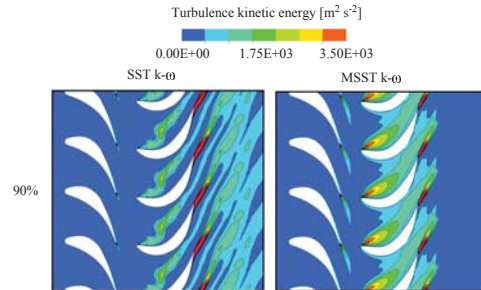


Figure 4. Predicted contours of the turbulence kinetic energy at 90% span.

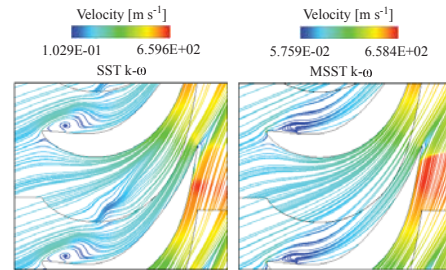


Figure 5. Predicted contours of the streamlines at 90% span.

blade rows. Moreover, the stator-rotor interaction strongly influences the flow phenomena. The wakes of stator blades enter the succeeding rotor blades, in which the flow is accelerated and rotated. Therefore, the accurate computational prediction of LP turbine flows requires the turbulence to be accurately modelled. Firstly, the influence of turbulence modelling has been analyzed with the turbulence properties. Figure 4 presents the contours of turbulence kinetic energy yielded by both models at 90% span. It is obvious that the maximum turbulent kinetic energy appears in the wake of the blades. The MSST  $k-\omega$  model predicted lower turbulent kinetic energy, particularly in the wake and at the downstream of rotor blade than the SST  $k-\omega$  model. This is resulted due to the viscosity modification and the effects of the added source terms, which increase the viscous dissipation considerably for the MSST  $k-\omega$  model case. Moreover, the rotor blade has been generated with high curvature and therefore, the flow deflection is higher at the leading edge of the pressure side of rotor blade. Due to that a separation bubble has been observed at rotor pressure side for 90% span (Figure 5) which contributes

to the turbulent kinetic energy in the mid passage of the rotor. The MSST  $k-\omega$  model estimated comparatively higher turbulent kinetic energy in the mid passage of the rotor.

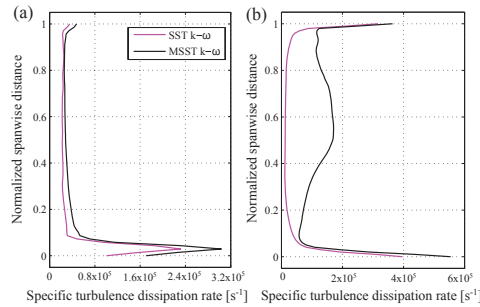


Figure 6. Predicted profiles of the specific turbulence dissipation rate at normalized spanwise distance (a) at the stator exit, and (b) outlet.

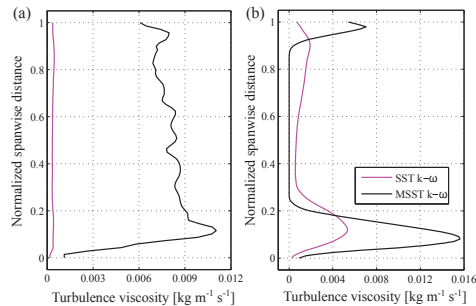


Figure 7. Predicted profiles of the turbulent viscosity at normalized spanwise distance (a) at the stator exit, and (b) outlet.

The turbomachinery flows are categorised as the wall-bounded flows in which fluid viscosity plays an important role in transport phenomena, particularly near wall surfaces. Also, the rapid variation of flow variables occurs within the boundary layer regions. These flows consist of a spectrum of different scales (eddy sizes). These structures are deformed and stretched by

the fluid dynamics. These eddy structures break into smaller eddies. This phenomenon continues until the energy is transported to smaller and smaller structures. However, at the end, the kinetic energy is dissipated by the viscosity of the fluid. The whole process of transport of energy from the large scale of injection to the small dissipative scale, through the hierarchy of eddies is known as the turbulent cascade. Therefore, it is worthwhile to examine the effect of model modification on turbulence properties which are responsible for taking into account above mentioned turbulent process. The predicted circumferential average profiles of specific turbulence dissipation rate and turbulent viscosity for both the models are displayed in Figures 6 and 7. The stator exit is at the 20% axial chord distance of stator blade from the trailing edge of stator blade. It can be seen that the specific turbulence dissipation rate is notably high near the hub surface due to boundary layer effect. At outlet, the rate of specific turbulence dissipation is significantly higher at hub and shroud surfaces due to the turbulent cascade process. The MSST  $k-\omega$  model yielded a higher value of specific turbulence dissipation rate at both planes than the SST  $k-\omega$  model. Further, the MSST  $k-\omega$  model estimated higher turbulent viscosity than the SST  $k-\omega$  model. This is likely due to the modified viscosity which contains the production to dissipation ratio. Particularly, the turbulent viscosity is maximum near hub and shroud surfaces for outlet plane.

The expansion rates at stator and rotor blades, particularly at the spanwise direction, are distinct from each other. In Figure 8, the contours of vapour temperature are displayed for both models. Some variation has been observed in temperature profiles at both planes after model modification, particularly at the throat region and the downstream of it, around trailing edge and in the wake regions of rotor blade. It is obvious that the flow temperature is higher in the blade wakes due to flow mixing. In the case of MSST  $k-\omega$  model, the increased viscous dissipation influenced the temperature distribution via energy source, which affected the heat transfer rates. Therefore, the temperature level is higher for the MSST  $k-\omega$  model than the SST  $k-\omega$  model in rotor blade wakes.

In condensing steam flow, the nucleating and growth processes are quite sensitive to local pressure distribution and expansion rate. Figure 9 shows the contours of the flow expansion rate for both models. The expansion rate varies in the blade passage, in which it is very low at the entrance and extremely high in the vicinity of the throat. As a consequence, the zone of rapid condensation occurs downstream of the throat region. As discussed previously, the rate of viscous dissipation is higher for the MSST  $k-\omega$  model. Consequently, the Reynolds stresses are lower due to lesser eddy viscosity. Therefore, the shear effect is minor which influences on the flow parameters in the MSST  $k-\omega$  model. Hence, the flow expansion in the MSST  $k-\omega$  model is higher than the SST  $k-\omega$  model.

The nucleation rate is especially large near the suction surface and at the trailing edge of the pressure surface in blade. This

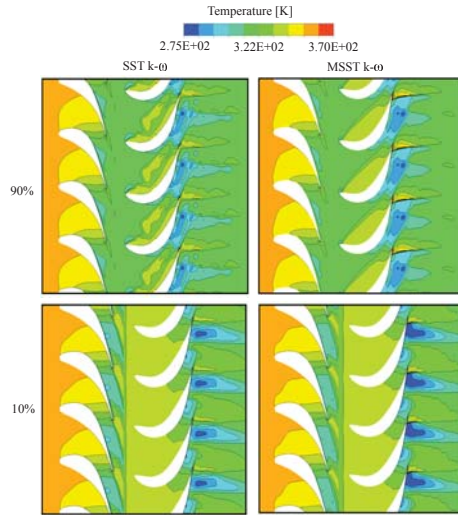


Figure 8. Predicted contours of the vapour temperature at spanwise planes.

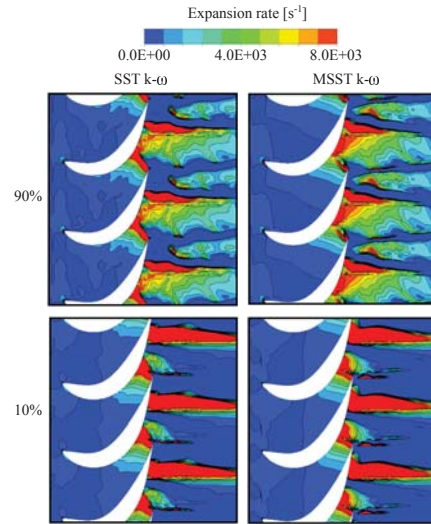


Figure 9. Predicted contours of the flow expansion rate of rotor at spanwise planes.

is caused by rapid acceleration and consequent high subcooling. The contours of subcooling and nucleation rate for both models are presented in Figures 10 and 11. The results show that the critical conditions for wetness formation have been accomplished near the hub surface for the stator within the throat region where the flow becomes transonic. The level of subcooling was reduced from the hub to the shroud surfaces for stator. While for rotor blade passage the level of subcooling was decreased from the shroud to the hub surfaces. The highest subcooling level reached was 36 K. However, some differences have been observed between the models. The MSST  $k-\omega$  model estimated a higher subcooling level than the SST  $k-\omega$  model. The intensity of nucleation is weaker from the hub to the shroud surfaces of stator. In addition, the nucleation region at 90% span is more uniformly distributed at rotor inlet. However, the nucleation is zeroed at the downstream of the interface at 10% and 50% span due to mixing plane assumption. The MSST  $k-\omega$  model yielded a wider nucleation region than the SST  $k-\omega$  model. Moreover, the expansion process is extended slightly to the downstream due to the turbulent viscosity modification and the source terms addition. Therefore, the nucleation region for the MSST  $k-\omega$  model has been shifted slightly towards the downstream. Also, the level of subcooling was not strong enough to attain thermal equilibrium, and consequently the secondary nucleation zone appeared

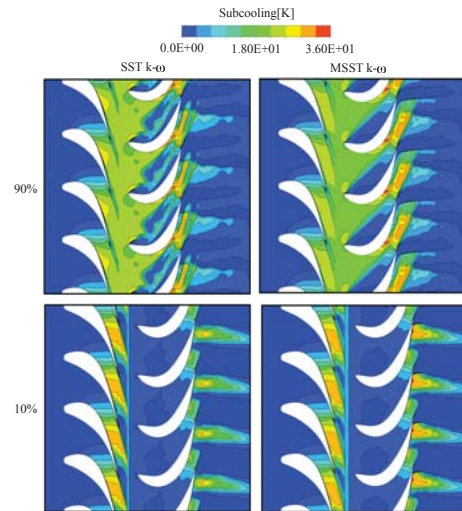


Figure 10. Predicted contours of the subcooling at spanwise planes.

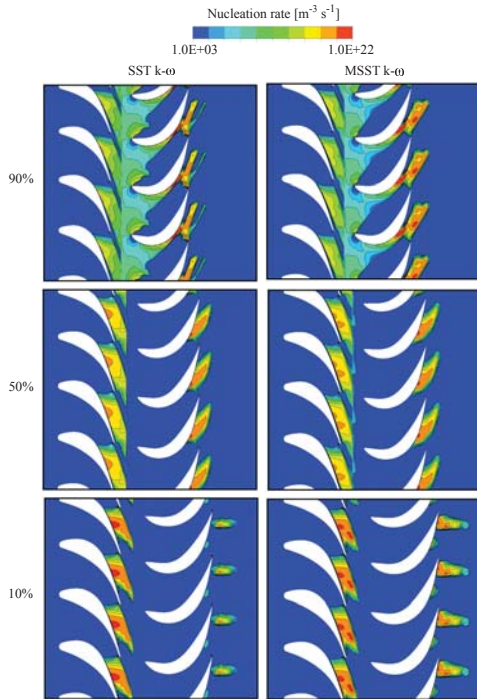


Figure 11. Predicted contours of the nucleation rate at spanwise planes.

in the rotor passage for all radial planes in both models. The intensity of secondary nucleation was decreased from the shroud to the hub surfaces of rotor for both the cases. The Wilson point fluctuates due to wake-chopping in the LP turbine flow. In the steady state calculations of this work, the secondary nucleation is stronger. This could be explained by the fixed Wilson point. The secondary nucleation region was larger for the MSST  $k-\omega$  model than the SST  $k-\omega$  model.

Further, the predicted contours of droplet average radius for both models at spanwise surfaces are displayed in Figure 12. If a large number of tiny liquid droplets nucleate, their growth is lower. In contrast, when a lower nucleation results, the growth rate is predominant and larger droplets are present. It can be seen that the droplet radius near the hub surface is lower due to large number of droplet. A larger droplet average radius has been observed near shroud surface. The turbulence modelling influenced the droplet sizes. The droplet radius distribution across the pas-

sage is mostly dependent on the total number of droplets created during the nucleation process, which is influenced by the distinct expansion rates along the blade passage and also the interaction between the trailing edge shock waves and the nucleation zone. It can be observed that, the growth rate is delayed in the case of MSST  $k-\omega$  model due to larger nucleation region. Subsequently, the number of droplets estimated by the MSST  $k-\omega$  model is lower compared to the SST  $k-\omega$  model. Therefore, the MSST  $k-\omega$  model yielded larger droplet average radius than the SST  $k-\omega$  model.

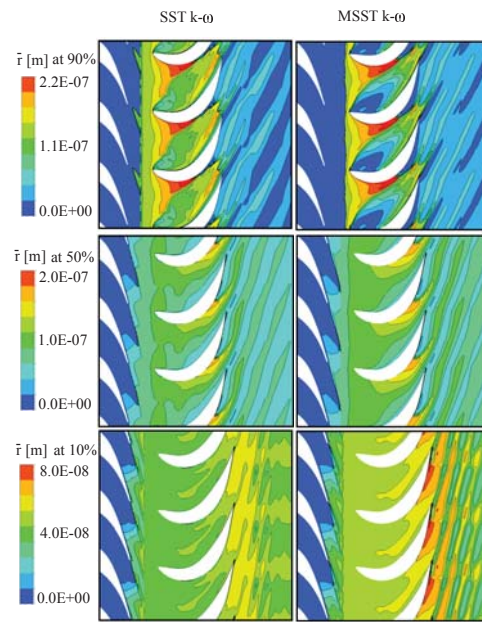


Figure 12. Predicted contours of the droplet average radius at spanwise planes.

The contours of wetness fraction are presented in Figure 13. It is clear that the level of wetness fraction increased from hub to shroud surfaces. Maximum wetness was observed in the downstream of rotor. It is clear that the SST  $k-\omega$  model yielded higher wetness distribution than the MSST  $k-\omega$  model. However, the MSST  $k-\omega$  model predicted higher wetness fraction up to 7.5% at 90% span of rotor blade, particularly at separation bubble region of pressure side and at suction surface near trailing edge. Around

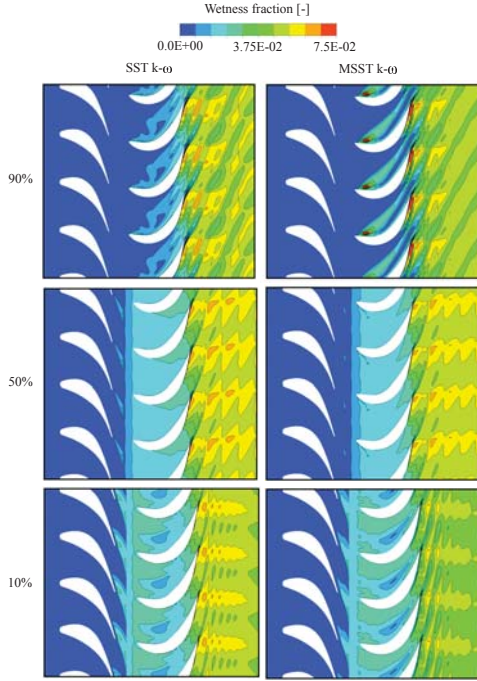


Figure 13. Predicted contours of the wetness fraction at spanwise planes.

separation bubble region, the mass generation rate is considerably high which increased the wetness fraction. While at suction surface near trailing edge the wetness level is higher due to separation and secondary flow effect. Moreover, the wetness fraction is lower in the blade wakes and this is the region where flow mixing is prominent. Hence, the temperature is higher, which reduces the wetness fraction.

Figure 14 presents the predicted contours of the entropy generation for both models. Regions of steep velocity gradients such as blade wakes, edges of separated regions and vortices, in which the shear stresses are relatively high, are responsible for a large amount of entropy generation. Moreover, the flow turbulence which governs the heat, mass, and momentum transfer processes is considerably high in these regions as shown in Figure 15. It can be observed that the maximum rate of entropy is generated at the suction surface of the blade. Further, in the case of stator, the entropy generation is lower at the 90% span surface than other

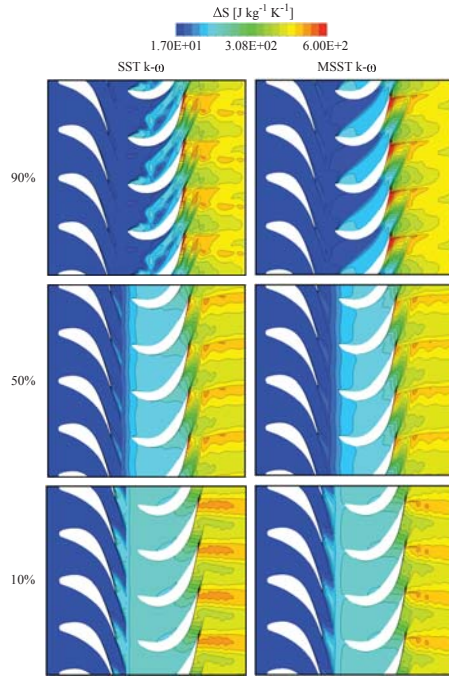


Figure 14. Predicted contours of the entropy rise at spanwise planes.

surfaces due to larger nucleation zone. In contrast, at the 90% span surface of the rotor, the production of entropy is raised because of very strong rotor secondary flow. However, the entropy production at the rotor is notably high compared to the stator due to the rapid release of latent heat by the droplets, flow separation and secondary flow effect. The SST  $k-\omega$  model predicted a higher entropy generation compared to the MSST  $k-\omega$  model particularly in the blade wake region for the 10% and 50% span surfaces, while the MSST  $k-\omega$  model yielded higher entropy near to the trailing edge of rotor at the 90% span surface likely due to the higher turbulent dissipation in that region.

Further, the losses which occur due to the irreversible heat and mass transfer during the condensation process are estimated. In this work, the Markov energy loss coefficient based on the entropy increase was calculated and it can be defined as  $\zeta = \frac{T_2 \Delta s}{0.5u_2^2}$ , where  $\Delta s$  refers to the increment in a specific entropy. Here,  $T_2$  and  $u_2$  refer the local static temperature and relative velocity, respectively. The loss coefficient was divided into two compo-

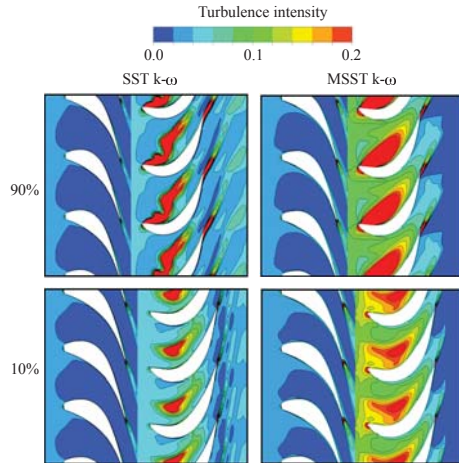


Figure 15. Predicted contours of the turbulence intensity at spanwise planes.

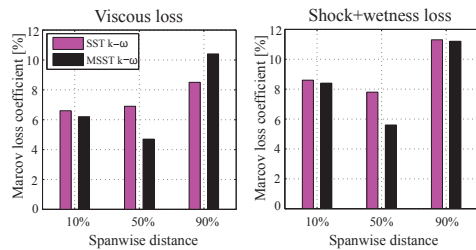


Figure 16. Predicted Markov loss coefficients.

ments: (i) shockwave plus wetness loss, which was calculated from the mass-averaged values across a section of the traverse plane excluding the wake regions, and (ii) viscous loss, which was calculated by subtracting the shockwave and wetness loss from the mass-averaged loss across the entire pitch at the traverse plane [14]. For the Markov loss coefficient estimation, all the parameters were calculated by the circumferential average at different span along the traverse plane. The traverse plane is located at the position of about 25% axial chord length from the rotor trailing edge in the axial direction. Figure 16 shows the calculated loss information. It can be seen that the SST  $k-\omega$  model predicted higher viscous loss compared to the MSST  $k-\omega$  model for the 10% and 50% span surfaces because of a large amount of

entropy production in the blade wake of rotor (Figure 14). Moreover, it is observed that the value of viscous loss at the 90% span with the MSST  $k-\omega$  was higher than with the SST  $k-\omega$  model due to intense viscous dissipation at the edges of the separated region immediately behind the trailing edge of rotor. The MSST  $k-\omega$  turbulence model predicted lower wetness loss due to higher viscous dissipation. It can be observed that the MSST  $k-\omega$  model yielded lower shock plus wetness loss compared to the the SST  $k-\omega$  model for all span surfaces.

## 5 CONCLUSIONS

The condensing steam flows at LP turbine involve rapid phase change, momentum and heat transport phenomena in which the role of turbulence is significant. Thus, the precise condensing steam flow prediction needs proper turbulence modelling. In this work, the preliminary study of the influence of turbulence modelling on non-equilibrium homogeneously condensing steam flow in 3D stator-rotor stage is discussed. For this purpose, the Eulerian-Eulerian approach based on compressible RANS equations was used. The SST  $k-\omega$  turbulence model was modified by introducing the modulation of turbulence kinetic energy and its dissipation due to liquid droplets via source terms. Furthermore, the original definition of turbulent viscosity was modified by introducing production to dissipation ratio.

Firstly, the performance of MSST  $k-\omega$  model was illustrated at 2D nozzles and turbine stator cascade flows. It can be concluded that the MSST  $k-\omega$  model corresponded well with the test results and mimicked an accurate condensation process. The presented simulation results of a 3D stator-rotor stage case show that the inclusion of the source terms and modified turbulent viscosity at SST  $k-\omega$  model caused notably higher estimates of viscous dissipation and, therefore, the increased viscous dissipation altered the temperature distribution through energy source, which impacted the heat transfer rates. Consequently, the nucleation process and droplet growth rates were influenced by the model modification. It can be seen that the MSST  $k-\omega$  model yielded a higher subcooling level because of higher flow expansion. Subsequently, the nucleation region was expanded and the droplet growth rate was delayed. Therefore, the wetness fraction was decreased due to larger droplet sizes. It can be concluded that the increased viscous dissipation via model modification decreases wetness fraction.

The significance of turbulence modelling on the loss mechanism was also presented. For this purpose, the loss coefficients were estimated from the simulated results. The presented loss assessment demonstrates that after model modification the measure of shock plus wetness loss reduced. Also the viscous loss estimation was affected by the model modification and the viscous loss was decreased except near shroud surface. Based on the presented results, it is observed that the accurate computational modelling of wet-steam flow at LP turbine requires the

turbulence to be accurately modelled. Because an inaccurate prediction of turbulence may lead to an imprecise evaluation of the crucial phenomena of condensing flow and ultimately erroneous losses. However, this study is at an introductory stage in which the influence of unsteadiness is absent. Results show that the influence of turbulence modelling affected on wet-steam phenomena even with steady state simulations. Therefore, corresponding comparative simulations are encouraged concerning the further analysis of turbulence modelling influence to condensing steam flow at multistage LP turbine with unsteady condition.

#### ACKNOWLEDGEMENTS

The authors would like to acknowledge the Finnish Graduate School in Computational Fluid Dynamics and the Academy of Finland for the financial support and CSC-IT Center for Science, Finland for providing the scientific computing platform.

#### REFERENCES

- [1] Yamamoto, S., Sasao, Y., Sato, S., and Sano, K., 2007. "Parallel-implicit computation of three-dimensional multistage stator-rotor cascade flows with condensation". In Proc. 18th AIAA Computational Fluid Dynamics Conference, AIAA 2007-4460, Miami, Florida, USA, June.
- [2] Yamamoto, S., Sasao, Y., Kato, H., Satsuki, H., Ooyama, H., and Ishizaka, K., 2010. "Numerical and experimental investigation of unsteady 3-d wet-steam flows through two-stage stator-rotor cascade channels". In Proc. ASME Turbo Expo, GT2010-22796, Glasgow, UK, June 14-18, 1-9.
- [3] Starzmann, J., Schatz, M., Casey, M. V., Mayer, J. F., and Sieverding, F., 2011. "Modelling and validation of wet steam flow in a low pressure steam turbine". In Proc. ASME Turbo Expo, GT2011-45, Vancouver, Canada, June 6-10, 1-12.
- [4] Starzmann, J., Kaluza, P., Casey, M. V., and Sieverding, F., 2013. "On kinematic relaxation and deposition of water droplets in the last stages of low pressure steam turbines". *J. Turbomachinery*, **Vol. 136** (7), pp. 1-10.
- [5] Avetissian, A. R., Philippov, G. A., and Zaichik, L. I., 2008. "Effects of turbulence and inlet moisture on two-phase spontaneously condensing flows in transonic nozzles". *Int. J. Heat Mass Transfer*, **Vol. 51**, pp. 4195-4203.
- [6] Patel, Y., Patel, G., and Turunen-Saaresti, T., 2015. "Influence of turbulence modelling on non-equilibrium condensing flows in nozzle and turbine cascade". *Int. J. Heat Mass Transfer*, **Vol. 88**, pp. 165-180.
- [7] Patel, Y., Turunen-Saaresti, T., Patel, G., and Grönman, A., 2014. "Numerical investigation of turbulence modelling on condensing steam flows in turbine cascade". In Proc. of ASME Turbo Expo, GT2014-26307, Düsseldorf, Germany, June 16-20, 1-14.
- [8] Guha, A., 1998. "Computation, analysis and theory of two-phase flows". *The Aeronautical Journal*, **Vol.102**, pp. 71-82.
- [9] Gerber, A. G., and Kermani, M. J., 2004. "A pressure based Eulerian-Eulerian multi-phase model for non-equilibrium condensation in transonic steam flow". *Int. J. Heat Mass Transfer*, **Vol. 44**, pp. 2217-2231.
- [10] McDonald, J. E., 1962. "Homogeneous nucleation of vapour condensation. I -thermodynamic aspects". *Am. J. Physics*, **Vol. 30**, pp. 870-877.
- [11] Kantrowitz, A., 1951. "Nucleation in very rapid vapour expansions". *J. Chem. Phys.*, **Vol.19**, pp. 1097-1100.
- [12] Gyarmathy, G., 1976. *Condensation in flowing steam*. A von Karman Institute Book on Two-Phase Steam Flow in Turbines and Separators, Hemisphere, London.
- [13] Menter, F. R., 1994. "Two-equation eddy-viscosity turbulence models for engineering applications". *AIAA Journal*, **Vol. 32** (8), pp. 1598-1605.
- [14] White, A. J., Young, J. B., and Walters, P. T., 1996. "Experimental validation of condensing flow theory for a stationary cascade of steam turbine blade". *Philos. Trans. Roy. Soc. London.*, **Vol. A 354**, pp. 59-88.
- [15] Moore, M. J., Walters, P. T., Crane, R. I., and Davidson, B. J., 1973. "Predicting the fog drop size in wet steam turbines". In Wet Steam 4 Conference, Institute of Mechanical Engineers (UK), University of Warwick, paper C37/73.
- [16] Moses, C. A., and Stein, G. D., 1978. "On the growth of steam droplets formed in a Laval nozzle using both static pressure and light scattering measurements". *J. Fluids Eng.*, **Vol. 100**, pp. 311-322.



## ACTA UNIVERSITATIS LAPPEENRANTAENSIS

700. OINONEN, MINNA. Management of customer co-development in business-to-business markets. 2016. Diss.
701. ALATALO, SARA-MAARIA. Hydrothermal carbonization in the synthesis of sustainable porous carbon materials. 2016. Diss.
702. UZHEGOV, NIKITA. Design and material selection of high-speed rotating electrical machines. 2016. Diss.
703. RICHTER, CHRIS. Digital collaborations and entrepreneurship – the role of shareconomy and crowdsourcing in the era of smart city. 2016. Diss.
704. JAFARI, SHILA. Investigation of adsorption of dyes onto modified titanium dioxide. 2016. Diss.
705. PATEL, YOGINI. Computational modelling of non-equilibrium condensing steam flows in low-pressure steam turbines. 2016. Diss.
706. LEVCHUK, IRINA. Titanium dioxide based nanomaterials for photocatalytic water treatment. 2016. Diss.
707. AMOUR, IDRISSE. Variational ensemble kalman filtering applied to data assimilation problems in computational fluid dynamics. 2016. Diss.
708. SHESTAKOVA, MARINA. Ultrasound-assisted electrochemical treatment of wastewaters containing organic pollutants by using novel Ti/Ta<sub>2</sub>O<sub>5</sub>-SnO<sub>2</sub> electrodes. 2016. Diss.
709. OLEKSIENKO, OLGA. Physico-chemical properties of sol-gel synthesized titanosilicates for the uptake of radionuclides from aqueous solutions. 2016. Diss.
710. PATALA, SAMULI. Advancing sustainability-oriented innovations in industrial markets. 2016. Diss.
711. KUORIKOSKI, TERO. Kohti resonoivaa urheilujohtamista – Tavoitteen muodostuminen urheilun kentässä. 2016. Diss.
712. LAHTELA, VILLE. Improving the properties of solid Scots pine (*Pinus sylvestris*) wood by using modification technology and agents. 2016. Diss.
713. NEVARANTA, NIKO. Online time and frequency domain identification of a resonating mechanical system in electric drives. 2016. Diss.
714. FANG, CHAO. Study on system design and key technologies of case closure welding for ITER correction coil. 2016. Diss.
715. GARCÍA PÉREZ, MANUEL. Modeling the effects of unsteady flow patterns on the fireside ash fouling in tube arrays of kraft and coal-fired boilers.
716. KATTAINEN, JARI. Heterarkkisen verkostoyhteistyön johtamistarpeet verkoston muotoutumisvaiheessa. 2016. Diss.
717. HASAN, MEHDI. Purification of aqueous electrolyte solutions by air-cooled natural freezing. 2016. Diss.
718. KNUTAS, ANTTI. Increasing beneficial interactions in a computer-supported collaborative environment. 2016. Diss.

719. OVASKA, SAMI-SEPPO. Oil and grease barrier properties of converted dispersion-coated paperboards. 2016. Diss.
720. MAROCHKIN, VLADISLAV. Novel solutions for improving solid-state photon detector performance and manufacturing. 2016. Diss.
721. SERMYAGINA, EKATERINA. Modelling of torrefaction and hydrothermal carbonization and heat integration of torrefaction with a CHP plant. 2016. Diss.
722. KOTISALO, KAISA. Assessment of process safety performance in Seveso establishments. 2016. Diss.
723. LAINE, IGOR. Institution-based view of entrepreneurial internationalization. 2016. Diss.
724. MONTECINOS, WERNER EDUARDO JARA. Axial flux permanent magnet machines – development of optimal design strategies. 2016. Diss.
725. MULTAHARJU, SIRPA. Managing sustainability-related risks in supply chains. 2016. Diss.
726. HANNONEN, JANNE. Application of an embedded control system for aging detection of power converter components. 2016. Diss.
727. PARKKILA, JANNE. Connecting video games as a solution for the growing video game markets. 2016. Diss.
728. RINKINEN, SATU. Clusters, innovation systems and ecosystems: Studies on innovation policy's concept evolution and approaches for regional renewal. 2016. Diss.
729. VANADZINA, EVGENIA. Capacity market in Russia: addressing the energy trilemma. 2016. Diss.
730. KUOKKANEN, ANNA. Understanding complex system change for a sustainable food system. 2016. Diss.
731. SAVOLAINEN, JYRKI. Analyzing the profitability of metal mining investments with system dynamic modeling and real option analysis. 2016. Diss.
732. LAMPINEN, MATTI. Development of hydrometallurgical reactor leaching for recovery of zinc and gold. 2016. Diss.
733. SUHOLA, TIMO. Asiakaslähtöisyys ja monialainen yhteistyö oppilashuollossa: oppilashuoltoprosessi systeemisenä palvelukokonaisuutena. 2017. Diss.
734. SPODNIAK, PETR. Long-term transmission rights in the Nordic electricity markets: An empirical appraisal of transmission risk management and hedging. 2017. Diss.
735. MONTONEN, JUHO. Integrated hub gear motor for heavy-duty off-road working machines – Interdisciplinary design. 2017. Diss.
736. ALMANASRAH, MOHAMMAD. Hot water extraction and membrane filtration processes in fractionation and recovery of value-added compounds from wood and plant residues. 2017. Diss.
737. TOIVANEN, JENNI. Systematic complaint data analysis in a supply chain network context to recognise the quality targets of welding production. 2017. Diss.

